DEVELOPMENT OF NOVEL SUPER-RESOLUTION AND VOLUME IMAGING TECHNIQUES FOR VISUALISING CELLULAR FUNCTION AND ULTRASTRUCTURE IN BIOMEDICAL APPLICATIONS

by

JONAS PHILIPP EUCHNER

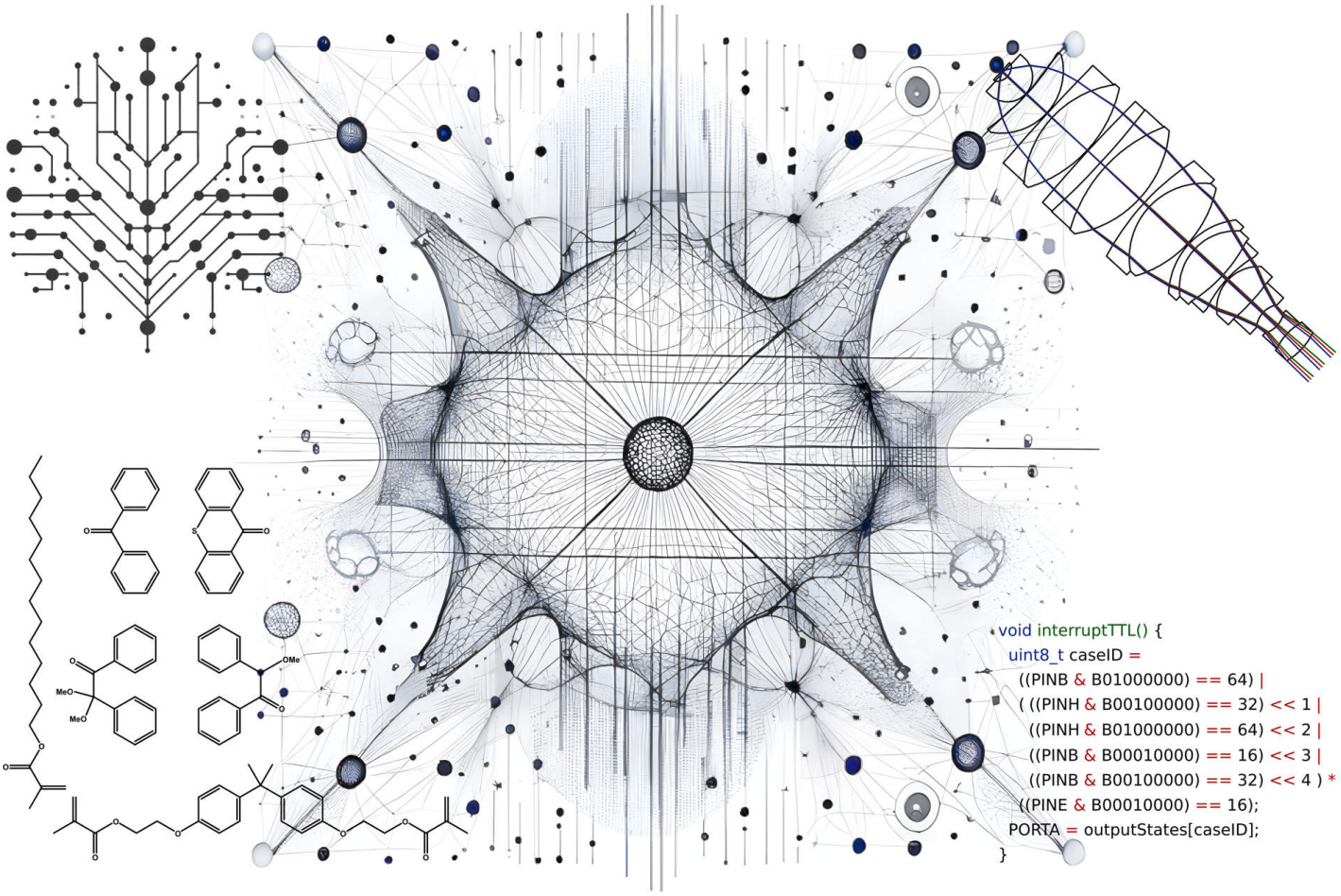

A thesis submitted to the University of Birmingham for the degree of DOCTOR OF PHILOSOPHY

Institute of Cardiovascular Sciences
College of Medical and Dental Sciences
University of Birmingham
January 2024

Declaration

I hereby declare that the work presented within this thesis titled ”Development of novel super-resolution and volume imaging techniques for visualising cellular function and ultrastructure in biomedical applications” is my own work, unless otherwise stated. The work was submitted to the Institue of Cardiovascular Sciences, College of Medical and Dental Sciences, University of Birmingham, United Kingdom as fulfilment of the degree of Doctor of Philosophy.

- Jonas Philipp Euchner

Abstract

Fluorescence and electron microscopy are at the forefront of resolving the complex intracellular dynamics at the cellular nanoscale, a task that continues to push the limits of biomedical research.

Within this thesis significant advancements in cellular nanoscale imaging are achieved through the development of novel super-resolution and volumetric imaging techniques. Central to this work is the custom-built super-resolution microscope, which underpins the methodological advancements elaborated in the subsequent chapters. These developments tackle key challenges in microscopy, including determining the degree of labelling for protein-tags, preserving fluorophores in acrylic resins for correlative light-electron microscopy (CLEM) and implementing novel super-resolution microscopy techniques in a cellular context.

Furthermore, the thesis demonstrates the utilisation of advanced super-resolution techniques in various biomedical applications. It unravels the structural changes of liver sinusoidal endothelial cells in a senescent microenvironment, shedding light on the underlying response mechanisms correlated to hepatocellular cancer.

Last but not least, a major focus within the thesis is put on the refinement and application of *in-resin* super-resolution microscopy as well as volumetric CLEM, facilitated by novel resin compositions. These compositions quantitatively preserve fluorophores during embedding, promising markedly improved imaging fidelity in super-resolution and volumetric CLEM. The findings within this thesis will have widespread implications in future research in resolving the functional organisation within the cellular ultrastructure.

Acknowledgement

First, I would like to thank Prof. Dirk-Peter Herten, for his continued support and guidance, as well as for allowing me the freedom to conduct my research independently when possible. His support has been important in shaping my growth as a scientist.

I also wish to thank the members of our UK lab, especially Stanimir Tashev for the collaborative work and the open exchange of ideas, Johan Hummert for assistance in programming and discussions on optical-engineering, Klaus Yserentant for encouraging me in my research ideas and assistance, and Yin Ho for engaging academic discussions.

I am grateful for the collaboration with various partners, both locally and internationally. I would like to mention Dan Nieves for the collaboration on ratiometric membrane PAINT, Dan Patten & Shishir Shetty for access and support with LSEC, and Irene Wacker & Rasmus Schröder for providing me with the opportunity to use their electron microscopes.

My PhD has benefitted from the scientific input of many throughout my academic career. I thank Richard Wombacher for his constant belief in my abilities, as well as Achim Wieczorek & Regina Wirth for their longstanding support.

This thesis was proofread by my supervisor, Dirk-Peter Herten, and my partner, Annabelle Kaiser, who provided valuable comments on language, spelling, and grammar. All corrections were carried out by myself.

Lastly, I would like to thank my parents, Silke & Werner Euchner, my sister Mira Kraft, and my partner, Annabelle Kaiser. Their continued belief in me, even from afar, has been the source of my positivity and strength.

Table of Contents

List of Figures

List of Tables

List of Abbreviations

3D	3-dimensional
ADU	analog-to-digital units
AF	Alexa Fluor
AFT	alignment by Fourier transform
AOTF	acousto-optic tunable filter
APD	avalanche photodiode
APTES	(3-aminopropyl)triethoxysilane
AS	Abberior Star
BDMA	benzyldimethylamine
BFP	back focal plane
BME	benzoin methyl ether
BP	benzophenone
BPF	band-pass filter
BSA	bovine serum albumine
BSE	back-scattered electron
bSOFI	balanced super-resolution optical fluctuation imaging
CI	confidence interval
CLEM	correlative light-electron microscopy
COMET	cost-function optimized maximal overlap drift estimation
CoPS	Counting by photon statistics
CRISP	continuous reflection interface sampling and positioning
CRLB	Cramer-Rao lower bound
Cy	cyanine
DDSA	dodecenyl succinic anhydride

DMEM	Dulbecco's modified eagle medium
DMPA	2,2-dimethoxy-2-phenylacetophenone
DOC	degree of colocalisation
DOL	degree of labelling
DOPC	1,2-dioleoyl-sn-glycero-3-phosphocholine
DPPC	1,2-dipalmitoyl-sn-glycero-3-phosphocholine
dSTORM	direct stochastical optical reconstruction microscopy
eGFP	enhanced green fluorescent protein
EGTA	ethylene glycol-bis(β-aminoethyl ether)-N,N,N',N'-tetraacetic acid
ELE	effective labelling efficiency
EM	electron microscopy
emCCD	electron-multiplying charge-coupled device
eN&B	enhanced number and brightness
Epi	epifluorescence
ESB	energy selective back-scattered electron detector
FBS	fetal bovine serum
FFT	fast Fourier transform
FIB	focused ion beam
FOV	field of view
FPS	frames per second
FRC	Fourier ring correlation
FWHM	full width at half maximum
GA	glutaraldehyde
GP	generalised polarisation
GUV	giant unilamellar vesicle

HDR	high dynamic range
HGF	hepatocyte growth factor
HILO	highly inclined and laminated optical sheet
HOMO	highest occupied molecular orbital
HW	half-wave plate
I/O	input-output
IFN	interferon
ITO	indium-tin-oxide
JOSEPH	justification of separation by employed persistent homology
LCD	liquid crystal display
LED	light-emitting diode
LP	long-pass filter
LSEC	liver sinusoidal endothelial cell
LUMO	lowest unoccupied molecular orbital
LUT	look-up table
MAP	matched achromatic doublet pair
MEA	2-mercaptoethylamine
MIET	metal-induced energy transfer
MOSFET	metal oxide semiconductor field-effect transistor
NA	numerical aperture
NdAc	neodymium acetate
NHS	N-hydroxysuccinimide
NMA	methyl-5-norbornene-2,3-dicarboxylic anhydride
NPC	nuclear pore complex
Oxa	oxazine
PAINT	point accumulation for imaging in nanoscale topography

PALM	photo activated localization microscopy
PBSA	photobleaching step analysis
PDF	probability density function
PFA	paraformaldehyde
PIPES	2,2'-(piperazine-1,4-diyl)di(ethane-1-sulfonic acid)
PLASMA	point label analysis of super-resolved membrane attributes
POI	protein of interest
ProDOL	protein-tag degree of labelling
PSF	point spread function
PTC	photon transfer curve
QE	quantum efficiency
quickPBSA	quick-photobleaching step analysis
RAMA27	rat mammary fibroblast cell 27
RAMM	rapid automated modular microscope
RCC	redundant cross-correlation
ROI	region of interest
ROXS	reducing and oxidising system
RTC	rat tail collagen
S	singlet state
SASP	senescence-associated secretory phenotype
sCMOS	scientific complementary metal–oxide–semiconductor
SD	standard deviation
SE	standard error
SE_{I}	type I secondary electron
SE_{II}	type II secondary electron
SEM	scanning electron microscopy

SFM	serum-free media
SMAP	super-resolution microscopy analysis platform
SMD	surface-mounted device
SMLM	single-molecule localisation microscopy
SNR	signal-to-noise ratio
SP	short-pass filter
SPAD	single-photon avalanche diode
STED	stimulated emission depletion
STORM	stochastic optical reconstruction microscopy
super-vCLEM	super-resolution and volumetric CLEM
T	triplet state
TEM	transverse electromagnetic mode
TIRF	total internal reflection fluorescence
TL	tube lens
TMA	4,N,N-trimethylaniline
TMP	trimethoprim
TMR	tetramethylrhodamine
TNF	tumour necrosis factor
TOMM20	translocase of outer mitochondrial membrane 20
TRIS	tris(hydroxymethyl)aminomethane
TTL	transistor-transistor-logic
TX	thioxanthone
UAc	uranyl acetate
UV	ultraviolet
VC	vibration criterion
VEGF	vascular endothelial growth factor

Chapter 1

General Introduction

1.1 Motivation

Fluorescence and electron microscopy have long been crucial for understanding the intricate network of life at its most fundamental level - the nanoscale interaction of proteins, DNA, lipids, and small molecules. These interactions shape the cellular homeostasis and thereby life itself. Since 2008, three Nobel Prizes have been awarded to advances in microscopy, namely fluorescent proteins, super-resolution microscopy and cryo-electron microscopy (1).

However, comprehending the complex network of connections at a functional and ultrastructural level still poses significant challenges to the scientific community (2, 3). In recent years, super-resolution microscopy has become increasingly pivotal in studying the spatio-temporal organisation of the cellular organisation (4). Yet, increasing the resolution does not necessarily correlate with a deeper understanding of the nanoscale dynamics. The development of novel methods accompanying super-resolution and volume imaging techniques stands at the forefront of this endeavour.

Here, the need for methods to calibrate cellular labelling efficiencies and thus recover the quantitative information are equally as important as the development of novel techniques to enhance the fidelity in correlative light-electron microscopy (5, 6). Within this work, challenges in fluorescence and electron microscopy are addressed to shed light on the unknown and to decipher the seemingly chaotic and yet structured network of interactions.

1.2 Fluorescence microscopy

Despite significant advances in the fields of biomedical research and fluorescence microscopy, understanding the intracellular dynamics continues to be a complex challenge to this day. To this end the need for novel fluorescence microscopy techniques remains pivotal in exploring the functional organisation of cellular biology. However, without the foundation laid by centuries of research and scientific discovery, the development of state-of-the-art and advanced microscopy techniques would not have been possible.

In 1665 Robert Hooke was the first scholar to study ”minute bodies” and hereby first described the cellular structure of biological objects (7). Similarly, in the 1670s, Antonie van Leeuwenhoek was able to observe ’animalcules’ - very small animals, culminating in the first report of single-celled organisms in 1676 (8). Today he is recognised as the father of microbiology (9). Over centuries the magnification and resolution of microscopes were continuously improved, with Joseph von Fraunhofer leading to a breakthrough by improving the optical resolution through the reduction of aberrations in optical elements (10). In 1873 Ernst Abbe was able to mathematically describe the fundamental principles of light microscopy with the Abbe diffraction limit (11):

$$d = \frac{\lambda}{2\mathrm{NA}} \tag{1.1}$$

where d is the minimal distance between two structures to resolve them as two objects, λ the wavelength of light and NA the numerical aperture of the system. Finally, in 1911 and 1913 the first fluorescence microscopy systems were developed (12). In 1941, Albert Coons was the first to develop fluorescently labelled antibodies, finally allowing the broad investigation of biological structures of interest (13). Following the invention

of immunolabelling, Shimomura isolated a fluorescent protein in 1961. In the 1990s genetic fusion proteins with fluorescent proteins allowed for investigation of intracellular processes in living cells and organisms (14, 15, 16).

Today, novel microscopy techniques and state-of-the-art research pushes the boundaries of feasibility. These methodologies necessitate fluorescent molecules with enhanced photophysical and structural properties to meet their high demands.

1.2.1 Photophysical principles of fluorescence

In 1852, George Stokes first reported on the red-shifted emission of fluorophores from incident light (Fig. 1.1 b). This shifted emission from incident light can be described using the energy states of fluorophores using a Jabłoński diagram (Fig. 1.1 a) (17, 18, 19). A photon can be absorbed by the fluorescent molecule, if the energy of the photon matches the energy difference between an excited singlet state (S) S_1-S_n and the ground state S_0 (Fig. 1.1 a - Absorption), thereby determining which excitation wavelength the fluorophore is sensitive to. Here, most commonly an electron from the highest occupied molecular orbital (HOMO) (S_0) becomes excited into the lowest unoccupied molecular orbital (LUMO) (S_1). The energy can next be partially dissipated through vibrational relaxation, reducing the energy level of the excited molecule (Fig. 1.1 a - Vibrational relaxation). To re-transition into the ground state, the excited electron can either transition into a lower singlet state through internal conversion or by emission of a photon with energy corresponding to the remaining energy difference for the S_1-S_0 transition, which is the origin of fluorescence (Fig. 1.1 a - Internal conversion, fluorescence).

The Pauli exclusion principle states that every electron in an atom must have a unique combination of the four quantum numbers (principal, azimuthal, magnetic, and spin). After an electron is excited into an unoccupied orbital, the unpaired electron may undergo a spin inversion, leading to an intersystem crossing into a triplet state (T). In this state, the two electrons that previously occupied the same orbital now share the same spin orientation, preventing their recombination into the ground state as it would violate the Pauli exclusion principle (Fig. 1.1 a - Intersystem crossing) (20). This triplet state can only revert back into the ground state by a second intersystem crossing or through the release of a phosphorescent photon. The release of a photon from a triplet state often takes significantly longer with a further increase in red-shift (10^3-10^{10} ns compared to 10^{-1}-10^2 ns) (Fig. 1.1 a - Phosphorescence).

The energy lost through vibrational relaxation corresponds to the Stokes red-shift observed between the excitation and emission spectrum (Fig. 1.1 b). For a system with identical vibrational energy level spacing in the ground and excited state, the emission spectrum is a mirror image of the excitation spectrum as the same transitions are favourable in both excitation and emission (21). This mirror image property is often partially observed in experimental conditions (21).

Besides the photophysical aspects of excitation and emission, other photophysical aspects such as extinction coefficient, quantum yield, fluorescence lifetime, and photo-stability are key characteristics of fluorophores. The extinction coefficient is a measure of how much light is absorbed at a given wavelength, with higher extinction coefficients allowing for a higher brightness of fluorescence (22). Similarly, the quantum yield represents the probability of fluorescent emission of light from an absorbed photon.

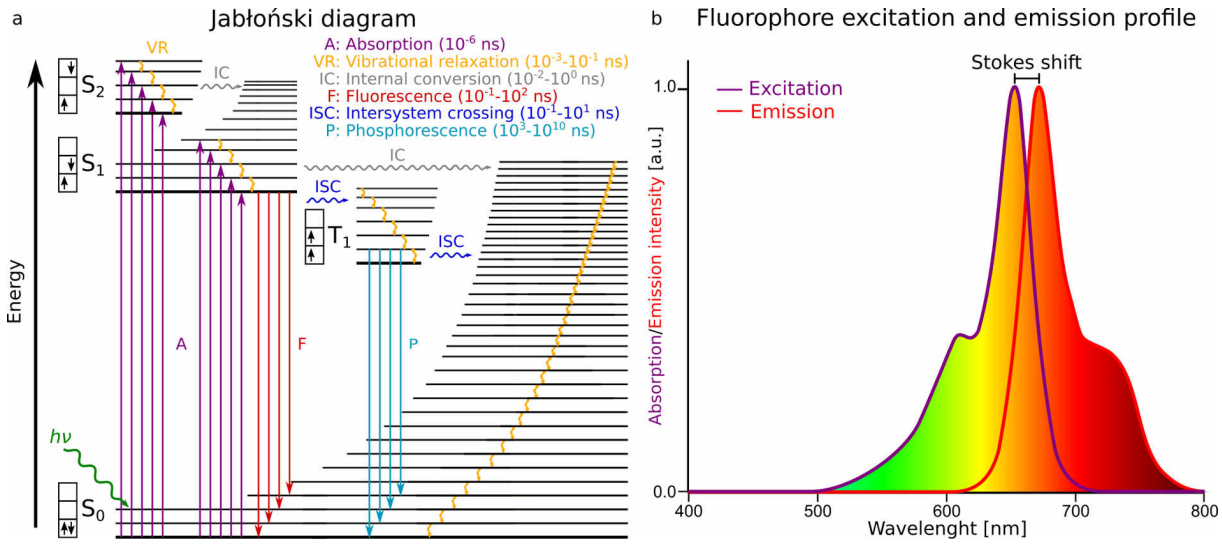

Fig. 1.1: Jabłoński diagram and excitation/emission profile of common organic emitters. a) Jabłoński diagram illustrating the energy states of fluorescent molecules. Absorption of a photon (A) can excite an electron from the singlet ground state (S_0) into an excited singlet state (S_n). Here some energy can be converted through vibrational relaxation (VR) before returning to the ground state by emission of a photon, in a phenomenon called fluorescence (F), or by non-radiative internal conversion (IC). Finally, excited electrons can experience a spin-inversion causing an intersystem crossing (ISC) into a long-lived triplet state (T), before returning into the ground state by emission of a photon from phosphorescence (P) or internal conversion (IC). b) Typical excitation and emission profile of an organic fluorophore highlighting the red-shifted emission (Stokes-shift). Adapted from Jablonski, Dzebo, and Đačanin Far *et al.* (17, 18, 19).

Therefore the brightness of a fluorophore is determined by the product of extinction coefficient and quantum yield.

Next, the fluorescence lifetime of a fluorophore is affected by many intrinsic and extrinsic factors. The lifetime is most critically affected by the energetic stabilisation of the excited state (23). Last but not least, the photostability of fluorophores and phototoxicity to the sample have become a major concern for demanding imaging techniques (24, 25, 26, 27). Here, far-red emitting dyes have become more popular as the excitation energy of red-shifted light is lower compared to blue-shifted light, reducing phototoxic effects (28). Additionally, modifications of the chromophore core have been established to reduce the likelihood of photochemical destruction of the chromophore from the excited radical state (24, 29). Here, a reducing and oxidising system (ROXS) provides both reducing and oxidising agents that can recover the ground state from the excited triplet state, preventing photobleaching (30).

Over the past decades, the most widely adopted organic fluorophores consist of mainly three core structures, namely cyanine-, oxazine- and xanthene-based fluorophores. The xanthene-based fluorophore category often also includes silicon rhodamines and carborhodamines, due to their structural similarity with this group (31, 32) (Fig. 1.2). Several other classes exist, with most relevant ones being coumarine, or BODIPY-based fluorophores (31). Besides these common structures, historic fluorophore developments still find extensive use in modern microscopy. Here, the DNA-specific dye Hoechst 33342 is a good example (33). Additionally, based on enhanced green fluorescent protein (eGFP), a variety of fluorescent proteins have been developed with optimised properties for e.g. brightness, spectral characteristics, photo- or chemical stability (34, 35, 36, 37, 38) (Fig. 1.2). Yet, fluorescent proteins are often less photostable compared to small organic fluorophores (3, 39).

1.2.2 Cellular labelling strategies

Having a plethora of organic fluorophores at hand, the previously mentioned immunolabelling is an established technique to label the protein of interest (POI) with the organic fluorophore. Here, the organic fluorophore is functionalised with a reactive acylating agent (40). Most commonly, a carboxylic group (R-COOH) of the fluorophore is functionalised with N-hydroxysuccinimide (NHS). This NHS-ester is reactive to amines, allowing for the coupling of the fluorophore to tertiary amine of lysines present in most proteins (41). In immunolabelling, the antibody is specific to an epitope of the POI and binds to it with high affinity and specificity. Using these fluorescently labelled antibody conjugates therefore allows for specific labelling of the target structure (Fig. 1.3 a). Besides direct

immunolabelling, where the antibody binding the epitope is already fluorescently labelled, indirect immunolabelling uses two antibodies where the first binds to the epitope

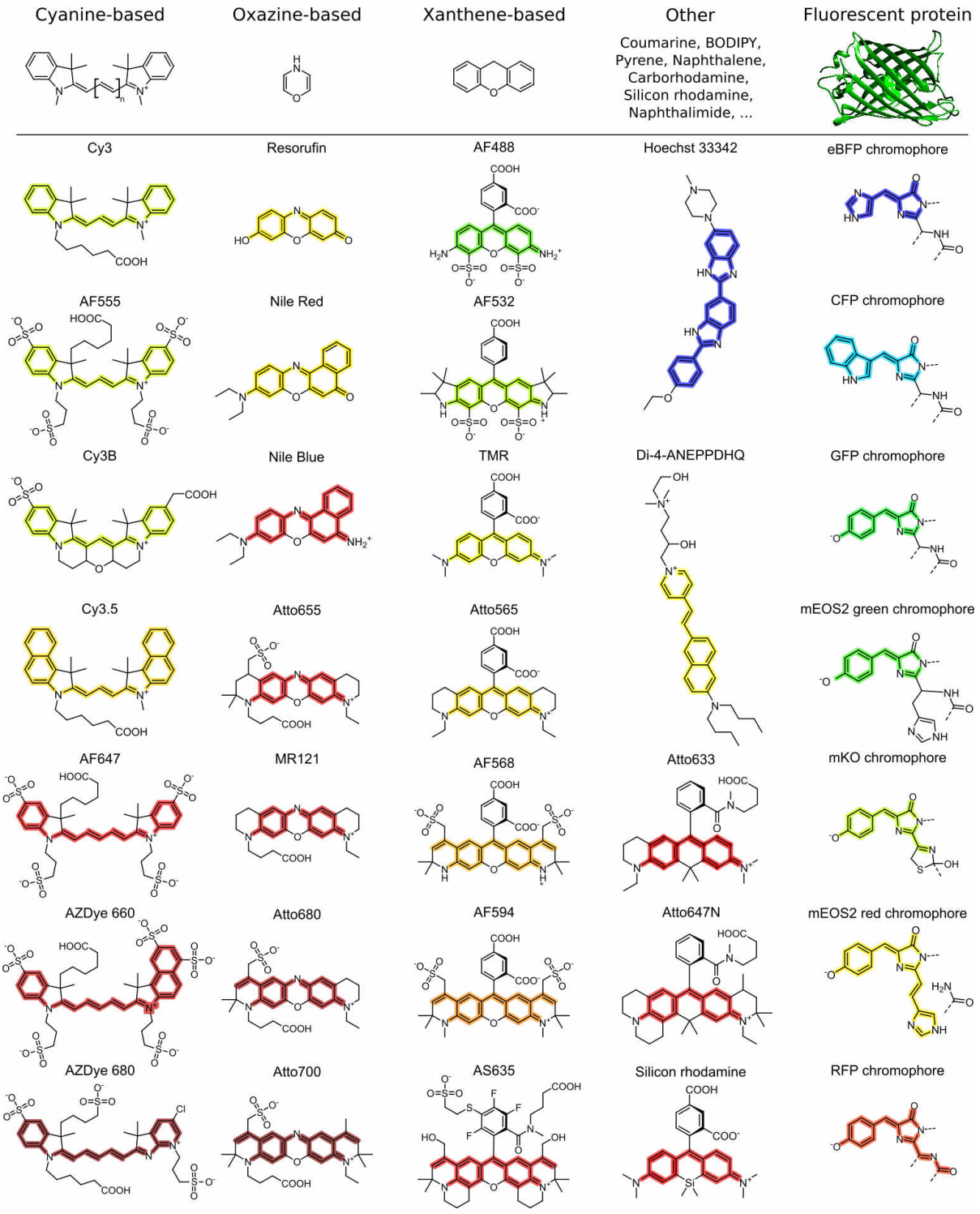

Fig. 1.2: Common organic fluorophore classes. Common organic fluorophores and fluorescent protein chromophores categorised by the core structure (Cyanine, oxazine and xanthene) as well as the colour-coded emission peak of the fluorescent system. Inspired by Grimm *et al.* (32) with additional data from Hell *et al.*, Tsien, and Shinoda *et al.* (24, 34, 35).

and the second is fluorescently labelled with specificity for the first antibody. Using indirect immunolabelling allows for a higher degree of freedom when choosing the fluorescent label and further can amplify the signal by having multiple antibodies bind to the first (42).

A second labelling strategy makes use of drugs and small molecules with high affinity to a specific structure. For example, the microtubule-specific drug Docetaxel is a known semi-synthetic analogue of Paclitaxel, a plant-based tetracyclic diterpene (43). Fluorescent labelling of this small molecule allows for staining of microtubules in living cells (Fig. 1.3 b). Similar labelling strategies exist for a select number of structures with known drugs or natural-product-based affinity probes, such as Phalloidin for actin (44, 45). Immunolabelling and if available affinity labelling are the only methods of choice for labelling samples of patient origin, as the POI cannot be genetically modified to have the fluorescent label directly attached to the POI.

Using genetically modified organisms allows for additional labelling strategies. The aforementioned fluorescent proteins can be genetically encoded into a fusion protein with the POI (Fig. 1.3 c) (15). Here, transient transfection of cells with a plasmid carrying the fusion protein allows for labelling of the target structure, while not modifying the cellular genome. Alternatively, using knock-in and knock-out techniques, the endogenous protein can be genetically modified to carry the fluorescent label of interest, while in theory not greatly affecting the native protein expression levels (46) (Fig. 1.3 c). Similarly, instead of genetic modification with a sequence expressing the fluorescent protein, protein-tags can be used, which allow for specific labelling with small organic fluorophores for higher photostability, increased brightness or variable other properties

specific to the vast selection of small-molecule fluorophores (Fig. 1.3 d). In recent years, the protein tags, HaloTag and SNAP-tag, have become the most widely adopted protein-tags (47, 48).

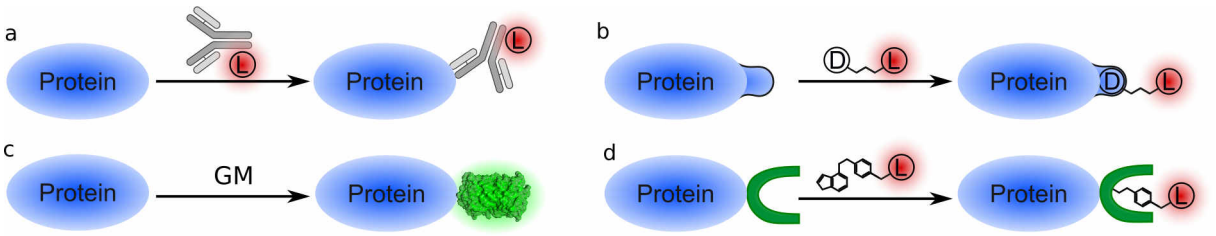

Fig. 1.3: Fluorescent labelling strategies. Schematic overview of four common labelling strategies in fluorescence microscopy. a,b) Affinity labelling of a protein of interest by a) immunolabelling or b) protein-specific small molecules coupled to a fluorescent moiety such as drug-fluorophore conjugates. c,d) Genetically modified fusion proteins using c) fluorescent proteins or d) protein-tags with subsequent labelling with fluorescent protein-tag substrates. Adapted from the master's thesis of Jonas Euchner (49).

1.2.3 Single-molecule localisation microscopy

In the late 1990s and early 2000s, several techniques were established (e.g. stimulated emission depletion (STED), stochastic optical reconstruction microscopy (STORM), photo activated localization microscopy (PALM), or point accumulation for imaging in nanoscale topography (PAINT)), allowing to resolve structures below the Abbe diffraction limit (Eq. 1.1) (50, 51, 52, 53, 54, 55). Among the established techniques, a subset of techniques (STORM, PALM, PAINT) utilised the principle of single-molecule localisation microscopy (SMLM). Here, the emission of single molecules is temporally separated by introducing a blinking of the fluorophores (Fig. 1.4). For a single emitter, the centre of localisation can be determined with high accuracy (Eq. 1.2) (51). Quickly the capabilities of these techniques were expanded upon, allowing for easier application, multi-colour imaging, or 3D localisation microscopy (56, 57, 58). In direct stochastical optical reconstruction microscopy (dSTORM) the blinking of fluorophores is established through pumping of the fluorophores into a long-lived dark state with stochastic recovery of

the ground state that is tunable using irradiation with blue-shifted light (56, 59). PAINT on the other hand uses transient binding of a diffusing fluorescent probe which can be localised accurately when immobilised during binding, before being bleached or released from the target (60).

The localisation precision of these blinking events can be determined using Eq. 1.2, given the point spread function (PSF) width (σ_{PSF}), the detector pixel width (a), the background intensity (N_{bg}) and the number of photons (N) (61, 62).

$$\sigma_{\mathrm{Loc}} = \sqrt{\left(\frac{\sigma_{\mathrm{PSF}}^2 + \frac{a^2}{12}}{N}\right)\left(\frac{16}{9} + \frac{8\pi(\sigma_{\mathrm{PSF}}^2 + \frac{a^2}{12})N_{\mathrm{bg}}}{Na^2}\right)} \tag{1.2}$$

Acquiring 10^4-10^5 frames allows for the reconstruction of a super-resolved image using the pointillistic representation of coordinates (63) (Fig. 1.4). Here, the resolution is mostly dependent on the localisation precision of the emission event and the emitter density (4). To increase the localisation precision based on Eq. 1.2, only the brightness of emitters and the background intensity can be feasibly adjusted, demanding for brighter and more photostable fluorophores as well as improved labelling strategies. The PSF width cannot easily be reduced due to the existing diffraction limit of light, and the detector pixel width has an optimal sampling frequency (64). To resolve single emitters,

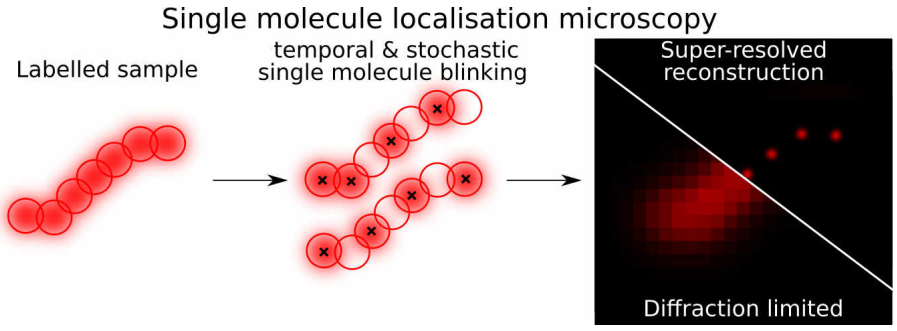

Fig. 1.4: Generalised principle of diffraction limited and single-molecule localisation microscopy. In SMLM, fluorophores are put into a prolonged dark-state, only stochastically emitting light. This "blinking" of single emitters allows for determination of the centre of emission with high accuracy. Acquiring a time series of several thousand frames allows for the reconstruction of a super-resolved image.

the PSF must be sampled over at least 2 pixels, as described by the Nyquist–Shannon sampling theorem (64, 65). Therefore, SMLM aims for a high signal-to-noise ratio with a high degree of labelling (DOL) as well as bright and photostable fluorophores for improved localisation precision and resolution. The full width at half maximum (FWHM) is a good approximation of the resolution limit as for an Airy pattern it is 2% larger than the Abbe diffraction limit and can be related to the localisation precision or total localisation error σ using Eq. 1.3 (66, 67):

$$\mathrm{FWHM} = 2\sqrt{2\ln(2)}\sigma \approx 2.355\sigma \tag{1.3}$$

However, the localisation precision must not necessarily correspond to the total localisation error. Further sources of error exist, including the temporal sample drift and vibrational localisation errors further reducing the resolution. Additionally, the site of fluorescence emission is not necessarily equivalent to the structure of interest. Various labelling techniques each have a nanometre-scale linkage-error between the POI and the centre of the detected PSF. Finally, polarised emission of labels and multiple labels in close proximity can lead to a reduced reconstruction quality from multi-emitter artefacts ($<$100 nm) and energy transfer-based reconstruction artefacts ($<$10 nm) (68, 69, 70).

1.2.4 Quantitative microscopy

Besides improving the spatial resolution in fluorescence microscopy, counting and estimating the POI density and absolute abundance has historically been a focus when studying the POI, as altered expression levels of a protein strongly relates to the cellular function (71, 72, 73, 74). Historically, relative comparison of intensity-levels was used as a comparative approach to detect changes in the relative abundance (71, 75).

Among the first absolute counting techniques, intensity-based counting was established (71, 76) (Fig. 1.5 a III). Here, homogeneous spatial illumination and detection is of high importance combined with a similar axial position of the structures. Still, the counting range is limited, as the uncertainty of a measured intensity scales with $\sigma_n \propto \sqrt{n}\sigma_1$, where n is the number of emitters and σ_1 the standard deviation in brightness of a single emitter (77).

Alternatively, instead of using the intensity from a single frame, the temporal bleaching and recovery of photobleaching steps can be used to determine the absolute emitter number of $\leq$35 emitters within a diffraction limited volume (Fig. 1.5 a IV) (78, 3). A third set of counting techniques relies on both the intensity and temporal fluctuation of the emitter to recover the absolute number or emitter concentration, as shown by using balanced super-resolution optical fluctuation imaging (bSOFI) or enhanced number and brightness (eN&B) (Fig. 1.5 a II) (79, 80, 81).

All aforementioned methods rely on the intensity-based information to some extent. Contrary, several other quantitative microscopy techniques have been developed utilising other photophysical principles, including Counting by photon statistics (CoPS). CoPS relies on the quantised nature of fluorescent emission (82). A single emitter can only emit a single photon within an excitation cycle, described as photon antibunching (83). Therefore, the second-order intensity correlation function at zero delay, equals zero for a single emitter (83). Using picosecond-pulsed laser excitation, each fluorophore can only be excited at most once, allowing for the absolute copy number determination from the ratio of multiple detection events in a multi-detector array (Fig. 1.5 a I) (82, 74).

Lastly, SMLM can be used to determine the absolute copy number. Here, various implementations exist, either using the ability to resolve the complex spatially and therefore determine the position and abundance of labels directly, or by utilising various frequency analyses (average off-time, temporal blinking density, photoswitching fingerprint analysis) (Fig. 1.5 a V,VI) (84, 68, 85).

However, in all quantitative microscopy techniques, only the fluorescent label number is determined (Fig. 1.5 b). Depending on the labelling strategy, an incomplete labelling of the POI is observed with typical DOLs between 20% to 70% for immunolabelling, protein-tag labelling (86, 74). Even homozygous knock-in cell lines, expressing a fluorescently labelled fusion protein, suffer from incomplete maturation efficiencies (74, 87). Furthermore, especially polyclonal and indirect immunolabelling can result in multiple labels for a single POI, further making a direct relation of labels to protein copy numbers difficult (74). Therefore, relating the emitter number to the POI is a challenge adressed in Chapt. 4 (Fig. 1.5 c).

Finally, to validate the correct counting, various strategies have been established using e.g. DNA origami, monomeric standards or protein complexes of known stoichiometry (Fig. 1.5 d) (88, 86, 76). However, performance on a standardised extracellular target do not necessarily reflect the cellular labelling. Similarly, counting standards using defined protein complexes have either proven challenging or are specific to a cellular compartment, making comparison of DOLs across cellular compartments difficult (88, 89).

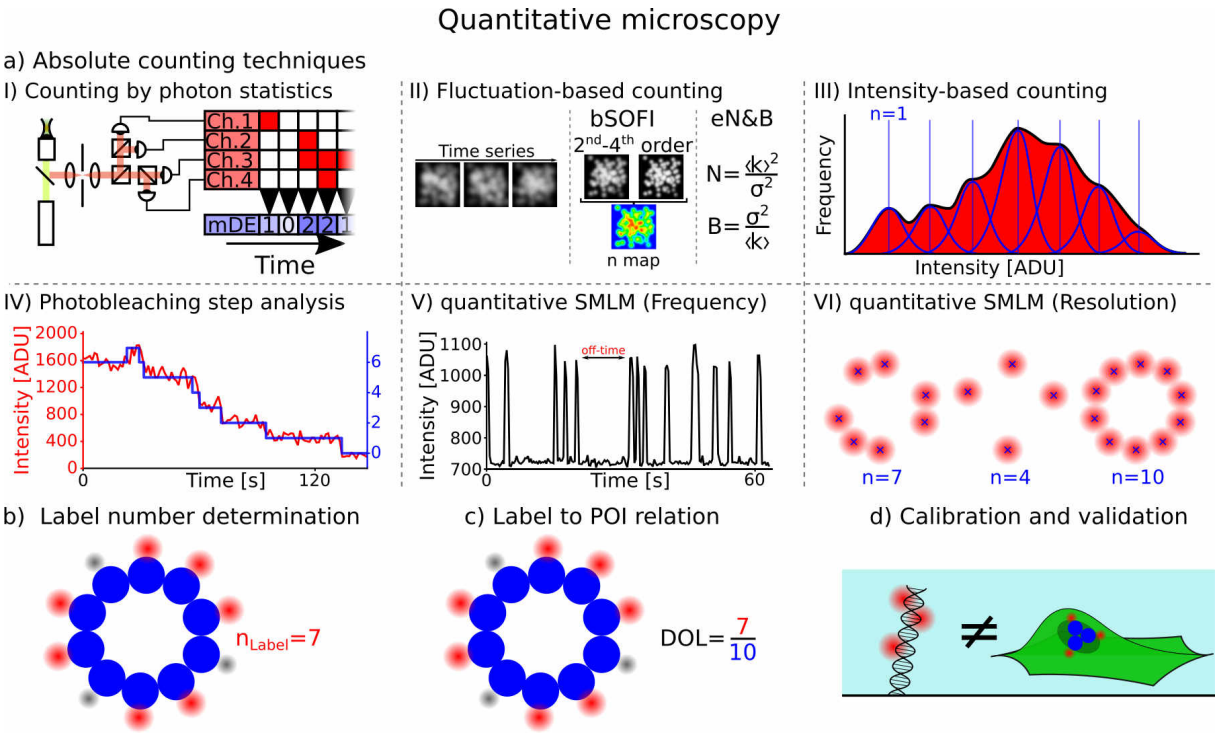

Fig. 1.5: Quantitative microscopy techniques. a) Comparison of available absolute counting techniques using microscopy, including I) counting by photon statistics, II) fluctuation-based counting, III) intensity-based counting, IV) photobleaching step analysis, V) frequency-based quantitative SMLM, and VI) resolution-based quantitative SMLM. b-d) Considerations when performing quantitative microscopy. b) In a first step, the absolute label number must be determined, followed by c) determination of the label to protein relationship, as most labelling techniques have an incomplete labelling and d) calibration and validation of the quantitative results within the structural context. Adapted from Grußmayer *et al.*, and Hummert *et al.* (73, 74).

1.3 Electron microscopy

Besides fluorescence microscopy in which photons are used for the imaging of the functional distribution of a POI, electron microscopy (EM) uses an electron beam to generate contrast from the electron-scattering cross-section of atoms and as such demands the use of a vacuum to mitigate the interaction with atoms in the air (90). Elements of higher atomic number correlate with a higher electron-scattering cross-section. For biological samples, most prevalent elements have low atomic numbers, resulting in a low EM contrast (91). Therefore, various heavy-metal contrasting agents (OsO_4, uranyl acetate (UAc), neodymium acetate (NdAc), or lead citrate) have been developed providing structure-specific contrast to lipids, proteins and/or nucleic acids (92, 93, 94, 95, 96). Therefore, electron microscopy is able to resolve the millimetre- to nanometre-scale structural cellular architecture, while only providing minimal functional context for a specific POI (Fig. 1.6 a) (97).

Depending on the elastic and inelastic scattering of the incoming electron beam, various detection methods exist. Transmission electron microscopy uses ultrathin sections of up to 100 nm where the transmission of electrons is recorded (98, 99). Contrary in scanning electron microscopy (SEM), several types of electrons can be recorded, including back-scattered electrons (BSE), type I secondary electrons (SE_I), and type II secondary electrons (SE_{II}) - each type having different properties and origin (100). BSE stem from the electron beam and are high-energy back-scattered electrons from elastic interaction with the nuclei (101). These can be specifically recorded using an energy selective back-scattered electron detector (ESB) (102). At 1.5 kV, BSE originate from a depth of up to 20 nm (101) (Fig. 1.6 b,c). Contrary, SE_I and SE_{II} stem from inelastic

scattering of the electron beam with nuclei generating secondary electrons, where SE_I originate from the first few nanometre (<5 nm) by interaction of the primary electron beam with the sample, and SE_{II} originate from interaction of BSE with the sample at up to 15 nm of depth (Fig. 1.6 b,c) (101). While complete separation of low-energy SE is not possible, various detector classes exist with higher detection preference of either SE type. Everhart–Thornley detectors generate a SE_{II}-rich image, while InLens detectors produce a SE_I-rich image (103). As SE_I are only generated on the site of impact, they have the highest spatial resolution, but suffer from weak contrast, charging artefacts and surface imperfections, while ESB generate the highest contrast but have the lowest spatial resolution as they interact with a larger sample volume (Fig. 1.6 c) (103, 101).

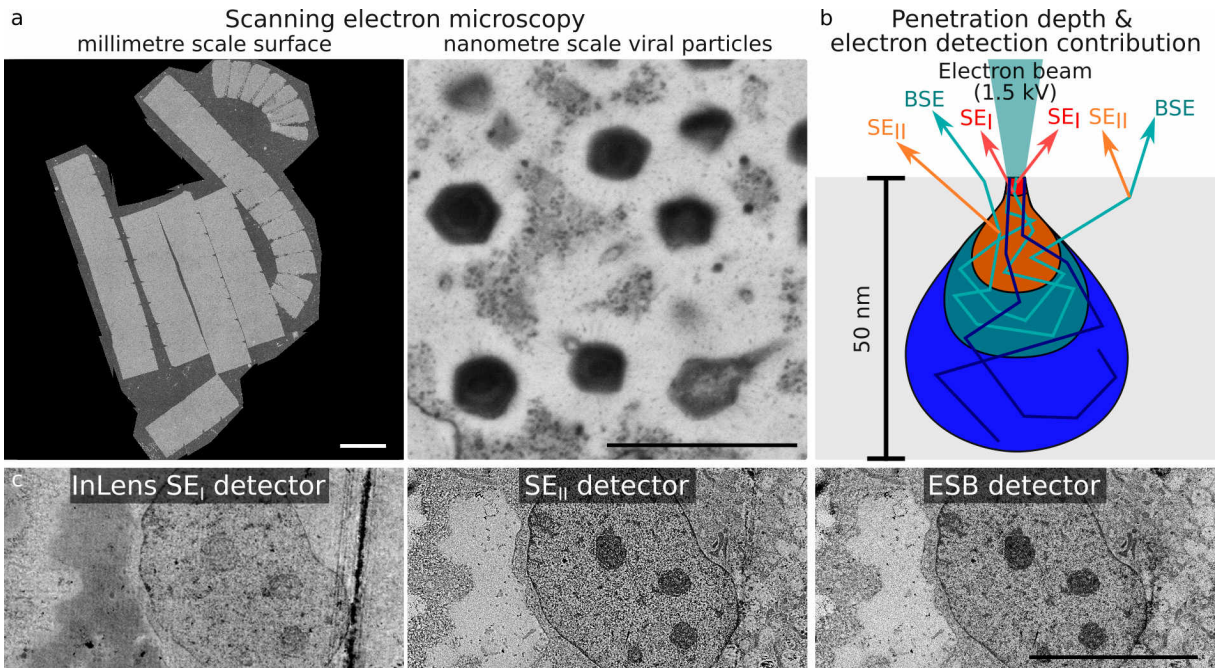

Fig. 1.6: Principle of Scanning electron microscopy and detector types in SEM. a) Exemplary *in-resin* biologicals at the millimetre- to nanometre-scale highlighting the variable maginification achievable in SEM. b) Penetration depth and scattered electrons observable in SEM. At 1.5 kV acceleration voltage, back-scattered electrons (BSE) sample a depth of up to 20 nm, with the generation of secondary electrons (SE) from inelastic scattering. SE_I originate from interaction of the electron beam with the sample surface and SE_{II} from inelastic scattering of the BSE. c) Available detector types in SEM, with InLens detectors generating a SE_I-rich image, Everhart–Thornley detector generate a SE_{II}-rich image and energy selective back-scattered electron detectors (ESB) a BSE selective image. Scale bar: a left) 1 mm, a right) 1 µm, c) 10 µm. Penetration depth estimation and detector classification from Bouwer *et al.*, Guthrey *et al.*, and Baatsen *et al.* (101, 104, 91).

1.4 Correlative light-electron microscopy

Correlating the specific fluorescence signal of a structure of interest from light-microscopic images with the ultrastructural context observed in electron microscopy can unravel the cellular processes and nanoscale organisation, impossible to reconstruct from either modality by itself (105, 106). However, combining fluorescence microscopy of cellular samples and electron microscopy results in many compromises favouring either the electron microscopy or light microscopy (107). For example, light microscopy is typically carried out in aqueous medium, while electron microscopy demands the use of a high vacuum. Similarly, fluorescence microscopy needs fluorescent labels containing a conjugated π-system (Fig. 1.2), while heavy-metal contrasting agents and resins are reactive to these double bonds and thereby destroy or quench the fluorescence (108). Additionally, epoxy resins have a known autofluorescence, interfering with the acquisition of *in-resin* fluorescence of the labelled protein structure (108, 38).

Therefore, while correlative light-electron microscopy (CLEM) has been of interest, various workflows have been developed, each optimised for their specific needs (Fig. 1.7) (107). Most notably, light microscopic acquisition has often been used as a supplementary method at various stages throughout the sample preparation process to find rare structures of interest in the sample, followed by further localised analysis in EM (Fig. 1.7) (109). Similarly, vitrification of samples opened up a whole new field of cryo-electron and cryo-light microscopy, better preserving the cellular ultrastructure, while increasing the technical challenges (Fig. 1.7 Fixation) (107, 108). Next, as samples need to be exposed to a high vacuum, the imaging either needs to be carried out under cryo-conditions or the aqueous media needs to be replaced. Here, polymeric resins are the most dominant

technique either from chemically fixed samples using dehydration and resin infusion or by freeze substitution from vitrified samples (Fig. 1.7 Embedding) (107). Alternatively, the Tokuyasu method embeds chemically fixed samples in a cryo-protective sucrose solution, preventing ice crystal formation (110).

To acquire electron microscopic images, various techniques have been established, as the penetration depth of the electron beam is less than 100 nm (101). A focused ion beam (FIB) can ablate the surface sequentially, recovering the 3D volume with isotropic nanometre scale resolution (106). Similarly, in serial block-face SEM, the surface gets ablated by a diamond knife. Alternative methods exist, including array tomography, which deposits serial ultrathin sections on an electrically conductive but transparent substrate for SEM or a transmission-EM-grid, to recover the 3D volume in a non-destructive approach from a series of 2D sections (111, 112). Lastly, for transmission-EM, the vitrified sample can be thinned to a lamella of only 10s of nanometre in height using FIB-milling, before being imaged in transmission-EM, limiting the reconstructed volume to the height of the lamella (Fig. 1.7 Sectioning & Imaging) (107).

Over the years, many advancements have been made, including fluorescent proteins which are better preserved during embedding and contrasting, the development of super-resolution light microscopy bridging the resolution gap between both modalities, as well as technical advancements with more sensitive detection systems reducing the concentration of contrasting agents such as OsO_4, thereby increasing the fluorophore preservation (38, 51, 113, 106, 108).

In 2020 several research groups from the Janelia Research Campus published a volumetric CLEM approach using three colour super-resolution imaging combined

with 4 nm isotropic EM resolution with high reconstruction quality in both modalities (106). However the workflow utilises instrumentation and techniques impractical for most research groups due to the use of highly customised equipment, in combination with e.g. cryo-light microscopy at 8 K, not readily available to most research centres (106). Therefore, the demand for novel approaches which allow for CLEM with little compromises remains a current topic (108).

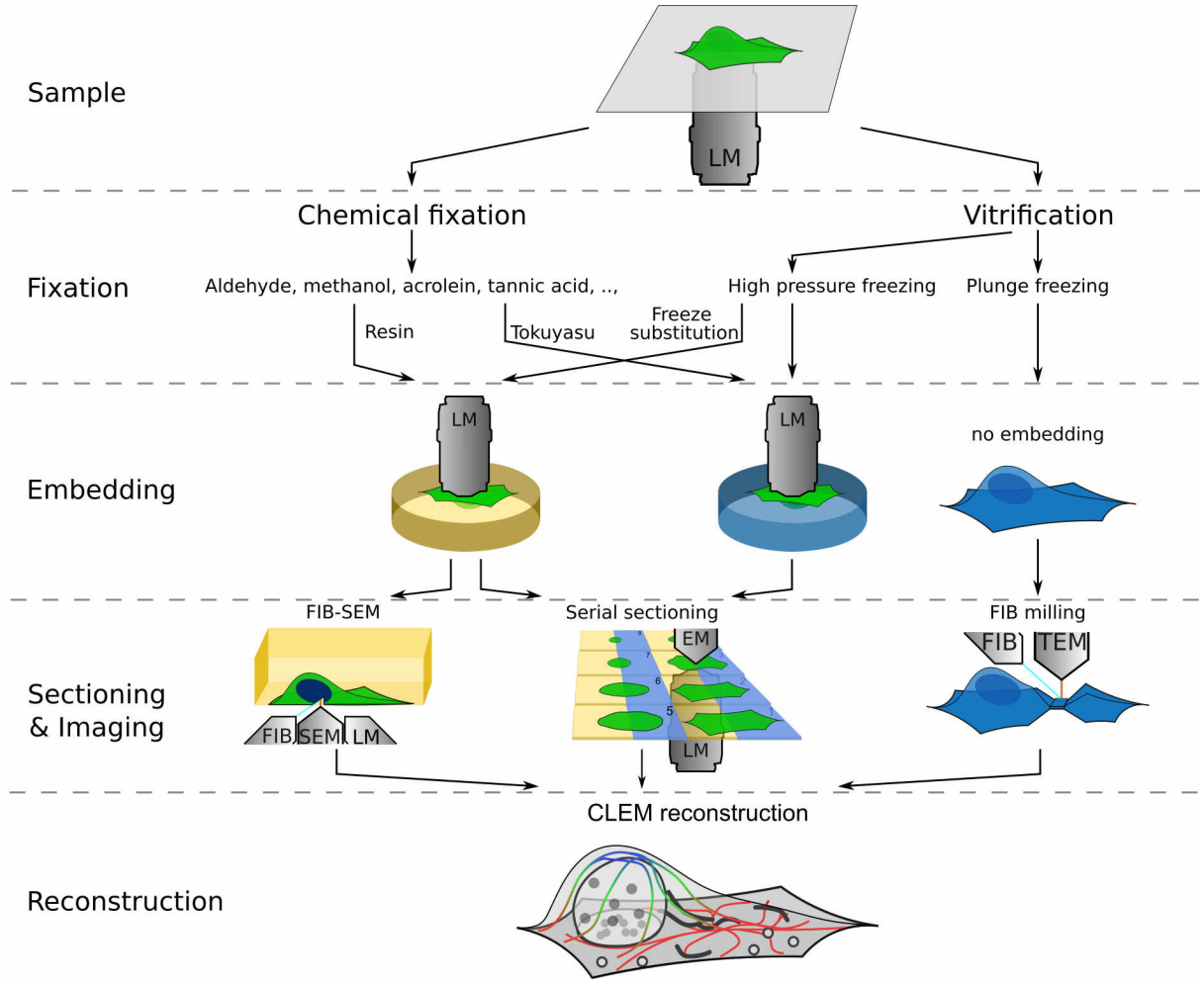

Fig. 1.7: CLEM workflow overview. Various sample preparation procedures for correlative light-electron microscopy (CLEM). Samples can be processed by chemical fixatives or vitrification using high pressure freezing or plunge freezing. Next, samples are embedded at room temperature (yellow) or under cryogenic conditions (blue). Polymeric resins are used for biological samples using a series of dehydration and infiltration of resin monomers or by freeze substitution from a vitrified sample. Alternative approaches exist, including the Tokuyasu method with cryo-protective sucrose solution. Samples are next sectioned and imaged in electron microscopy using a variety of available imaging techniques such as focused-ion beam (FIB)-SEM, serial sectioning, or FIB-milling, before reconstruction of the correlative light-electron microscopy data. Light microscopy (LM) can be performed at various stages throughout the CLEM workflow, representing various purposes, including the localisation of rare events or full correlative analysis in both modalities. Adapted from Bykov *et al.* (107).

1.5 Aims

Within this thesis, a focus is put on the development of quantitative and correlative super-resolution microscopy techniques to advance our understanding of the complex nanoscale cellular architecture. This goal is achieved through the construction of a sophisticated, yet versatile custom-built super-resolution microscope. Key developments include the improvement of cellular labelling calibration strategies and techniques for quantitatively preserving fluorophores for *in-resin* CLEM. The methods and techniques developed herein are set to advance our understanding of the nanoscale interactions of cells by elevating the fidelity of functional reconstruction in an ultrastructural context.

In the first results chapter (Chap. 3) a highly-automated SMLM microscope optimised for dSTORM acquisition is conceptualised and built. The design utilises a large field of view (FOV) of 133$\times$133 µm with homogeneous illumination and an irradiance for the relevant 647 nm dSTORM laser line of $\geq$3.5 kW/cm^2. The system is equipped with 3D dSTORM optics as well as dual scientific complementary metal–oxide–semiconductor (sCMOS) cameras for spectral demixing at full FOV. In a next step, the sCMOS cameras are calibrated on a per-pixel basis, allowing for correction of pixel-inhomogeneity induced fitting errors in dSTORM and gain inhomogeneity induced intensity corrections for improved quantitative microscopy acquisitions. Lastly, the theoretical SMLM performance of the system is estimated by quantification of the illumination profile across the FOV, the 2D/3D localisation precision on bead samples and the stability of the system with respect to vibrations and other error sources affecting the theoretical SMLM performance.

In the second results chapter (Chap. 4) the performance to resolve nanoscale structures in dSTORM is validated on microtubules by comparison to theoretical performance characteristics as well as established dSTORM microscope performance characteristics of colleagues. Next, dSTORM imaging is applied to targets of biomedical relevance, followed by the utilisation in quantitative microscopy for validation of a novel degree of labelling construct, coined ProDOL. Here, both the validation of the construct and the optimisation of the accompanying software package is performed. Lastly, the high modularity of the system is utilised in ratiometric PAINT imaging for assessing the nanoscale membrane order of cells using the solvatochromic dye di-4-ANEPPDHQ. Recovery of the nanoscale membrane order distribution is then used to develop cluster analysis routines for classification of sub-diffraction limited patches of persistent homologies.

In the last results chapter (Chap. 5) the development of novel fluorophore-preserving resin composition is investigated, followed by a molecular validation of fluorophore preservation. The compatibility of established resin compositions with serial ultrathin sectioning is confirmed, with a subsequent validation of compatibility with both dSTORM and SEM. A next focus is put on volumetric reconstruction of serial-sectioned samples, followed by the characterisation of the dSTORM performance, with a focus on the benefits from lack of out-of-focus blinking and premature bleaching. Finally, the established *in-resin* CLEM workflow is used to study the response of liver sinusoidal endothelial cells (LSECs) to a senescence-associated secretory phenotype and the implications it has on hepatocellular cancer treatment. With this strategy, the nanoscale ultrastructure of the cell can be linked to the functional microtubule cytoskeleton, unravelling the cellular organisation to aid in detection of underlying cellular response mechanisms.

Chapter 2

Material and Methods

2.1 Material

2.1.1 Biologicals

Cell lines

In Tab. 2.1, the eukaryotic cell lines used within this thesis are shown. COS-7, HeLa, RAMA27, and U2OS are immortalised cell lines stored in liquid nitrogen and thawed/cultured prior to use in experiments. HeLa cells stabily expressing the ProDOL construct were generated by Salopiata *et al.* (5). Liver sinusoidal endothelial cell (LSEC) and platelets were obtained from patient-derived tissue or blood samples of consenting patient under ethical approval. Isolation of primary cell lines was performed by the respective collaboration partners as described in Hoare *et al.* for LSEC (114) and in Jooss *et al.* for platelets (115).

Tab. 2.1: List of cell lines.

Cell line	Transfection	ATCC/CLS code	Supplier
COS-7 (*Cercopithecus aethiops*, fibroblast)	-	CRL-1651	ATCC
HeLa (*Homo sapiens*, epithelial)	-	CCL-2	ATCC
HeLa (*Homo sapiens*, epithelial)	ProDOL construct	-	Herten-Lab
LSEC (*Homo sapiens*, endothelial)	-	-	Shetty-lab
Platelets (*Homo sapiens*, blood)	-	-	Platelet group
RAMA27 (*Rattus*, fibroblast)	-	-	Fernig-Lab
U2OS (*Homo sapiens*, epithelial)	-	300364	CLS
U2OS (*Homo sapiens*, epithelial)	Nup107-SNAP	300294	CLS

Plasmids

Two plasmids for expression in eukaryotic cell lines were used within this thesis. pTOMM20-Halo, expresses a fusion protein consisting of the domains translocase of outer mitochondrial membrane 20 (TOMM20) and HaloTag (gift from Wombacher-lab) (47, 116). ProDOL construct was generated by Siegfried Hänselmann in the Herten-lab

and carries a fusion protein with Lyn kinase anchor, enhanced green fluorescent protein (eGFP), HaloTag, SNAP-tag (5).

Antibodies and fluorescent labels

In Tab. 2.2, 2.3 the antibodies and fluorophores used within this thesis are shown, respectively. Fluorophores for tag-labelling were either purchased pre-coupled to the tag-substrate or as N-hydroxysuccinimide (NHS)-ester. NHS-esters were functionalised with a HaloTag-substrate or SNAP-tag ligand based on manufacturer's protocol and purified by HPLC (30 to 70% H_2O/acetonitrile with 0.1% trifluoroacetic acid over 30 min).

As bead sample, TetraSpeck or FluoSpheres microspheres (Yellow-Green, Red) with 100 nm diameter or Dark Red FluoSpheres with 20 nm diameter were used (ThermoFisher).

Tab. 2.2: List of antibodies. Antibodies were split into aliquots of 10 µl and the number of freeze-thaw cycles was recorded on each vial.

Primary antibodies

Antigen	Host	ID/clone no.	Fluorophore	Concentration
α-tubulin	mouse	DM1A	-	1:300
α-tubulin	mouse	DM1A	AF647	1:300
GP1bα	mouse	AK2 and 2D4	-	1:300
S100A8/A9	mouse	A15105B	-	1:300

Secondary antibodies

Antigen	Host	ID/clone no.		Concentration
anti-Mouse IgG	rabbit	A-21239	AF647	1:300

Tab. 2.3: List of organic fluorophores. Alexa Fluor (AF), Abberior Star (AS), cyanine (Cy), oxazine (Oxa), tetramethylrhodamine (TMR).

Fluorophores

AF488	Atto633	di-4-ANEPPDHQ
AF532	Atto647N	Fluorescein
AF555	Atto655	Hoechst 33342
AF568	Atto680	MR121
AF594	Atto700	Nile Red
AF647	CF660C	Oxa12
AS635	CF680	Silicon rhodamine
Atto565	Cy3B	TMR

Cytokines, growth factors and biological substances

All cytokines, growth factors and other biological substances were purchased from commercial sources as indicated. senescence-associated secretory phenotype (SASP) was collected by the Shetty lab from RAS-induced senescent IMR90 human diploid fibroblasts according to (114).

Tab. 2.4: Cytokines, growth factors and biological substances. Fetal bovine serum (FBS), hepatocyte growth factor (HGF), interferon (IFN), rat tail collagen (RTC), senescence-associated secretory phenotype (SASP), tumour necrosis factor (TNF), vascular endothelial growth factor (VEGF).

Compound	Supplier	Concentration
Catalase	Sigma-Aldrich	40 µg/ml
FBS	Thermo Fisher	10%
Glucose Oxidase	Sigma-Aldrich	500 µg/ml
HGF	Peprotech	10 ng/ml
Human Serum	TCS Biosciences	10%
Hydrocortisone	Life Technologie	50 ng/ml
IFNγ	Peprotech	10 ng/ml
Insulin	Life Technologie	50 ng/ml
RTC type I	Corning	4 mg/ml
S100A8/A9	BioLegend	40 µg/ml
SASP	Shetty-lab	25%
TNFα	Peprotech	10 ng/ml
VEGF	Peprotech	10 ng/ml

Cell media and buffers

Media

Cell media were prepared according to Tab. 2.5 on the basis of endothelial serum-free media (SFM) and Dulbecco's modified eagle medium (DMEM).

Tab. 2.5: Cell media. Composition of cell media used for culturing cell lines.

LSEC media		RAMA27 media		General cell media	
Endothelial SFM		DMEM		DMEM	
Human serum	10%	FBS	10%	FBS	10%
VEGF	10 ng/ml	Insulin	50 ng/ml	GlutaMAX	2 mM
HGF	10 ng/ml	Hydrocortisone	50 ng/ml	Sodium pyruvate	1 mM
Penicillin	10 U/ml	Penicillin	10 U/ml	Penicillin	10 U/ml
Streptomycin	10 µg/ml	Streptomycin	10 µg/ml	Streptomycin	10 µg/ml

Buffers

Most buffers were purchased from commercial sources. Tab. 2.6 shows custom buffers, prepared according to a standard operating procedure by Jimenez *et al.* (63).

Tab. 2.6: Common buffers. tris(hydroxymethyl)aminomethane (TRIS), 2-mercaptoethylamine (MEA), 2,2'-(piperazine-1,4-diyl)di(ethane-1-sulfonic acid) (PIPES), ethylene glycol-bis(β-aminoethyl ether)-N,N,N',N'-tetraacetic acid (EGTA).

dSTORM buffer		GOD/glycerol		PEM buffer	
TRIS	50 mM	PIPES	12 mM	PIPES	80 mM
NaCl	10 mM	EGTA	1 mM	EGTA	5 mM
Glucose	10%	$MgCl_2$	2 mM	$MgCl_2$	2 mM
MEA	30-100 mM	Glycerol	50%		
Glucose oxidase	500 µg/ml				
Catalase	40 ug/ml				
	pH = 8.0		pH = 6.8		pH = 6.8

Resins

Novel UV-cured LR White resin compositions consist of LR White medium grade (uncatalysed) with 22 mM photoinitiator (benzoin methyl ether (BME), benzophenone (BP), 2,2-dimethoxy-2-phenylacetophenone (DMPA), or thioxanthone (TX)). For Norrish type II photoinititators (BP and TX) 1/250 vol% 4,N,N-trimethylaniline (TMA) is added.

Heat curing of LR White and EMbed812 as well as UV-curing of HM20 was carried out according to standard operating procedure by the manufacturer EMS[1,2]. For heat-curing, LR White was mixed with 2 wt% catalyst. HM20 was mixed from a three component kit with 14.8 wt% Crosslinker D, 84.7 wt% Monomer E and 0.5 wt% Initiator C. EMbed812 was mixed from a four component kit containing EMbed812, dodecenyl succinic anhydride (DDSA), methyl-5-norbornene-2,3-dicarboxylic anhydride (NMA), and benzyldimethylamine (BDMA). EMbed812 was prepared for medium grade hardness with 44.2 vol% EMbed812, 35.4 vol% DDSA, 17.7 vol% NMA, and 2.65 vol% BDMA.

[1] `https://www.emsdiasum.com/docs/technical/datasheet/14120`, as of 03/01/2023
[2] `https://www.emsdiasum.com/docs/technical/datasheet/14381`, as of 03/01/2023

2.1.2 Chemicals & consumables

All chemical and consumables were purchased from Sigma-Aldrich/Merck where possible. Reagents for cell culture were purchased from Thermo Fisher Scientific unless otherwise stated. Resins and contrasting agents were purchased from Electron Microscopy Sciences unless otherwise stated.

2.1.3 Microscope

Fluorescence microscope for widefield microscopy

Construction described in detail in Chap. 3. In short, an Epifluorescence-TIRF widefield microscope (ASI RAMM body with a Nikon 100X 1.49 NA immersion oil objective) was built with motorised stage and autofocus system (CRISP ASI). Four laser lines (405 nm, 488 nm, 561 nm and 647 nm) were used for illumination under control of acousto-optic tunable filter (AOTF) or direct laser control. Beams were transformed into a flat-top profile for homogeneous sample illumination using a refractive field mapping device (piShaper, AdlOptica). Fluorescent signal was detected on two scientific complementary metal–oxide–semiconductor (sCMOS) cameras (Prime95B, Photometrics) at 133×133 µm^2 field of view (FOV). Excitation and emission were split using a dichroic mirror (405/488/561/640, Chroma) and fluorescence was further filtered using a notch-filter (405/488/532/635 or 561 Semrock) in combination with appropriate band-pass filter (470/24, 525/50, 593/46, 685/70, or 731/137, Chroma and Semrock). For ratiometric PAINT a 640 nm long-pass filter (Semrock) with 552/96 band-pass filter (600 short-pass with 505 long-pass filter, Thorlabs) in the reflective channel was chosen. For ratiometric

dSTORM, a 662 nm long-pass filter (Semrock) with 731/137 band-pass filter (Semrock) in the transmission path and a 685/70 band-pass filter (Chroma) in the reflection path was chosen. The widefield microscope was controlled using µManager 2.0 (117). Exposure time, laser power and number of frames were adapted for each sample.

Fluorescence microscope for confocal microscopy

A laser-scanning confocal (Flimbee laserscanner with Nikon Eclipse Ti microscopy body with a Nikon 100x 1.49 NA immersion oil objective) was built with motorised stage and PFS autofocus (Nikon). Pulsed excitation was performed using a picosecond pulsed laserdiode of 640 nm (LDH P-C-640B, 90 ps, 20 MHz). Fluorescent light was detected on 4 avalanche photodiode (APD) with equal detection probability. Excitation and emission were split using a dichroic mirror (z532/640, Chroma) and fluorescence was further filtered using a band-pass filter (BP) (685/70, Chroma) with additional 100 µm pinhole in the conjugate focal plane. Signals were correlated using a time-correlated single photon counting system (HydraHarp400, PicoQuant).The confocal microscope was operated using SymPhoTime 64. Exposure time, laser power, repetition rate and dwell time were adapted for each sample as described in Tashev *et al.* (5).

2.1.4 Optics and optomechanics

All optical components and optomechanics, except filters, were purchased from Thorlabs, unless otherwise stated. Optical filters were purchased from Chroma or Semrock. Optical components were purchased from other manufacturers if an exclusivity contract was present. Optical tables and dampening equipment were purchased from Newport.

2.1.5 Electronics

All electronic components, microcontrollers and PCBs were purchased from RS Components and JLCPCB, respectively unless otherwise stated.

2.1.6 Software

Software Code

Tab. 2.7: List of software. Commonly used software with software version.

Software		Programming languages	
Atlas	5.0	Arduino	1.8.10
Chimera	1.16	Java	1.8.0
Fiji	2.15.0	MATLAB	2021b
GraphPad Prism	10.1.2	Python	3.9.5
ImageJ	1.54f	R	4.3.2
µManager	2.0.0		
Oslo	23.2		
RStudio	2023.12.0		
SmartSEM	7.0.0		
TracePro	23.1		

Tab. 2.8: List of scripts. Commonly used scripts and routines with version number.

Java/Fiji		MATLAB		Python	
3Dscript	0.2.2	AFT	1	pycops	not tracked
BigWarp	9.0.0	ProDOL	1.1	quickPBSA	2020.0.1
CameraCalibrator	2	ResinFit	not tracked	Raytracing	1.3.10
CLIJ2	2.5.3.1	SMAP	201217		
MultiStackReg	1.46.5	SuperVoronoi	1.2	R	
PolarTransformer	3			CameraSimulator	1
ProDOL	1.1	µManager		PLASMA	1
StackReg	2011-07-07	BatchImager	3.5		
ThunderSTORM	1.3	EMU	1.1	Arduino	
TrakEM2	1.0a	htSMLM	2.0.0	HardwareControl	1.3

2.2 Methods

2.2.1 Cell culture

Immortalised cells were cultured from frozen stock by quick thawing of the vial, followed by mixing of the cell suspension with 9 times the volume of complete media. Next cells were pelleted down at 200×g for 3 min, the supernatant was discarded and all cells were transferred into a T25 flask for culturing. Cells were passaged until passage 20 for immortalised cells and passage 6 for LSEC. If morphological abnormalities were detected, or cells slowed down in growth rate, the flask was discarded.

All adherent cell lines were cultured in T25 or T75 culture flasks using the appropriate media, as outlined in Sec. 2.1.1, at 37 °C, high humidity and 5% CO_2. Immortalised cell lines were passaged at 80% confluency and 1.0-1.2×10^4 cells/cm^2 were seeded into a new flask. LSEC were split 1-2 times a week at full confluency and 3.0×10^4 cells/cm^2 were seeded into a new flask pre-treated with 40 µg/ml RTC at 75 µl/cm^2 for 30 sec.

To split the cells, cells were aspirated, washed once with PBS, followed by addition of 60 µL/cm^2 TrypLE. Once cell were completely detached, 2 times the volume of DMEM or PBS (for LSEC) was added and cells were pelleted at 350×g for 5 min. Supernatent was discarded and cell were resuspended to 1.0×10^6 cell/ml. A prewarmed flask with 0.2 ml/cm^2 of media was prepared to which the appropriate cell count was added.

2.2.2 Sample preparation

2.2.2.1 Seeding

All glass coverslips and glass surfaces to which cells were seeded onto for imaging were cleaned by using 0.1 M hydrofluoric acid for 60 s followed by two washes in H_2O. The process was repeated once, and successful treatment was visually confirmed by complete surface wetting. Next, coverslips were stored in PBS with magnesium and calcium for 5 min before being used.

Adherent cells

Adherent cells were seeded at 1.0-1.2$\times 10^4$ cells/cm^2 and incubated for 24 h before further use.

LSEC

Collagen coating was initially adopted from Yin *et al.* (118). Here, coverslips were treated overnight with 40 µg/ml RTC at 75 µl/cm^2. The coverslips were then aspirated and fully dried, before addition of LSEC. Later, covalent linking of RTC to glass by silanisation was performed, adopted from (116, 119). Surfaces were treated with HF activation before silanisation with 2% (3-aminopropyl)triethoxysilane (APTES) in acetone for 10 min. Then, 0.5% H_2O is added to the solution and mixed. The reaction is allowed to continue for 20 min, before being rinsed twice in water. The coverslips are next submerged in an aqueous 2.5% glutaraldehyde (GA) solution for 1 h. Coverslips are washed twice in water before being cross-linked to RTC I (0.2 mg/mL in PBS) overnight at 4 °C. The coverslips are aspirated, washed twice with water and stored until use.

LSEC are seeded at a density of 3.0×10^4 cells/cm^2 in LSEC media. 24 h after seeding, LSECs were exposed to 25% SASP from RAS-induced senescent IMR90 fibroblast media, or 25% growth control media of IMR90 fibroblasts and incubated for 18 h. Next, 10 nM colchicine (10 mM stock) or 0.1 µg/ml nocodazole (5 mg/ml stock) were added to the cells and incubated for 2 h for colchicine and 1 h for nocodazole before fixation.

Platelets

Coverslips were cleaned using the HF treatment, before being coated with 100 µg/ml fibrinogen, 10 µg/ml collagen, or 100 µg/ml poly-L-lysine overnight at 4 °C. Next, coverslips were rinsed once and blocked using 5 mg/ml bovine serum albumine (BSA) in PBS for 1 h. Platelets were isolated and seeded by collaboration partners as described in Jooss *et al.* (115). In short, if treatment of platelets was performed before seeding, 2.0×10^8 cells/ml in Tyrode's buffer were stimulated with S100A8/A9 (40 µg/ml). Then, washed platelets were diluted to 2.0×10^7 cells/ml in Tyrode's buffer and 1 ml was added to each coverslip. Platelets were allowed to settle onto the coverslip for 45 min in an incubator. Next, the sample was washed once in PBS.

GUV

Giant unilamellar vesicles (GUVs) preparation was performed by the collaboration partner Maria Makarova from the University of Birmingham using a protocol established by Morales *et al.* (120). In short, a monolayer of lipid bilayers (1,2-dioleoyl-sn-glycero-3-phosphocholine (DOPC) or 30 mol% cholesterol in 1,2-dipalmitoyl-sn-glycero-3-phosphocholine (DPPC)) was deposited on ITO coverslips and GUVs were subsequently formed using electroformation at 50 °C, 11 Hz, and 1 V for 2 h in a 200 mM sucrose solution.

Fixation and labelling

HaloTag labelling

Cells were fixed in 4% paraformaldehyde (PFA) with 0.05% GA in PEM buffer for 30 min at room temperature. Next, samples were permeabilised for 10 min using 0.1% Triton X-100 in PBS. Samples were then rinsed twice in PBS and washed twice for 5 min each. Next, samples were flipped on a 200 µl drop containing 100 nM AF647-HaloTag-ligand in PBS and fluorescently labelled for 2 h. Samples were rinsed twice in PBS, followed by 3 washing steps in PBS (30 min, 30 min, 60 min). Samples were either used for dSTORM imaging or preparation was continued by post-fixation using 2% GA in PBS for 10 min before proceeding with EM contrasting.

SNAP-tag labelling

SNAP-tag labelling was adapted from Thevathasan *et al.* (86). Cells were prefixed in 2.4% PFA in PBS for 30 sec at 37 °C. Next, samples were permeabilised for 3 min using 0.4% Triton X-100 in PBS. Samples were then fixed using 2.4% PFA in PBS for 30 min at 37 °C. Samples were next quenched using 100 mM ammonium chloride solution in PBS for 5 min at room temperature. All subsequent steps are carried out at room temperature. For blocking, the samples were flipped on a 200 µl drop of Image-iT FX and incubated for 30 min. Next, samples were placed on a 200 µl drop containing 200 nM AF647 SNAP-tag substrate, 1 µM dithiothreitol and 0.5% BSA in PBS for 2 h. Samples were rinsed twice in PBS, followed by 3 washing steps in PBS (30 min, 30 min, 60 min). Samples were either used for dSTORM imaging or preparation was continued by post-fixation using 2% GA in PBS for 10 min before proceeding with EM contrasting.

ProDOL labelling

For ProDOL experiments, the cells were processes according to SNAP-tag labelling and/or HaloTag labelling, though concentration and incubation time was varied between 15 min to 16 h and between 100 pM and 250 nM. If µ-Slide 8 Well 1.5 Glass were used, samples were not flipped on droplet, but 250 µl of dye solution was added to the well.

Immunolabelling dSTORM

Immunolabelling was adapted from Jimenez *et al.* (63). All steps were carried out at 37 °C until cells were fully fixed, then all steps were performed at room temperature. Cells were treated with a prefixation extraction using 0.25% Triton X-100 and 0.1% GA in PEM buffer for 30 sec. Next, samples were fixed for 10 min using 0.25% Triton X-100 and 0.5% GA in PEM buffer. Samples were next quenched using 0.1% $NaBH_4$ in PBS for 7 min. Samples were rinsed twice in PBS before blocking using 3% BSA and 0.1% Triton X-100 in PBS (blocking buffer) for 60 min. Samples were flipped on a 200 µl drop of primary antibody solution (typically 1:300 dilution) in blocking buffer and incubated for 1 h. Samples were washed three times for 10 min each in PBS before incubation with the secondary antibody (1:300 dilution) in blocking buffer for 1 h. Samples were washed three times for 10 min each in PBS and post-fixed using 4% PFA in PBS for 10 min. Samples were stored at 4 °C until used for dSTORM imaging.

Immunolabelling CLEM

Immunolabelling was adapted from Jimenez *et al.* with a focus in ultrastructural preservation (63). All steps were carried out at 37 °C until cells were fully fixed, then all steps were performed at room temperature. Cells were fixed using 4% PFA and 0.05% GA in PEM buffer for 30 min at 37 °C. Samples were rinsed twice in PBS and washed twice

for 5 min each in PBS. Next, blocking of samples using 3% BSA and 0.1% Triton X-100 in PBS was performed for 60 min. Samples were flipped on a 200 µl drop of primary antibody solution (typically 1:300 dilution) in PBS with 3% BSA and incubated for 1 h. Samples were washed three times for 10 min each in PBS before incubation with the secondary antibody (1:300 dilution) in PBS with 3% BSA for 1 h. Samples were washed three times for 10 min each in PBS and post-fixed using 2% GA in PBS for 10 min. Samples were stored at 4 °C until EM contrasting.

Platelets

Immunolabelling of platelets was adapted from Jooss *et al.* and Colicchia *et al.* (115, 121). All steps were carried out at room temperature. Samples were fixed using 4% PFA and 0.05% GA in PBS for 30 min. Samples were rinsed three times in PBS. Samples were then permeabilised using 0.1% Triton X-100 in PBS for 5 min. Next, blocking of samples using 1% BSA and 2% normal goat serum in PBS (blocking buffer) was performed for 30 min. Samples were flipped on a 200 µl drop of primary antibody solution (typically 1:300 dilution) in blocking buffer for 1 h. Samples were washed three times for 10 min each in PBS before incubation with the secondary AF647-labelled antibody (1:300 dilution) in blocking buffer for 1 h. Samples were washed three times for 10 min each in PBS and post-fixed using either 4% PFA for dSTORM or 2% GA for CLEM in PBS for 10 min. Samples were stored at 4 °C until further use.

EM contrasting

If samples were used exclusively for electron microscopy, samples were fixed using 2% GA in PEM buffer for 10 min and rinsed twice with PBS.

All fixed and labelled samples for EM contrasting were rinsed twice in PBS before washing in 0.1 M PIPES buffer at pH = 8.0 for 10 min. Next, osmium contrasting was performed. All CLEM samples were using 0.1% OsO_4 and 0.16% $K_3[Fe(CN)_6]$ in 0.1 M PIPES buffer at 4 °C for 30 min. All samples for EM only were using 1% OsO_4 and 1.6% $K_3[Fe(CN)_6]$ in 0.1 M PIPES buffer at 4 °C for 30 min. Samples were rinsed once in 0.1 M PIPES buffer, washed for 10 min in 0.1 M PIPES buffer before being washed twice in pure H_2O for 10 min each. Samples were then stained with 4% neodymium acetate in H_2O for 1 h before embedding.

After dSTORM imaging, on-section contrasting was performed using 600 µL of 2% uranyl acetate solution in H_2O for 10 min. The sample is rinsed twice in H_2O, before being stained using 600 µL of Reynolds lead citrate solution in a basified chamber (high pH using NaOH pellets) for 5 min. Samples are washed 3-5 times in H_2O before being dried and placed in the scanning electron microscopy (SEM).

2.2.2.2 Embedding

Embedding of LR White resins was carried out according to Tab. 2.9. Embedding of UV-cured HM20 was performed accordingly, by substitution of LR White with HM20. Heat-cured EMbed812 was performed according to Tab. 2.9 until 100% ethanol was reached. Then ethanol was replaced by 25% acetone for 5 min, 50% acetone for 5 min, 75% acetone for 5 min, 100% acetone for 5 min. Then the embedding procedure was continued according to Tab. 2.9 with EMbed812, substituting ethanol with acetone. No additional initiator was needed for EMbed812 at 100% resin composition. UV-cured

samples were polymerised for 24 h using a Leice AFS2 at 23 °C or -30 °C. Heat-cured samples were polymerised for 24 h using an oven at 60 °C.

Tab. 2.9: Standard procedure for embedding procedure for dehydration and resin infiltration.

Condition	Duration
25% ethanol in H_2O	5 min
50% ethanol in H_2O	5 min
75% ethanol in H_2O	5 min
90% ethanol in H_2O	5 min
96% ethanol in H_2O	5 min
100% ethanol	2×5 min
25% resin in ethanol	10 min
50% resin in ethanol	10 min
75% resin in ethanol	10 min
100% resin with initiator	3×10 min

Samples were embedded by placing them on a Sylguard 184 mold adhered to a glass coverslip (14 mm inner diameter, 18 mm outer diameter, and 5 mm height).

2.2.2.3 Sectioning

Sectioning was carried out on a RMC Powertome XL using Diatome trim 45 diamond knives for pre-trimming and Diatome ultra 35 jumbo diamond knives for sectioning. Resin blocks were released from the mold and split into 4-8 resin blocks. These were glued on sacrificial Embed812 dummies with contact cement and stored overnight for full curing of the contact cement. Next samples were pre-trimmed to the region of interest using a razor knife, followed by trimming using the trim45 to a region of interest not exceeding 1 mm in all directions. A combination of 25% ”Pattex Kraftkleber” in Xylol was applied to two parallel sites of the resin and allowed to settle for 30 min before sectioning. Sectioning was performed at 50-200 nm section height at 1 mm/s cutting speed using a ultra 35 jumbo diamond knife. Serial section ribbons were separated in regular intervals of 10-20 sections and moved on the water surface using micromanipulators. After

sectioning was completed, ribbons were placed next to each other and adhered on a glass coverslip or ITO coverslip that has been surface treated to increase hydrophilicity (HF treatment or plasma cleaner). Coverslips were carefully dried and imaged in either light microscopy or electron microscopy.

2.2.3 Microscopy techniques

2.2.3.1 Light microscopy

In general, the sample was placed on the microscope and the focus was adjusted manually, next the autofocus was activated and an overview area was scanned using the SlideExplorer in µManager. Relevant cells were selected and automatically acquired using the BatchImager script. Within the BatchImager, the exposure time, frame count, laser line, filter selection, laser power and inclusion of additonal optics could be chosen (e.g. cylindrical lens for astigmatic PSF). Additionally, options for interleaved z-stack acquisition or 405 nm power-ramping were available for single-molecule localisation microscopy (SMLM) acquisition.

Diffraction-limited microscopy

Samples for qualitative diffraction-limited microscopy images were acquired in PBS using the appropriate laser line and filters on the widefield microscope in Epifluorescence-TIRF mode using the BatchImager script.

ProDOL

For protein-tag degree of labelling (ProDOL), samples were imaged using TIRF mode with 10 frames per fluorescent label at lowest possible laser-power and exposure time where a clear detection of single-molecule fluorescence was still possible.

PBSA

For photobleaching step analysis (PBSA), samples were measured using a laser power of 1.2 kW/cm^2 at 640 nm or 0.5 kW/cm^2 at 561 nm with 50-200 ms exposure time, until all fluorescence was bleached (typically 2000-8000 frames) using a protocol established by Hummert *et al.* (3). Samples were imaged in a air-tight imaging chamber with reducing and oxidising system (ROXS) buffer containing 50 mM of sodium phosphate buffer at pH = 7.4, 13.5 mM KCl, 0.69 mM NaCl, 10 mM $MgCl_2$, 12.5% glycerol, 50 nM protocatechuate-3,4-deoxygenase and 2.5 mM protocatechuic acid.

dSTORM

Samples were prepared in dSTORM buffer (Sec. 2.1.1) with 30-100 mM of MEA depending on the expected emitter density. Typically, nuclear pore complex (NPC) were imaged at 30-40 mM MEA, whole cell microtubules at 100 mM MEA and sectioned samples at 30-50 mM MEA. For dSTORM imaging, the 647 nm laser line was used at 100% laser power, corresponding to 3.5 kW/cm^2 of irradiance. 405 nm illumination was automatically increased over time to maintain a constant level of blinking suitable for SMLM. Based on expected performance characteristics a first test was performed and analysed. Then the optimal acquisition parameters were selected. Typically, the

exposure time was between 30-100 ms, frame count between 1.0-8.0$\times 10^4$ and 405 nm was increased until the acquisition finished, roughly following an exponential increase or up to 40 W/cm^2 of irradiance. For 3D dSTORM, a bead calibration z-stack was acquired on a per experiment bases. For ratiometric dSTORM a bead calibration for both camera channels was acquired.

ratiometric PAINT

Samples were imaged using 20 nM di-4-ANEPPDHQ in PBS for GUV and 80 nM di-4-ANEPPDHQ in phenol red-free DMEM. 8.0-10$\times 10^3$ frames at 50 ms were acquired using 50 W/cm^2 of 488 nm highly inclined and laminated optical sheet (HILO) illumination. The microscope was configured as described in Sec. 2.1.3.

CoPS

For Counting by photon statistics (CoPS), the confocal microscope was used, described in Sec. 2.1.3. Samples were imaged in an air-tight imaging chamber with ROXS buffer containing 50 mM of sodium phosphate buffer at pH = 7.4, 13.5 mM KCl, 0.69 mM NaCl, 10 mM $MgCl_2$, 12.5% glycerol, 50 nM protocatechuate-3,4-deoxygenase and 2.5 mM protocatechuic acid. First, an overview scan was performed, allowing for the detection of clusters. These were localised in ThunderSTORM and the position was imported into SymPhoTime64. Next, 3 s of time-correlated single photon counting was performed for each localisation at 10 µW laser power.

2.2.3.2 Electron microscopy

SEM

For serial section volumetric SEM a Zeiss Ultra55 was used. For single high-resolution SEM micrographs, a Zeiss CrossBeam 540 was used. For each SEM, a micrograph from two detectors was generated using a combination of a back-scattered electron (BSE)-specific energy selective back-scattered electron detector (ESB) electron detector, type I secondary electron (SE_I)-rich InLens detector, or type II secondary electron (SE_{II})-rich Everhart–Thornley detector. Micrographs were recorded at a dwell time of 128-512 ns/pixel, with 1.5 kV acceleration voltage and a 20 µm aperture. Pixel size was between 4-10 nm for high-resolution images. Astigmatism and focus was optimised for each region before automated acquisition.

2.2.4 Spectroscopy techniques

For spectroscopic ensemble resin measurements a standard procedure was followed. First 497 µL of resin in an Eppendorf UVette were placed in the absorption spectrometer to perform a baseline acquisition. Next 2.5 µL of a 200 µM dye solution in 4:1 water:DMSO was added, the cuvette was sealed and the fluorophore-specific absorption spectrum was recorded. For a post-polymerisation baseline correction, a control with 2.5 µL of 4:1 water:DMSO was prepared. Next, the fluorescence spectrum was recorded and the resins were polymerised for 24 h in a Leica AFS2. Thereafter, the absorption and fluorescence were recorded again, as well as the fluorescence lifetime, where applicable.

Absorption spectroscopy

Ensemble absorption measurements were performed in a Cary 500 Scan UV-Vis-NIR-spectrometer between 400-800 nm at 1 nm intervals and 0.1 s per interval.

Fluorescence spectroscopy

Ensemble fluorescence measurements were performed in a Cary Eclipse fluorescences spectrophotometer. For each dye, the recorded emission spectrum was chosen 8 nm red-shifted of the excitation wavelength and recorded to 800 nm. The excitation wavelength was chosen close to the excitation maximum of the fluorophore. Excitation slit width and emission slit width were set to 2.5 nm and the scan rate was set to 120 nm/min at 1 nm intervals. The sensitivity of the detector (PMT voltage) was set, such that the fluorescence intensity pre-polymerisation was not exceeding 500 counts.

Fluorescence lifetime spectroscopy

Fluorescence lifetime measurements were performed in a FluoTime 100 fluorescence lifetime spectrometer, equipped with a PDL 800-D picosecond laser diode and a TimeHarp 200. For TMR, a 500 nm laser diode was chosen and for AF647 a 640 nm laser diode. The acquisition was performed at a repetition rate of 5 MHz and a -100 mV offset.

2.2.5 Statistical analysis

All statistical analysis was performed in the respective programming language of the analysis workflow. E.g. ELE, dSTORM performance, and ProDOL were performed in MATLAB, PLASMA and the camera simulation were performed in R, gain analysis was

performed in Java/Fiji, and CoPS and PBSA were performed in Python. All comparative analysis of lists (e.g. cross-correlation of degree of labelling (DOL) techniques or polarity comparison of cells) was performed in GraphPadPrism using appropriate statistical analysis. Kolmogorov–Smirnov test was used for normality and log-normality testing. Non-linear and linear regression was used for curve fitting. For two sample comparative analysis t tests or Mann–Whitney U tests were chosen based on the sample distribution. For multiple analysis ANOVA was performed. Additional, Kruskal-Wallis test and z-scores were calculated where appropriate. Q-Q-plots were used to test if two probability distributions have a statistically non-significant difference. For all statistical analysis representative results are presented using either the mean, median, or modal value, combined with standard deviation (SD), standard error or the mean (SE_{mean}), confidence interval (CI), R^2 or p-value. Boxplots are represented by a standard box-and-whisker plot. Analysis of samples with multiple repeats was performed using SuperPlots (122). Here, the variability of biological replicates is considered, correcting for the intra-experiment variability between repeats.

2.2.6 Calibration and simulation

Optical simulation

Raytracing and performance of optical elements was performed using a combination of Oslo, TracePro (Lambda Research) and Raytracing (123). Raytracing was used for simple doublet lens configurations, while Oslo and TracePro were used for full modeling of the detection pathway with correct optical representation of the objective, tube lens and other optics.

Flatness calibration

Flatness calibration of the *in-sample* illumination was adapted from Ibrahim *et al.* using relevant beam properties to describe the flatness, uniformity and steepness of a flat-top profile (124). The analysis was modified by using the 99th percentile (I_{99}) instead of the maximal pixel value, as this improved robustness from single-pixel outliers. Additionally, the *in-sample* illumination was corrected for the theoretical position-dependent transmission loss as calculated in Fig. 3.12. Finally, each analysis was normalised, such that 1 represents the ideal profile. The flatness factor uses the illumination intensity (I), plateau uniformity the histogram of intensity values and edge steepness the width of the beam (D_i) at 10% and 90% intensity relative to the plateau.

Flatness factor: $\frac{I_{\mathrm{mean}}}{I_{99}}$ **Plateau uniformity:** $1 - \frac{I_{\mathrm{FWHM}}}{I_{99}}$ **Edge steepness:** $1 - \frac{D_{0.1} - D_{0.9}}{D_{0.1}}$

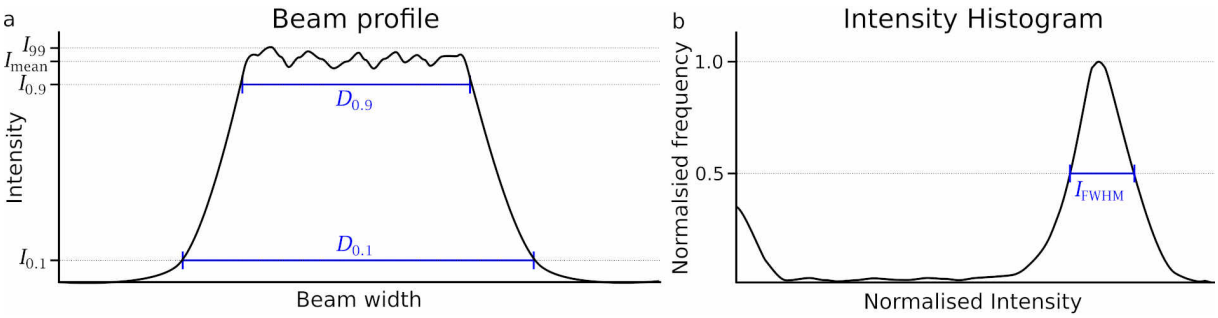

Fig. 2.1: Schematic of relevant beam properties extracted for flatness calibration. a) Mean plateau intensity (I_{mean}), 99th intensity percentile (I_{99}) and beam width at 10% and 90% relative intensity ($D_{0.1}, D_{0.9}$) are highlighted for a flat-top beam profile. b) Histogram of intensity distribution of the beam profile to determine the full width at half maximum (FWHM) of the intensity distribution (I_{FWHM}). Inspired by Ibrahim *et al.* (124).

Gain calibration

Acquisition of image-stacks is described in detail in Sec. 3.2.2.2. In short, at 10 logarithmically-spaced intensity levels a stack of 8000 frames was recorded. Additionally, with using a closed shutter (dark set), 8000 frames were recorded at 12.5 ms and

1012.5 ms. From the pixel-wise mean intensity of the dark set, the offset and dark current were calculated according to:

$$\text{intensity} = \text{offset} + \text{dark current} \times t \tag{2.1}$$

Using the pixel-wise variance within the dark set, the read noise and thermal noise were determined according to:

$$\text{variance} = (\text{read noise})^2 + (\text{thermal noise})^2 \times t \tag{2.2}$$

Finally, using the thermal noise corrected variance and dark current corrected intensity of each pixel, the photon transfer curve (PTC) was plotted (variance over intensity). Here, a linear fit was performed using the Simplex method on a per-pixel basis where the slope represent the gain of a pixel (125).

Camera performance simulation

The theoretical localisation error expected from the pixel inhomogeneities was simulated based on a sCMOS camera model described by Mandracchia *et al.* (126, 127):

$$I = \gamma_p \text{Pois}\{S_p\} + N(0, \sigma_n) + B \tag{2.3}$$

where I is the intensity of a pixel, γ_p the multiplicative photon conversion factor, S_p the quantised photon signal, $N(0, \sigma_n)$ the distribution of read noise, and B the baseline. Given a sufficiently high photon count S_p, the Poisson distribution can be approximated by a Gaussian distribution with $N\left(S_p, \sqrt{S_p}\right)$ (central limit theorem), resulting in:

$$I \approx \frac{1}{G} \cdot N\left(S_p, \sqrt{S_p}\right) + N(0, \sigma_n) + B \tag{2.4}$$

with $\gamma_p = \frac{1}{G}$ and G being the experimentally calibrated gain of the camera. Based on the approximated intensity formula, 100 sets of 1764 emission events in a 50×50 pixel

region were simulated for 5000 photons specific emission, 100 ms exposure time and 0 photons background intensity. Images were localised in super-resolution microscopy analysis platform (SMAP) and compared to the ground-truth emitter localisation.

2.2.7 Ensemble analysis

Absorption

To determine the absorption maximum, the absorption spectrum needs to be baseline corrected. Here, a fifth degree polynome was fitted to the absorption spectrum of a blank resin sample. The polynome was then adjusted to best match the measured profile containing the fluorophore. This was performed based on the absorption spectrum of the fluorophore pre-polymerisation. The wavelength at which the absorption of the fluorophore falls below 25% of the maximum is selected [λ_{low}, λ_{high}]. Next, 50 nm is subtracted from λ_{low} and 50 nm is added to λ_{high}. A region of 25 nm is used from each λ_{i}, and the polynome is scaled such that the sum of squared distances is minimised. Next, the absorption maxima is determined (wavelength and transmission percentage). Based on the transission value, an absorption coefficient is determined.

Fluorescence

To determine the fluorescence maximum, the fluorescence spectra are averaged and a peakfinding is performed in MATLAB using a topographic prominence of $>$5 units. Then, the highest intensity of the dominant peak is used as fluorescence maximum.

Fluorescence lifetime

To determine the fluorescence lifetime, a three-parameter exponential decay is fitted to the lifetime trace between 1.2 ns and 13.6 ns after the peak (A_0, τ, and d), with τ representing the fluorescence lifetime.

$$A(t) = A_0 e^{-t/\tau} + d \tag{2.5}$$

2.2.8 Section analysis

Section height

Section height is analysed using a Dektak XT stylus profilometer. Line profiles are baseline-corrected using piecewise interpolation. The per-section height is calculated by manual definition of section start and end, between which the mean height and height-variability is determined. The section to section variability is calculated from the mean of each section.

Solvent accessibility

To determine the solvent accessibility in resin section, $NaBH_4$ was used as strong reducing agent, bringing fluorophores into a non-fluorescent state. A mask containing the cellular region was generated. Here, based on the first 30 s prior to $NaBH_4$ addition the bleaching rate was determined. This bleaching rate was used to recover the bleaching-corrected intensity trace. Next, an three-parameter exponential decay was fitted to the intensity trace using Eq. 2.5 . The time at which the half-maximal intensity was reached was used to determine the solvent accessibility.

2.2.9 Image analysis

2.2.9.1 SMLM

All localisation, filtering, drift-correction and rendering was performed in SMAP (128). Here, the fit_fastsimple workflow was chosen with offset correction and sCMOS correction enabled. As peak finder an edge detection algorithm using a difference of Gaussian of 1.2 and a dynamic factor between 1.2 and 1.7 was chosen. A ”PSF free” fitting algorithm was chosen for 2D SMLM data and Spline fitting for 3D SMLM data. Data was subsequently filtered on localisation precision, photon count, log-likelihood, PSF width, asymmetry and on-time. Additionally, all frames until a good emitter density was reached were discarded. Finally, a frequency-based filtering was performed, where all localisations within a diffraction-limited spot were discarded if emitters were detected in $>$10% of 150 frames.

For ratiometric SMLM, the two camera streams were combined vertically. The dual camera image stack was localised in SMAP and ratiometric analysis was performed according to[3]. In short, the localisation in each channel are registered and an affine transformation matrix is generated. Next, the data is reanalysed and the intensity in both channels is recorded for each emission event detected in the initial dataset. Then, the dataset can be split based ratiometric information to separate multiple fluorophores. Alternative, the generalised polarisation (GP)-value was calculated in ratiometric PAINT according to Eq. 2.6 based on the photon count in the reference channel (fit_{nr}) and

[3] https://www.embl.de/download/ries/Documentation/Example_SMAP_Step_by_step.pdf, as of 04/01/2023

target channel (fit_{nt}):

$$\mathrm{GP} = \frac{\mathrm{fit}_{nr} - \mathrm{fit}_{nr}}{\mathrm{fit}_{nr} + \mathrm{fit}_{nr}} \tag{2.6}$$

SMLM-based analysis

Super-resolved images were reconstructed after filtering of coordinates as described in the previous section. A Gaussian-based rendering with a minimum sigma of 3 nm and 0.7 pixel chosen. Each localisation was rendered having the same cumulative intensity and the image was scaled between 0 and 99.97% of pixel intensities. Using the localisation list, various analysis was performed within SMAP, including line profile generation, FRC resolution estimation, decorrelation analysis, photophysical & statistical analysis, vibration analysis, 3D bead calibration and effective labelling efficiency (ELE)[4,5] (128, 86).

2.2.9.2 Cluster analysis

Voronoi analysis

In MATLAB, a Delaunay Triangulation is performed on the set of XY coordinates of all ratiometric PAINT localisations. Next, the Voronoi diagram is generated based on the Delaunay triangulation. Here, all unique pairs of Voronoi tessellates sharing an edge are determined. The list of pairs of Voronoi tessellates is randomly permutated to reduce artefacts and for each pair in the list. Two Voronoi tessallates are merged into a superVoronoiCluster, if the difference in general polarisation (GP) of the membrane order is less than a threshold T, typically T=0.05. The merging of tessellates is iterated, until no more areas sharing an edge exist that have a GP difference below threshold

[4] `https://www.embl.de/download/ries/Documentation/SMAP_manual_NPC.pdf`, as of 04/01/2023
[5] `https://www.embl.de/download/ries/Documentation/SMAP_UserGuide.pdf`, as of 04/01/2023

T. This process is repeated at least 3 times each having a permutated list of Voronoi tessellate pairs and an output is generated with the area, mean GP value, and emitter density within each super-tessellation.

The size distribution is analysed by comparing it with a randomised dataset through a Q-Q plot. This method plots the quantiles of the probability distributions from both datasets against each other. Observing a linear relationship in the plot suggests that the two datasets have similar probability distributions. Conversely, any deviation from this line highlights the dissimilarities between the distributions. For the randomised dataset, the GP value of each coordinate was permutated with the GP value of a coordinate within 10×10 µm^2. For the Q-Q-plot the mean $\pm$ 95% CI was calculated.

PLASMA

For each point, the similarity in GP value to all other points within 50 nm is calculated and normalised (0 corresponds to identical and 1 to lowest similarity in neighbourhood). Next, a ordered list is generated from highest similarity to lowest similarity for all point pairs. Then, all point pairs are clustered iteratively, starting from the top of the list until a similarity threshold is reached corresponding to the maximum difference between two points. A graph is generated for each point cluster and the convex hull of each cluster is used to estimate the boundary of each domain[6] (from unpublished work).

[6] `https://github.com/lucapanconi/PLASMA`, as of 04/01/2023

2.2.9.3 Quantitative microscopy

CoPS

The first 1.0×10^7 excitation cycles during CoPS acquisition are used to generate a histogram of multi-detection events (1 to 4 detection events). These histograms are then fitted to an analytical model of n emitters at p excitation probability. An additional single background emitter at low excitation probability p_{bg} is included into the model to account for unspecific fluorescence signal. Using a Levenberg-Marquardt algorithm, the parameters best representing the observed histograms are fitted (from unpublished work by Johan Hummert).

ELE

Effective labelling efficiency (ELE) analysis was performed as described by Thevathasan *et al.* (86). In short, the orientation of the nuclear pore best representing the observed localisation pattern is determined. Next, each segment within the 8-fold symmetry of a NPC having at least 2 localisation was classified as fluorophore positive. The probability of having at least one label in a segment can be represented as $1 - p_{dark}$, where p_{dark} is the observable probability of no label within a segment. Based on the distribution of how many segments are labelled within each NPC, a binomial distribution can be fitted that best represents the observed distribution of up to 8 labelled segments.

quickPBSA

Quick-photobleaching step analysis (quickPBSA) was performed as described by Hummert *et al.* (3). In short, a diffraction-limited spot detection is performed on the first frame in ThunderSTORM. For each spot, the intensity of the central region is corrected for the background intensity in each frame. Next, the complete trace is analysed to detect the

final bleaching step. The bleaching step height is recorded for all traces and traces with a step height not corresponding to the expected mean step height are removed. The emitter number is then estimated throughout the full trace based on a Bayesian model of posteriors, allowing for simultaneous bleaching of multiple emitters and blinking.

ProDOL

Protein-tag degree of labelling (ProDOL) was performed as described by Tashev *et al.* (5). In short, images recorded for the target and reference channel are analysed in a 7 step process (See Fig. 4.8). First, the cell is segmented, generating a mask based on the ”Triangle” thresholding algorithm in ImageJ. Then, the single molecules emissions are detected for each channel using ThunderSTORM. In a third step, the two channels are registered relative to each other using affine transformation limited to 3 pixel shift, 5° rotation and 5% scaling. Next a threshold is generated at which the probability of specific colocalisation is maximised (compared to 90° rotated target channel). A density correction is performed to correct for multiple detection events, missed detections, and false positive detections, resulting in the corrected degree of labelling from the degree of colocalisation.

2.2.9.4 Registration

3D rendering of volumetric reconstructions was performed using 3Dscript based on work by Schmid *et al.* (129).

Rigid and affine transformation

A first coarse alignment based on rotation and translated was performed manually in TrakEM2. Next, an automated rigid and affine transformation was performed using MultiStackReg for fluorescence microscopic images, based on a pyramidal approach of iterative coarse-to-fine alignment utilising the Levenberg-Marquardt-algorithm at each iteration. Alternatively, a landmark-based registration and transformation was performed in TrakEM2 for electron microscopic images.

Landmark-based transformation

Landmark-based transformation using affine transformation was performed in TrakEM2 when automated affine alignment in consecutive sections was non-successful. A correlative alignment of light- and elctron microscopy modalities was performed using BigWarp. The volumetric electron microscopy reconstruction was used as reference. Multiple landmark-based alignment markers were selected for each section, allowing for a spline interpolated deformation of corresponding structures. Exemplary alignment shown in Fig. 5.24.

3D rendering

3D rendering of volumetric reconstructions was performed using 3Dscript based on work by Schmid *et al.* (129). 2D projection of volumetric datasets was performed using a two step approach. In a first step, the z-stack was colourised based on the z-depth, the the z projection was performed. To do so, the ”Spectrum” look-up table (LUT) within ImageJ was converted to a list of 171 RGB values transitioning from red to green to blue. Then the list was reduced with equal spacing between entries to match the number of slices in the z-stack. Each section was next coloured using a linear intensity interpolation

from black to the RGB value of the nth entry in the reduced LUT list. Subsequently, the coloured 2D projection was generated using either maximum or SD z-projection.

2.2.9.5 Microtubule and cell orientation

Orientation analysis was performed based on the software developed by Marcotti *et al.* and Cetera *et al.* (130, 131). Here, the matrix of all angles, eccentricities, and alignment order were exported to perform subsequent analysis. In short, alignment by Fourier transform (AFT) is used to determine the dominant orientation of structures within a square region based the Fourier spectrum. The angle is then compared to neighbouring quadrants to determine the alignment order. The alignment order is calculated by:

$$S = \frac{2\sum_{i=1}^{n^2-1}\cos^2\theta(\vec{v}_0, \vec{w}_i)}{n^2-1} - 1 \tag{2.7}$$

where S represents the average alignment order relative to the central reference vector $\vec{v}_0$, with $\vec{w}_i$ denoting any vector from the set of all vectors located within an $n\times n$ neighbourhood (excluding the central vector itself). θ represents the angle between the two vectors. A value of 1 corresponds to perfect local alignment, 0 random local alignment and -1 orthogonal local alignment (Fig. 2.2).

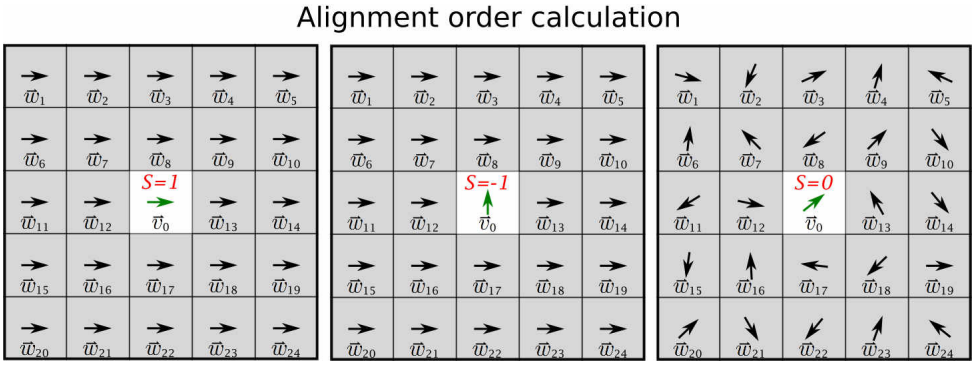

Fig. 2.2: Schematic of calculating the alignment order parameter. The central dominant alignment vector ($\vec{v}_0$, green) is compared to all vectors in an $n\times n$ neighbourhood ($\vec{w}_i$, black). Using Eq. 2.7, the alignment order parameter S (red) can be determined. $S = 1$ corresponds to perfect local alignment, $S = -1$ corresponds to orthogonal local alignment, and $S = 0$ corresponds to random local alignment. Figure inspired by Marcotti *et al.* (131).

Chapter 3

Design of a single-molecule localisation microscope

3.1 Introduction

Since the inception of microscopes capable of resolving beyond the diffraction limit, researchers either had to have the optical engineering capabilities to develop and build their own implementation or have relied on commercial systems. While commercial systems have known performance characteristics, modifying them to meet specific needs in terms of automation, field of view (FOV), multi-colour imaging, flat-field illumination, or 3-dimensional (3D) reconstruction capabilities remains limited - all while being relatively costly (132). In contrast, custom-built systems can be tailored to specific needs but may suffer from instabilities, limited interoperability, and the requisite knowledge of the laboratory. A recent estimate for (re-)building and validating a previously developed custom-built microscope is 3-6 months (132), with more time needed for iterating and improving on a newly developed microscope. Nonetheless, given the expertise and equipment available, a custom-built single-molecule localisation microscopy (SMLM) microscope was developed within this thesis to implement relevant features while being highly adaptable to specific needs.

3.1.1 3D super-resolution

The lateral resolution of a single emitter can be determined with high accuracy by finding the centre of a point spread function (PSF), contrary, the axial localisation remains mostly unaffected due to the ambiguity of the out-of-focus PSF width, both above and below the focal plane (Fig. 3.1 a). To resolve this ambiguity, several methods exist.

Most notably, phase plates at the Fourier plane can introduce a modified PSF resolving the 3D position. Here, the double-helix is the most prominent method, offering good localisation precision over a large imaging depth ($\pm$1 µm) (133), while only performing slightly worse with respect to localisation precision in focus compared to other techniques (Fig. 3.1 b). Yet, due to the larger PSF size close to the focus, high-density samples can result in worse reconstruction performance due to fitting errors.

Similarly, astigmatism can be introduced using a phase plate at the Fourier plane (Fig. 3.1 c). This is typically implemented by adding a cylindrical lens, thus resolving the ambiguity by shifting the focal plane of one axis while not affecting the orthogonal axis, effectively leading to a different focus for the x and y axes. This method is easy to implement and leads to good localisation precision around the focus, but drops off more quickly than other methods (133).

A third option is biplane imaging, a method where the emission is split and a path-length difference is introduced, thus resolving the depth ambiguity by comparing the PSF width in both images (Fig. 3.1 d) (134). While this method benefits from not having to modify the PSF, the comparison of two images either doubles the acquired data or halves the FOV.

Alternative methods exist, limiting the axial resolution to the proximity of the coverslip, making use of total internal reflection fluorescence (TIRF) illumination and the effect that the intensity of emission follows an exponential decay with increasing axial distance due to the decay of the evanescent field (135).

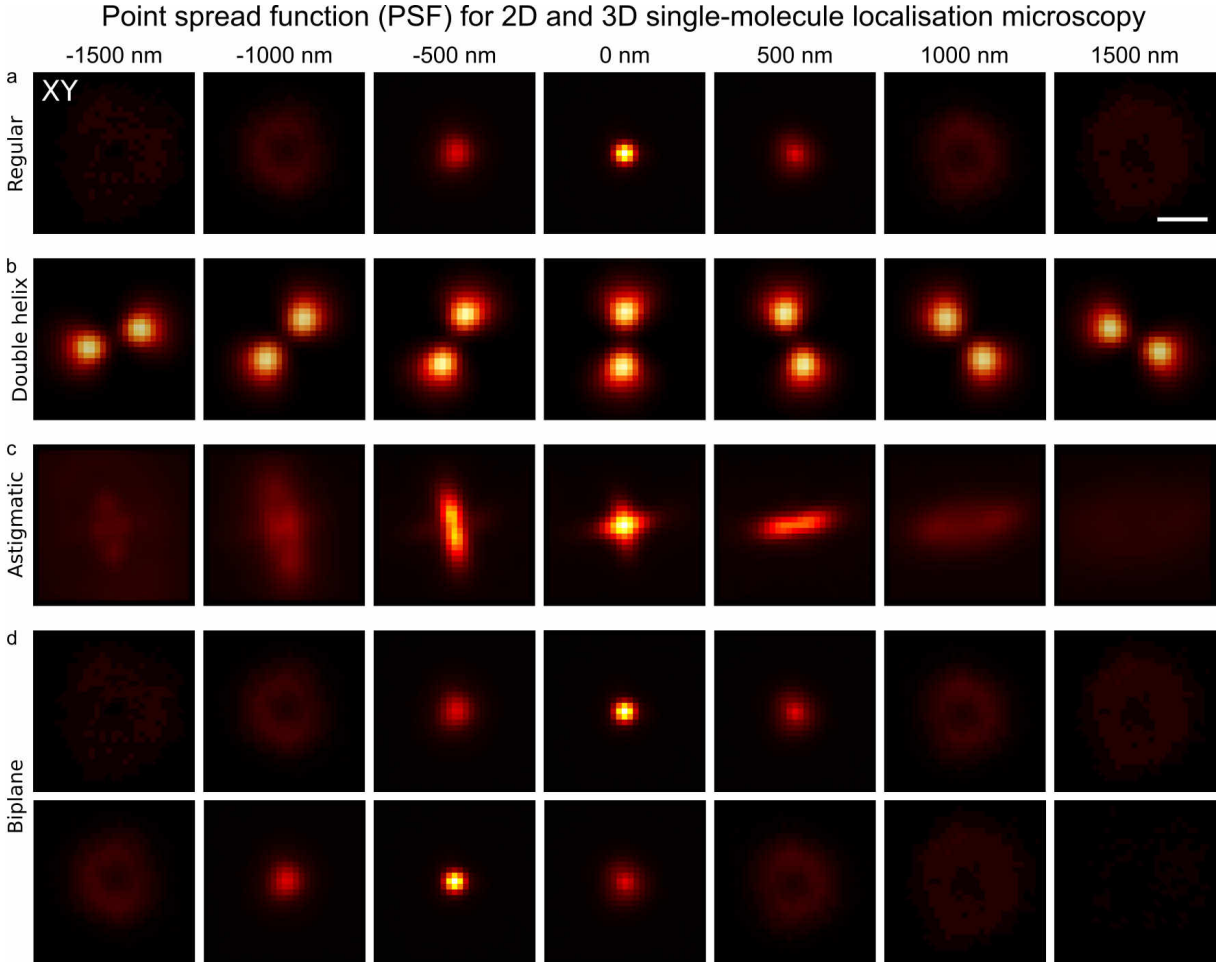

Fig. 3.1: Schematic representation of PSF models for 2D and 3D localisation microscopy at various focus depths a) 2D localisation microscopy PSF, b-d) 3D localisation microscopy setups using b) houble helix, c) astigmatic, and d) biplane microscopy. a) Conventional 2D localisation microscopy setups exhibit an ambiguity in PSF shape for emitters having the same axial distance to the focal plane (above and below) (experimental data). b) Double helix setups use a phase-mask at the back focal plane (BFP) where the depth information is represented by the rotational angle of the double helix (schematic representation). c) Astigmatic setups utilise a cylindrical lens to shift the focus along one axis, leading to an offset in focus for the two orthogonal axes, resolving the ambiquity of depth (experimental data). Depth information can be retrieved from fitting the observed PSF to a calibrated depth standard. d) Biplane setups split the image path and introduce a path-length difference to resolve the depth ambiguity without the need of modifying the PSF shape. Depth information is retrieved from comparing the PSF width measured for both image paths (schematic representation from shifted 2D PSF model).

3.1.2 Flat-field illumination

Various systems exist to transform a non-homogeneous illumination profile, typically a Gaussian transverse electromagnetic mode $(TEM)_{00}$, into a uniform flat-top illumination (Fig. 3.2). Popular implementations include field-mapping devices, multi-mode fibres, Köhler integrators, or laser scanning, alongside specialised systems using, e.g. waveguide chips (124, 136). Field-mapping devices use refractive or diffractive optics to transform a known input beam into a flat-top laser beam with strict input beam requirements, at low complexity and high transmission efficiency (124, 137). Multi-mode fibres have been shown to also produce good homogeneity but suffer from coupling losses and require a vibrator to reduce speckling through temporal averaging (124, 138). Köhler integrators, on the other hand, use a microlens array to homogenise the illumination profile, allowing for a variable input beam characteristic at the cost of lower transmission efficiency (124, 139). Finally, laser scanning typically utilises a confocal microscope setup to scan the beam over a variable FOV, leading to high flexibility in the illumination profile, but come at a high cost and complexity (124, 140).

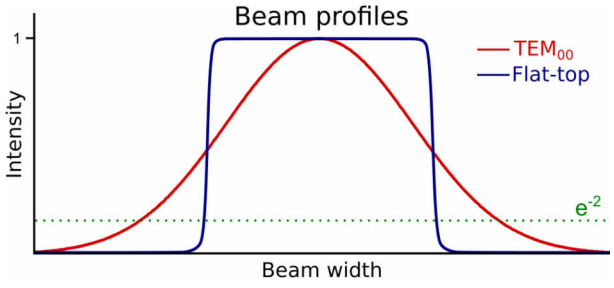

Fig. 3.2: Beam profiles. Comparison of an ideal TEM_{00}/Gaussian profile and a flat-top profile. The beam diameter can be defined by the distance between two points at which the beam intensity surpasses 13.5% of the maximum intensity (e^{-2}).

3.1.3 Camera

Besides the previously mentioned importance of pixel pitch to resolve the sub-diffraction limited position of a single emitter in line with the Nyquist–Shannon sampling theorem, three camera sensor types exist that can be used for super-resolution imaging (64, 65).

Historically, electron-multiplying charge-coupled device (emCCD) cameras have been the most common camera type, known for their high pixel uniformity and high photon sensitivity (quantum efficiency (QE)$\geq$90% between 500 - 700 nm) combined with $<$1 e^- read noise[1]. However, the sensor architecture results in a lower readout speed compared to other camera architectures, effectively limiting the FOV (Fig. 3.3) (141).

Scientific complementary metal–oxide–semiconductor (SCMOS) cameras, on the other hand, can read out an image significantly faster at an equal pixel count. Yet, for the longest time, sCMOS cameras had a lower quantum efficiency (QE$\geq$80% between 500 - 700 nm) and thus lower sensitivity. The lower QE combined with pixel-to-pixel non-uniform photon response, originating from the per pixel photon to voltage conversion, made single-emitter imaging impractical (Fig. 3.3) (142). Technical advancements now make sCMOS cameras the most common type in super-resolution microscopy (143).

Lastly, single-photon avalanche diode (SPAD)-array cameras are beginning to be commercialised (Fig. 3.3). Avalanche photodiodes (APDs) have a low photon detection noise, combined with high frame rates and the additional benefit of resolving the fluorescence lifetime. However, they have a lower photon detection probability in part due to the low fill factor ($\leq$55% between 500 - 700 nm) (144, 145).

[1] `https://andor.oxinst.com/products/ikon-xl-and-ikon-large-ccd-series`, as of 27/11/2023

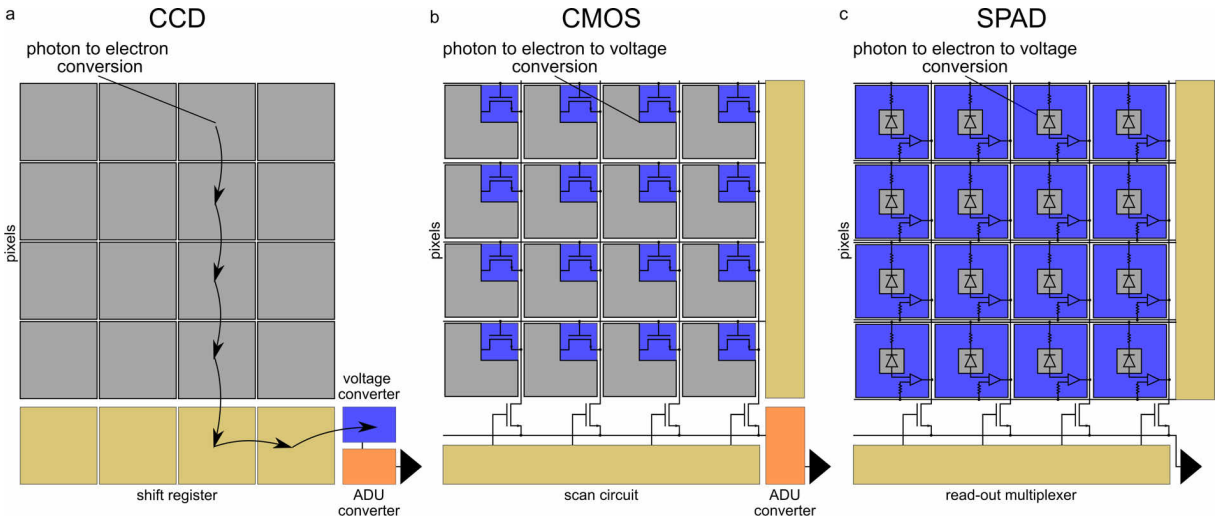

Fig. 3.3: Camera architectures. a-c) Exemplary schematic of CCD (a), CMOS (b) and SPAD (c) camera architecture. Gray indicates the photon sensitive area, blue corresponds to the electron to voltage conversion circuit, dark yellow represents the read-out circuit, orange represent the analog-to-digital units (ADU) converter. a) CCD cameras operate on a shift register, transferring the accumulated charge in a potential well from pixel to pixel before being converted to a voltage level. b) CMOS cameras convert the photoelectrons to voltage on a per pixel basis. Charge is accumulated during the exposure time and transferred to the readout circuit. c) SPAD arrays use a photodiode that results in the breakdown of the voltage potential when a single photon is absorbed (141, 142, 146).

Furthermore, state-of-the-art SPAD array cameras suffer from up to 1.5% high dark current pixels[2]. Additionally, for each pulse, a binary image is generated, representing if at least one photon was detected, making the intensity calculation of n-bit images an indirect approach (145, 146, 147, 148).

3.1.4 Camera correction

Scientific grade cameras used in microscopy generally have a high pixel uniformity, linear photon response, and low noise levels (143). Yet, sCMOS cameras can suffer from a higher pixel inhomogeneity compared to emCCD. This non-uniformity can introduce systematic localisation errors in SMLM. Therefore, a per-pixel camera characterisation can minimise these artefacts (149).

[2] `https://www.axiomoptics.com/products/spad512s/`, as of 27/11/2023

Various noise sources exist in sCMOS sensors including thermal noise, read noise, 1/f noise, shot noise, popcorn noise, and others (150). When calibrating cameras, the noise is typically expressed as a static noise map, dominated by read noise, and a variable noise map with temporal dependence, dominated by thermal noise. Therefore, these maps are generally referred to as read noise map and thermal noise map (149). Read noise represents the variability introduced when reading and converting the sensor signal into a digital unit (Fig. 3.4) (151). Thermal noise results in an increased noise floor for longer exposure times, due to the thermal movement of electrons in the metal oxide semiconductor field-effect transistor (MOSFET) channel of the sCMOS sensors (152).

Similarly, the offset and dark current can be determined. Offset represents the static average value of a pixel, and dark current the temporal dependence of the average value of a pixel. Generally, an offset is added by the camera logic to prevent a pixel value smaller than 0. Dark current, on the other hand, results from leakage currents in the MOSFETs, altering the charge in the sensor over time (153).

Finally, the ADU recorded in a camera can be reconverted into photon counts by applying a conversion factor, named gain. For significantly high ADU, the dominant source of noise in a camera image originates from photon noise. Here, the variance of photon noise (and thus ADU variance) correlates to the number of photoelectrons (central limit theorem for a Poisson distribution). Using this relation, the gain can be calculated from the slope of a variance-intensity plot (Fig. 3.4) (149).

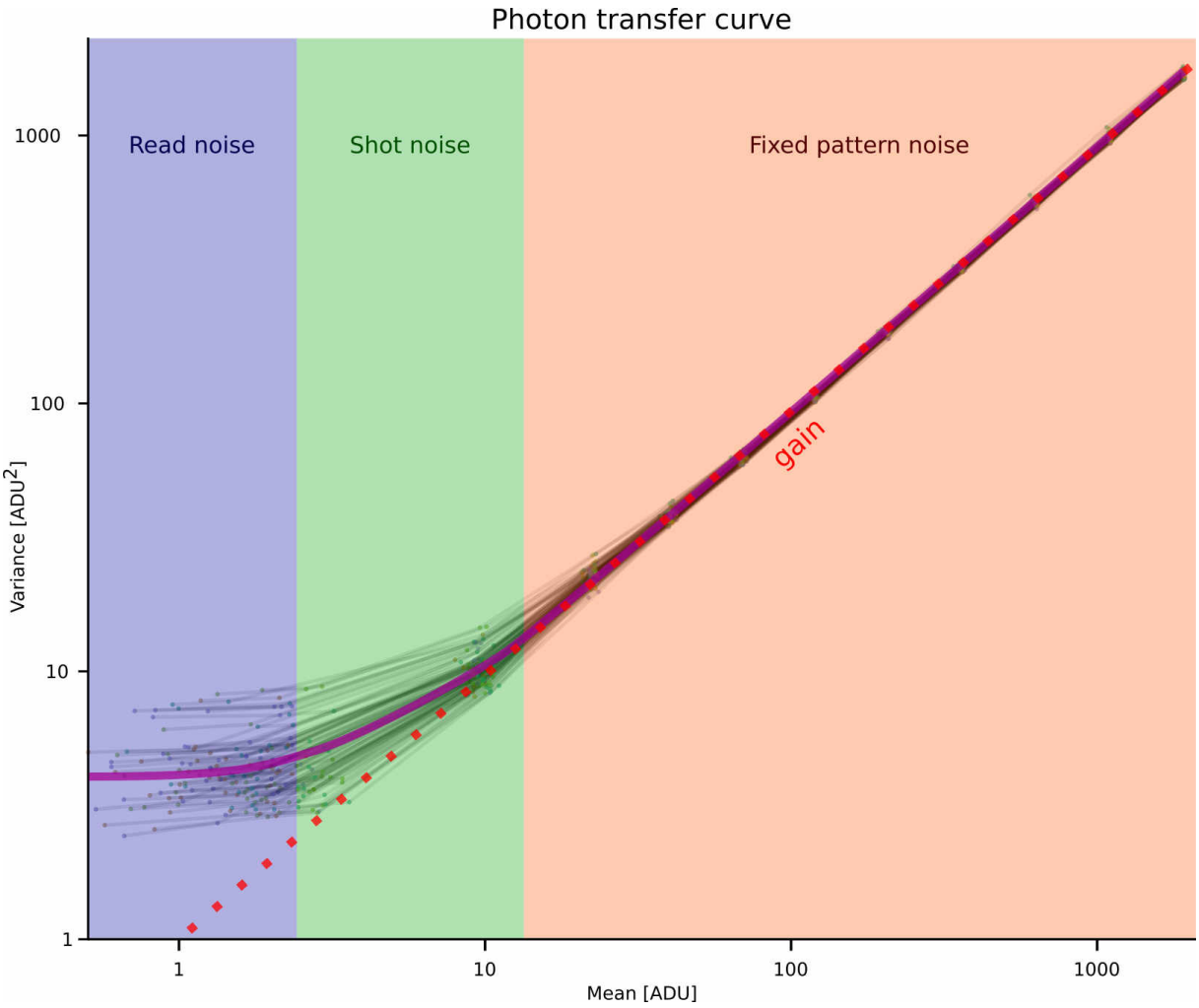

Fig. 3.4: Photon transfer curve. A photon transfer curve relates the variance of a pixel to the mean intensity. Various types of noise exist in camera sensors. The read noise, indicated in blue, shows variability that occurs during the reading and conversion of the sensor signal to ADU. Shot noise, shown in green, represents the variability from the quantised nature of the photon detection. The fixed pattern noise region, represented in orange, is a linear response and effected by pixelwise gain inhomogeneity. The red line denotes the gain of the camera. The relationship between the variance of a pixel and its intensity is linear at higher intensities, enabling the calculation of gain from the slope of the photon transfer curve.

3.1.5 Aims

Within this work, the inception, construction, and validation of an advanced SMLM microscope, specifically tailored for the development of novel direct stochastical optical reconstruction microscopy (dSTORM) and quantitative imaging techniques is described. This design features a large FOV measuring 133$\times$133 µm^2, with uniform illumination across the illuminated sample combined with an irradiance of 3.5 kW/cm^2 at 647 nm, crucial in dSTORM. The microscope is outfitted with optics to perform ratiometric multi-colour and astigmatism-based 3D dSTORM. To maintain a large FOV, dual sCMOS cameras are used for efficient spectral separation over the entire FOV. The construction is subdivided into four modules, allowing for iterative optimisation and validation. Following the construction, the sCMOS cameras undergo per-pixel gain calibration. This step is pivotal for mitigating pixel-related localisation errors that can affect the dSTORM reconstruction quality. Additionally, using the gain correction maps, pixelwise intensity variances can be corrected allowing for an improved quantitative image reconstruction. The final segment of this chapter delves into a thorough evaluation of the microscope's theoretical SMLM performance. This assessment encompasses a detailed examination of the illumination distribution over the FOV, the precision of 2D/3D localisation on bead samples, and the overall stability of the system, particularly vibrations among other factors that could potentially impact the theoretical performance of the SMLM setup.

3.2 Results

3.2.1 Microscope setup

The construction is subdivided into four modules, allowing for independent iterations on them. In module 1, the beams are expanded to 6 mm and superimposed (Beam combination, Fig. 3.5 a, 3.6), followed by a module of beam shaping, enabling homogeneous illumination in the sample plane, variable beam expansion, and automated epifluorescence (Epi)-TIRF illumination (Beam shaping, Fig. 3.5 a, 3.7). The third module of the optical setup involves the sample illumination and fluorescence collection using the framework of an open-frame microscope structure (Microscope body, Fig. 3.5, 3.8). The emitted fluorescence is collected, spectrally filtered and projected onto two sCMOS cameras in the final module (Detection pathway, Fig. 3.5 a, 3.11). For operational simplicity and automation, all modules have been engineered to be controlled via a unified software interface, with µManager serving as the integration tool for this purpose (117).

3.2.1.1 Beam combination

To illuminate spectrally non-overlapping fluorescent samples, multiple laser lines need to be superimposed and controlled to allow for sub-millisecond switching between laser lines. Additionally, due to the refractive field-mapping device used in microscope module 2 (Sec. 3.2.1.2), all laser lines need to be expanded to a collimated beam width of 6.0$\pm$0.1 mm (Fig. 3.6 i,h,k). For the system, commonly used laser lines were chosen

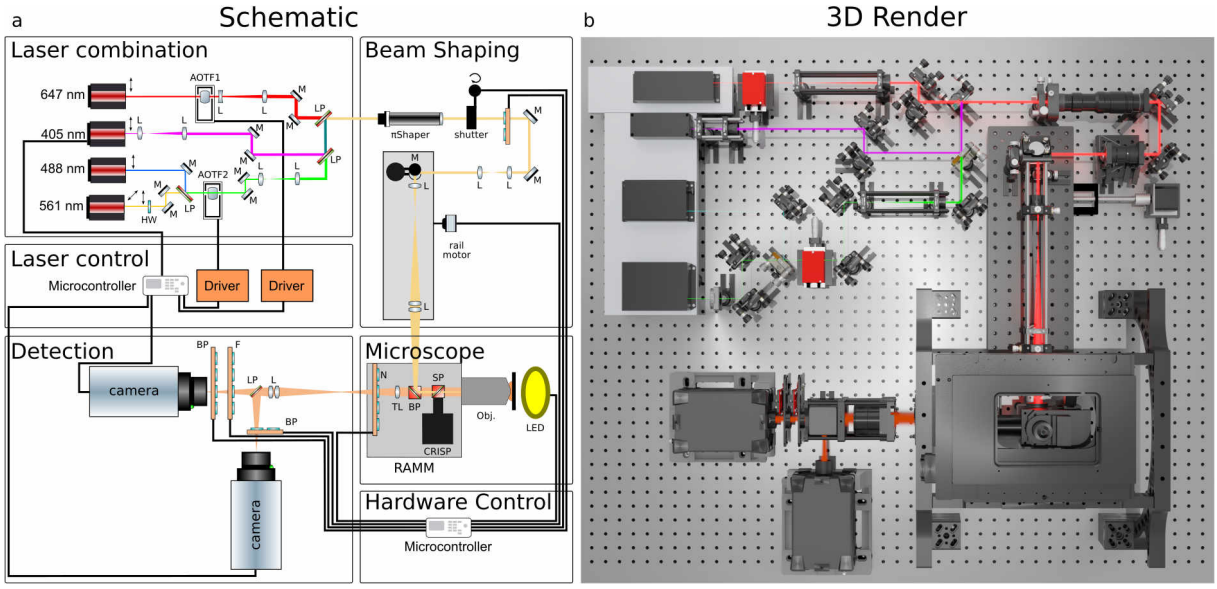

Fig. 3.5: Microscope setup. Schematic and 3D render of the custom-built large FOV dSTORM setup with homogeneous illumination. The system is subdivided into four microscope modules and two microcontroller modules, allowing for independent development of each. Dual sCMOS cameras allow for ratiometric imaging at high frame rates. The setup uses a Nikon 100x 1.49 numerical aperture (NA) oil immersion objective. Acousto-optic tunable filter (AOTF), band-pass filter (BPF), filter (F), half-wave plate (HW), lens (L), long-pass filter (LP), mirror (M), short-pass filter (SP).

- 405 nm (Fig. 3.6 c), 488 nm (Fig. 3.6 b), 561 nm (Fig. 3.6 a) and 647 nm (Fig. 3.6 d), with 405 nm and 647 nm being crucial for dSTORM imaging (56).

A laser module of 647 nm and 2 W output power was chosen to achieve an irradiance exceeding 3 kW/cm^2 in the sample plane, necessary for dSTORM. This is crucial for pumping sufficient dye into a prolonged dark state to be able to generate single molecule emitters (154). Given the proposed large FOV of 133x133 µm^2, a fibre laser was chosen for having a narrow line-width, excellent beam quality close to the ideal gaussian beam propagation ratio M^2 of 1.0 (TEM$_{00}$, experimental M$^2 \leq$1.05) and sufficient power (2RU-VFL-P-2000-647, MPB Communications Inc).

For 405 nm, a TEM$_{00}$ diode laser was chosen with M$^2 \leq$1.2 at 100 mW, as 405 nm reactivation of dark-state emitters in dSTORM is typically limited to $\leq$40 W/cm^2 with less critical constraints on beam quality (iBeam smart-405S-100mW, Toptica Photonics AG) (155). The 488 nm module was a pre-existing 40 mW TEM$_{00}$ solid-state laser

with $M^2 \leq 1.1$. As 488 nm is only intended for diffraction-limited imaging of fiducials and secondary structures of interest, this laser is sufficiently suited for the system (40 mW Cyan Scientific Laser, Spectra-Physics Corp). For 561 nm, a solid-state laser was chosen with 350 mW TEM_{00} and $M^2 \leq 1.1$ (350 mW gem 561, Laser Quantum GmbH). 350 mW was chosen to allow for the potential of spectral multiplexing in dSTORM in a reduced FOV of 65×65 µm^2. All lasers but the 561 nm laser line are vertically polarised (*s*-polarisation), with 561 nm being horizontally polarised (*p*-polarisation). To control the laser power and to switch between laser lines, AOTFs were used (AOTFnC-VIS, AA Opto-Electronic). As these require *s*-polarised light, a $\lambda/2$ wave plate was used at the 561 nm laser exit to rotate the polarisation and allow for AOTF modulation of the 561 nm laser line (Fig. 3.6 e). In general, between optical beam modulating components, two fine-adjustment steering mirrors were placed to independently adjust the position and angle of each laser and produce co-linear beams. Here, broadband dielectric mirrors with a coating for 400–750 nm were chosen for having a reflectivity exceeding 99% at all laser lines. 488 nm and 561 nm lasers were able to share a single AOTF as they were of the same beam diameter. Therefore, the two laser lines were superimposed using a 540 nm LP before passing through the AOTF (Fig. 3.6 f,g). An AOTF only allows light to propagate in a co-linear path if a specific standing acoustic wave is generated matched to the wavelength of the incident laser line. Powering off the AOTF results in the beam being blocked, as mandated by the non-ionising radiation risk assessment (diffracted light is blocked by a beam dump). The 647 nm laser is coupled into a separate AOTF (Fig. 3.6 g). Finally, the 405 nm laser has no need for a modulator, as the output of the diode laser can be switched at the microsecond scale.

Next, beams were expanded to a $1/e^2$ diameter of 6.0 mm, necessary for transforming the TEM_{00} beam into a flat-top profile at the refractive field-mapping device in microscope module 2. For the high-power 647 nm laser line, a Galilean beam expander setup was chosen, expanding the beam from 0.80 mm to 6.0 mm (lens (L_1): plano-concave, focal length (f_1)= 16 mm; L_2: achromatic doublet, f_2=120 mm) (Fig. 3.6 k). For 405 nm, the beam was expanded from 1.2 mm to 6.0 mm using a Keplerian beam expander with available lens combinations (L_1: achromatic doublet, f_1=10 mm; L_2: achromatic doublet, f_2=50 mm) (Fig. 3.6 i). The last beam expander was used to expand both 488 nm and 561 nm beams from 0.75 mm to 6.0 mm (L_1: achromatic doublet, f_1=16 mm; L_2: achromatic doublet, f_2=125 mm) (Fig. 3.6 h). The 405 nm line was superimposed with 488 nm and 561 nm using a 450 nm LP filter (Fig. 3.6 j). Finally, the 647 nm laser was superimposed using a 585 nm LP filter (Fig. 3.6 l).

In general, great efforts have been made to keeping the path lengths as short as possible to increase pointing stability at the sample, minimising any losses and minimising the overall footprint of the system. For example, the first iteration of the system used single-mode fibres to improve the M^2 of 405 nm, 488 nm, and 561 nm, as the specification of the piShaper stated the need for a high-quality TEM_{00} input beam. After testing the output beam profiles with and without fibre coupling, the slightly reduced output beam quality was accepted to minimise the power losses from the fibre setup (Fig. SI 1).

3.2.1.2 Beam shaping

In microscope module 2, the beam characteristics were modulated (width, profile, position) to allow for high performance widefield microscopy with Epi or TIRF illumination.

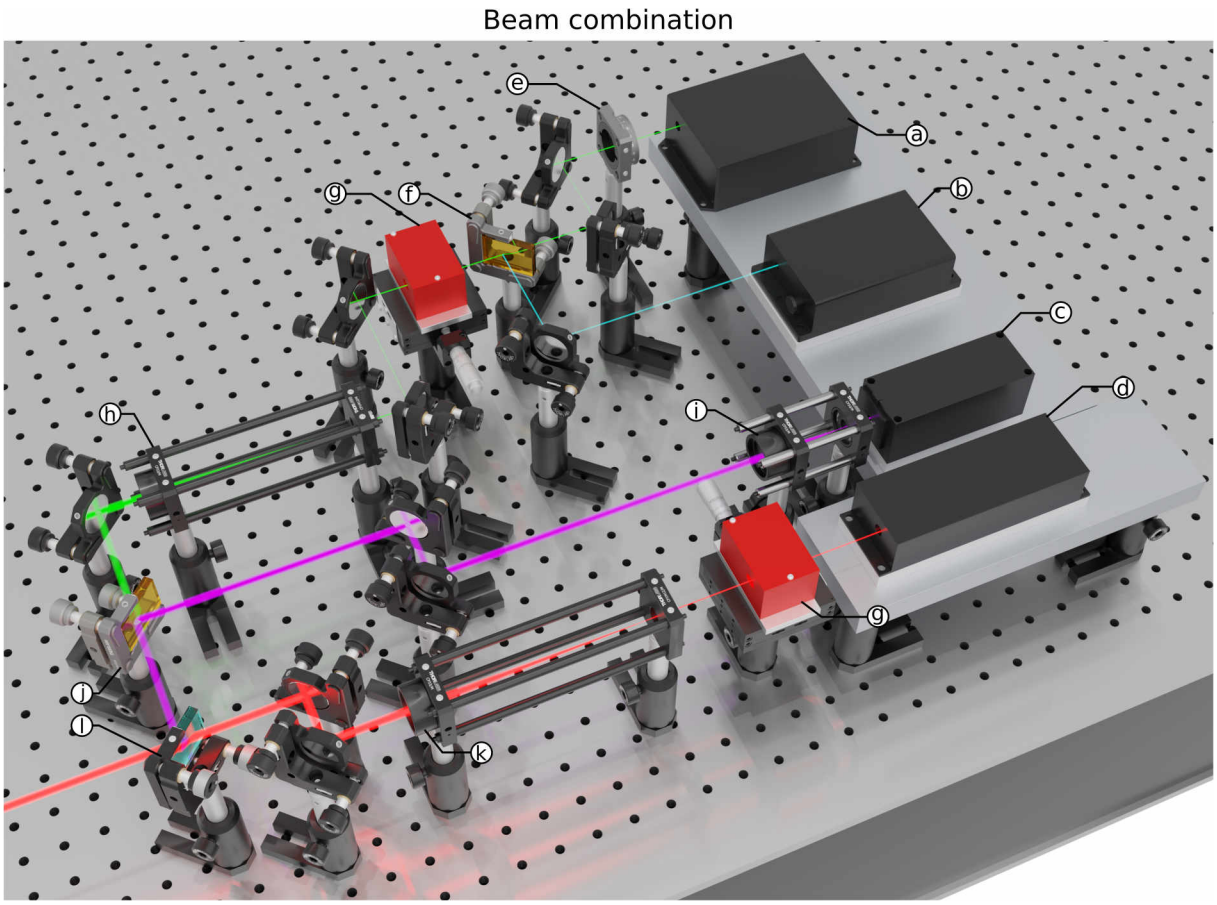

Fig. 3.6: Beam Combination. CAD render of the beam combination setup. Consisting of 4 laser lines (405 nm, 488 nm, 561 nm, and 647 nm; a-d), illumination control (AOTF; g), beam expansion (h, i, k) and beam super-positioning using dichroic filters (f, j, l). Additionally, a HW is used for the 561 nm laser line to rotate the polarisation (e).

First, all beams were expanded to 6.0 mm and superimposed. Then, the Gaussian TEM_{00} beam profiles were converted to flat-top profiles for homogeneous illumination at the sample plane (Fig. 3.7 a). Non-homogeneous illumination introduces position-dependent effects such as a variable signal-to-noise ratio (SNR) and inconsistent photobleaching. Furthermore, the photophysics of emitters are highly affected by the irradiance, causing changes to the photoswitching rate and emitter density in dSTORM. These effects result in an inconsistent and position-dependent SMLM reconstruction quality. Therefore, the homogeneous illumination of a sample highly benefits quantitative and super-resolution microscopy.

Here, a lens-based refractive field-mapping beam shaper (PiShaper 6_6 VIS, AdlOptica Optical Systems GmbH) was chosen over a multi-mode fibre approach or Köhler integrator, among other flat-fielding techniques (Sec. 3.1.2) (124). The high transmission efficacy, relative achromaticity, and low complexity made this system favourable with the drawback of having stringent requirements on input beam diameter and collimation as well as being more susceptible to deterioration over prolonged path lengths (124). As two commercial refractive field-mapping beam shapers exist, piShaper was chosen over TopShape for having better intensity uniformity and better edge steepness with the drawback of a faster decrease in plateau uniformity by producing an Airy disk-pattern (156, 124). Therefore, space after the piShaper was minimised to reduce deterioration of the top-shape beam.

On a motorised Epi-TIRF rail (Fig. 3.7 e), a Keplerian beam expander was placed to expand the beam from 6.0 mm to 20 mm (L_1: achromatic doublet, f_1=60 mm; L_2: achromatic doublet, f_2=200 mm). Given a tube lens of f=200 mm and a Nikon 100x objective (f_{Obj}=2.00 mm), homogeneous illumination with a width of 200 µm is obtained (Fig. 3.7 c). Correct alignment of all components on the Epi-TIRF rail was checked with alignment lasers coming from the objective mount at the microscopy body in combination with pinholes at multiple positions throughout the system. In general, correct alignment was validated after insertion of each lens by confirming continued co-linearity of the 647 nm laser path and the “alignment laser” path. To correct for minor translational inconsistencies, all lenses were placed on XY translation mounts. The expanded beam was focused on the BFP using an achromatic doublet as tube lens (TL) (Fig. 3.7 d). The Epi-TIRF rail was moved between both Epi and TIRF illumination after

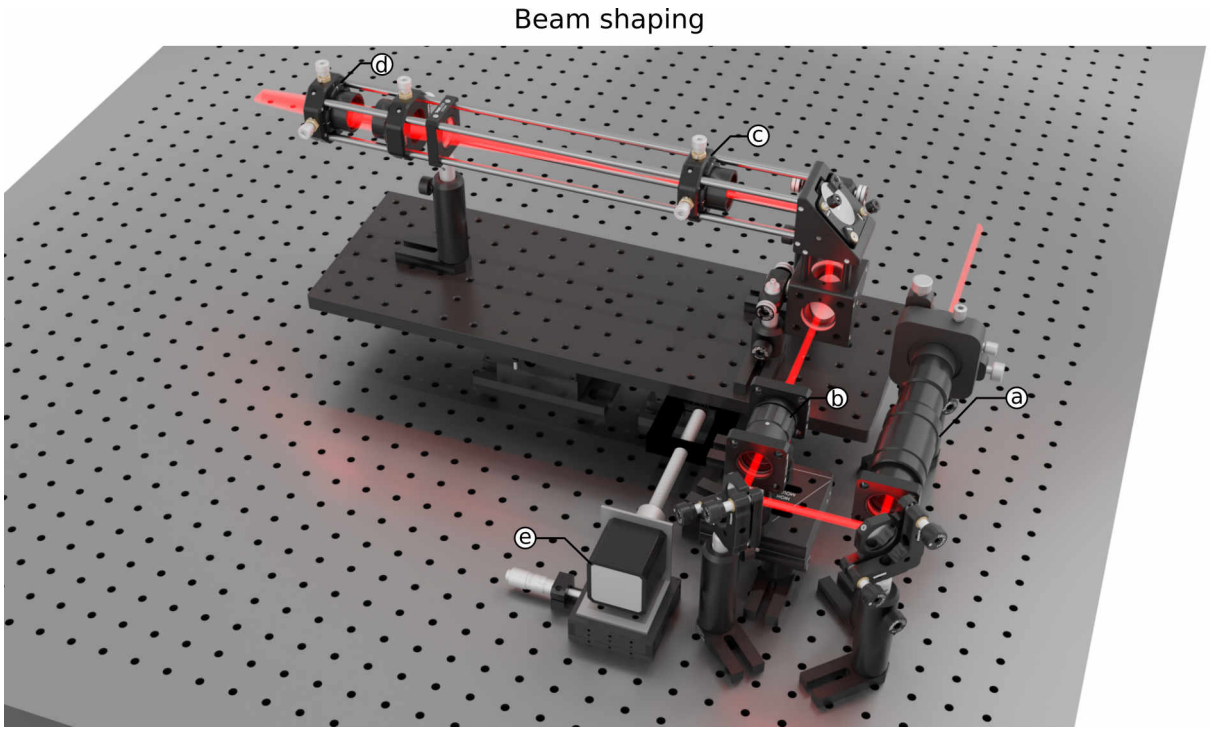

Fig. 3.7: Beam shaping. CAD render of the beam shaping module using a refractive field-mapping device for homogeneous illumination. a) PiShaper – for 6 mm TEM_{00} input beams, b) optional 0.5x Galilean beam expander, c) 3.3x permanent Keplerian beam expander, d) achromatic doublet lens as TL (L_{TL}: Achromatic doublet, f_{TL}=500 mm), and e) motorised Epi-TIRF rail (NEMA17 stepper motor controlled linear stage). The beam shaping module underwent iterative optimisation to improve robustness and *in sample* illumination optimisation (Fig. SI 2, SI 3).

insertion of each lens, and correct positioning of the optical element was confirmed by validating an unchanged beam propagation using a 2 pinhole approach within the cage system. The Epi-TIRF rail was automatically controlled using a NEMA17 stepper motor in combination with an A4988 stepper motor driver and an Arduino Uno (Sec. 3.2.1.5). Finally, a removable 0.5x achromatic Galilean beam expander was placed into the beam path, to allow for 4x higher irradiance while reducing the illuminated region to 100 µm in diameter.

3.2.1.3 Microscope body

As a microscope body, an open-frame system named rapid automated modular microscope (RAMM) was chosen (Fig. 3.8 a, ASI Imaging Inc), allowing for a highly configurable system with flexibility in the used objectives, filter sets, and optical com-

ponents. Using optomechanical components consisting of a dichroic mount, a 3-axis fine steering mirror, and a continuous reflection interface sampling and positioning (CRISP) autofocus system completed the optical excitation pathway of the microscope (Fig. 3.8 b,h,i,j). Stage control was handled by a MS-2000 stage with a 120x75 mm XY-travel range at 22 nm stepping resolution and a LS-50 linear Z-stage at 22 nm rotary encoder resolution for coarse Z-stepping (Fig. 3.8 c,d). The system was supplemented with a piezo-electric focus scanning Z-stage for 1 nm Z-stepping (Fig. 3.8 e, P-725.1CDE2, Physik Instrumente GmbH).

The RAMM system was chosen over other modular microscope systems such as the RM21 (Mad City Labs Inc) for the expertise in the lab with ASI systems for stage and autofocus control. Initially, a fully custom-machined body was conceived similar to recent modular microscopy platforms (157, 155) (Fig. SI 4) and validated in simulations, similar to the design of the RM21, but was replaced by the RAMM system for guaranteed performance and ease of expandability.

For focus control, a CRISP autofocus was equipped with a 850 nm LED and a 800 nm short-pass filter (Fig. 3.8 g), allowing for maximal photon detection while not reflecting the emission of far-red dyes (AF647, CF680). Atop the system, a custom-built Koehler illumination setup was placed using a Thorlabs cage system with three lenses (collector lens, field lens, and condenser lens). At the sample conjugate plane, an iris was placed to function as a field diaphragm. Furthermore, at the source conjugate plane, a second iris was placed as an aperture stop, allowing for optimal illumination with good contrast of the sample.

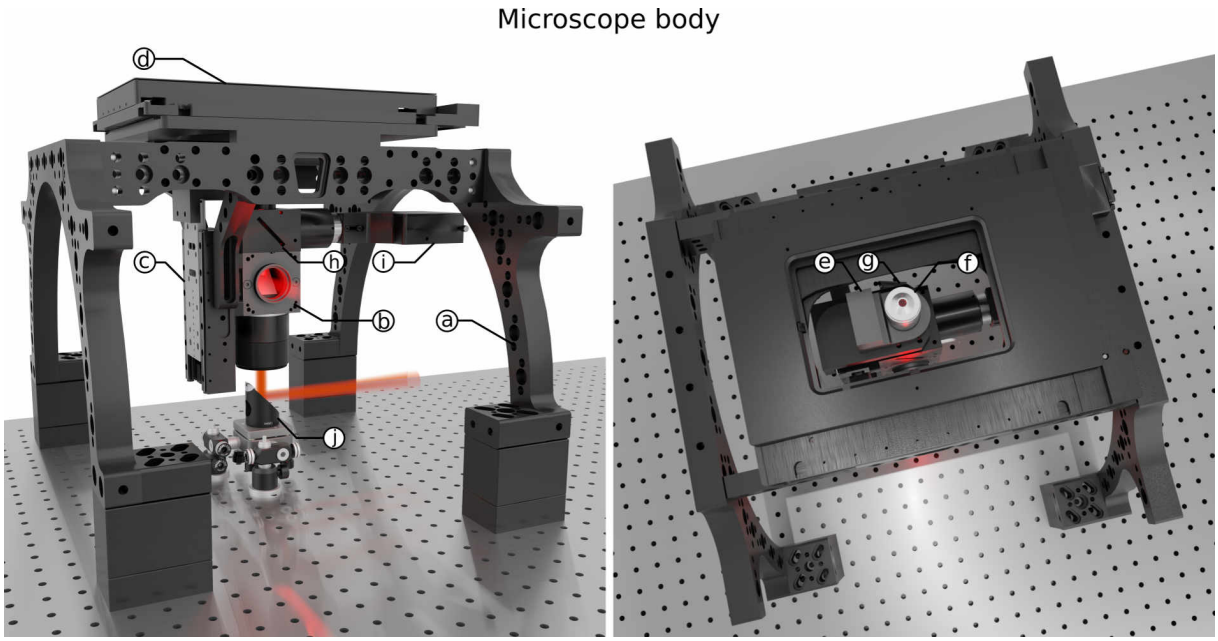

Fig. 3.8: RAMM microscope body. a) 3D render of the open-frame RAMM microscope used for dSTORM with homogeneous illumination. The system consists of a dichroic mount (b), a 3-axis fine steering mirror (j), and a CRISP autofocus system (g, h, i). The system uses XYZ-stages for 22 nm XY-stepping resolution and 1 nm Z-stepping resolution (c, d, e). Compatible objectives from Olympus and Nikon are used with the corresponding tube lens (UPlanXApo 100x 1.45 NA or CFI Apo TIRF 100x 1.49 NA oil immersion objectives).

The system was implemented to work with both an Olympus UPlanXApo 100x 1.45 NA or a Nikon CFI Apo TIRF 100x 1.49 NA oil immersion objective (Fig. 3.8 f, SI 5). Both have excellent performance in super-resolution microscopy and result in the correct magnification (matched to the optimal projected pixel width of the camera at the Nyquist limit of $\sim$110 nm) with high NA and broad chromatic and spherical aberration correction. To use each objective, the tube lens is exchanged to the matching Nikon or Olympus tube lens - no further modification is needed, as the specific implementation ensures having the same image plane for both objectives. For most applications, the Nikon objective was preferred for having a correction collar for variable thickness coverslips at both 23 °C and 37 °C.

One drawback of open-frame systems is that the tube lens typically used for a Nikon or Olympus objective is not sold separately from a microscope body. Therefore, custom-made bodies often utilise either achromatic doublets, achromatic doublet pairs (Plössl

configuration), or third-party tube lenses (155). As the optical design files for the Nikon objective, tube lens, and Thorlabs lenses were available for ray-tracing simulation (158, 159), the 3 optical systems were modelled in Oslo and TracePro (Lambda Research) as well as modelling in Raytracing (123) (Fig. 3.9, SI 8 a, SI 9). The performance characteristics for all options were compared for astigmatism, spherical and chromatic aberrations, as well as coma (Fig. 3.9 a,b). It was found that the achromatic doublet pair performed best with roughly a 50% reduction in chromatic aberration ($D_{min/max}$) from a 1 mm chromatic focal shift to a 0.5 mm chromatic focal shift (400 - 800 nm), while having increased spherical aberrations of roughly 200% (0.3 mm vs 0.15 mm at 6 mm entrance beam height). The tube lens sold by Thorlabs suited for Nikon objectives, on the other hand, has very low spherical aberrations ($<$0.1 mm at 6 mm entrance beam height) with a 1 mm chromatic focal shift (400 - 800 nm) (Fig. 3.9 c). Overall, the Nikon-style tube lens and Olympus-style tube lens had the best characteristics for each objective and were therefore chosen for the system.

3.2.1.4 Detection pathway

To collect the generated fluorescence and allow for ratiometric imaging, a two-camera system in the detection pathway was set up using back-illuminated Prime95B sCMOS cameras (Fig. 3.11 a,b). At 11 µm pixel pitch and 1200x1200 pixels, 133x133 $µm^2$ of the sample were in the FOV. sCMOS cameras were chosen over emCCD cameras for having a faster acquisition speed with far higher pixel counts at the expense of slightly lower photon sensitivity and pixel non-uniformities (160). Higher frame rates are crucial in dSTORM for optimal image reconstruction, with the higher pixel count

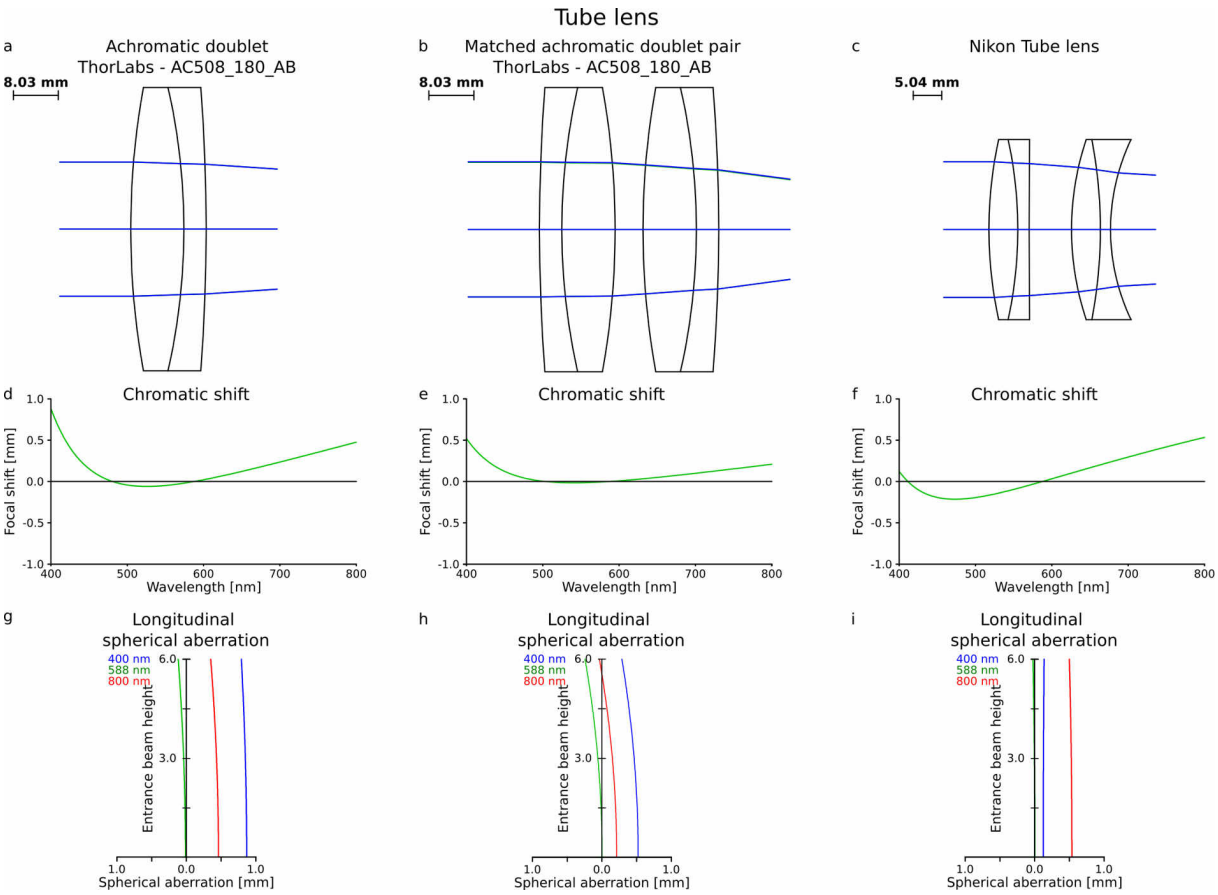

Fig. 3.9: Chromatic and Spherical characteristics for 3 tube lenses. a-c) Several lens designs exist to focus a collimated beam with varying performance with respect to chromatic and spherical aberrations. Lens configurations are a) achromatic doublet lenses, b) matched achromatic doublet pairs, and c) Thorlabs tube lenses for Nikon objectives. a) Achromatic doublet lens consisting of two optical elements. b) Achromatic doublet pairs consist of two matched achromatic doublet pairs in Plössl configuration. c) Tube lenses consist of two achromatic doublet lenses with the second correcting the spherical aberration introduced by the first doublet. d-f) Each tube lens design has a low chromatic shift with (b - matched achromatic doublet pairs) having the lowest chromatic shift. g-i) The lens configurations have a low longitudinal spherical shift with (c - Nikon tube lens) having the best performance between 400 - 800 nm.

allowing for larger FOV acquisitions. The Prime95B sCMOS camera was chosen for good gain characteristics at 1 ADU per photon, low read noise (RMS$\leq$1.8 e^-) and good quantum yield ($\geq$80% at the relevant spectral range) in combination with moderate pixel inhomogeneities (Sec. 3.2.2.2).

Traditionally, most systems, especially split-view and two-camera systems, utilise a 4f relay lens system to allow for the splitting and filtering of fluorescence within the detection path (155). Here, optical elements (e.g.: notch, band-pass, or beam-splitter) are placed between f_3 and f_4 close to the back-focal plane to mitigate artefacts in the image. We

decided against this configuration, by installing an air-spaced matched achromatic doublet pair (MAP) (Plössl configuration) (2x AC508-180-A-ML, Thorlabs Ltd) to reduce the length of the detection pathway (Fig. 3.11 f). At the time of construction, it was believed that this configuration leads to significantly improved chromatic characteristics[3]. Optical ray-tracing simulations later showed virtually identical chromatic and spherical performance compared to a 4f configuration (Fig. 3.10).

Using a MAP design generated major constraints on the setup of the detection pathway as filters are ideally placed near the BFP to reduce specular patterns from imperfrections on the optics at the image plane. In this configuration, the BFP is between the MAP

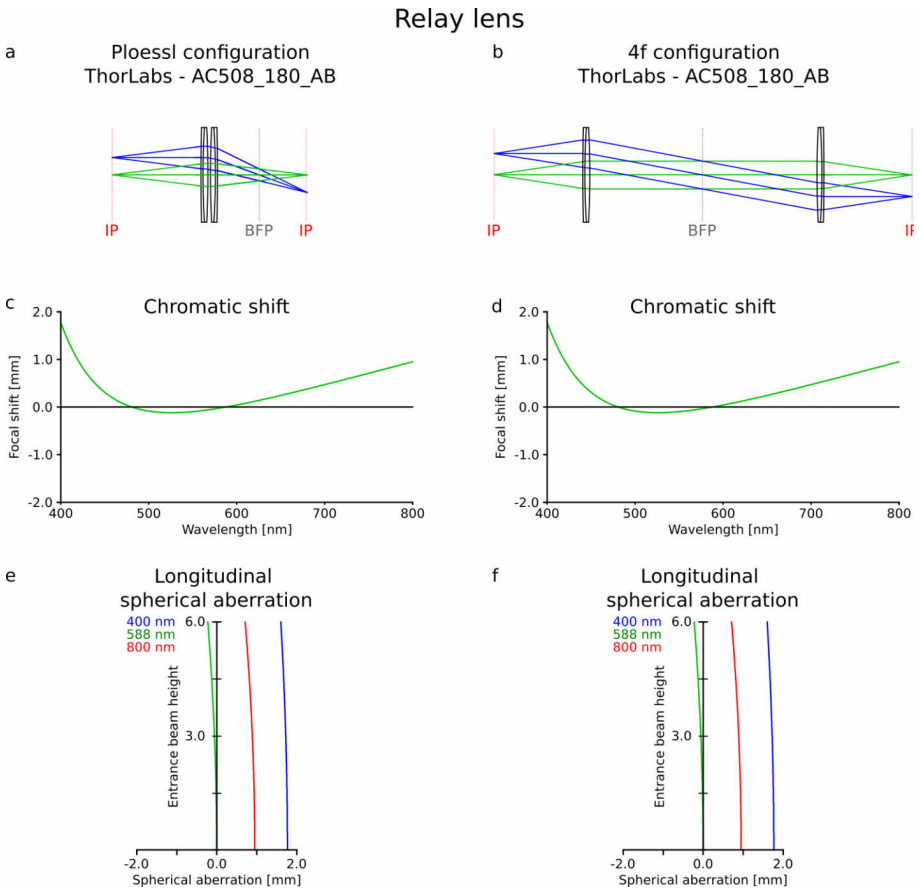

Fig. 3.10: Chromatic and Spherical aberration for 4f and Plössl relay lens setup. Chromatic (c, d) and spherical aberration (e,f) for a matched achromatic doublet pairs in a) Plössl configuration and b) 4f configuration. a) The image is relayed at 2f distance with the BFP in between the second lens and the relayed image plane (IP). b) The image is relayed at 4f distance with the BFP between the first and second lens.

[3] `https://www.thorlabs.com/newgrouppage9.cfm?objectgroup_id=1716`, as of 10/11/2023

and the camera sensor at f/2 (Fig. SI 8). Longer focal lengths allowed for more spacing to place the optical components while resulting in an increased beam width of the fluorescent signal. At f=180 mm, all necessary components could be integrated while still allowing for standard 2” lenses.

Most optical components were placed close to the BFP on motorised sliders (ELL6/9, Thorlabs Ltd) for automated switching between optical components (Fig. 3.11 c,d). Here, two sliders consisting of band-pass filters were placed, to filter the fluorescent signal from unwanted spectral ranges as well as special optics allowing for 3D dSTORM imaging or BFP inspection. Notch filters to remove reflections of the excitation light were placed as close to the tube lens as possible to reduce the possibility of stray reflections (Fig. 3.11 g). As notch filters, an existing quad-notch (405/488/532/635 notch, Semrock) and a 561 nm notch (Semrock) were chosen. Additionally, a magnetic kinematic cage base was installed into the beam path for quick manual but reproducible switching of beam splitters (Fig. 3.11 e). Finally, for the reflective camera (Fig. 3.11 a), a magnetic quick-mount for optics was installed to allow for manual but reproducible insertion of optical components such as filters. This was necessary as commonly used optical components were highly dependent on the specific experimental conditions.

Using the optical design files, the full detection pathway was simulated (Fig. SI 8 a,b, SI 9) (158, 159) and the transmission efficiency of spherically emitting point-sources 10 nm from the coverslip surface was determined across the FOV for water, an eukaryotes plasma membrane and the cytoplasm of a cell (Fig. 3.12) (161, 162, 163).

Subsequently, this transmission efficiency is in line with literature (159) and was used in Sec. 3.2.2.1 to determine the irradiance at the sample plane corrected for the theoretical

spatial losses in the detection pathway (Fig. SI 6). Overall, the refractive index of the medium was the major contributing factor. For all simulated distances of emitters from the coverslip in the cytoplasm up to 1 µm, simulations showed no significant difference in the transmission efficiency profiles.

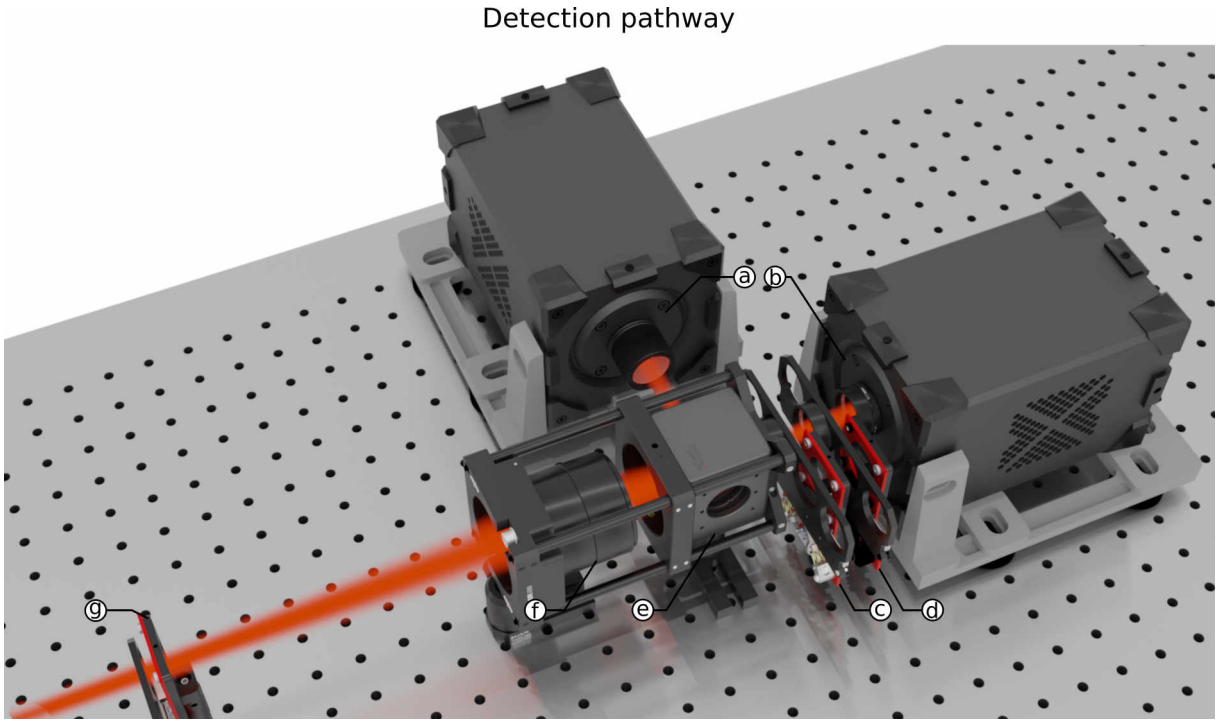

Fig. 3.11: Detection pathway. 3D render of the detection pathway with dual sCMOS camera and Plössl relay lens. a, b) Two Prime 95B sCMOS cameras for ratiometric imaging. c, d, g) Filter sliders for c) special optics, d) band-pass filters and g) notch filters. e) Variable image splitting filters (band-, long-, short-pass and polarisation filters. f) Relay lens in Plössl configuration.

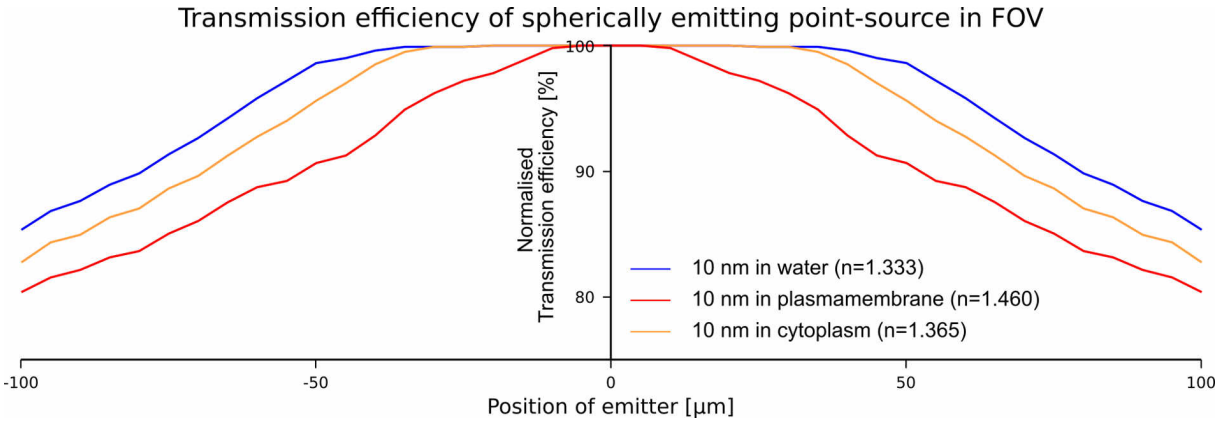

Fig. 3.12: Theoretical relative transmission efficiency across the FOV of the full detection pathway. Optical simulation of full detection pathway yielded the relative transmission efficiency for spherically emitting point-sources at various lateral displacements from the centre. Efficiencies were determined for emitters in water, in the cytoplasm and the plasma membrane. Higher refractive indices have a smaller plateau region, consistent with Kurvits *et al.* (159).

3.2.1.5 µManager integration and automation

To control all hardware and handle the data acquisition, µManager was chosen as a microscope control software for being open-source, highly modular with a large library of device adaptors (117). Alternatives to µManager are either closed-source, proprietary or lack support for a variety of hardware devices (164). Within this thesis, a more powerful and modernised version has been released (µManager 2.0). Switching to the newer version demanded the rewriting of all established acquisition scripts of µManager[4].

For most hardware, existing device adaptors made integration easy (dual camera, 405 nm laser, 561 nm laser, XYZ stage, sliders) but other components were missing (647 nm laser, Epi-TIRF rail, transistor-transistor-logic (TTL) controller, brightfield illumination, laser safety controller). Here, custom-written code, usage of serial command interface modules or self-built interpretation hardware was needed. The 647 nm laser engine was communicating through serial commands with the proprietary software with minimal documentation available. By monitoring the commands sent and received at the respective COM-port, essential commands were extracted and implemented in µManager using a serial command interface module[5]. To control the brightfield illumination within µManager, an adjustable circuit was built using the Arduino interface to power the brightfield LED. All other hardware components (safety shutter, interlock, and Epi-TIRF rail) were controlled by an Arduino executing commands based on the use of a 64-state device adaptor from µManager (Fig. 3.14).

[4] `https://micro-manager.org/Version_2.0_API_Transition_Guide`, as of 10/11/2023
[5] `https://github.com/fjovine/SerialSniffer`, as of 10/11/2023

A second control circuit was implemented to control the AOTF drivers and diode lasers. A limitation of the Prime95B camera is the TTL output trigger. Besides a rudimentary ”SMART controller”, the camera is only able to output one TTL signal to control all laser lines. To redistribute this signal to the corresponding lasers, or AOTF, a microcontroller was programmed using direct port manipulation and interrupts to relay the signal within 7 µs rising time and 16 µs falling time (Fig. 3.13). Direct port manipulation was necessary, as the TTL low time between two frames was measured to be only 41 µs (Fig. 3.13), equal to the time to digitise 4 rows of the camera in 12-bit mode (2 rows in 16-bit mode). To implement the necessary logic, 41 µs was found to be too short using regular read and write instructions. Using direct port manipulation, the 8-bit input-output (I/O) port register of an Arduino can be read and modified in 2 clock cycles (0.12 µs), reducing the time from invoking the interrupt to changing the output pin state to 5-7 µs. Initially, if-else statements were avoided as branching is known to cause significant computational overhead. A first implementation using direct port manipulation in combination with output states was utilised. Later, if-else statements were implemented for better readability, while still relaying the signal in $\ll$40 µs. As the AOTFs required a 10 V signal, an additional opto-isolator circuit was built and integrated at the specific outputs to boost the voltage at the cost of an additional delay (Fig. 3.13). For the rising TTL signal, the delay was negligible, the falling TTL signal was delayed by an additional 9 µs. Still, at 7 - 16 µs total response time, the circuit was fast enough to not miss any trigger signals. This micro-controller was controlled by a second Arduino interface board integrated into µManager to change the relaying of the input TTL signal and address all laser lines individually (Fig. 3.13).

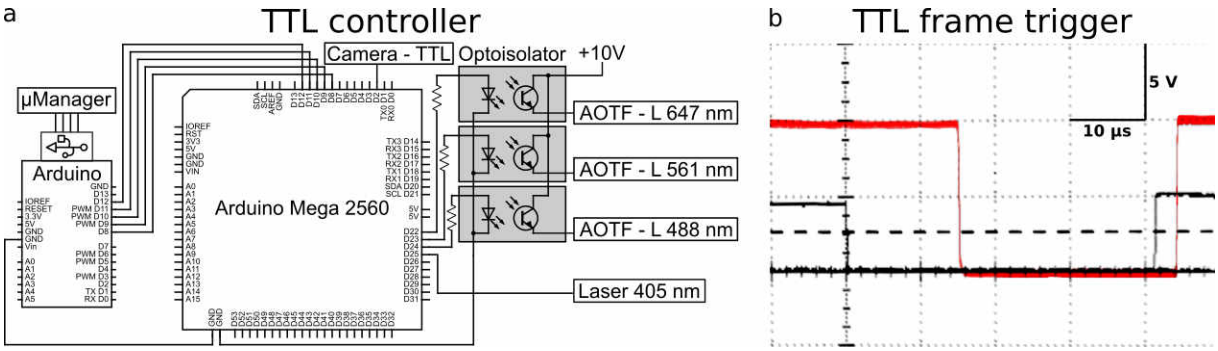

Fig. 3.13: Laser TTL controller. a) Laser illumination controlled by an Arduino Mega 2560 in combination with a Arduino Uno. The Arduino Uno microcontroller is connected to µManager using a 64-state device adaptor. Device states are forwarded to the Arduino Mega, corresponding to a specific laser excitation pattern. The TTL trigger output by the camera is used to synchronise the sample illumination with the image acquisition. An opto-isolator circuit is used to convert the 5 V output signal into a 10 V signal compatible with the AOTF driver. b) Relay time from receiving the TTL input signal to generating a 10 V output signal was measured to be 5-7 µs rise time and 16 µs fall time.

Finally, to comply with laser safety regulations, controllers were installed throughout the system confirming a fully sealed enclosure using magnetic non-contact safety switches. Laser safety features were wired in series, interrupting the 5 V line when being triggered. A drop in the 5 V signal led to the activation of the laser interlock, and a physical shutter was moved into the beamline to block any laser light from causing harm to the user (Fig. 3.14). Additionally, when accessing the microscope body to change samples, the shutter was also moved into the beamline to temporarily block the lasers. This shutter was implemented in a way that constant power was needed to remove it from the beamline, any loss in power led to the complete blockage of the beam.

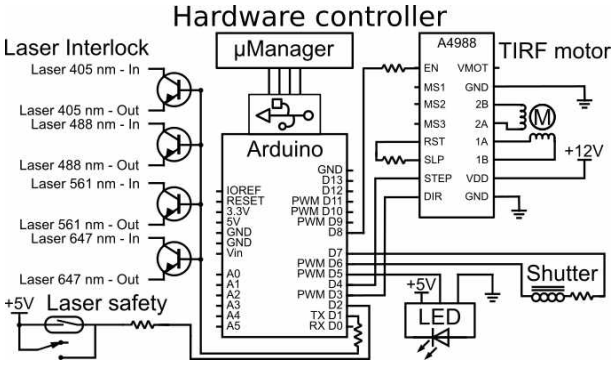

Fig. 3.14: Schematic of hardware controller. An Arduino Uno controls all hardware including the Epi-TIRF-rail, the laser safety circuit including laser interlock, laser shutter and magnetic non-contact safety switches. Additional logic controls the high-power light-emitting diode (LED) used for Köhler illumination in brightfield microscopy. The Arduino microcontroller is connected to µManager using a 64-state device adaptor.

3.2.2 Setup Characterisation

After completion of the setup, the characteristics of the microscope needed to be validated to confirm optimal performance. Here, the capability of the system to dampen vibrations and the overall spatial stability was determined. Additionally, the illumination profile of the sample was characterised. Finally, the PSF (2D and astigmatic) across the FOV were determined, as well as the focus-dependent PSF shift in the lateral plane.

3.2.2.1 Flatness characterisation

Another crucial characteristic is the illumination homogeneity at the sample plane and within the FOV. As described in Sec. 3.2.1.2, a piShaper was used to transform all TEM_{00} beam profiles into flat-top profiles. At various distances in front of and behind the piShaper, the beam profiles were characterised (See Method Sec. 2.2.6). All input beams had a collimated beam width between 5.9-6.0 mm ($1/e^2$) (Fig. 3.15 a). Immediately after the piShaper, the beam profile for 647 nm had a flatness factor of 0.90 (0 - 1, where 1 represents the ideal profile), a plateau uniformity of 0.86 (0 - 1, where 1 represents the ideal profile), and an edge steepness of 0.88 (0 - 1, where 1 represents infinite steepness) (Fig. 3.15 b, Tab. 3.1) (124). After a 40 cm path length, the beam characteristics reduced in quality as the flat-top profile started to deterioration into an Airy pattern (124) (flatness factor of 0.76, plateau uniformity of 0.83 and edge steepness of 0.78) (Fig. 3.15 c, Tab. 3.1). In the sample plane, the edge steepness was further reduced to 0.6, but plateau uniformity and flatness factor improved due to an averaging of axial Airy patterns in the sample plane and refractive blurring introduced by the optical elements between piShaper and sample plane.

Using the intensity at the BFP of the objective combined with the determined area of illumination, an irradiance of 3.4 kW/cm^2 was determined. To obtain the corrected intensity profile at the sample plane, the raw images recorded by the camera were corrected using the theoretically determined transmission efficiency across the FOV (Fig. 3.12, SI 6, n=1.47). Averaging 4000 frames of densely labelled surfaces with TetraSpeck beads recorded in highly inclined and laminated optical sheet (HILO), confirmed the generally good and uniform illumination in the sample plane, though a radial Airy pattern was notable (Fig. SI 6). Here, a flatness factor of 0.86 and plateau uniformity of 0.81 was determined, though due to the nature of inhomogeneity stemming from the unequal distribution and intensity of beads, this can only be seen as a lower bound for the beam quality at the optical sample plane.

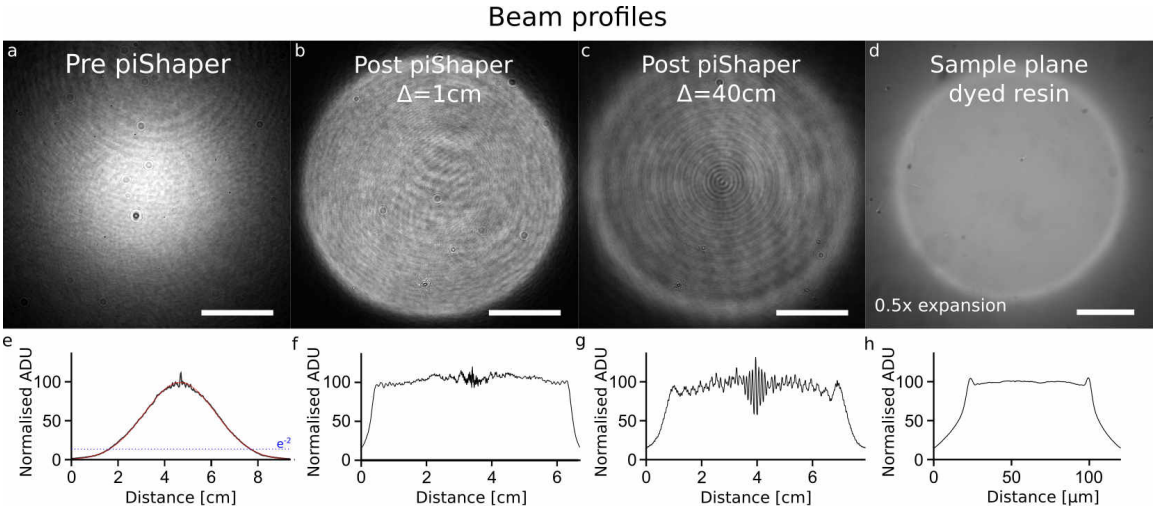

Fig. 3.15: Beam profiles measured at 4 positions in the excitation pathway. a-d) Beam profiles before the flat-fielding device and at 3 positions along the optical path after the piShaper (1 cm, 40 cm and *in sample*). a, e) Pre piShaper beam profile fitted to a Gaussian distribution for width determination. Post piShaper (b, f: 1 cm; c, g: 40 cm) beam profiles with flat-top illumination. Airy pattern deterioration increasing over the optical path-length (1 cm vs 40 cm). d, h) In sample fluorescence of a dyed acrylic resin using Epi illumination at 0.5× beam expansion to acquire the full beam width. d) Intensity corrected for theoretical transmission efficiency across the FOV using Fig. 3.12. Scale bar: a-c) 1.5cm, d) 20 µm.

Tab. 3.1: Summary of flatness performance. Flatness factor, plateau uniformity and edge steepness for 3 positions (1 cm, 40 cm and in sample) along the optical path after the flat-fielding device.

	post piShaper $\Delta = 1$ cm	post piShaper $\Delta = 40$ cm	sample plane dyed acrylic resin
flatness factor	0.90	0.81	0.95
plateau uniformity	0.87	0.83	0.90
edge steepness	0.88	0.78	0.60

3.2.2.2 Camera correction

State-of-the-art super-resolution microscopes often utilise sCMOS cameras due to their high frame rate compared to emCCD cameras. Yet, pixel-to-pixel inhomogeneities can introduce several nanometres of systematic localisation error. Correcting these variations is crucial for minimising artefacts and enabling advanced quantitative microscopy techniques such as photobleaching step analysis (PBSA) (3). Unlike emCCD cameras, where offset, dark current, read noise, thermal noise, and gain can be determined on a camera-wide basis from $\leq$5 images per condition for homogeneously illuminated sensor, sCMOS correction requires pixelwise calibration with $\gg$1000 frames at multiple brightness levels and exposure times to achieve sufficient statistical robustness (149). Using Monte Carlo simulations, it was calculated that the number of frames needed for 10 logarithmically spaced brightness levels, at which the 5σ uncertainty per pixel (1 in 3.5 million) was $\leq$10% of the expected gain, is 4000 frames. To compensate for any subsequent filtering of frames, 8000 frames were acquired for each image set.

At the time of calibration, no packages for generating these pixelwise maps were available. In 2022, Diekmann *et al.* published software to characterise sCMOS cameras using photon-free calibration (149). However, the measured gain correction is crude and requires additional correction maps from flat-field imaging. Using this software, the image-wide gain is robust while the pixelwise value is not precise (149). Similarly, Etheridge *et al.* published a pixelwise sCMOS calibration for offset, read noise and gain in 2022 (165).

To calculate the offset and dark current, 8000 frames at 2 exposure times (12.5 ms, 1012.5 ms) with a closed shutter were acquired, using the relation:

$$\text{intensity} = \text{offset} + \text{dark current} \times t \tag{3.1}$$

Here, the pixelwise average intensity is generated from each image set. The dark current per pixel [ADU/s] was determined by subtracting the average on the long exposure time from the average of the short exposure time (Fig. 3.16 a-c). The resulting dark current map was then used to correct for the dark current in the measured pixelwise intensity maps. This generated the offset map of the camera (Fig. 3.16 d-f). The dark current for 94% of pixels was $\leq \pm 1$ ADU/s (99.3% within ± 3 ADU/s), though some hot pixels exist, where the dark current exceeds 100 ADU/s (Fig. 3.16 e,f).

Conversely, the offset is less prone to single hot pixels. In the offset map, a line-based alternation of intensities is detected, leading to a bimodal distribution in the offset map with a mode of 100.7 ADU in odd-numbered lines and a mode of 99.7 ADU in even-numbered lines (Fig. 3.16 b,c). The global average totals 100.1 ADU (Fig. 3.16 b,c).

Using the same set of 8000 frames at 2 exposure times, the pixelwise maps for read noise and thermal noise can be generated. Using the relation:

$$\text{variance} = (\text{read noise})^2 + (\text{thermal noise})^2 \times t \tag{3.2}$$

For each image set, the variance per pixel is calculated. The ADU-based thermal noise per pixel [ADU/s$^{0.5}$] is the square root of the difference in variance between long and short exposure times (Fig. 3.17 d-f). The resulting thermal noise map was then used to correct for the thermal noise in the measured pixelwise variance maps. This generated the ADU-based read noise map [ADU] of the camera (Fig. 3.17 a-c). Both maps are

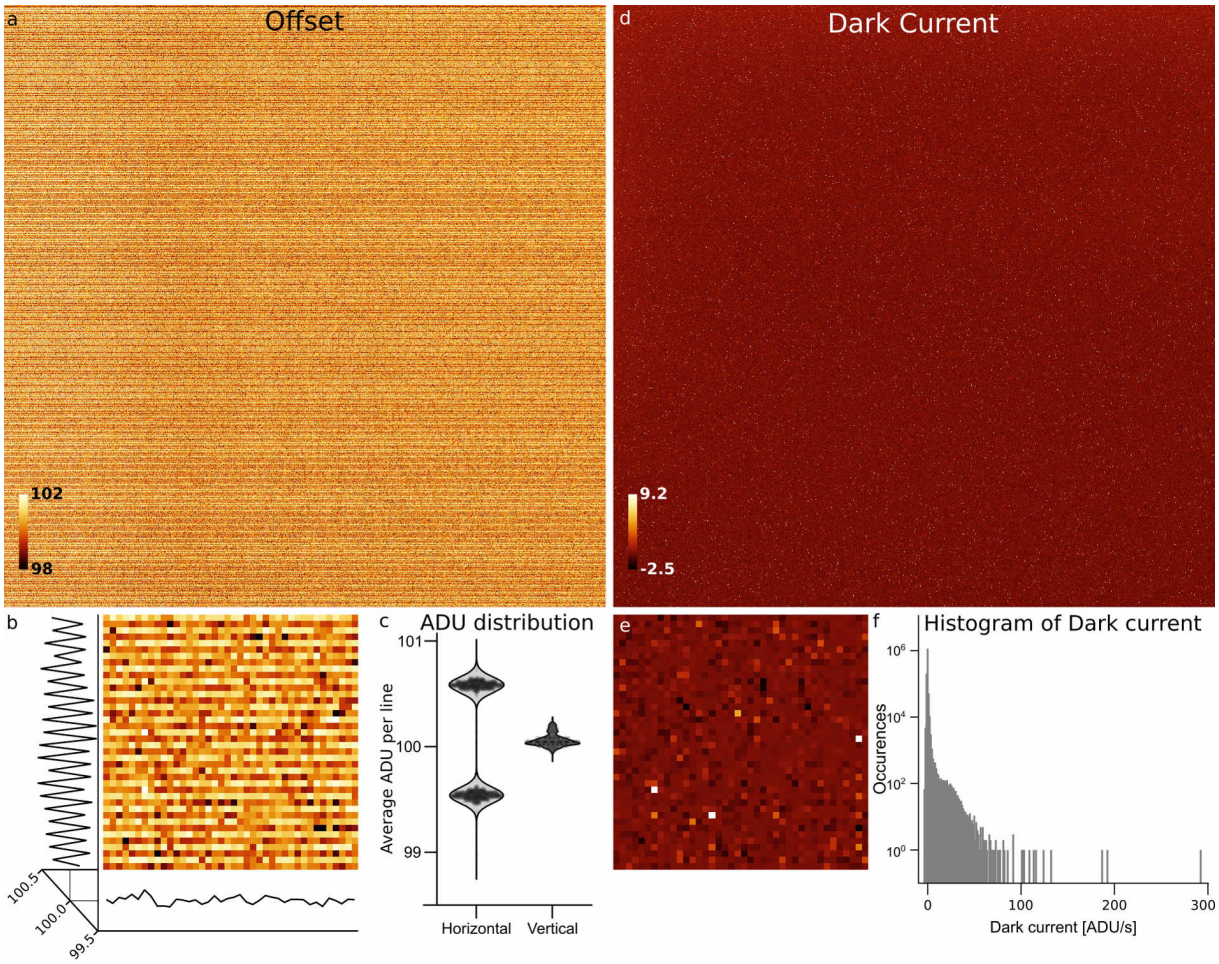

Fig. 3.16: Pixelwise correction map of offset and dark current. Pixelwise calibration for a) offset and d) dark current. b, c) The offset map represents the systematic offset added to each pixel, with alternating intensity lines leading to a bimodal distribution. e, f) The dark current map shows the temporal increase in pixel values [ADU/s]. 94% of pixels have an increase $\leq \pm 1$ ADU/s, despite the presence of noisy 'hot pixels' at up to 293 ADU/s.

multiplied with the gain map (Fig. 3.18) to generate the final read noise [e^-] and thermal noise map [$e^-/s^{0.5}$]. A median read noise of 2.3 e^- with RMS of 2.5 e^- was found.

In the read noise map, column-based variability of noise is detected (Fig. 3.17 b,c). The thermal noise map, on the other hand, had a higher noise level on the left and top of the sensor with an exponential decay from top to bottom and left to right (Fig. 3.17 d,f). The mean of the thermal noise map was determined to be 0.47 $e^-/s^{0.5}$. Both maps had high uniformity with all outliers below 14 $e^-/s^{0.5}$ (16 pixels $\geq$ 7 $e^-/s^{0.5}$ and 13 e^- respectively (959 pixels $\geq$ 7 e^-).

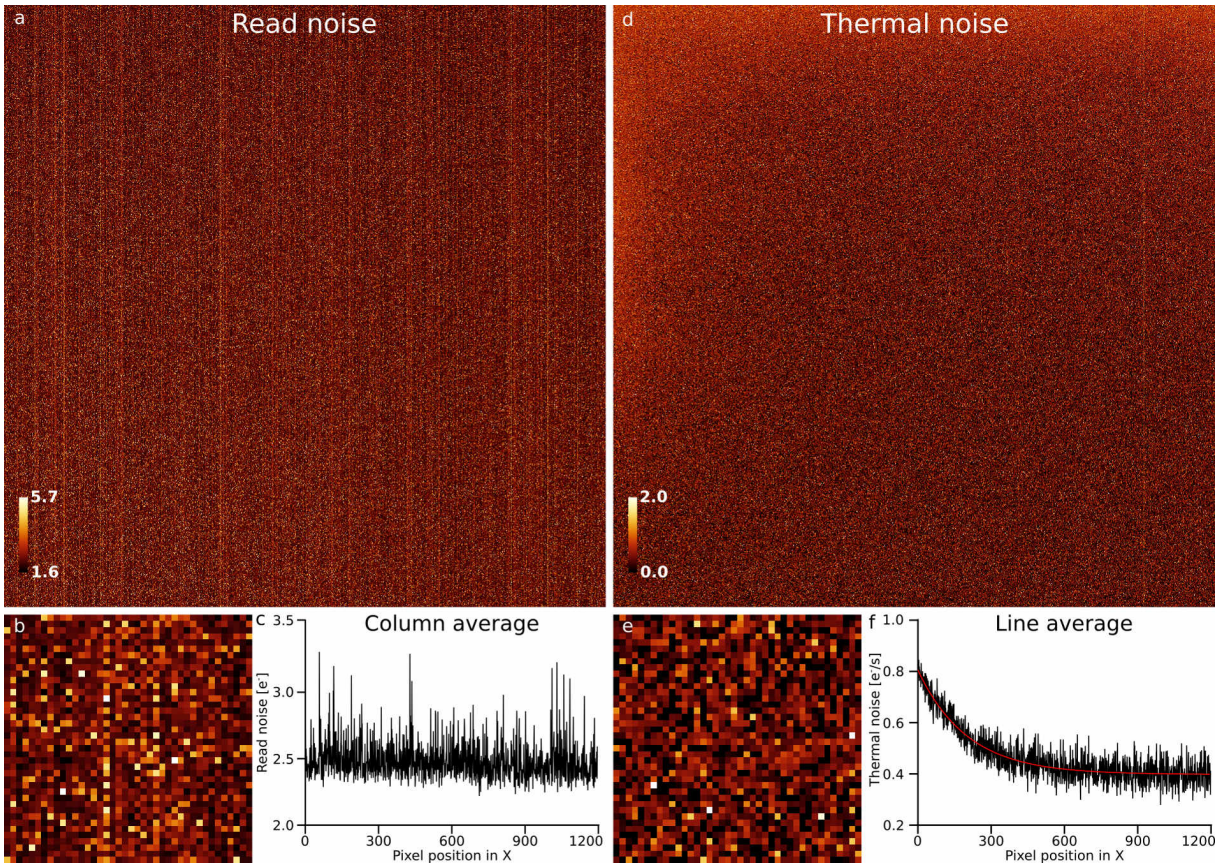

Fig. 3.17: Pixelwise correction map of read noise and thermal noise. Pixelwise correction for a) read noise and d) thermal noise. b, c) A column based variability is observed in read noise with a median read noise of 2.3 e^-. e, f) Thermal noise is highest in the top-left corner, showing an exponential decay towards bottom-right. A mean thermal noise level of 0.47 $e^-/s^{0.5}$ is detected.

Here, having a temporally highly stable light source is crucial, as all temporal irradiance instabilities lead to an increased apparent noise, thus inflating the measured gain. As a control experiment, the image-wide gain was determined from 50 images and later compared to the average of the pixelwise determination. After testing multiple light sources including the implemented laser lines, and various non-coherent light sources (halogen lamps, liquid crystal display (LCD) screens, and LED arrays), a 0805 surface-mounted device (SMD)-LED with a 1 kΩ resistor (approximately 3 mA) connected to a 3 V power line was found to have brightness instabilities of $\ll$0.1%.

Using each set of 8000 frames, the variance and mean for each pixel are calculated (corrected for offset and dark current) in bins of 50 frames. This binning was crucial for

minimising the effect of temporal brightness instabilities and shot noise artefacts. Each bin of 50 frames was analysed independently for the global and pixelwise mean intensity, as well as the highest pixel-value in each bin. All parameters for each bin were stored and subsequently compared. All bins with a global mean intensity deviating $\pm$0.06% from the global median were discarded. Similarly, only pixels with a mean binned intensity between 0.6$\times$ and 1.67$\times$ the global median pixel intensity were used. Lastly, all bins were discarded if a single pixel had 65535 ADU (16-bit mode) or 4095 ADU (12-bit mode), as this indicated a saturated pixel. All bins satisfying the conditions were used in the gain analysis.

Here a photon transfer curve (PTC) was generated by plotting the variance over mean. The gain of a pixel corresponds to the slope of the PTC (Fig. 3.4) (165). At low light levels $\leq$10 e^-, the noise is dominated by read noise and thermal noise, then a region dominated by shot noise is observed, followed by a region of fixed pattern noise (166). In this PTC, the slope below $\leq$50 e^- was found to be non-linear and was thus omitted from fitting. On all remaining data points (fixed pattern noise region), a linear fit was performed using the Simplex method on a per-pixel basis (125). A gain map was generated for each of the 4 gain settings available in the camera (12-bit modes - ”Balanced”: 1.07±0.02 e^-/ADU, ”Sensitivity”: 0.53±0.02 e^-/ADU, ”FullWell”: 2.09±0.02 e^-/ADU, 16-bit mode ”HDR”: 0.97±0.11 e^-/ADU) (Fig. 3.18). For all 12-bit modes, the coefficient of determination (R^2) was $\geq$0.991 for all measured pixels and the average R^2 was larger than $\geq$0.9992.

In the 16-bit high dynamic range (HDR) mode, the coefficient of determination was $\geq$0.668 for all measured pixels and an average R^2 of 0.970. When investigating this lower R^2, it was found that the gain in HDR mode is a ”dual gain mode” with a gain of

1/1.137=0.87 e^-/ADU between 0-2048 ADU (low intensity gain) and 1.02 e^-/ADU from 2048-65535 (high intensity gain) (Fig. 3.18 bottom right panel) (confirmed by Teledyne). This composite of two gains results in the overall worse fit when performing a global linear fit. As most quantitative microscopy techniques require a linear relation of ADU to photoelectrons, a lookup table was generated to re-linearise the acquired image data. This was necessary as, for example, the software quick-PBSA estimates the step-size on the last photobleaching event (low intensity gain) and subsequently runs the step detection on the whole bleaching trace (low and high intensity gains) (3). As this re-linearisation can lead to falsified ADU values around the switching region of gains, the HDR mode was omitted from all SMLM acquisitions.

Having calibrated the camera for the offset, dark current, read noise, thermal noise, and gain, the camera's performance in SMLM can be simulated (Fig. 3.19). With this, the effect and magnitude of pixel inhomogeneities on single-molecule fitting can be estimated. Based on the PTC described by Mandracchia et al., which, in turn, is based on the work by Foi *et al.* (126, 127). 176.400 frames of single emission events were generated in a 50x50 pixel region to determine the localisation error (Fig. 3.19).

$$I = \gamma_p \text{Pois}\{S_p\} + N(0, \sigma_n) + B \tag{3.3}$$

where I is the intensity of a pixel, γ_p the multiplicative conversion factor, S_p the quantised photon signal, $N(0, \sigma_n)$ the distribution of read noise, and B the baseline. Given a sufficiently high photon count S_p, the Poisson distribution can be approximated by a Gaussian distribution with $N\left(S_p, \sqrt{S_p}\right)$ (central limit theorem), resulting in:

$$I \approx \frac{1}{G} \cdot N\left(S_p, \sqrt{S_p}\right) + N(0, \sigma_n) + B \tag{3.4}$$

with $\gamma_p = \frac{1}{G}$ and G being the experimentally calibrated gain of the camera.

The baseline is generated based on the offset and dark current map for a 100 ms exposure time. Similarly, the noise was generated for a 100 ms exposure time using the read noise and thermal noise map. The amount of photoelectrons was calculated for an ideal diffraction-limited PSF of 5000 photoelectrons based on the system-specific performance characteristics of the detection pathway (Sec. 3.2.1.4). This simplified model does not consider the quantum yield of the camera or unspecific background increasing the mean ADU-level. Fitting the XY position in the 176.400 frames of single emission events for the central 42x42 pixels, the average displacement error in X, Y, and total displacement were determined (Fig. 3.19).

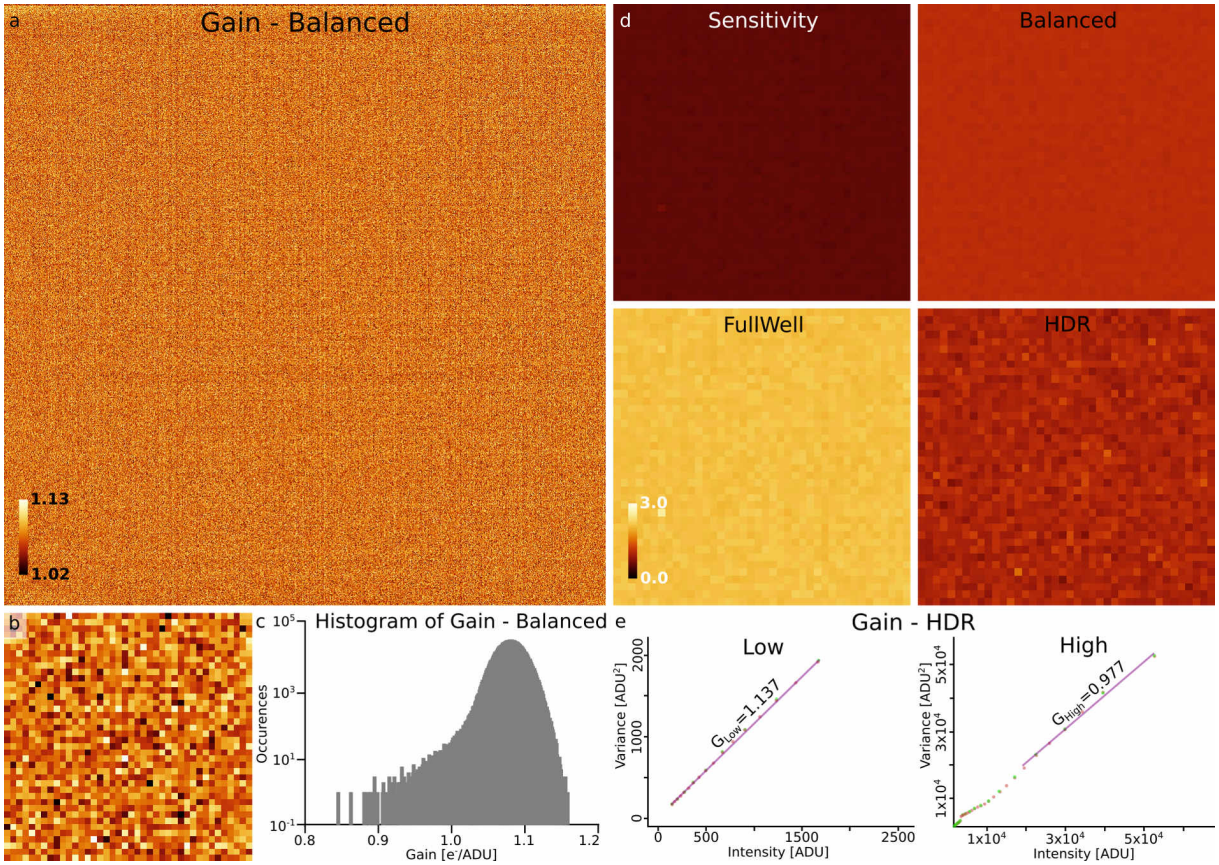

Fig. 3.18: Pixelwise correction map of the camera gain. a) Full frame correction for ”Balanced” gain. b, c) Gain distribution of the ”Balanced” gain reveals a left-skewed distribution of pixels being more sensitive in photon-electron to ADU conversion. d) Smaller region of the gain correction maps for the four gain settings of the sCMOS camera: d) ”Sensitivity” (top left), ”Balanced” (top right), ”FullWell” (bottom left), and ”HDR” (bottom right). Each map is a visual representation of the camera’s pixelwise photon response. Sensitivity, Balanced, and FullWell have a mostly uniform photon response across the sensor. e) 16-bit HDR mode show variations in pixel response for low and high photon intensities, resulting in a higher variability in global gain calibration.

At approximately 5000 collected photons per emission event, the dominant factor contributing to a localisation error was found to be pixels of higher and lower gain. Therefore, in this simulation, a region around a low gain (0.86 e^-/ADU) was chosen. An adjacent pixel to the low gain pixel additionally had a high baseline (dark current of approximately 293 ADU/s), inflating the baseline by approximately 30 e^-. This combination of pixel inhomogeneities provides a good estimation for the upper limit on localisation error introduced by pixel non-homogeneities. It was found that the maximum localisation error for a pixel was less than 7 nm (Fig. 3.19). Nearly all pixel inhomogeneities introduced a localisation error of less than 1 nm (Fig. 3.19). Still, these camera correction maps were used in all subsequent dSTORM analyses (128).

3.2.2.3 3D characterisation

As this system is capable of using cylindrical lenses for astigmatic 3D dSTORM, its performance was calibrated on a per-experiment basis using TetraSpeck beads. Exemplary, the system's performance is shown in Fig. 3.20. Compared to 2D dSTORM, where optimal performance is at the focal plane for both axes, the cylindrical lens introduces a shifted focus between the X and Y axes, thus having different optimal performance for each axis. However, this configuration can resolve the ambiguity of being above or below the focal plane. For instance, in this implementation, when the focal plane is 500 nm below the symmetrical PSF position, the PSF is mostly elongated along the Y-axis (Fig. 3.20). Conversely, if the focal plane is 500 nm above the symmetrical PSF position, the PSF is mostly elongated along the X-axis (Fig. 3.20). Using the spline fit of the astigmatic PSF, the theoretical localisation precision (square-root of Cramer-Rao

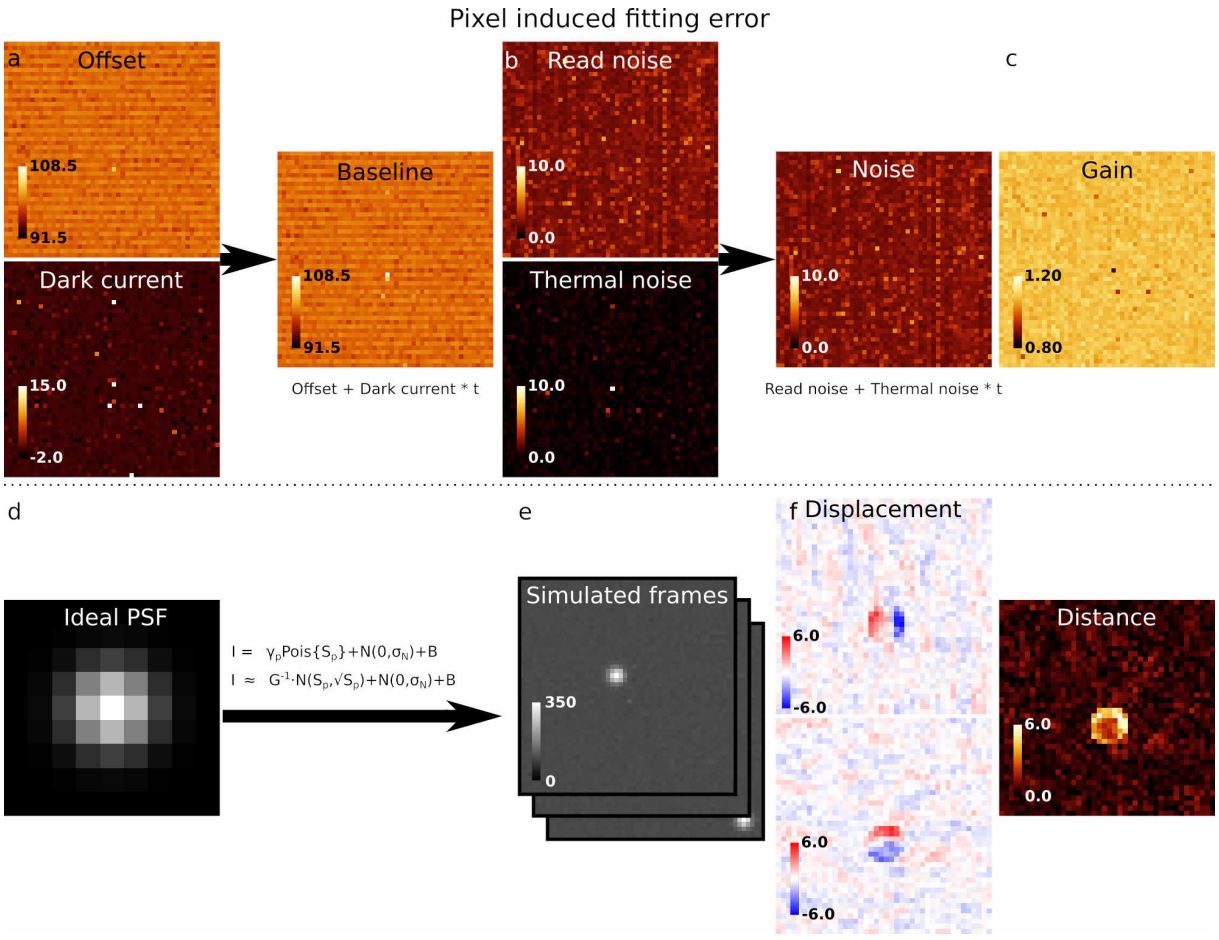

Fig. 3.19: Simulation of fitting errors from pixelwise inhomogeneities. a) Pixelwise maps of offset, dark current, are used to simulate a baseline for frames at 100 ms exposure time. b) Read noise and thermal noise maps are used to generate a total noise map at 100 ms exposure time. c) Gain for balanced mode acquisition is used at an average 1.08 e^-/ADU. d-e) Using an ideal PSF (d), 1.8×10^5 frames are simulated for a 50×50 pixel region, sampling each pixel $\sim$100-fold. Simulated frames represent the pixelwise ADU response for a single emitter with 5000 photons at 0 ADU background. Here, the sCMOS camera photon response model by Mandracchia *et al.* is used (126). Fitted localisation positions are compared to the theoretical localisation position. Displacement along X-axis (top) and Y-axis (bottom) highlight a region effected by a combination of high dark current pixel and low gain pixel (high photon response) leading to a total displacement error of $<$7 nm.

lower bound (CRLB)) was calculated for 5000 photons and 50 ADU background using super-resolution microscopy analysis platform (SMAP) (Fig. 3.20) (128).

In our implementation, at a Z position of 0 nm (symmetrical PSF), the system exhibits a 1.4-fold worse localisation precision compared to performance without the astigmatic lens in focus. At or near 0 nm in Z, the axial localisation precision was lowest at approximately 13 nm, with a lateral localisation precision of about 8 nm (5000 photons and 50 ADU background). Within $\pm$400 nm, the lateral localisation precision was found to be less than 18 nm, and the axial localisation precision approximately 27 nm.

As the system utilises a large FOV, field-dependent aberrations were present in both 2D and 3D dSTORM (Figs. 3.21, SI 7). In 3D dSTORM, the PSF was skewed, having an outward-facing lobe along the astigmatic axes that increased in magnitude with increasing distance from the centre (Fig. 3.20). Generally, to minimise the influence of these field-dependent PSF aberrations in 3D dSTORM, the region of interest (ROI) was located close to the centre, and the FOV was reduced to the ROI.

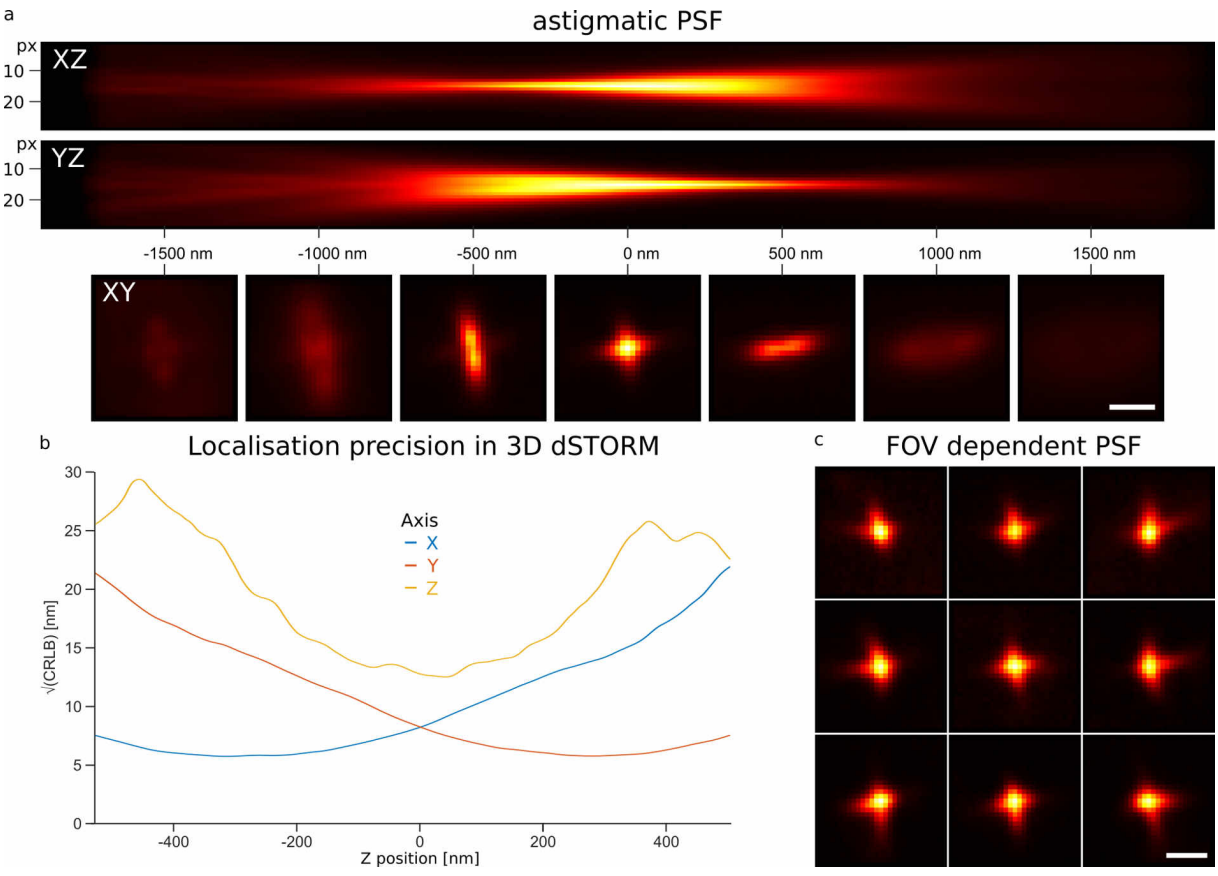

Fig. 3.20: Astigmatic PSF for ±2 µm from sample plane and Cramer-Rao lower bound estimation. a) XZ and YZ astigmatic PSF along the central axis between -2 µm and 2 µm of central region. b) Full FOV Cramer-Rao lower bound estimation for lateral and axial localisation precision at 5000 photons and 50 photons/px background. c) FOV dependent PSF shape determined on a 3×3 grid. Scale bar: a, c) 1 µm

Having calibrated the microscope, the system was used in various experiments (Chap. 4, Chap. 5). After extensive experimentation, a FOV and focus-dependent XY-shift was observed (Fig. 3.21 c). When defocusing from -400 nm to 400 nm, the XY-localisation showed a linearly constant displacement along a relative axis through the centre. The magnitude of this effect linearly increased with increasing radial distance from the centre. At the corners of the image (94 µm from the centre), the shift was determined to be approximately 125 nm for 800 nm of axial movement. For focal planes exceeding a defocusing of 400 nm, field-dependent aberrations started to dominate (Fig. 3.21 a).

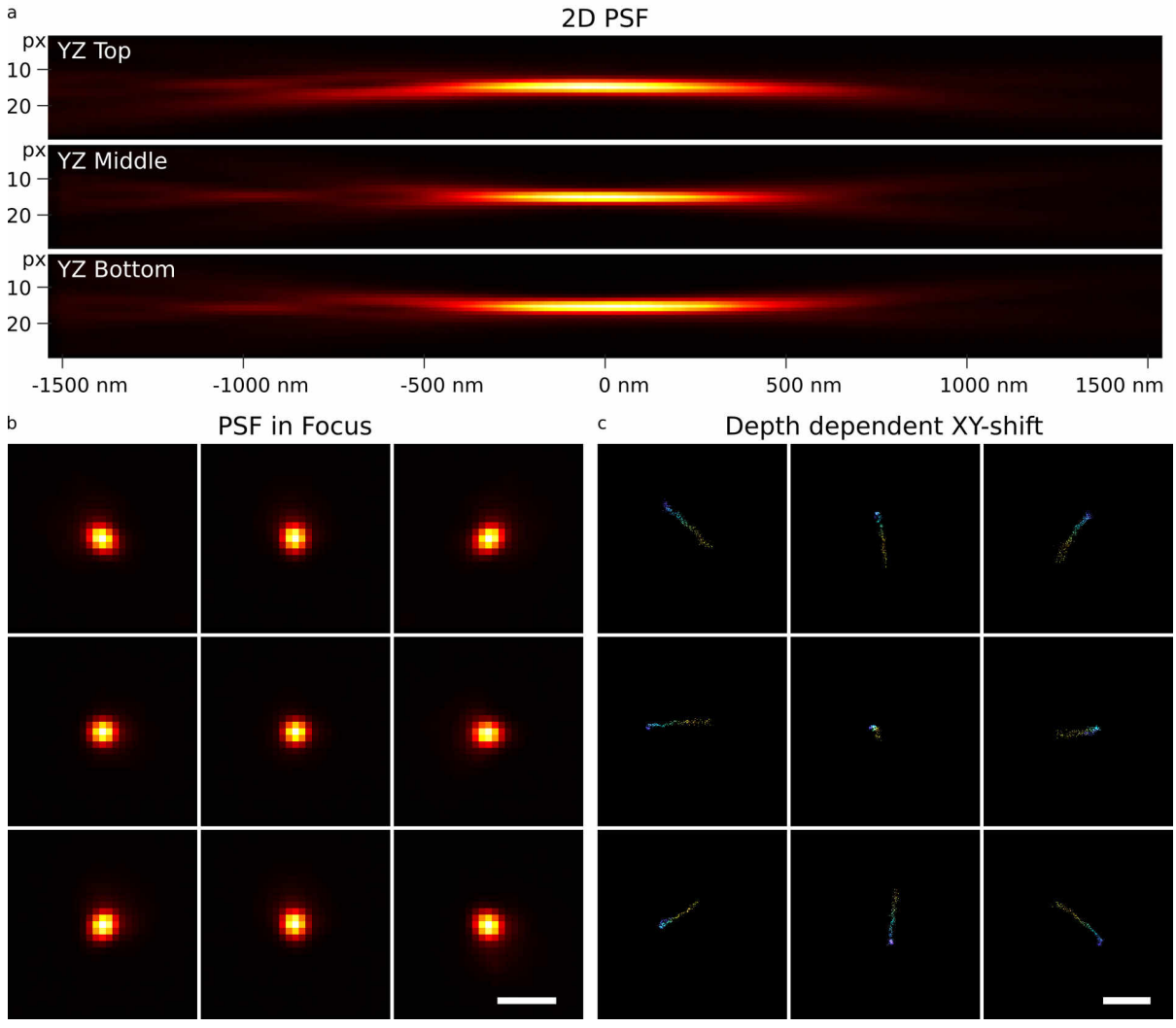

Fig. 3.21: Depth dependent PSF-drift. a) 2D dSTORM PSF (YZ) for ±1.6 µm from sample plane. YZ plot for top, middle and bottom region of FOV. b) FOV dependent PSF shape determined on a 3×3 grid. c) FOV-position dependent lateral shift of localisation centre for 800 nm of axial movement around sample plane. A depth-dependent shift increasing with distance to the centre is observed. Scale bar: b) 1 µm, c) 100 nm.

Simulations confirmed this observation (Fig. SI 9). The Plössl optic installed in the detection pathway (Sec. 3.2.1.4) results in a tilted imaging beam path (Fig. SI 9). While there is also a slightly tilted imaging beam path present for 670 nm using a 4f optical configuration, the effect is significantly smaller in magnitude (less than 15 nm in 4f configuration vs. 125 nm in Plössl configuration - from ray tracing simulations in TracePro, Lambda Research Corp.) (Fig. SI 9).

3.2.2.4 Stability measurements

Using TetraSpeck fluorescent microspheres of 100 nm diameter, the total displacement error of the system was calculated. Here, the microspheres were imaged at 144 frames per second (FPS), and the localisation was fitted in SMAP (128). Next, the standard deviation of the XY displacement was compared to the per-frame localisation precision (Fig. 3.22 a,b). Assuming non-correlated errors of fitting and XY displacement, the contribution of all other sources on localisation error can be estimated using the propagation of uncertainty with σ_{fit} being the uncertainty in fitting and σ_{other} the uncertainty in other sources, with f being the function of XY displacement and their respective partial derivatives $\frac{\partial f}{\partial i}$:

$$\sigma_f = \sqrt{\left(\frac{\partial f}{\partial \mathrm{fit}}\right)^2 * \sigma_{\mathrm{fit}}^2 + \left(\frac{\partial f}{\partial \mathrm{vib}}\right)^2 * \sigma_{\mathrm{vib}}^2 + \left(\frac{\partial f}{\partial \mathrm{drift}}\right)^2 * \sigma_{\mathrm{drift}}^2 + \dots} \tag{3.5}$$

Assuming non-correlated uncertainties and linear combination of errors, result in:

$$\sigma_{\mathrm{other}} \approx \sqrt{\sigma_{\mathrm{fit}}^2 - \sigma_f^2} \tag{3.6}$$

Using this formula, the error contribution of all other sources for the undamped table was estimated to be σ_{other} ≈7.4 nm (undamped) and for the damped table to be σ_{other} ≈4.8 nm (damped). Additionally, in the fast Fourier transform (FFT), a 56 Hz

frequency component was clearly noticeable, with a second at 28 Hz. This source was found to be originating from centrifuges in a neighbouring room. The damped table was able to reduce this contribution to below the detection limit (Fig. 3.22 b). In collaboration with the company Hoare Lea, the conformity of the room with a minimum vibration criterion (VC) standard (IEST-RP-CC012.2) matching or exceeding VC-C for sensitive equipment was determined (Fig. 3.22 c) (167). On average, the room was passing VC-C with the 95th percentile passing VC-B (Fig. 3.22 c). Using heel-drop events of approximately 70 kg, the transmissibility ratio for the optical system was calculated. The table isolated vibrations effectively, passing VC-E for the average and VC-D for the 95th percentile and was below VC-G above 3 Hz (Fig. 3.22 c) . These results, in combination with the determined overall displacement uncertainty of $\leq$7 nm, confirmed the capability of the system to resolve single emitters at a localisation error suited for dSTORM microscopy.

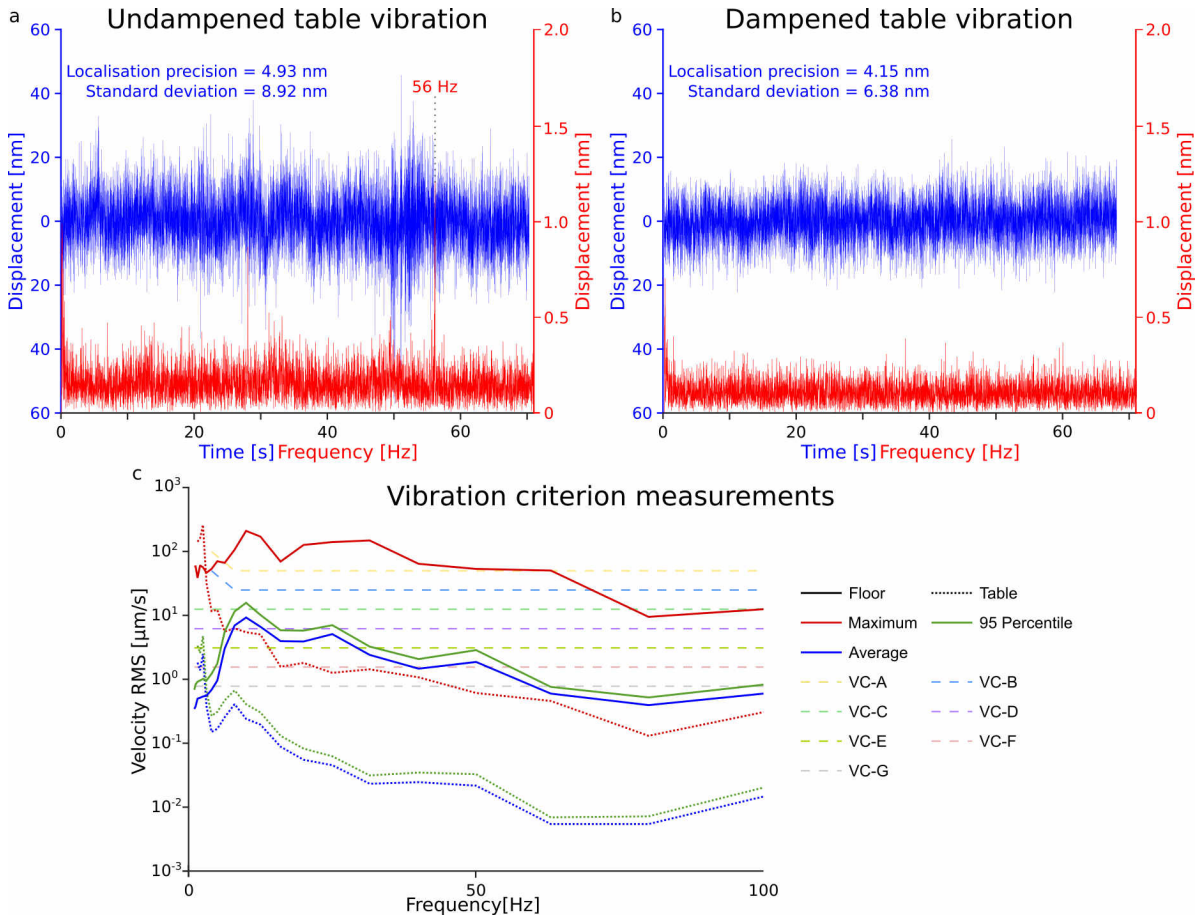

Fig. 3.22: Vibration measurements. Vibration anaylsis with frequency analysis on an (a) undamped and (b) damped optical table. a,b) TetraSpeck microspheres were imaged at 144 FPS to perform a vibration analysis. Data was drift corrected using redundant cross-correlation (RCC). A 56 Hz frequency contribution is detectable on an undamped table resulting in a vibration induced localisation error of $\sigma \approx$7.4 nm. On a damped table the vibrations are reduced to $\sigma \approx$4.8 nm with no detectable frequency component. c) Vibration criterion measurements on the floor and on the damped table. Reduction in vibration from VC-C ($<$12.5 µm/s average) on the floor to VC-E on the table (average$<$3.12 µm/s). Above 3 Hz on the table passed VC-G criterion (average$<$0.78 µm/s).Vibration criterion measurements were carried out in collaboration with the company Hoare Lea.

3.3 Discussion

System Performance Considerations

A first aim within this thesis was the design and construction of a large FOV setup with homogeneous illumination, capable of 3D SMLM and ratiometric SMLM. This was successfully achieved having a large FOV setup with good illumination homogeneity, high automation and fast acquisition.

In terms of illumination, the decision to use a refractive field-mapping device over other flat-fielding techniques demonstrates the priority for high transmission efficiency and low complexity, despite the challenges in maintaining beam uniformity over prolonged path lengths (Fig. 3.15) (124). Here, using a fibre laser with superior beam quality is a notable decision, particularly beneficial in combination with the used refractive field-mapping device achieving high irradiance and good beam qualities with 3.4 kW/cm^2 irradiance at a FOV of 133$\times$133 µm^2, combined with a flatness factor of 0.9 (Fig. 3.15, Tab. 3.1). The edge steepness of 0.6 significantly minimises the phototoxicity outside the FOV compared to a Gaussian illumination.

The measured localisation error of 4.8 nm, estimated from the vibration measurements, includes a combination of all other error sources, including vibration and residual drift errors. The FWHM is 2% larger than the Abbe diffraction limit and therefore a good approximation of the resolution (66). Under the assumption, that this localisation error is not influenced by blinking or polarisation effects from the TetraSpeck microspheres, the standard deviation of a single emitter over 10000 frames was found to be 6.4 nm with an average localisation precision in a single frame of 4.1 nm (Fig. 3.22). This indicates a

localisation error from non-fitting origin of approximately 4.9 nm, leading to a theoretical resolution limit for the system of 11 nm.

Using the dual-sCMOS camera setup, full-frame acquisitions can be acquired at 80 FPS and 12-bit depth (0-4095 ADU). These charactersistics allow the analysis of spatial information spanning 4 orders of magnitude in a single FOV (10 nm to 100 µm). Additionally, using astigmatic PSF shaping the axial localisation precision can be improved to 15 nm.

Camera correction

Within this work, pixelwise offset, dark current, read noise, thermal noise and gain correction maps were generated in combination with a software package to routinely perform the calibration for sCMOS cameras. Unlike CCD cameras with a more homogeneous photon response, the pixel-to-pixel variability require the acquisition of $>10^5$ frames to generate the robustness needed to calibrate each pixel individually. Therefore, unlike the spatially homogeneous illumination needed in CCD camera photon-response calibration, a temporally homogeneous illumination is needed. Diekmann *et al.* circumvented this problem by using a photon-free approach (149). Similarly to the method used within this thesis, Etheridge *et al.* adapted the analysis used for CCD cameras to sCMOS cameras, first described by Huang *et al.* in 2013 (168, 165). Yet as they have focused on the software aspect, the practical implication of temporal brightness stability is not addressed. Within this work, the practical limitations were explored and a temporally stable light source was established with brightness instabilities $\ll$0.1%. To further address the problem of temporal instabilities and acquisition artefacts, binning of data into 50 frames and analysing each subset for the brightness stability was found to be crucial to recover high quality gain maps (Fig. 3.18).

Having established the photon response maps for the sCMOS camera allowed for characterisation of the fitting error introduced due to the pixel-to-pixel varieties. Using 176.400 simulated frames, the fitting error was found to be negligible $<$1 nm for most pixels in dSTORM like settings (5000 photons, see Fig. 4.4). Still, correcting for these inhomogeneities can improve the image reconstruction for the pixels with high dark current and high photon sensitivity (Fig. 3.19). More importantly, in the ratiometric PAINT acquisition using di-4-ANEPPDHQ, the photon-count was significantly lower, having an order of magnitude less photons per emitter and frame (median of 1400 photons for sum of both cameras). Here, the pixel non-uniformity have affected the image reconstruction more significantly. Therefore, applying the camera correction maps was routinely performed to minimise the influence of pixel inhomogeneities.

Limitations

One major drawback of the current implementation is the relay lens used. While Plössl lens configurations are used in modern microscopy setups as relay lens, including SMLM setups (159, 155), the focus-dependent XY shift was found to introduce significant lateral shift when acquiring 3D SMLM data at various focal depths (Fig. 3.21). For axial drift stabilisation a CRISP autofocus system with a focus accuracy $<$5% of the depth of focus (DOF) is used, resulting in a focus accuracy of ±28.5 nm ($\sim$570 nm DOF). At the most distal regions of the FOV this can lead to a XY-shift of up to 9 nm at optimal performance of the autofocus system.

A second limitation introduced by the large FOV are the field dependent PSF aberrations (Fig. 3.20, 3.21). These optical aberrations affect both 2D and 3D SMLM data and introduce systematic fitting errors. While full FOV astigmatic PSF 3D localisation still

performs well (Fig. 3.20, b), axial localisation precision is improved for a smaller FOV with 3D astigmatic PSF-calibration matching the acquired ROI.

Future Directions

In a next iteration, the Plössl relay lens will be replaced with a 4f relay lens. While increasing the path length of the detection path, this will reduce the systematic focus-dependent XY-shift, leading to an expected improvement in localisation performance for large FOV image acquisitions. Additional upgrades can include the improvement of the TTL laser trigger circuit, as currently only a binary on/off function is implemented. A FPGA-based implementation has been published, allowing for continuous laser power adjustments using the AOTF (132). Finally, an active 3D drift stabilisation and liquid cooling of the camera can help minimise drift and vibration induced reduction of image resolution (169). Though, achieving a resolution sub 10 nm is challenging, as here electron transfer effects among other limitations come into effect (68). Instead, novel software packages such as COMET might further improve on the drift error currently observed without the need for a modification of the system (unpublished work, Bates-laboratory).

In collaboration with the Rieger and Stallinga lab at TU Delft a Zernike polynomial based vectorial 2D PSF correction is currently investigated to reduce the effect of optical aberrations (170). The field dependence was found to be dominated by Z_2^{-2} and Z_2^2 modes ranging from $\pm$100 mλ for Z_2^{-2} and $\pm$50 mλ for Z_2^2 modes. These Zernike modes correspond to oblique astigmatism and vertical astigmatism, respectively (171). Other Zernike polynomial Z_2^0, Z_3^{-1}, Z_3^1, Z_4^0 corresponding to coma and defocus modes show only minor contributions throughout the FOV.

Overall, a versatile single-molecule localisation microscope has been established for Epi-TIRF imaging using 2D and 3D imaging techniques combined with the possibility for ratiometric imaging. The modular design will allow for fast iteration on the design and optimisation tailored to the specific needs of experiments as outlined in Chap. 4, 5. Here, the modular filter options, and state-of-the-art capabilities are utilised to perform novel super-resolution and volume imaging techniques in a cellular context.

Chapter 4

Novel quantitative and super-resolution imaging techniques

Part of this work (Sec. 4.2.2, 4.2.3) is currently in the process of publication:

S.A. Tashev*, J. Euchner*, K. Yserentant*, S. Hänselmann, F. Hild, W. Chmielewicz, J. Hummert, F. Schwörer, N. Tsopoulidis, S. Germer, Z. Saßmannshausen, O.T. Fackler, U. Klingmüller, D-P. Herten, 2023, bioRxiv, *"A General Method to Accurately Count Molecular Complexes and Determine the Degree of Labelling in Cells Using Protein Tags"*

Author contributions:
J.E., S.A.T., and K.Y. performed all data analysis. J.E., S.A.T., K.Y., S.H., F.H., W.C., S.G., and Z.S. acquired the data. S.H. generated the ProDOL probe. S.H., F.H., K.Y. J.E., J.H. and S.A.T. generated the ProDOL analysis workflow. W.C., S.H., N.T., and F.S. generated stable cell lines. O.T.F. and D-P.H. performed conceptualisation, supervision, resource management, and project administration on T cell work. O.T.F. and U.K. contributed general ideas and concepts. S.H. and D-P.H. conceived the method. J.E., S.A.T., K.Y., O.T.F., and D-P.H. wrote the manuscript with input from all authors.

L. Panconi*, J. Euchner*, M. Makarova, D-P. Herten, D.M. Owen, D. Nieves, 2023, in revision, *"Detection of nanoscale membrane order via solvatochromic PAINT"*

Author contributions:
J.E. built the optical set-up, acquired di-4-ANEPPDHQ PAINT data, performed ratiometric analyses, and wrote the Voronoi-super-tessellation code. L.P. performed membrane analyses, wrote simulation, and PLASMA analysis code. M.M. prepared GUVs for di-4-ANEPPDHQ PAINT. D-P. H. contributed ideas and concepts. D.J.N. developed the di-4-ANEPPDHQ approach, optimised generation of membrane patches, and wrote the MOM code. D.M.O and D.J.N conceived the work. All authors contributed to drafting and writing of the manuscript.

4.1 Introduction

Various advanced fluorescence microscopy techniques exist which can be performed to unravel the biological function and distribution of a protein of interest (POI). Established methods include quantitative microscopy techniques such as degree of labelling (DOL) analysis. Using the DOL, the relation of fluorescent signal to protein copy number can be recovered. Similarly, various multi-colour imaging techniques exist to determine the localisation of multiple POIs relative to each other. Here, spectral demixing is a technique used to separate the fluorescent signal from multiple fluorescent dyes with overlapping excitation and emission. To do so, the emission is split at a cutoff wavelength with short-pass emission detected in one channel, and long-pass emission detected in a second channel. Based on the ratiometric profile, the overlapping fluorophore emissions can be robustly separated and assigned to a specific fluorophore. Using this technique of ratiometric imaging cannot only be utilised to demix multiple fluorophores, but also to analyse solvatochromic dyes with shifted emission based on their environment. These environment-sensitive dyes have found multiple application, including the polarity sensing of membranes, with application in tumour diagnosis (172, 173, 174, 175, 176).

4.1.1 Degree of labelling analysis

Fluorescence microscopy is crucial in biological research for detecting a POI. To accurately measure POI copy numbers, both the fluorophore number and the relation of fluorophore to POI needs to be determined. However, determining this relation of fluorophore to POI, which is also known as DOL, can be challenging. Several methods have been developed to determine the DOL. A common approach is to use a calibration

standard of known stoichiometry in combination with an absolute label counting technique such as effective labelling efficiency (ELE), Counting by photon statistics (CoPS), or quick-photobleaching step analysis (quickPBSA) (Fig. 4.1 a-d, SI 13) (86, 177, 82, 3). These approaches have drawbacks: Counting standards such as the nuclear pore complex (NPC) requires the use of a homozygous knock-in cell lines. Furthermore, methods such as ELE only work for labels compatible with super-resolution microscopy. CoPS additionally requires specialised instrumentation not commonly available. Alternatively, colocalisation analysis of two labels can be used to estimate the DOL of both tags, using one fluorescent label as reference and determine the percentage of colocalisation for the second tag (Fig. 4.1 e-f) (5, 178, 179). Here, unspecific labelling of the reference label or the overlap of unspecific target labels with the reference can skew the DOL analysis.

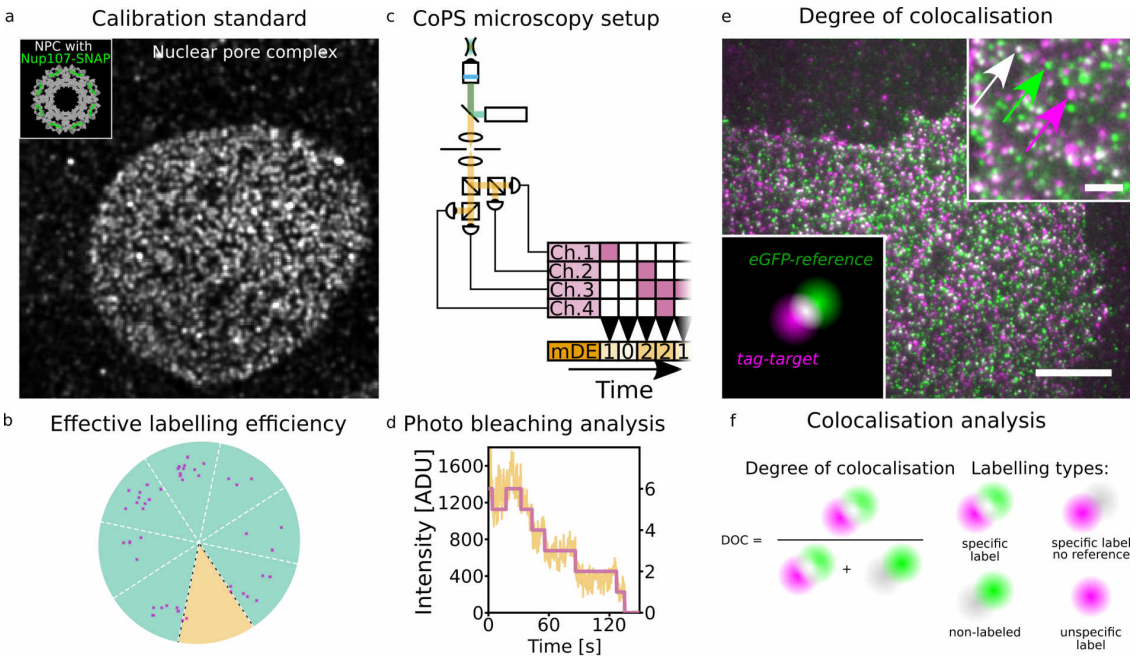

Fig. 4.1: Principle to determine the DOL. a) U2OS cell with Nup107-SNAP knock-in as counting standard used for ELE, CoPS, or quickPBSA. Inset: 8-fold symmetry with 4 protein copies per segment (green). b) ELE analysis based on direct stochastical optical reconstruction microscopy (dSTORM) acquisition and assignment of segments with at least 2 labels. c) CoPS analysis based on the antibunching principle to determine the emitter number from the distribution of multiple detection events (mDE). d) quickPBSA based on the detection of bleaching events from the intensity trace. e) Colocalisation based analysis to determine the DOL of a target (magenta) from the degree of colocalisation (DOC) to a reference (green). f) Principle of determining the degree of colocalisation from the ambiguity of specific label with no reference and unspecific label. Modified from submitted work of Tashev *et al.* (5).

4.1.2 Multi-colour imaging

Traditionally, multi-colour imaging was achieved by having a laser line specific for each fluorophore, thus being able to image four labels of interest using four laser lines. Yet, in SMLM, the best-performing fluorophores typically emit in the red to far-red region, with the best-performing fluorophores all being excited around 650 nm (AF647, CF660C, CF680) (180). Additionally, due to the high irradiance required for dSTORM ($\geq$1 kW/cm^2), the cost of having four high-power lasers increases the cost of the system. Therefore, many systems use either spectral demixing or temporal multiplexing. In spectral demixing, the image is split, and the ratio between a short-pass filtered and long-pass filtered image is determined, with the ratio being specific to the emission profile of a fluorophore (Fig. 4.2) (180). Here, the fluorescence emission must be significantly different to ensure a clear split of the ratios, minimising any overlap.

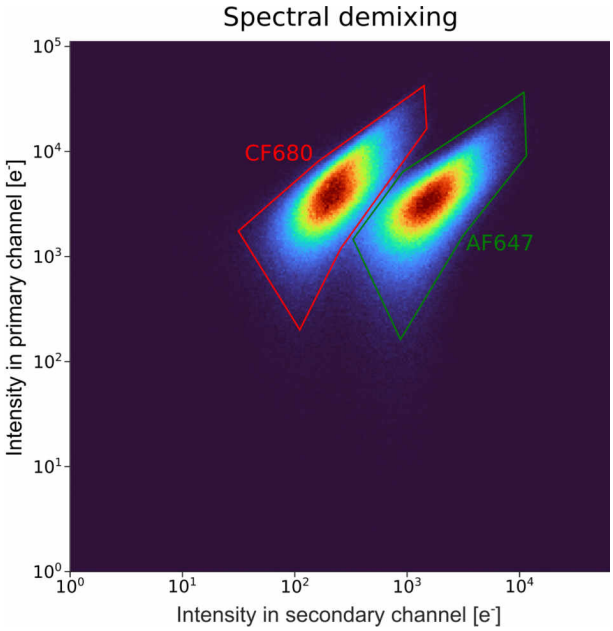

Fig. 4.2: Spectral demixing in multi-colour imaging. Spectral demixing of AF647 and CF680 based on their distinct emission spectra by splitting the emission into a long- and short-pass emission. The two regions marked in red and green represent the intensity distributions specific for CF680 and AF647. Data acquired independently with settings optimised for each fluorophore using a 662 nm long-pass beam splitter.

Temporal multiplexing, on the other hand, uses a single fluorophore for which the system can be optimised (181). Between acquisitions, the fluorophore (typically labelled antibodies in dSTORM) is washed away before a new label is added. It is critical to validate that all labels have been washed off without interfering with the structural integrity of the sample.

4.1.3 Membrane polarity sensing

Eukaryotic plasma membranes are crucial for maintaining cellular activities like transport and signalling. Its biophysical properties, especially lipid order, are hypothesised to be crucial in these processes, segregating into liquid ordered (L_o) and liquid disordered phases (L_d) (Fig. 4.3 a, b) (182, 183). Ordered domains are rich in saturated lipids, and cholestrol, with disordered domains rich in unsaturated lipid (183). To this date, the presence and biological importance of lipid nanodomains is debated (182).

Here, solvatochromic probes can aid in detecting the presence of ordered and disordered lipid packing (184, 185). Recently, solvatochromic dyes, such as Nile Red and Abberior STAR RED, have been used to investigate the presence of sub-diffraction limited nanodomains in plasma membranes (184, 186). Di-4-ANEPPDHQ is a previously reported dye with 60 nm blue-shift in ordered membranes and can be used in point accumulation for imaging in nanoscale topography (PAINT) imaging to map the nanoscale membrane order of the plasma membrane (185). Using ratiometric imaging, a generalised polarisation (GP) can be determined for each emission (Fig. 4.3 c, d). This value ranges from -1 to +1 and reflects the lipid order of the region.

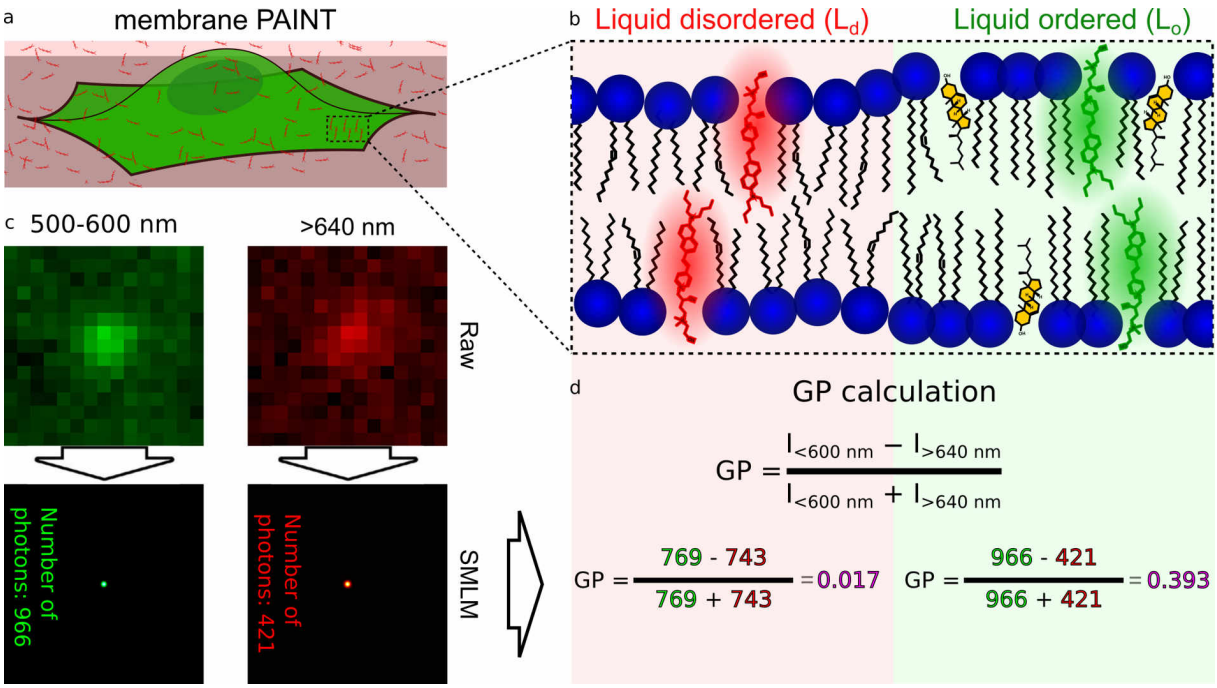

Fig. 4.3: Visualising Membrane Lipid Order using ratiometric PAINT. a) Schematic of cellular membrane PAINT using a cell in suspension with the dye di-4-ANEPPDHQ. b) Hypothesised segregation of a plasma membrane into liquid-ordered (L_o) and liquid-disordered (L_d) phases and the resulting spectral shift from di-4-ANEPPDHQ. c) Ratiometric detection of emission for the wavelength ranges of 500-600 nm and >640 nm. d) Intensities in the two channels are used to calculate a generalised polarisation (GP) value for each emission event. GPs have a range from -1 to +1 and indicate the degree of lipid order. Modified from submitted work (L. Panconi, and J. Euchner *et al.*).

4.1.4 Aims

In this chapter, the performance of the system developed in Chap. 3 is first evaluated and is subsequently applied to advance the field by developing novel quantitative and super-resolution imaging techniques. The single-molecule localisation microscopy (SMLM) performance is validated based on indirect immunolabelling of microtubules. Characteristic performance parameters are compared to theoretical and experimental benchmarks of established state-of-the art dSTORM systems. Next, an overview of its practical application in platelet research is presented. Then, a focus is put on the development of advanced imaging techniques, such as ”Protein-tag Degree of Labelling” (ProDOL), a construct designed for efficient, easy and robust determination of the labelling efficiency. Here, the validation of ProDOL and the refinement of the software developed alongside it is shown. The chapter concludes with an exploration of the system’s versatility, specifically its adaptation for advanced ratiometric PAINT imaging using the membrane-polarity sensitive dye di-4-ANEPPDHQ. This section highlights how the development of nanoscale cluster analysis techniques based on marked point patterns (XY coordinate, with polarity value) is pivotal for identifying and classifying sub-diffraction limited regions, exemplified by the identification of consistent homologies in the nanoscale membrane order.

4.2 Results

Having built and calibrated the microscope, the system was used to develop novel quantitative and super-resolution imaging techniques. Before, indirectly immunolabelled microtubules were used as a target to validate the dSTORM performance (Fig. 4.5, 4.4) (4, 155), followed by the application of dSTORM to study the distribution of relevant proteins in platelets. Thereafter, novel imaging techniques were established and validated, including a colocalisation based approach to determine the DOL (Fig. 4.8) (187, 188) and an advanced ratiometric PAINT analysis to investigate the nanoscale distribution of the membrane order using the solvatochromic dye di-4-ANEPPDHQ (Fig. 4.3) (185, 189).

4.2.1 dSTORM

Using microtubules of liver sinusoidal endothelial cell (LSEC) with an optimised labelling protocol by Jimenez *et al.*, the performance in large field of view (FOV) 2D dSTORM was validated (63, 155). All characteristics but FRC resolution, localisation precision and residual localisation displacement error were determined for full-frame images of 133×133 µm^2 (Fig. 4.5). Due to the large FOV, leveling of the sample orthogonal to the objective is crucial as any sample tilt can introduce out-of-focus effects at the distal areas. Exemplary, a sample tilt of 0.1% introduces a focus shift of 175 nm for each 100 µm lateral distance. Therefore, the remaining characteristics were determined on smaller region of interest (ROI), exceeding 30×30 µm^2 (Fig. 4.4).

Generally, a good homogeneity of performance is observed throughout the FOV with only the corners of an image dropping off in reconstruction quality, in line with the determined irradiance profile (Fig. 3.15). Given a measured laser-power at the backfocal plane of the objective, an irradiance of 3.4 kW/cm^2 was determined. This is sufficiently high to not introduce image artefacts commonly observed below 1.6 kW/cm^2 (154). Similarly, irradiance between 1.6 kW/cm^2 and 24 kW/cm^2 were found to result in optimal Fourier ring correlation (FRC) resolution (155). For dSTORM, many relations for the varying parameters exist and can therefore be used as a quality characteristic. The point spread function (PSF) width (σ_{PSF}) should be independent of the dSTORM conditions (Fig. 4.4 e) and can be estimated by (165):

$$\sigma_{\mathrm{PSF}} \approx \sqrt{\left(P \times 1.323 \times \frac{\lambda_{\mathrm{geom}}}{2 \times \pi \times \mathrm{NA}}\right)^2 + \frac{a^2}{12}} \tag{4.1}$$

where P corresponds to the proportionality factor to account for optical focus errors and system-specific aberrations ($P \geq$1, typical $P \approx$1.52). 1.323 is the equivalence constant to convert an Airy width into a Gaussian standard deviation, λ_{geom} is the geometrical mean emission wavelength, NA the numerical aperture of the setup and a the pixel-width. The experimentally found modal PSF width of 137 nm corresponds to a proportionality factor of 1.41, in line with state-of-the-art setups (155).

To validate the performance of the system in SMLM, several parameters can be extracted from a time series of single-emitter emission events (Fig. 4.4). 2-Mercaptoethylamine (MEA), an active compound of the dSTORM buffer, forms a reversible product with the excited fluorophore state, causing the prolonged dark state of the fluorophore. Therefore, the concentration of MEA should be inversely proportional to the on-time in millisecond and photons per localisation - both key parameters of the dSTORM

performance (Fig. 4.4 f,g) (photons: 11298±657 (35 mM) vs 4267±243 (100 mM), on-time: ∼160 ms (35 mM) vs ∼50 ms (100 mM)). To keep the number of frames consistent at varying on-time of a single emitter, the exposure time is typically chosen inversely proportional to the MEA concentration, to have the emission of a single emitter over roughly 2 frames (Fig. 4.4 a,f). Similarly, the localisation precision inversely scales with the square root of the photon count $\propto 1/\sqrt{N}$ (See Eq. 1.2). Therefore at 35 mM MEA, the localisation precision should be ∼1.7× improved compared to 100 mM MEA (Fig. 4.4 h) for all other parameters being equal (localisation precision: 4.9±3.5 (35 mM) vs 7.2±4.1 (100 mM)) (See Sec. 1.2.3). All these relations were found to be consistent for the measured samples. Additionally, 405 nm laser irradiation can be used to keep the emitter density at a constant level, by promoting the decomposition of the transient MEA-fluorophore adduct and a return of the fluorophore into an excitable ground state (Fig. 4.4 b) (56). Again, this regulation of emitter density was found to work robustly for the system.

Next, the ability to correct for the nanoscale temporal drift of the sample is analysed. The sample drift is caused most prominently by thermal fluctuation of both system and sample induced by thermal expansion of components from the laser irradiation. Correcting this drift can be achieved using various drift correction methods. Routinely, redundant cross-correlation (RCC) was used to correct for sample drift (190) (Fig. 4.4 c). Due to the long temporal binning needed for RCC, non-linear displacement errors occurring in the 10^0-10^1 s scale cannot be corrected for. Using cost-function optimized maximal overlap drift estimation (COMET), a pre-publication software by the Mark Bates group at the Institute for Nanophotonics in Göttingen, the displacement on the

second scale was estimated[1] (80 frames per COMET bin, vs 1000 frames per RCC bin) (Fig. 4.4 d) and was found to be 4.5±0.1 nm along both X- and Y-axis, resulting in a total residual drift error of 6.4±0.1 nm, as estimated by COMET.

Using the localisation data, the FRC resolution estimation was found to be 29±0.1 and 35±0.3 nm for 35 mM and 100 mM MEA respectively, again in line with with experimental results by Diekmann *et al.* (Fig. 4.4 i, (155) - Extended Data Fig. 9). For both conditions, the microtubules were resolved having a tube like intensity profile with a peak-to-peak distance of 54±7 nm (Fig. 4.4 j). All these characteristics confirm a high-performance setup capable of resolving sub 50 nm scale structures across a FOV of 133 µm, spanning 4 orders of magnitude.

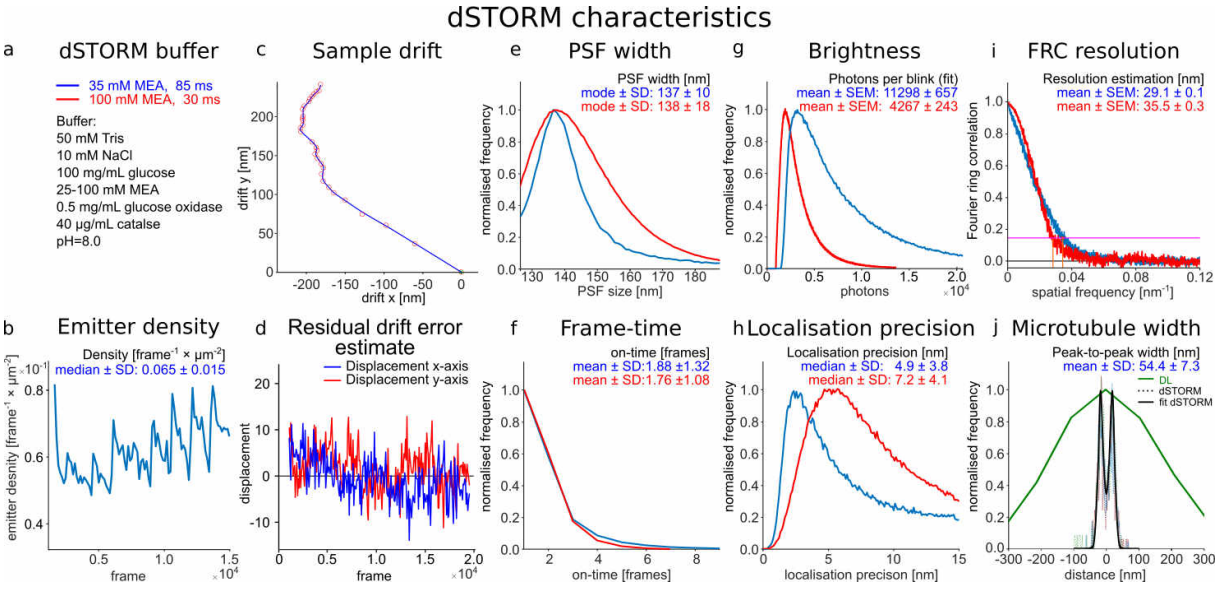

Fig. 4.4: dSTORM performance characteristics using microtubules as validation target. a) Microtubules were imaged at 35 mM and 100 mM of MEA in dSTORM buffer and relevant dSTORM parameters are shown in b-j). b) Emitter density over time using 405 nm to compensate for bleaching induced reduction of emitter density. c) Exemplary sample drift for 100 mM MEA sample (Fig. 4.5). d) Residual drift error estimated using COMET at 80 frames per bin. e-h) Distribution of fitting parameters for PSF width, on-time, brightness and localisation precision. i) FRC resolution estimation, j) line profiles with 500 nm line width each from (Fig. 4.5 c) showing a peak-to-peak width of 54±7 nm, below the resolution limit in diffraction-limited microscopy (DL).

[1] https://github.com/gpufit/Comet

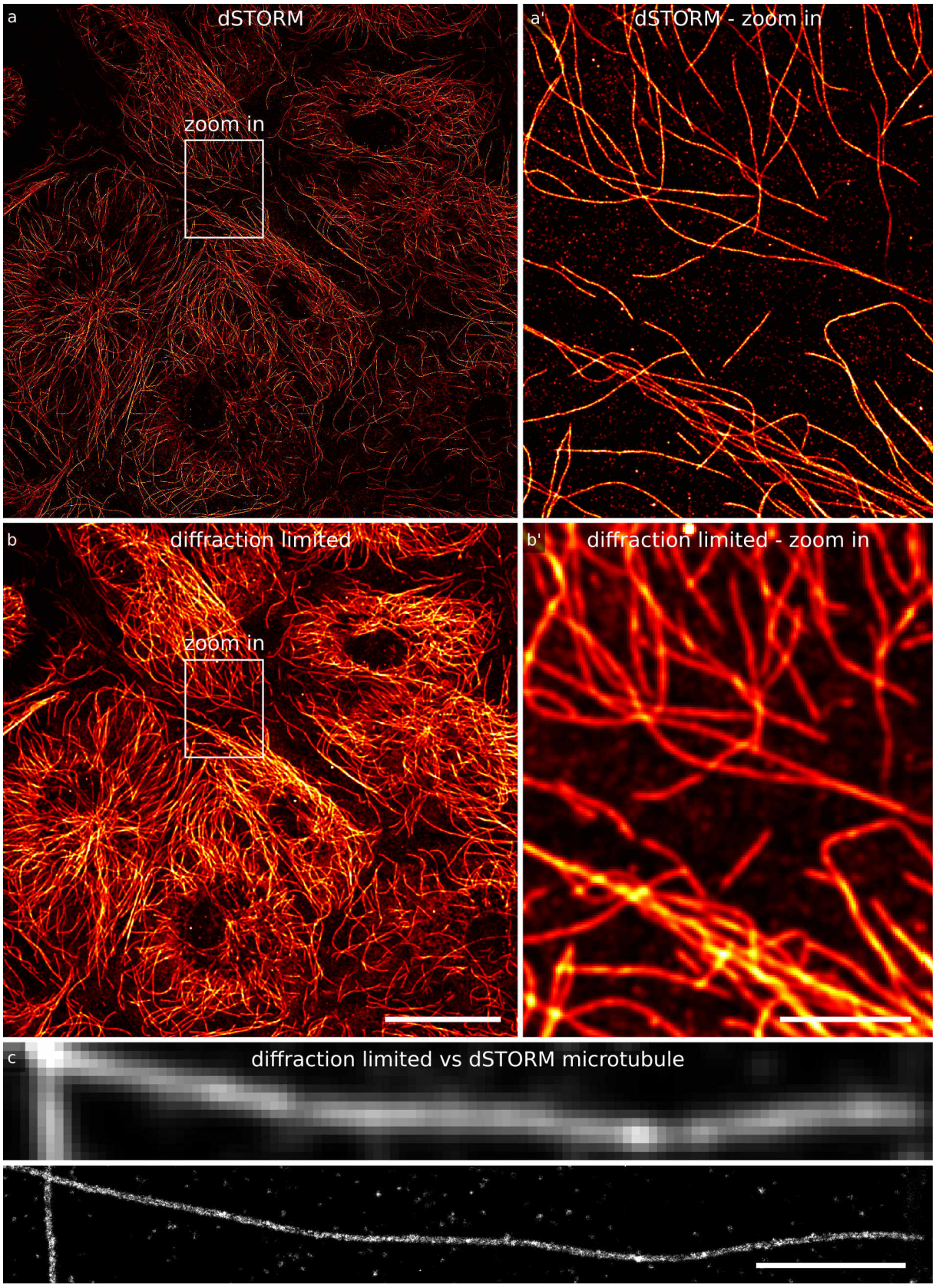

Fig. 4.5: Large FOV microtubule imaging in diffraction-limited microscopy and dSTORM. a,b) Super-resolution reconstruction and diffraction-limited full FOV acquisition of indirectly immunolabelled microtubules in LSEC. a',b') Zoom in to ROI. c) Zoom in to individual microtubules to visualise the ability to resolve the tube-like structure of microtubules in LSEC. dSTORM characteristics shown in Fig. 4.4 for 100mM. Scale bar: a,b) 30 µm a',b') 10 µm c) 2 µm.

The setup was subsequently used in multiple collaborations to study the distribution of various receptors and proteins in platelets, megakaryocytes, and T cells, among other cells of biomedical interest. In collaboration with Neil Morgan and Natalie Poulter, the clinically relevant mutation in GP1bα (G138V), causing mild bleeding, was studied for their altered receptor distribution of GP1bα (Fig. 4.6) (unpublished work). Spread platelets from a healthy donor have been shown to exhibit a predominantly homogeneous GP1bα distribution with locally distinct areas of GP1bα accumulation as a response to the collagen-coated surface (Fig. 4.6 a, red arrows). This is consistent with findings from correlative light-electron microscopy (CLEM) investigations, where platelets exhibit a discernible variation in GP1bα density in proximity to collagen fibres (Fig. SI 11). Conversely, platelets from the patient donor failed to exhibit these distribution response structures on collagen-coated surfaces (Fig. 4.6 b). Instead, a heightened prevalence of GP1bα-rich clusters was detected, though the precise ultrastructural localisation remains elusive (Fig. 4.6 b, cyan arrow). The contrasting GP1bα distribution on collagen-coated surfaces between healthy and patient donors can help to better understand the clinical relevance of the G138V mutation. For this, further experiments, probing the nanoscale functional and ultrastructural organisation, need to be performed but were beyond the scope of this thesis.

Similarly, the heterogeneous response of platelets to the alarmin S100A8/A9 was investigated, as high S100A8/A9 levels were found to correlate with worse COVID-19 prognostic outcomes and the interaction of S100A8/A9 with GP1bα on platelets results in a prothrombotic pathway (Fig. 4.7) (121, 191). Here, various subpopulations of platelets from healthy donors were detected, showing either low or high binding of

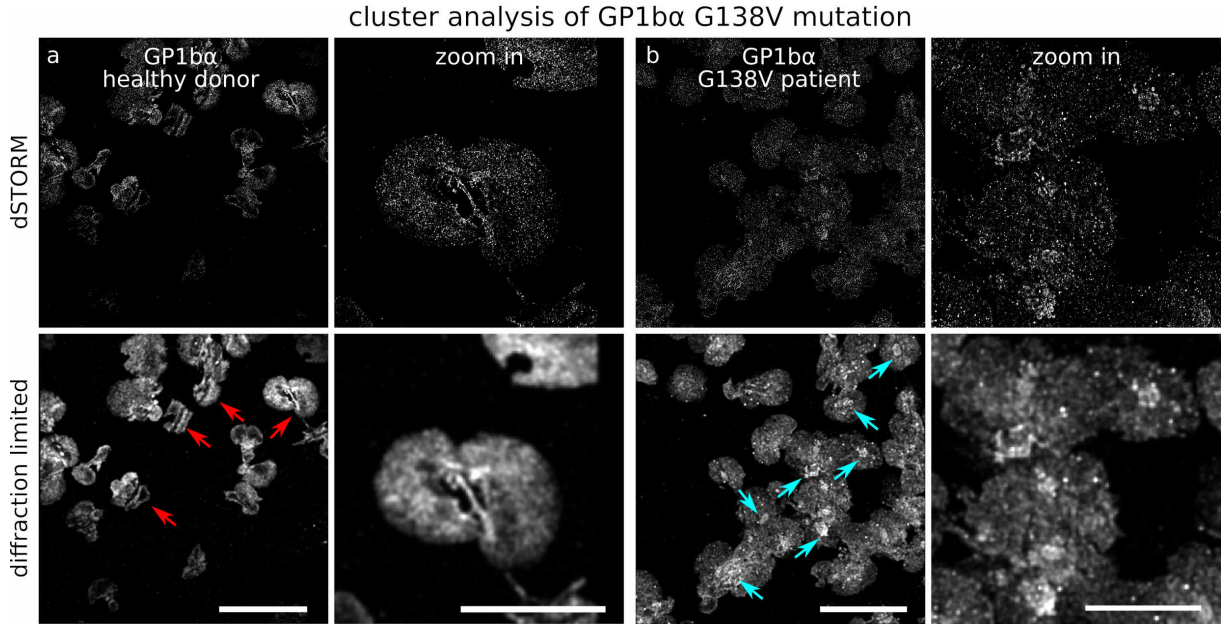

Fig. 4.6: Comparative analysis of GP1bα receptor distribution in platelets from a healthy donor and a patient with a G138V mutation in GP1bα. a) Platelets from a healthy donor exhibit a predominantly homogeneous GP1bα distribution on a collagen-coated surface, with locally distinct areas of GP1bα accumulation as a response to the collagen-coated surface (red arrows). These patches of altered GP1bα distribution correlate with the proximity of GP1bα to collagen fibres, as confirmed by CLEM experiments (Fig. SI 11). b) Platelets carrying the G138V mutation in GP1bα demonstrate a reduced response to the collagen-coated surface, yet exhibit atypical GP1bα-rich clusters (cyan arrows). Platelets were spread on collagen-coated coverslips for 45 min before being fixed with 4% PFA, permeabilised with 0.1% Triton X-100 for 5 min, and indirectly immunolabelled for GP1bα. dSTORM acquisition was performed in 50 mM MEA-containing dSTORM buffer. Scale bars: a, b) 20 µm; zoom-ins a, b) 10 µm.

S100A8/A9 (Fig. 4.7 b). Furthermore, the high S100A8/A9 binding platelet population was further classified by their extent of endocytosis (Fig. 4.7 b). The binding partners of S100A8/A9 on platelets, such as RAGE, TLR4, CD36, and GP1bα are currently under investigation for their role in this heterogeneous response (121). Further analysis of the distribution and abundance of these relevant receptors will be carried out to aid in better understanding the clinical relevance of low and high responders with respect to S100A8/A9.

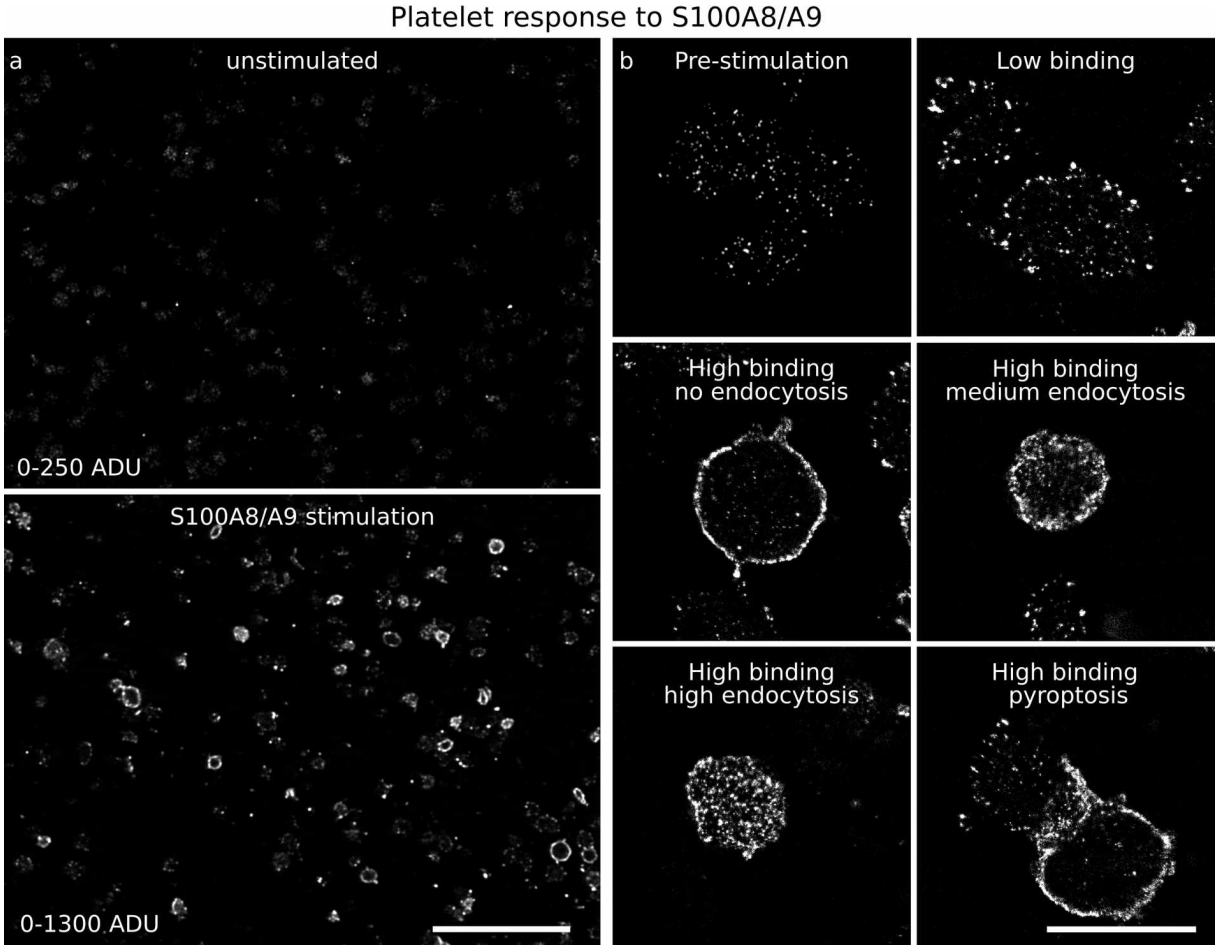

Fig. 4.7: Classification of the heterogeneous platelet response to an external S100A8/A9 stimulus. a) Representative FOV of unstimulated and S100A8/A9 stimulated platelets. After stimulation a heterogeneous population of platelets with respect to binding and uptake of recombinant S100A8/A9 is observed. b) Low level endogenous S100A8/A9 is detected pre-stimulation. After external stimulation with S100A8/A9, a heterogeneous platelet response is detected and includes low and high S100A8/A9 binding platelets. The high binding subpopulation can be further grouped by the presence and extend of S100A8/A9 endocytosis. Platelets were fixed with 4% PFA, permeabilised with 0.1% Triton X-100 for 5 min, and indirectly immunolabelled for S100A8/A9. dSTORM acquisition was performed in 50 mM MEA-containing dSTORM buffer. Abbreviation: ADU = Analog-to-digital units. Scale bar: a) 30 µm b) 5 µm.

4.2.2 Degree of labelling analysis

Based on previous work by Yserentant and Hänselmann, a method to determine the DOL of a protein-tag from the degree of colocalisation to a reference signal was continued in a collaborative project with Stanimir Tashev (5, 187, 188). The method is termed protein-tag degree of labelling (ProDOL) and consists of fusion construct for labelling efficiency determination (Fig. 4.10 a, 4.1). The ProDOL fusion construct is anchored to the plasma membrane of cells using the Lyn kinase anchor moiety allowing for defined localisation of the probe as well as total internal reflection fluorescence

(TIRF) imaging to minimise background. Enhanced green fluorescent protein (eGFP) is used as a nearly background-free reference signal in combination with the commonly used protein-tags HaloTag and SNAP-tag (Fig. 4.10 a) (47, 48).

To determine the DOL from images acquired of the labelled ProDOL construct, a routine was developed (Fig. 4.8) to convert the degree of colocalisation (DOC) into a DOL. The DOC can be described by Eq. 4.2 and is schematically shown in Fig. 4.1 f.

$$\mathrm{DOC} = \frac{\mathrm{target} \cap \mathrm{reference}}{\mathrm{reference}} \tag{4.2}$$

First, the acquired images are segmented (I-II), emitters for both eGFP-reference and tag-target are localised (III) and an affine transformation is performed to correct for aberrations between the two channels (IV). Next a distance cutoff is determined that maximises the specific degree of colocalisation (V), followed by a density correction to recover the underlying degree of labelling (VI). Using this routine, the experiment-specific DOL can be determined (VII) (Fig. 4.8).

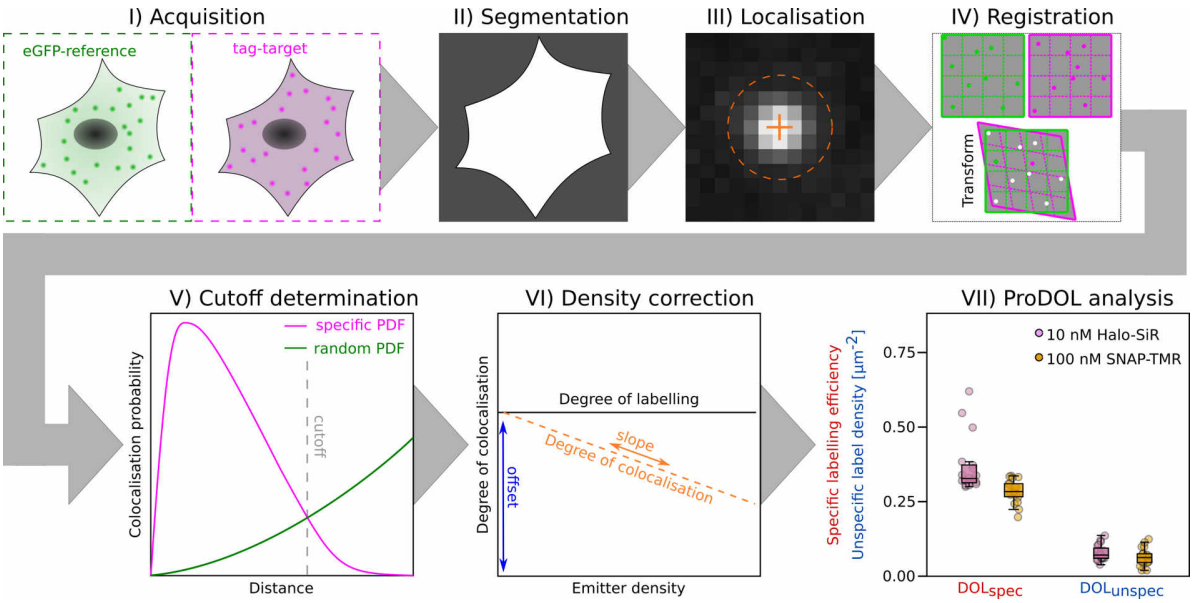

Fig. 4.8: ProDOL analysis workflow. I) Images are acquired for both the eGFP-reference and tag-target. II) images are segmented to the region containing a cell. III) Using ThunderSTORM, the localisation of the single emitters is determined. IV) Based on the localised emitters a global transformation using affine registration is performed. V) Distance cutoff T is determined at which the likelyhood of specific labelling is maximised. VI) Based on the emitter density a correction is applied to convert the DOC into a DOL. VII) The median DOL is calculated from the image set. Based on work by Yserentant and Hänselmann (188, 187). Modified from Tashev *et al.* (5).

To perform the ProDOL analysis, the code for segmentation and localisation was modified to allow for a generalisability of the method (Fig. 4.9 a,b). Additionally, registration and cutoff determination (Fig. 4.8 IV,V) were improved to better handle edge-cases, including unsuccessful registrations and a low signal-to-noise ratio (SNR) probability density function (PDF) during threshold determination (Fig. 4.9 c,d). For example, when a low SNR in the colocalisation threshold determination was detected, the colocalisation score was smoothed to reduce the chance of outliers effecting the peak-finding algorithm (Fig. 4.9 d, red). Furthermore, the maximal spatial tolerance for the threshold was limited to a reasonable search space estimated from analyses with high SNR (Fig. 4.9 c). Finally, the code was streamlined from an emission-based analysis to a tag-based analysis while also allowing for user-defined input parameters[2].

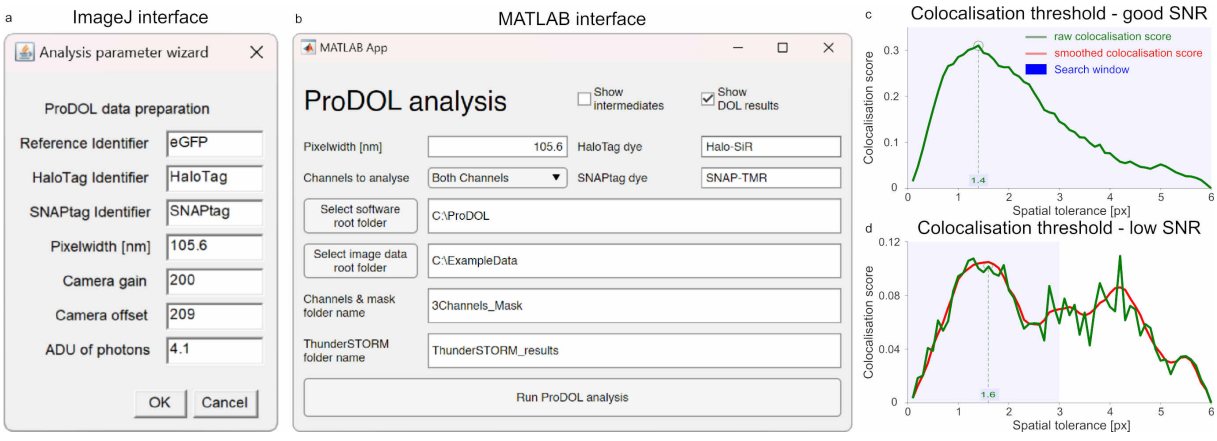

Fig. 4.9: ProDOL software a,b) User interface generated for ProDOL software. c,d) Colocalisation threshold determination for image sets with high and low SNR of the colocalisation score. d) For colocalisation analysis with low SNR, a smoothing of the raw colocalisation score was performed (red), combined with restriction of the spatial tolerance based on colocalisation thresholds of samples with good SNR (blue).

[2] `https://github.com/hertenlab/ProDOL`, as of 05/12/2023

Using the ProDOL-probe in combination with the ProDOL-workflow, the degree of labelling with respect to incubation time and label concentration can be determined to identify optimal labelling conditions for a given imaging technique. To validate the correct experimental determination of the DOL, the method was cross-validated using existing DOL calibration techniques utilising the nuclear pore complex as counting standard (Fig. 4.1, 4.10 b).

U2OS expressing the genetically modified Nup107-SNAP-tag, a subunit of the nuclear pore complex, were used to determine the DOL in ELE, quickPBSA, and CoPS using SNAP-AF647 (86, 3). Using the same labelling conditions, wild-type U2OS cells transiently expressing the ProDOL probe were labelled with SNAP-AF647. The ProDOL analysis found a DOL of 42.6±5.3% (Mean±standard deviation (SD)). All counting methods used for cross-validation yielded a similar DOL not significantly different from the ProDOL approach (p=0.33, Kruskal-Wallis, 42.2±4.1% (ELE), 40.6±5.8% (quickPBSA) and 40.5±4.9% (COPS)) (Fig. 4.10 b).

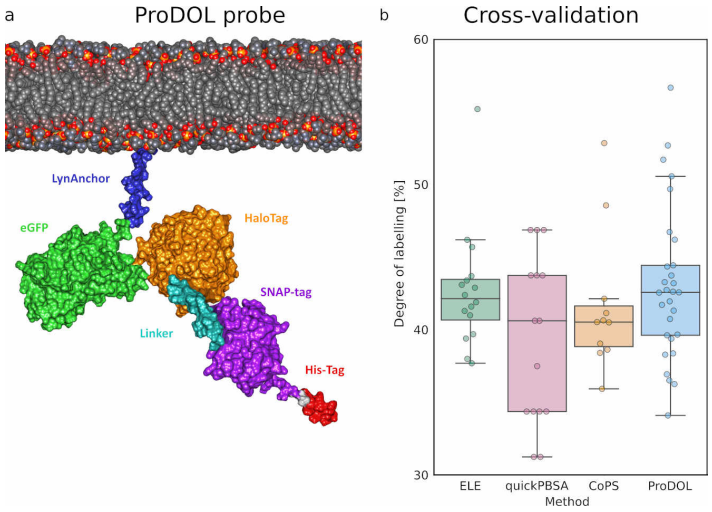

Fig. 4.10: Cross validation and DOL analysis using ProDOL a) Model of the ProDOL probe, generated using AlphaFold with manual modification based on crystallographic data for each domain (PDB: 2B3Q, 6Y8P, 6U32). Bilayer from Heller *et al.* (192). b) Cross-validation of the DOL determined by ProDOL with established counting techniques in U2OS cells. Box-and-whisker plot. b) Number of analysed cells - ELE: 16, quickPBSA: 17, CoPS: 11, ProDOL: 29. Modified from submitted work of Tashev *et al.* (5).

Therefore, ProDOL has been successfully established as a robust, fast and reliable technique to determine the cellular protein-tag labelling efficiency, without the need for advanced microscopy systems or reliance on absolute counting techniques.

4.2.3 Ratiometric PAINT

In collaboration with Dylan Owen, Dan Nieves and Luca Panconi from the University of Birmingham, the solvatochromic membrane polarity sensitive dye di-4-ANEPPDHQ was used to develop a methodology to recover the nanoscale membrane order of live cell plasma membranes using ratiometric PAINT microscopy (185, 184). The polarity of membranes has been found to have crucial implications for cellular signalling and homeostasis (172). Some cancer types can be classified by the presence of a lowered membrane polarity allowing for a tumour diagnosis aided by membrane polarity sensing (172, 173, 174, 175, 176).

Using giant unilamellar vesicles (GUVs) as well as live and fixed cells, the ability to recover the membrane order in ratiometric PAINT microscopy consistent with established publications and diffraction-limited TIRF-microscopy was validated first (Fig. 4.11) (193, 194, 185). Here, the orderedness of membranes was recorded as a generalised polarisation (GP), where GP-values can range from -1 to 1 and represent the polarity of a membrane with lower values corresponding to disordered membranes and higher values corresponding to ordered membranes (See Eq. 2.6). For GUVs the general charactersistic of higher GP-values in ordered membranes (DPPC/cholesterol) compared to disordered membranes (DOPC) was confirmed (DOPC (TIRF): -0.05 vs DOPC (PAINT): 0.11; DPPC/cholesterol (TIRF): 0.43 vs DPPC/cholesterol (PAINT):

0.45) (Fig. 4.11). Notably, all PAINT data showed a higher modal GP value compared to GP values acquired in TIRF. This is expected as during the fitting of single emitters the high intensity background from freely diffusing dye is separated from the specific single emitter emission. Cellular membranes of COS-7 and RAMA27 cells similarly showed a higher modal GP-value for PAINT data compared to TIRF data (fixed cell (TIRF): -0.03 vs fixed cell (PAINT): 0.04; live cell (TIRF): 0.18 vs live cell (PAINT): 0.21). For cellular membranes, the PAINT acquisition was performed on the plasma-membrane facing the solvent using highly inclined and laminated optical sheet (HILO) illumination, while the coverslip-facing membrane was used for TIRF microscopy (Fig. 4.11). Still, using ratiometric PAINT, the membrane specific spatial polarity of biological membranes was successfully determined.

Having shown the capability to consistently and robustly resolve the differences in GP for membranes with varying lipid order in ratiometric PAINT, the presence of immobile nanoscale domains was explored next on rat mammary fibroblast cell 27 (RAMA27) (Fig. 4.12). Here, the localisations were binned (35×35 nm^2) to have an average of 2.5 localisations per bin, reducing the effect of outliers while maintaining a higher spatial resolution compared to TIRF.

In a first cluster analysis, Voronoi tessellation was used. Voronoi tessellation is a mathematical method of dividing the image plane into tiles. Each tile is defined by a localisation of the PAINT acquisition, where a tile corresponds to all the places closer to one particular localisation than to any other localisation. Based on this initial Voronoi diagram, neighbouring tiles could be combined into a super-tessellate if two neighboring tiles were within a threshold value (T). In this super-tessellation analysis the outline

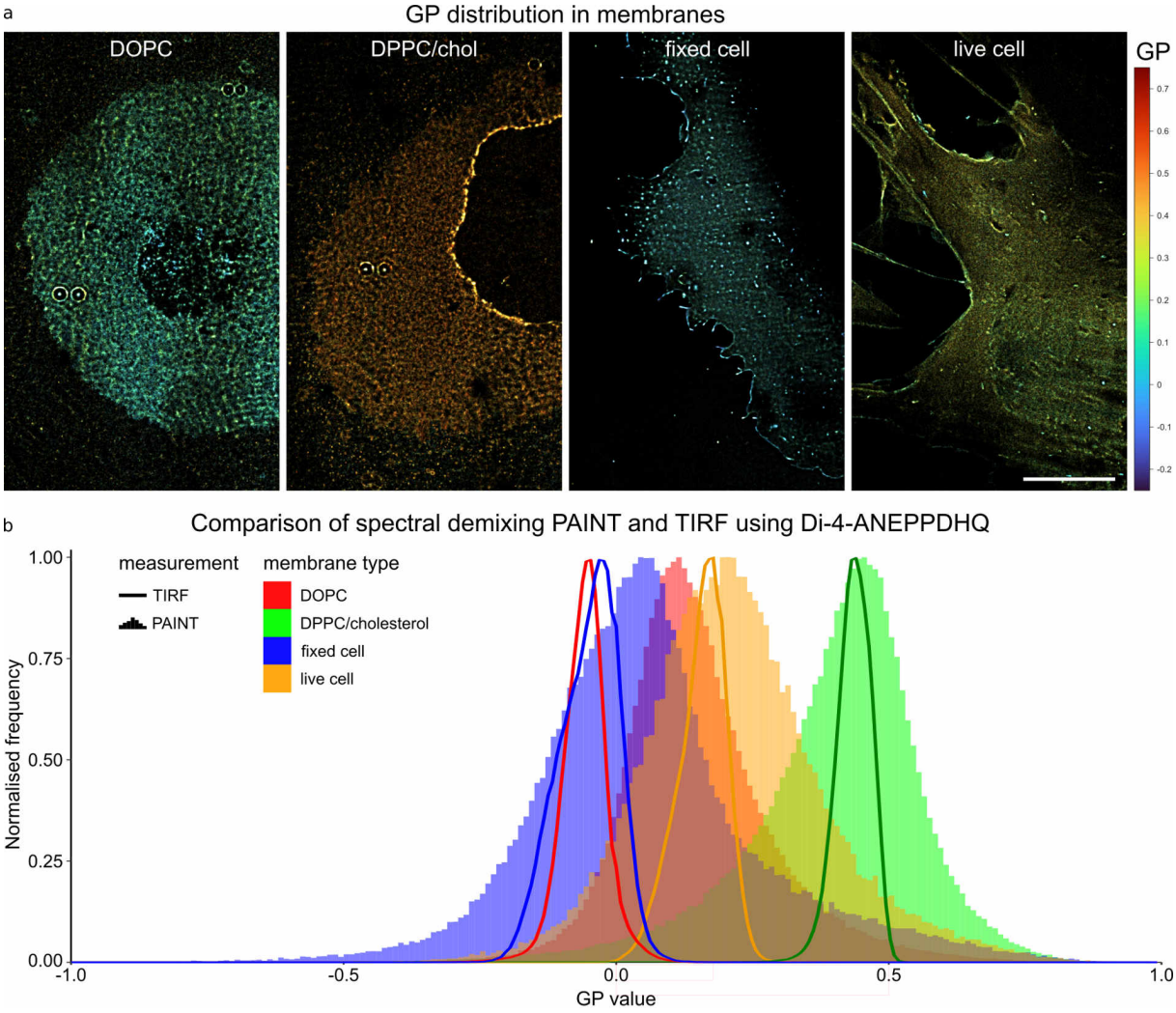

Fig. 4.11: ratiometric membrane PAINT. a) Representative GP-dSTORM reconstruction of a DOPC GUV membrane patch, DPPC/Cholesterol GUV membrane patch, fixed cell and live cell data. GP values colour coded according using Turbo-look-up table (LUT). b) Histogram of the calculated GP values using 50 nm binning of localisations for all membranes. (raw data distribution in Fig. SI 12). DOPC: n=4, DPPC/cholesterol: n=4, live cell: n=4, fixed cell: n=11. Representative live cell image from RAMA27. Representative fixed cell image from COS-7 cells. Scale bar: a) 10 µm. Modified from submitted work (L. Panconi, and J. Euchner *et al.*).

of all individual tiles is preserved (Fig. 4.12) (185). Voronoi super-tessellation was run multiple times with varying starting seeds, but generally yielded highly similar super-tessellates. Next, to investigate if the found clusters are statistically significant, datasets with randomly resampled GP values were generated (GP and intensity information from a Voronoi tessellate within 10×10 µm^2). In Fig. 4.12 a, various super-tessellates of higher and lower membrane polarity can be found in the experimental data, not present in randomised datasets. However, these regions are at or above the diffraction limit

and could therefore be detected in a non-PAINT acquisition. Therefore, the presence of sub-diffraction limited nanodomains was investigated next. Here, the area distribution of super-tessellates was compared to the randomised dataset. For super-tessellates below the size of a single diffraction-limited pixel (111×111 nm^2), a small but significant increase of nanodomains is observed (Fig. 4.12 c). Here, observing a linear relationship in the plot would suggest that the two datasets have similar probability distributions. Conversely, any deviation from this line highlights the dissimilarities between the distributions. However, while the presence of nanoscale domains can be implied from the Q-Q-plot, the only slightly lower prevalence of similarly sized nanodomains in randomised data makes the robust detection of true nanodomains challenging.

Therefore, in collaboration with the Owen group from the University of Birmingham, a topological data analysis technique was established to improve the sensitivity and specificity of nanodomain detection. Here, Luca Panconi developed a clustering algorithm generating convex hulls of regions with persistent homologies, coined Justification of

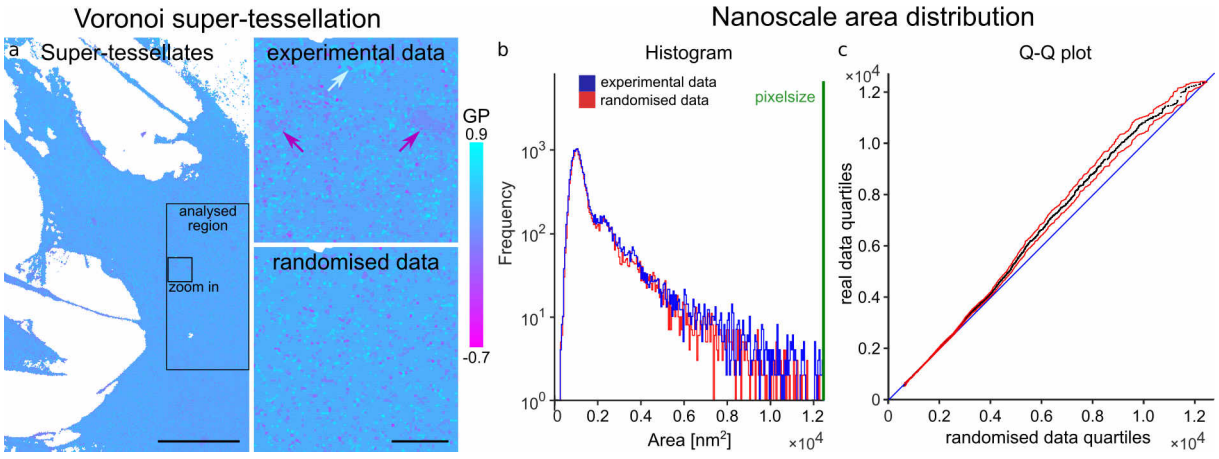

Fig. 4.12: Voronoi super-tessellation analysis of ratiometric membrane PAINT. a) Representative Voronoi cluster of GP values generated for live cell membrane. Voronoi cluster analysis and subsequent merging of Voronoi tiles with similar GP (1 standard deviation) resulted in Voronoi super-tessellation map. Zoom in of experimental data and control Voronoi super-tessellates with randomised GP-values. Arrows indicate membrane patches above the diffraction limit with GP distributions deviating from the global mean (purple for lower GP, pale blue for higher GP). b, c) Nanoscale area distribution (<110×110 nm^2) in experimental data shows a higher than expected clustering of similar GPs compared to randomised data. a) 413k localisation detected in 10×20 µm^2 patch and binned to 35×35nm^2. c) Q-Q-plot: mean ± 95% CI. 10.000 frames acquired at 50 ms per frame. 8.7% of tessellates consists of single emitter. Scale bar: a) 10 µm, zoom in) 500 nm.

separation by employed persistent homology (JOSEPH). JOSEPH was implemented into a larger software workflow coined point label analysis of super-resolved membrane attributes (PLASMA)[3]. Using this analysis, 61% of 3×3 µm^2 regions showed the presence of non-random homogeneities in RAMA27 cells, compared to only 5% and 4% of 3×3 µm^2 regions in DOPC and DPPC/cholesterol GUVs, respectively (Fig. 4.13). Using JOSEPH an average deviation from the global mean of ±0.24 GP was detected with high order nanodomains being roughly twice as prevalent as low order domains (Fig. 4.13 d). However, due to the high variability of GP values, the minimum area to detect nanodomains robustly was limited to 0.03 µm^2 with the average nanodomain being 0.15 µm^2 in size. Further studies need to show, if the sampling frequency can be further improved or the spread of GP values can be reduced during ratiometric PAINT acquisition, allowing for the robust detection of even smaller nanodomains.

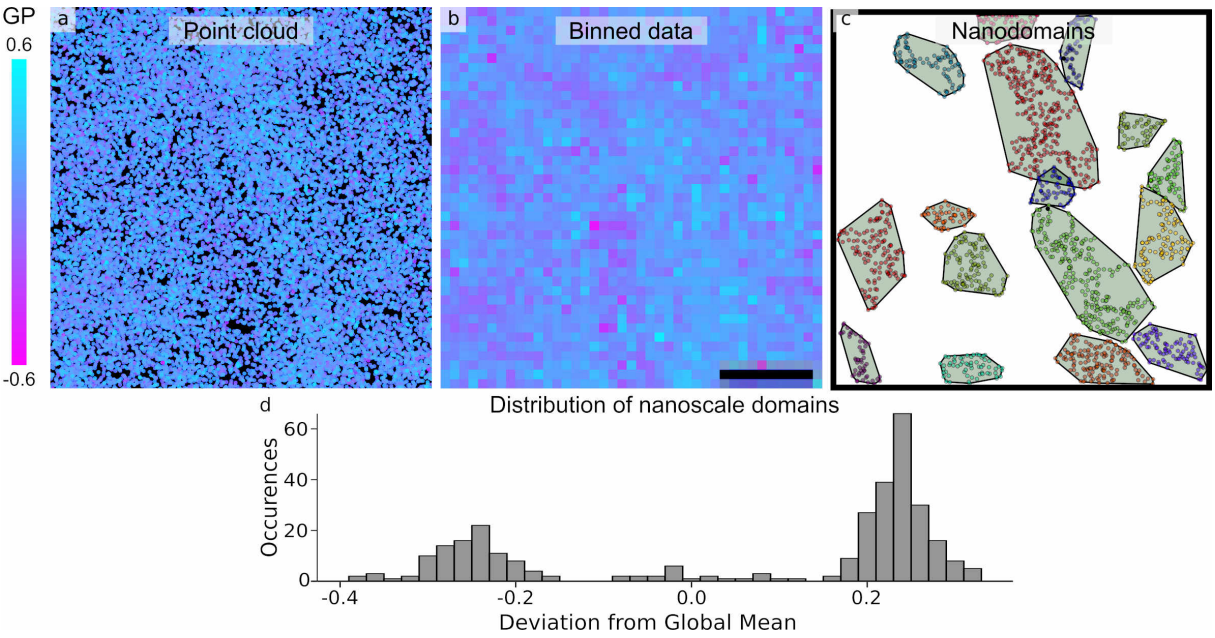

Fig. 4.13: PLASMA cluster analysis of ratiometric membrane PAINT a-c) Exemplary 3×3 µm^2 patch of live cell data (316 ROI analysed), showing a) point cloud data, b) binned data, and c) nanodomains found in JOSEPH analysis. d) $\frac{2}{3}$ of all clusters have a domain order ∼0.24 GP above the global mean. $\frac{1}{3}$ of all clusters have a domain order ∼0.24 GP below the global mean. c) 90% of all nanodomains were between 0.03 µm^2 and 0.29 µm^2, corresponding to circular domains of 100 to 300 nm. JOSEPH analysis by Dan Nieves and Luca Panconi, code by Luca Panconi. Modified from submitted work (L. Panconi, and J. Euchner *et al.*). Scale bar: b) 500 nm.

[3] `https://github.com/lucapanconi/PLASMA`, as of 07/01/2024

In summary, it has been successfully demonstrated that the solvatochromic probe di-4-ANEPPDHQ can be used in ratiometric PAINT acquisitions to recover the nanoscale membrane polarity. By utilising advanced topological cluster analyses, the nanoscale spatial arrangement of structured lipid domains in cell membranes can be successfully delineated. While further validations need to be performed, the established technique provides a further insight into the presence of temporally stable and distinct ordered membrane domains separate from disordered regions on a nanoscale level (195).

4.3 Discussion

Within this chapter, microtubules were used as a validation target followed by the investigation of the distribution of GP1bα in platelets for a clinically relevant mutation (G138V). Next, the heterogeneous response of platelets to S100A8/A9 stimuli was investigated. Then, novel imaging techniques were established, including a colocalisation based approach to determine the DOL and a ratiometric PAINT imaging approach with topological cluster analysis to study the cellular nanoscale membrane order.

dSTORM performance

For the evaluated dSTORM performance, all analysed parameters were in line with reported characteristics of modern dSTORM setups (149, 86). Using COMET, an expected residual drift error of 6.4 nm was calculated. In Chap. 3, total localisation error from non-fitting origin, was estimated to be 4.8 nm (Fig. 3.22), significantly below the determined residual drift error. The larger residual drift error might be an effect of the high irradiance under dSTORM conditions, leading to increased thermal movement. In the vibration measurements to estimate the total error, a 10 fold lower irradiance was used. Alternatively, the found residual drift error is within the noise floor of the drift estimation software and not necessarily corresponds to the true residual drift error. Therefore, while the residual drift error cannot be determine from the data, it can be expected to be $<$6.4 nm.

While the total localisation error from non-fitting origin of Chap. 3 and the drift error determined in COMET are non-orthogonal to each other, a total error estimation for dSTORM using Gaussian propagation of uncertainty was still used to give an upper limit

of the error. Hence, the true localisation error σ_{total} from non-fitting origin is expected to be between 4.8 and 8.0 nm. Given a fit-based localisation precision (σ_{fit}) of 4.8 nm, combined with the σ_{total} of 4.8-8.0 nm (Fig. 3.22, 4.4), results in a theoretical expected FWHM resolution of 16-22 nm.

The FRC resolution for microtubules using indirect immunolabelling of 29-35 nm is higher than the upper limit of the theoretical FWHM resolution. While FWHM and FRC resolution often are similar for protein-tag labelling in dSTORM, indirect immunolabelling of microtubules is known to lead to an increased FRC resolution estimation (NUP96-SNAP-AF647: 13 nm, microtubule-immunofluorescence-AF647: 23 nm, at 2.5 nm localisation precision and 6.4 kW/cm^2 each - Diekmann *et al.*, Extended Data Fig. 9). A combination of multiple labels within the localisation precision, polarised emission of labelled antibodies, and energy transfers between emitters in close proximity ($<$10 nm) could be attributed to this reduced FRC resolution in immunolabelled samples with a dye to antibody ratio $>$1 (68, 69, 70). The resolution estimation was further validated using the decorrelation analysis established by Descloux *et al.* with similar results (Fig. SI 10) (196). Similarly, using the fit of a tubular intensity profile for microtubules (Fig. 4.4), the width between the half maximum and peak was used to estimate the full width at half maximum (FWHM). Here, a FWHM resolution estimation of 25$\pm$1 nm was found.

As the performance of the setup has been shown to yield good results, the setup was routinely used to study samples of biomedical relevance where sub-diffraction limited structures were expected to have an implication on the cellular function (Fig. 4.6). Here, analysing the nanoscale receptor cluster distributions and the heterogeneous response

of platelets to S100A8/A9 highlights the potential SMLM has to investigate clinically relevant samples (Fig. 4.7).

Quantitative microscopy

Using the ProDOL probe and analysis workflow to determine the DOL, a good agreement with previously established DOL calibration techniques was found. As the NPC and the ProDOL probe are localised at different compartments, this work therefore provides a first insight that the labelling efficiency for cytosolically accessible labels can be considered comparable under certain constrains. The NPC is a high density multimeric structure at the nuclear membrane with labels both at the outwards and inwards facing nuclear envelope. Contrary, the ProDOL probe is a sparsely distributed monomeric fusion protein at the plasma membrane. However, the validity of measuring the DOL at the plasma membrane and assuming a comparable DOL at compartments such as lysosomes, mitochondria or other cellular organelles has not been validated. Locally different concentration of fluorophores is a known phenomenon for rhodamines which accumulate at mitochondria, leading to an increased local concentration and therefore potentially leading to a higher DOL at low labelling concentration (197).

Ratiometric membrane PAINT

Lastly, within this work novel approaches to measure the nanoscale distribution of membrane order have been established using di-4-ANEPPDHQ. Though, this only serves as a proof of concept. The temporal resolution was low, as data from 4 min is analysed during cluster analysis. This limits the detection to patterns temporally stable at the nanoscale. Methods to stabilise the membrane architecture by paraformaldehyde (PFA)

and glutaraldehyde (GA) fixation proofed non-successful, as the GP was significantly altered during fixation, making all subsequent analysis error prone to fixation artefacts.

To increase the temporal resolution, the localisation data was split into 2 temporal bins. This gave first indications of a spatially and temporally consistent GP distribution. However, as the size of detected nanodomains already exceeded 0.15µm^2 for the full dataset, temporal subsetting of data was mitigated until either the sampling density could be further improved or the GP-distribution was reduced. Additionally, morphological changes started to be detectable for exposure times $>$5 min induced by phototoxic effects. The presence of nanoscale phototoxic effects within the acquisition time of 4 min needs to be evaluated in future experiments. Generally, at an experimental sampling density of 22 nm/emitter the theoretical resolution is limited to approximately 50 nm. Therefore, a balance between temporal and spatial resolution needs to be found.

Still, given these limitations it was successfully shown that ratiometric PAINT of di-4-ANEPPDHQ can determine the presence of 0.03 µm^2 - 0.29 µm^2 nanodomains which are close to or below the diffraction limit and are spatially stable over a duration of 4 min. The presence of clusters below 0.01 µm^2 is indicated by the Voronoi super-tessellation analysis, though further studies need to be performed to validate these findings.

Future directions

This microscope found routine use in a plethora of SMLM imaging experiments of biomedical relevance and has been successfully implemented for the development of novel imaging techniques. As the system is well calibrated far beyond the scope of most systems (pixelwise camera correction, illumination characterisation), it is ideally suited for the development of novel image processing and image correction techniques

with a current focus on a Bayesian illumination correction approach in collaboration with the Pressé lab (unpublished work) (198, 199). Currently, projects to study GPVI, S100A8/A9 and T cell microclusters are being performed with preliminary data already acquired and used for grant applications. Therefore, this system will be crucial for future experimental work.

Furthermore, within this work the ProDOL technique to determine the labelling efficiency for SNAP-tag and HaloTag has been successfully established and validated. The method can next be expanded to other peptide and protein-tags such as CLIP, TMP-tag or HA-tag (200, 201, 202). Moreover, the ProDOL approach can find application beyond protein-tag DOL analysis. Here, determining the DOL in direct and indirect immunolabelling can be established. Though, additional challenges arise, as the relation of fluorescent signal to POI is further convoluted by the distribution of fluorophore per antibody and in the case of indirect immunolabelling the distribution of secondary antibody per primary antibody. Still, determining the fraction of labelled POI could can find an application in determining the specificity and sensitivity of different antibody constructs and antibody-drug conjugates.

Finally, the established cluster analysis techniques to analyse ratiometric PAINT data, can be easily adapted for other solvatochromic dyes already used in super-resolution microscopy such as Nile red derivatives (184) or expanded to other properties linked to the photophysical properties of single emitters, such as fluorescent lifetime or dipole orientation (203, 204). Ultimately, while the established analysis pipelines have only been shown to work in a proof of concept, they should be capable to analyse arbitrary marked point patterns and recover the underlying structural cluster information.

Chapter 5

Quantitative 3D super-resolution CLEM

This work is currently in preparation for submission and publication:

J. Euchner*, K. Yserentant*, D. Patten, S.A. Tashev, L. Korn, F. Hild, J. Hummert, L. Meesmaecker, R. Curticean, I. Wacker, S. Shetty, R. Schröder, D-P. Herten, 2023, in preparation, *"Novel embedding strategies for quantitative preservation of fluorophores in 3D super-resolution correlative light-electron microscopy"*

Author contributions:
J.E., and K.Y. performed all data analysis. J.E., K.Y., S.A.T., and L.K. acquired the data. J.E. performed dSTORM and SEM imaging, molecular fluorophore preservation validation and cellular application. K.Y., L.K., J.E., and L.M. performed ensemble resin screening. S.A.T. assisted in molecular preservation validation. F.H., J.H. assisted in programming. R.C. assisted in SEM sample preparation and SEM imaging. D.P. and S.S. provided access to clinical samples of liver sinusoidal endothelial cell (LSEC) and resources for LSEC work. D-P.H. performed conceptualisation, supervision, resource management, and project administration. I.W., S.S., and R.S. contributed general ideas and concepts. K.Y., R.S., and D-P.H. conceived the method. J.E., K.Y., I.W., S.S., R.S., and D-P.H. wrote the manuscript with input from all authors.

5.1 Introduction

5.1.1 Correlative array tomography

As previously described in Sec. 1.4, various implementations for correlative light-electron microscopy (CLEM) exist. In recent years, CLEM has undergone a quiet revolution with demand increasing drastically as correlative ultrastructural and functional information is needed to further advance our understanding of cellular structural biology (2, 1). The information obtainable in volumetric EM is mostly limited to ultrastructural information and light-microscopy mostly resolves the distribution of a limited number of protein of interest (POI). One workflow established for correlative light-electron microscopy utilises array tomography with chemical fixation and resin embedding (Fig. 5.1). Here, in a first step, the sample is chemically fixed, followed by labelling for fluorescence microscopy and constrasting with OsO_4 and neodymium acetate for electron microscopy (Fig. 5.1 a). In the next step, the sample is dehydrated, embedded in resin and polymerised (Fig. 5.1 b). Subsequently, the polymerised resin is prepared for sectioning (Fig. 5.1 c). Using an ultramicrotome, the sample of interest is sectioned into serial ultrathin sections of 50-200 nm (Fig. 5.1 d). The sections are collected on a transparent but electrically conductive substrate, typically indium-tin-oxide (ITO), before being imaged in both fluorescence and electron microscopy (Fig. 5.1 e). Acquired imaging modalities are then reconstructed to the volumetric image (Fig. 5.1 f). Array tomography benefits from a significantly improved z-axis resolution by means of physical separation of the axial profile, improved fluorescence signal from the lack of depth-dependent aberrations and lack of premature bleaching (111). Contrary to other CLEM implementations, volu-

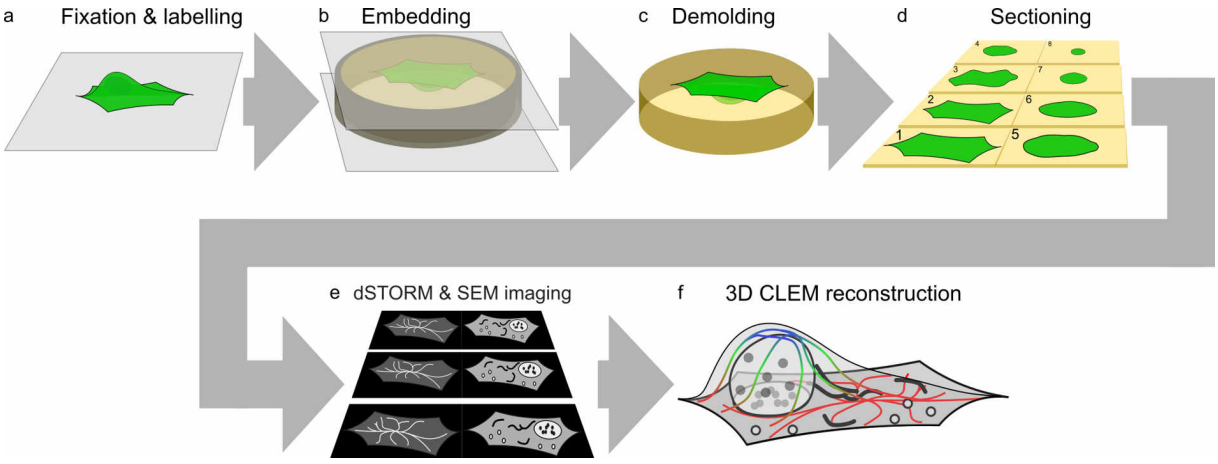

Fig. 5.1: Workflow of *in-resin* CLEM using array tomography. a) Samples are fixated and labelled with fluorescent labels and contrasted with $NdAc_3$ and OsO_4. b) Samples are next dehydrated and embedded in resin. c) Samples are demolded and trimmed to the region of interest. d) Using an ultramicrotome, the samples are serially sectioned into ribbons with 50-200 nm section height. e) Serial sections are acquired in dSTORM light-microscopy followed by *on section* post-staining and SEM imaging. f) Consecutive sections are registered and the volumetric image is reconstruced.

metric imaging in array tomography is sample preserving and allows for easier handling compared to cryogenic samples. On the other hand, FIB-SEM allows for a further improved z-resolution and cryo-CLEM benefits from improved structural preservation from vitrification of samples (106, 205).

5.1.2 Liver sinusoidal endothelial cell (LSEC)

The liver is responsible for a variety of different functions, including the elimination and metabolic conversion of small molecules, macronutrient metabolism, and nutrient storage (206, 207). Up to 70% of the blood supply originates from the portal vein of the intestines, allowing the liver to filter, clear and metabolise the absorbed molecules of the digestive system (208). As the hepatocytes need to have a high metabolic conversion, especially for toxins and have a direct connection to the gut with potential contact to pathogens, a tight immunological control is important. Here, LSEC are responsible for facilitating the immune response as they line the sinusoids, separating the hepatocytes from the blood. When hepatocytes become senescent, they release

the senescence-associated secretory phenotype (SASP) into their microenvironment (Fig. 5.2 1) (118). LSEC respond to SASP priming by upregulation of the NFκB signalling pathway, increased expression of the adhesion molecules such as ICAM1, remodelling of the microtubule cytoskeleton, and release of chemokines to facilitate an immune response (Fig. 5.2 2) (118, 209). Immune cells are able to then increase the surveillance of the local hepatic volume to respond to early stage cancerous cells, virally infected cells or other cellular damage arrests (210). Through the increased expression of adhesion molecules on LSEC, immune cells can pass between (paramigration) as well as through (transmigration) LSEC (Fig. 5.2 3). Within the hepatic lumen, the immune cells can then mediate the immune response to eliminate senescent cells (Fig. 5.2 4). Yet, SASP has also been shown to promote the progression of tumorigenesis (211, 118, 212, 213). With an estimated 1 million annual cases of hepatocellular cancer by 2025, understanding the role LSEC have on the immune migration and progression of hepatocellular carcinoma is crucial (214).

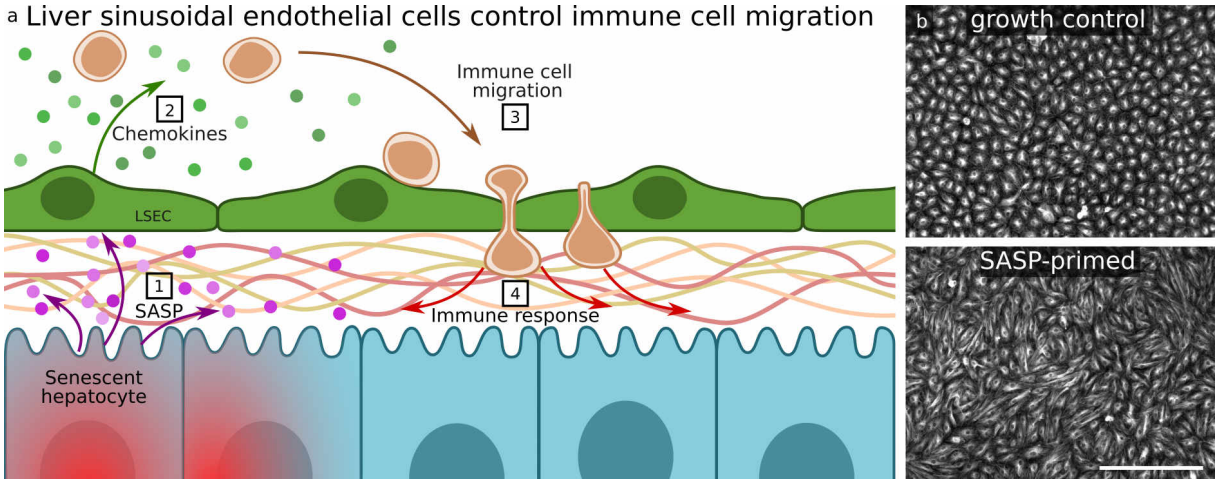

Fig. 5.2: LSEC control the immune response. a) Schematic of SASP induced immune response. 1) Senescent cells release a SASP containing a mix of signalling factor, including interleukins, chemokines, growth factors, proteins and extracellular matrix components (212). 2) LSEC sense the presence of these factors and activate a transcriptional profile leading to immune cell recruitment through release of chemokines. 3) Chemokines in combination with increased expression of adhesion molecules such as ICAM1 facilitate the transmigration and paramigration of immune cells into the hepatic volume. 4) Immune cells have a tumour suppressive role by eliminating and aiding in the removal of senescent cells. b) Changes of the cellular morphology and microtubule cytoskeleton of LSEC in growth control or in presence of SASP. Scale bar: 300 µm.

5.1.3 Serial ultrathin sectioning

A crucial step in array tomography is the serial ultrathin sectioning of resin embedded samples. Here, samples are cut using a diamond knife with a chosen section height in a range from 50-200 nm. In general, due to the section height being only in the tens of nanometre range, a focus on vibration isolation is important as even nanometre-scale vibration can lead to section defects (Fig. SI 15 a). In a first step, the resin sample is trimmed to the region of interest, adhesive is applied to the sides next to the region of interest and the surface is aligned to the diamond knife (Fig. 5.3 a). The surface of the resin and the diamond knife need to be fine-aligned along the spatial axes as well as the three rotational axes. The parallel alignment of both surfaces is crucial, such that the full surface is cut within the first few sections. This is achieved by aligning the sample with $<0.05°$ rotational accuracy. After successful alignment, the serial sections are generated (Fig. 5.3 b). Serial sections are automatically transferred from the knife edge to a water bath. The surface tension allows the sections to float on the water, while causing minimal shear forces. Next, the ribbon is iteratively split to continue collection of serial sections (Fig. 5.3 c). After completion of sectioning, the substrate on which the serial sections are deposited needs to be aligned with the sections floating on the water surface (Fig. 5.3 d). Sections are then grouped by micromanipulating the surface tension of water (Fig. 5.3 e). In a next step, the section raft is continuously manipulated to maintain its position over the substrate, while the water is slowly removed from the water tray (Fig. 5.3 f). Finally, samples are dried on the substrate before being inspected for insufficient adhesion and other artefacts (Fig. 5.3 g,h). The ultrathin sections are now ready for imaging in dSTORM and SEM microscopy.

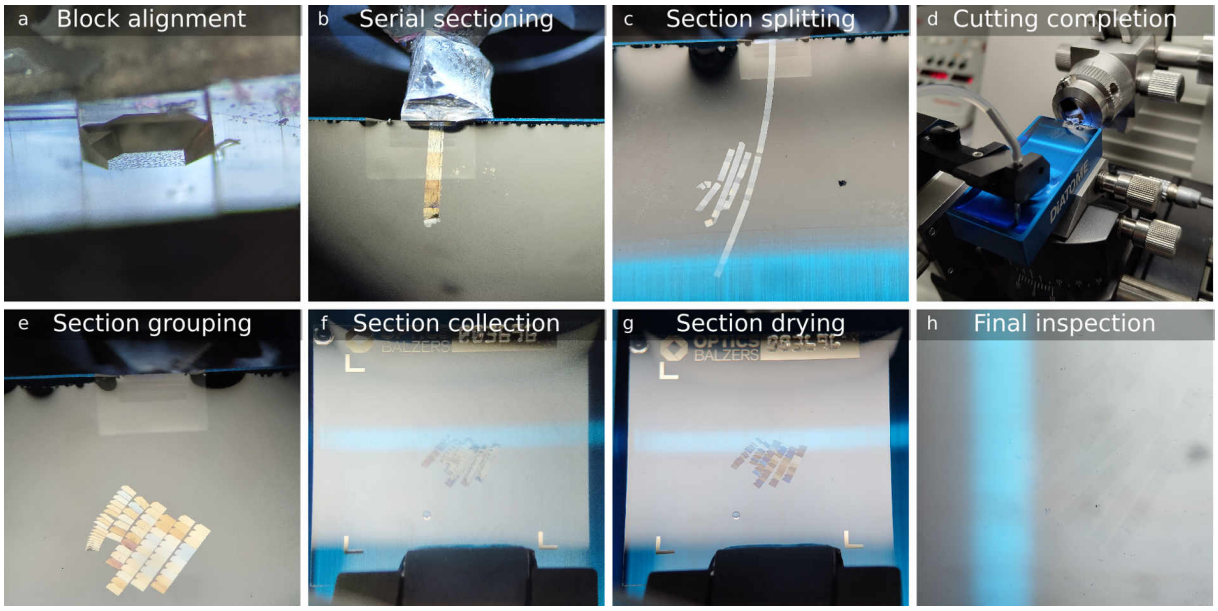

Fig. 5.3: Principle of serial ultrathin sectioning. a) Resin blocks are pre-trimmed to the region of interest with a square surface profile. The block is then aligned to the diamond knife with $<0.05°$ rotational accuracy and high spatial precision. b) Serial sections are acquired in straight ribbons. c) ribbons are regularly split to collect up to several 10^2 serial sections. d) The substrate on which the serial sections are deposited is aligned to the sections. e) Sections are grouped by micromanipulation. f) Sections are collected on the substrate. g) Sections are dryed on the substrate while minimising shear forces. h) Sections are inspected for adhesion artefacts.

5.1.4 Aims

In this chapter, the development of novel resin composition for quantitative preservation of organic fluorophores is explored. The novel resin compositions are then validated on a molecular basis using quantitative microscopy of selected fluorophores. Next, the compatibility with serial ultrathin sectioning as well as dSTORM and SEM imaging is established. This is complemented by an assessment of dSTORM's performance, particularly noting the advantages of lack of out-of-focus blinking and avoidance of premature bleaching. The chapter concludes with the application of the *in-resin* CLEM workflow in examining the reaction of liver sinusoidal endothelial cells (LSECs) to a senescence-associated secretory phenotype (SASP). This approach enables the nanoscale reconstruction of the cellular ultrastructure in relation to the functional microtubule cytoskeleton, revealing intricate details of cellular organisation that are crucial for identifying underlying cellular response mechanisms.

5.2 Results

5.2.1 Resin screening

5.2.1.1 Polymerisation

To improve the preservation of organic fluorophores during resin polymerisation used for electron microscopy, sterically hindered photoinitiators in combination with established LR White methacrylate resin components were investigated. Here, two classes were investigated for being established initiators of methacrylate polymerisation, namely Norrish type I ultraviolet (UV) photoinitiators benzoin methyl ether (BME) and its derivate 2,2-dimethoxy-2-phenylacetophenone (DMPA) (Fig. 5.4 a - blue), as well as Norrish type II UV photoinitiators benzophenone (BP) and the structurally related thioxanthone (TX) in combination with 4,N,N-trimethylaniline (TMA) to enable the initiation through an electron transfer mechanism (Fig. 5.4 - purple) (215, 216). All reaction schemes were optimised towards a slow rate of polymerization for their respective polymerisation type to increase the chain length and reduce polymerisation induced distortions (215, 217).

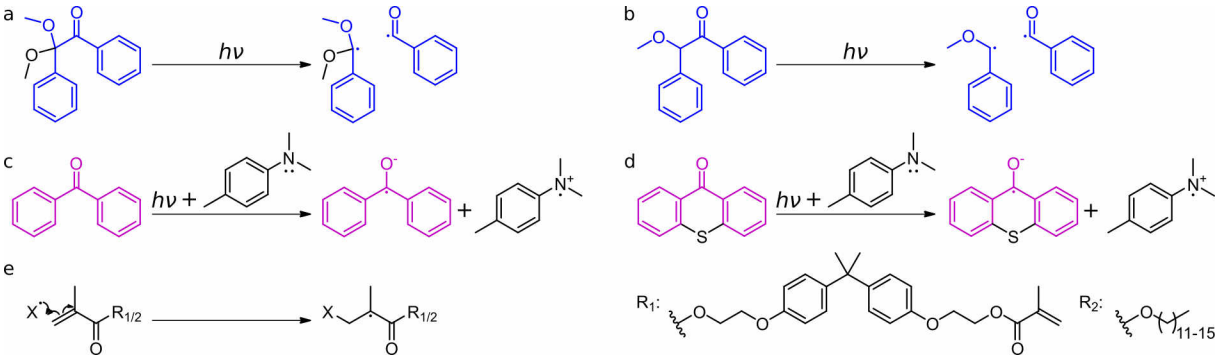

Fig. 5.4: Reaction mechanism of polymerisation initiation of Norrish type I/II photoinitiators. a, b) Norrish type I photoinitiation of BME (a) and DMPA (b) (blue represents structure motive). c, d) Norrish type II photoinitiation of BP (c) and TX (d) using TMA as accelerator (purple represents structure motive). e) Reaction of radical initiator (X°) with methacrylate components in LR White resin to start the polymerisation reaction.

Traditionally, LR White is polymerised using thermal curing at 60 °C for 24 h using benzoyl peroxide. Here, nearly all fluorescence in the resin is lost (Fig. 5.5 a - blue). A cold curing method using only TMA exists, but was found to still result in a reduction of fluorescence after polymerisation (Fig. 5.5 a - green). Contrary, the four established resin compositions utilising BME, BP, DMPA, and TX all lead to an increase in fluorescence intensity for the fluorophore AF647, likely caused by solvatochromic effects (Fig. 5.5 a - red). Notably, while BP and TX both use TMA as accelerator, the altered reaction conditions in a Norrish type II reaction allow for a significantly improved retention of fluorescence intensity. Finally, a non cured control exhibited a low but measurable fluorescence reduction over 24 h, indicating that the liquid resin components react with the chromophore over time if no polymerisation is initiated (Fig. 5.5 a - gray).

Osmium tetroxide (OsO_4) is crucial for generating contrast in electron microscopy, but is known to react with chromophore systems, resulting in a loss of fluorophores (218). Several investigations to preserve fluorophores when exposed to OsO_4 have been performed, but were beyond the scope of this study (219, 38). Therefore, the extent of fluorophore destruction introduced by a low concentration of OsO_4 contrasting was determined using intensity-based comparison of indirectly immunolabelled microtubules (0.1% for 30 min at 4 °C). Here, roughly a 50% reduction for both tag-labelled and immunolabelled AF647 was found (Fig. 5.5 b - orange).

Analysing the ensemble absorption and emission spectra for AF647 showed a strong change in the absorption spectrum after polymerisation (Fig. 5.6 a - shown for DMPA). All resins introduced a wide-band absorption after polymerisation with high variability between repeats (Fig. 5.6 a - shown for DMPA). Contrary, no autofluorescence was

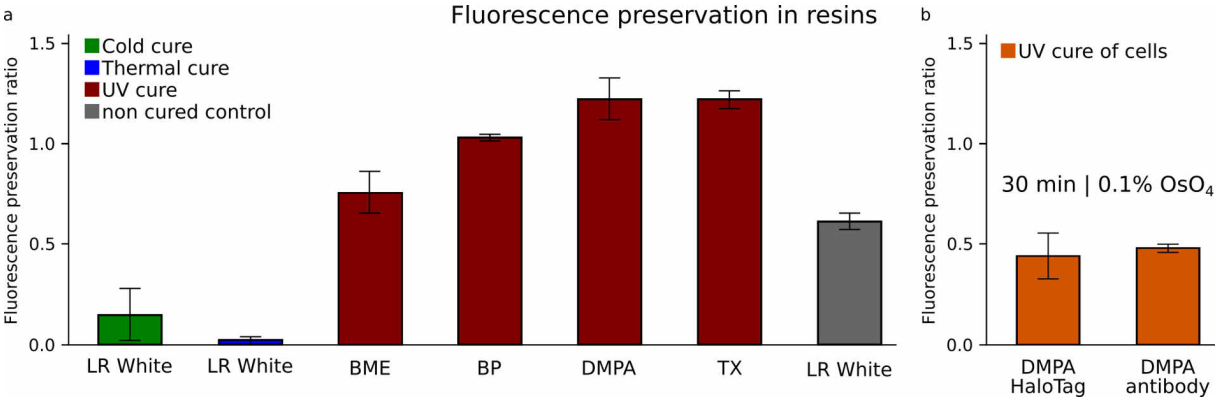

Fig. 5.5: Fluorescence preservation in resin. A high fluorescence preservation ratio is beneficial for CLEM. a) Fluorescence preservation of AF647 in LR White using cold curing (green), thermal curing (blue), no curing (gray) and UV curing with photoinitiators of interest (red). b) Fluorescence preservation of AF647-HaloTagged and AF647-immunolabelled cells after 30 min of 0.1% OsO_4 contrasting. a) Number of analysed cuvettes: n=3-5 per condition, b) number of analysed cells - HaloTag: n=62, antibody: n=32. Barplot represents Mean±standard deviation (SD). a) Reanalysed from data acquired by Lucas Korn during his Lehramt-Staatsexamen internship (220). b) Reanalysed from data acquired by Jonas Euchner during his Master's thesis (49).

detected for all resin compositions, resulting in an emission spectrum originating only from the fluorophore in the polymerised resin (Fig. 5.6 b - shown for DMPA). Finally, AF647 was found to have an altered absorption and emission peak compared to the spectrum in water, due to solvatochromic effects. The absorption spectrum was shifted from 653 nm in water to 659±1 nm pre polymerisation and 660±1 nm post polymerisation. Similarly, the emission was shifted from a maximum of 669 nm in water to 678±1 nm pre polymerisation and 666±1 nm post polymerisation. This change in absorption and emission spectra led to a reduced Stokes-shift from 16 nm in water to 6±2 nm post polymerisation. The increase in fluorescence intensity was stable over the duration of 7 days with a small decrease in fluorescence intensity (Fig. 5.6 b - blue, green).

5.2.1.2 Ensemble fluorescence characteristics

Having found conditions that retain the fluorescence intensity after polymerisation for AF647, combined with beneficial solvatochromic effects, a screening of commercially available and commonly used fluorophores was initiated to investigate the compatibility

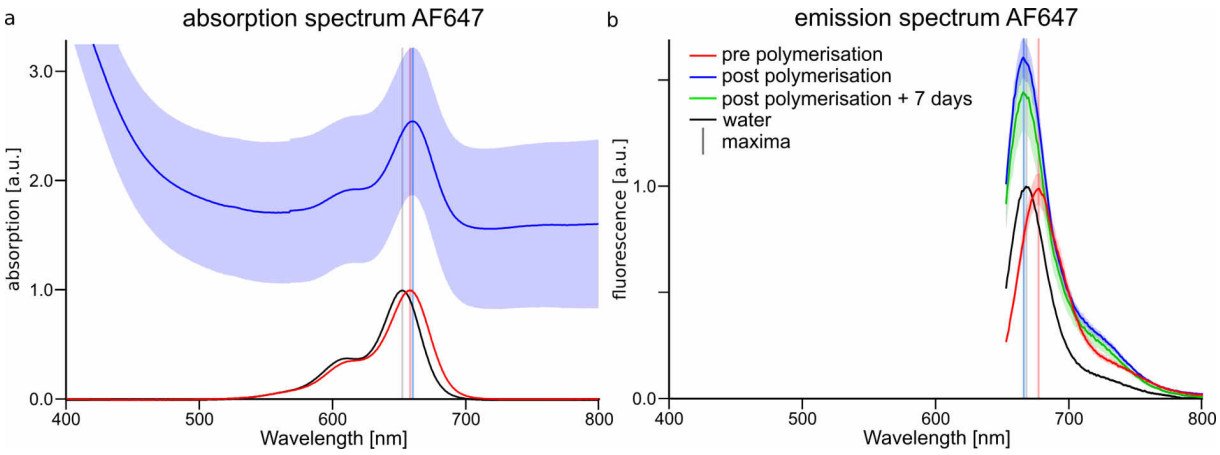

Fig. 5.6: Absorption and emission spectrum of AF647. a) Absorption spectrum of AF647 in water (black), pre polymerisation (red) and post polymerisation (blue). Pre polymerisation the absorption maximum is shifted from 653 nm in water to 659±1 nm pre polymerisation. Post polymerisation a wide-band absoprtion of the resin is observed. b) Emission spectrum of AF647 in water (black), pre polymerisation (red), post polymerisation (blue), and 7 days after post polymerisation (green). Fluorescence intensity of post polymerisation is normalised to pre polymerisation. Vertical lines represent the absorption/emission maxima. Data represents mean±standard error of the mean (SE_{mean}). Reanalysed from data acquired by Lucas Korn during his Lehramt-Staatsexamen internship (220).

with other fluorophores and fluorophore classes, namely xanthene-based, cyanine-based, and oxazine-based fluorophores (Tab. 5.1). TX was found to result in the lowest change of fluorescence intensity upon polymerisation and was highly compatible with all shown fluorophores, though TX was unable to generate a polymerised resin at -30 °C. BP on the other hand, while also being a Norrish type II initiator, did introduce a high fluorescence intensity loss after polymerisation for 5 of the 17 tested fluorophores (AT655, AT680, AT700, MR121, Oxa12) (Tab. 5.1). Similarly, BME and DMPA, as Norrish type I initiators, also had the same 5 fluorophors resulting in a fluorescence retention below 50%. BME and DMPA had a higher average fluorescence intensity in the polymerised resin compared to TX and BP. Similarly to the described reduction of the Stokes-shift for AF647 in Fig. 5.6, the majority of tested fluorophores also experienced a reduction of Stokes-shift (220).

Using the baseline corrected absorption spectra (Tab. 5.2), a change of the brightness of fluorophores was investigated (Fig. 5.7). For all resins, the linear regression of fluores-

cence over absorption revealed a significantly higher fluorescence after polymerisation, normalised to the absorption (BME: 1.19±0.12, BP: 1.13±0.05, DMPA: 1.47±0.08, TX: 1.52±0.05; mean±SE), indicating a higher brightness of the tested fluorophores in the polymerised resin.

Similarly, all resins significantly increased the fluorescence lifetime for AF647 and tetramethylrhodamine (TMR) compared to their respective lifetime in water (Fig. 5.8). For TMR, the fluorescence lifetime increased from 2.38±0.01 ns in water, to 3.15±0.01 ns for TX, 3.17±0.02 ns for BP, 3.46±0.02 ns for DMPA and 3.65±0.02 ns for BME. Notably, for both AF647 and TMR the Norrish type I/II initiators were most similar to each other. While the fluorescence lifetime is affected by many intrinsic and extrinsic factors, the lifetime is most critically affected by the stability of the excited state, indicating a stabilisation of excited state of fluorophores (23).

Tab. 5.1: Ensemble fluorescence preservation in novel resin compositions. 17 commercial fluorophores were screened for the ensemble fluorophore preservation in the established resin compositions (BME, BP, DMPA, TX) at 2 temperatures (21 °C and -30 °C). Mean±SE_{mean}. Reanalysed from data acquired by Lucas Korn during his Lehramt-Staatsexamen internship (220). Alexa Fluor (AF), Abberior Star (AS), cyanine (Cy), oxazine (Oxa), tetramethylrhodamine (TMR).

Dye	Resin condition						
	21 °C				-30 °C		
	BME	BP	DMPA	TX	BME	BP	DMPA
AF488	1.24±0.11	0.34±0.11	1.49±0.09	1.12±0.31	1.40±0.08	0.61±0.07	1.80±0.02
AF532	1.04±0.16	0.89±0.29	1.29±0.12	1.08±0.15	1.44±0.01	(0.81)	1.45±0.24
AF555	1.31±0.09	1.70±0.13	1.56±0.08	1.23±0.17	1.68±0.11	1.10±0.09	1.74±0.06
AF568	1.75±0.40	1.16±0.09	1.26±0.08	1.36±0.07	1.26±0.51	1.06±0.31	1.83±0.01
AF594	1.46±0.17	1.19±0.13	1.71±0.06	0.98±0.11	1.59±0.02	1.30±0.20	1.68±0.28
AF647	0.78±0.11	1.06±0.01	1.25±0.11	1.26±0.09	0.68±0.13	0.78±0.14	1.66±0.21
AS635	1.02±0.20	0.96±0.10	0.96±0.14	0.98±0.13	1.10±0.06	0.64±0.10	1.51±0.19
Atto565	0.95±0.11	0.90±0.21	1.31±0.09	1.34±0.07	1.06±0.11	(0.86)	1.71±0.13
Atto633	1.55±0.19	0.61±0.32	1.56±0.13	1.31±0.04	1.44±0.07	0.80±0.07	1.83±0.04
Atto647N	0.99±0.18	0.55±0.24	1.18±0.01	1.23±0.07	1.10±0.15	0.80±0.05	1.34±0.09
Atto655	0.65±0.10	-	0.46±0.01	0.78±0.12	0.34±0.01	(0.17)	-
Atto680	-	0.20±0.01	0.47±0.02	1.06±0.13	0.60±0.33	-	-
Atto700	-	-	0.42±0.03	0.74±0.08	0.30±0.08	-	-
Cy3b	0.90±0.03	0.96±0.09	1.15±0.13	0.56±0.07	1.02±0.02	0.91±0.10	1.24±0.16
MR121	-	0.32±0.12	0.13±0.06	0.67±0.14	0.43±0.08	-	-
Oxa12	-	0.12±0.06	0.17±0.01	0.96±0.05	0.39±0.04	-	0.15±0.06
TMR	1.59±0.17	1.38±0.28	3.00±0.23	1.80±0.40	1.80±0.05	1.44±0.01	3.28±0.57

Tab. 5.2: Ensemble absorption spectra in novel resin compositions. 17 commercial fluorophores were screened for the ensemble absorption spectrum in the established resin compositions (BME, BP, DMPA, TX) at 2 temperatures (21 °C and -30 °C). Mean±SE_{mean}. Reanalysed from data acquired by Lucas Korn during his Lehramt-Staatsexamen internship (220). Alexa Fluor (AF), Abberior Star (AS), cyanine (Cy), oxazine (Oxa), tetramethylrhodamine (TMR).

Dye	Resin condition						
	21 °C				-30 °C		
	BME	BP	DMPA	TX	BME	BP	DMPA
AF488	-	0.39±0.02	2.39±0.46	-	0.61±0.16	0.83±0.13	(0.52)
AF532	1.36±0.28	-	-	1.54±0.42	0.72±0.12	0.35±0.02	1.12±0.40
AF555	0.26±0.17	-	0.04±0.01	0.67±0.37	0.65±0.07	0.47±0.22	-
AF568	0.78±0.30	1.02±0.11	1.55±0.08	1.05±0.27	1.00±0.22	0.55±0.04	0.80±0.04
AF594	1.35±0.20	1.03±0.14	0.59±0.23	0.57±0.28	1.03±0.09	0.31±0.10	1.18±0.09
AF647	0.74±0.15	0.95±0.08	0.91±0.03	0.73±0.08	0.37±0.06	0.10±0.01	0.95±0.04
AS635	1.60±0.61	0.85±0.03	0.95±0.05	0.77±0.04	0.90±0.10	0.17±0.02	1.01±0.03
Atto565	1.79±0.75	0.81±0.05	1.05±0.01	1.09±0.58	0.74±0.08	0.41±0.24	1.86±0.65
Atto633	1.22±0.17	0.39±0.09	0.87±0.03	0.84±0.07	0.84±0.04	0.06±0.01	0.91±0.08
Atto647N	1.00±0.03	0.75±0.10	0.95±0.03	0.77±0.03	0.83±0.10	0.12±0.03	1.00±0.02
Atto655	0.43±0.11	0.29±0.15	0.12±0.02	0.48±0.01	0.15±0.01	0.05±0.01	0.04±0.01
Atto680	0.44±0.10	0.22±0.02	1.41±0.26	0.51±0.08	0.24±0.04	0.08±0.01	0.02±0.01
Atto700	0.27±0.03	(1.03)	0.52±0.35	0.38±0.15	0.14±0.02	0.08±0.01	0.05±0.02
Cy3b	0.96±0.03	0.96±0.06	1.22±0.35	-	1.00±0.05	0.18±0.04	0.92±0.01
MR121	0.34±0.15	0.29±0.11	-	0.51±0.15	0.14±0.03	0.06±0.01	0.06±0.02
Oxa12	0.29±0.06	0.07±0.01	0.02±0.01	0.44±0.02	0.23±0.01	0.07±0.03	0.02±0.01
TMR	2.20±0.20	1.01±0.16	3.58±0.37	(2.32)	2.41±0.28	0.61±0.12	1.88±0.92

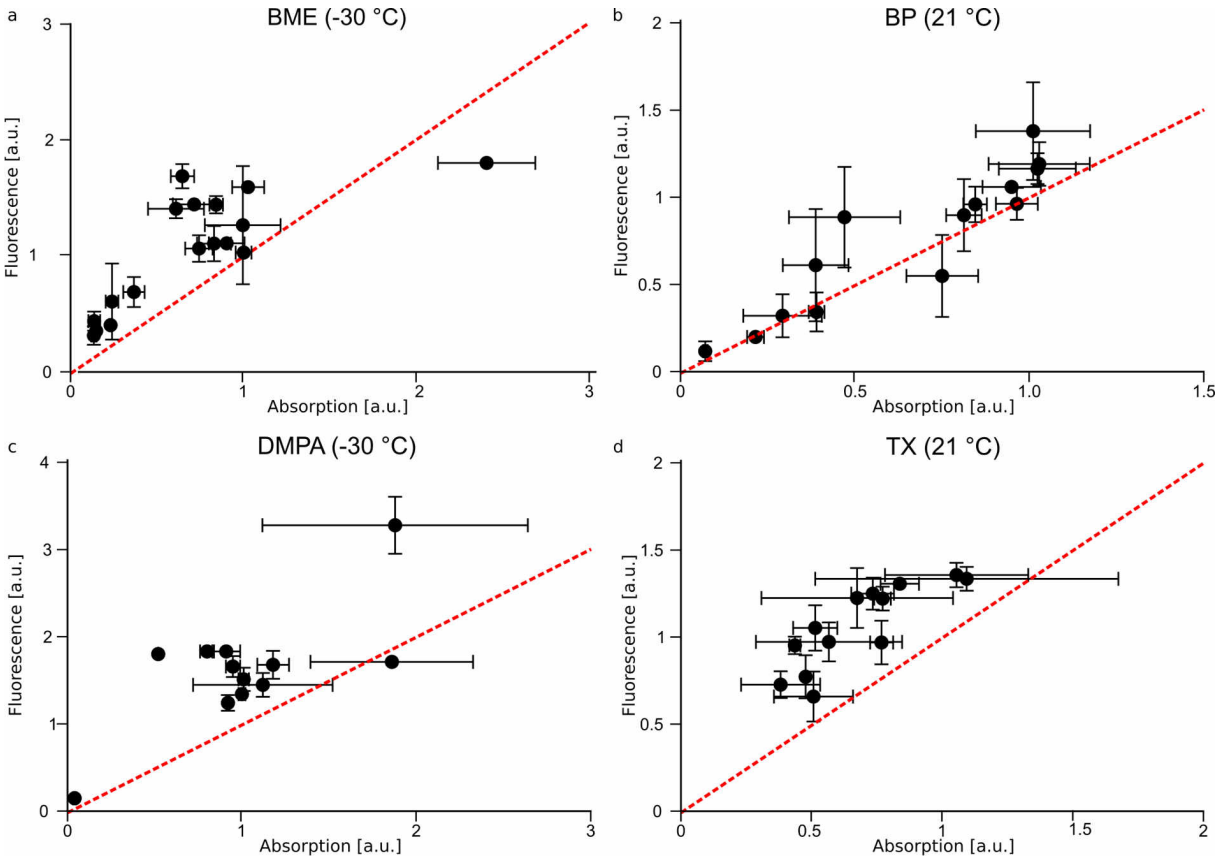

Fig. 5.7: Relationship of fluorescence intensity and absorption. Fluorescence intensity and absorption after polymerisation for BME, BP, DMPA and TX at -30 °C for Norrish type I initiators and 21 °C for Norrish type II initiators. Red line represents equal fluorescence-to-absorption relation compared to pre polymerisation condition. All resins have a significantly increased fluorescence normalised to the absorption. Mean±SE_{mean}. Reanalysed from data acquired by Lucas Korn during his Lehramt-Staatsexamen internship (220).

Subsequent analysis to find trends in the various photophysical properties of the fluorophores were performed to better predict the compatibility of a fluorophore with each resin. Here, e.g. the fluorophore class and emission wavelength were compared to the respective fluorescence preservation or Stokes-shift on a per resin and per initiator class analysis. Unfortunately, due to the multivariate nature of fluorophores, no consistent correlation was found (data not shown). Exemplary, fluorescein and TMR are both xanthene-based fluorophores. Due to the acidic nature of the acrylic resin, fluorescein likely existed in its lactone form, resulting in complete loss of fluorescence, while TMR likely existed in the highly fluorescent quinoid form (Fig. 5.9), explaining the strong increase in fluorescence post polymerisation (Tab. 5.1) (108, 221, 222).

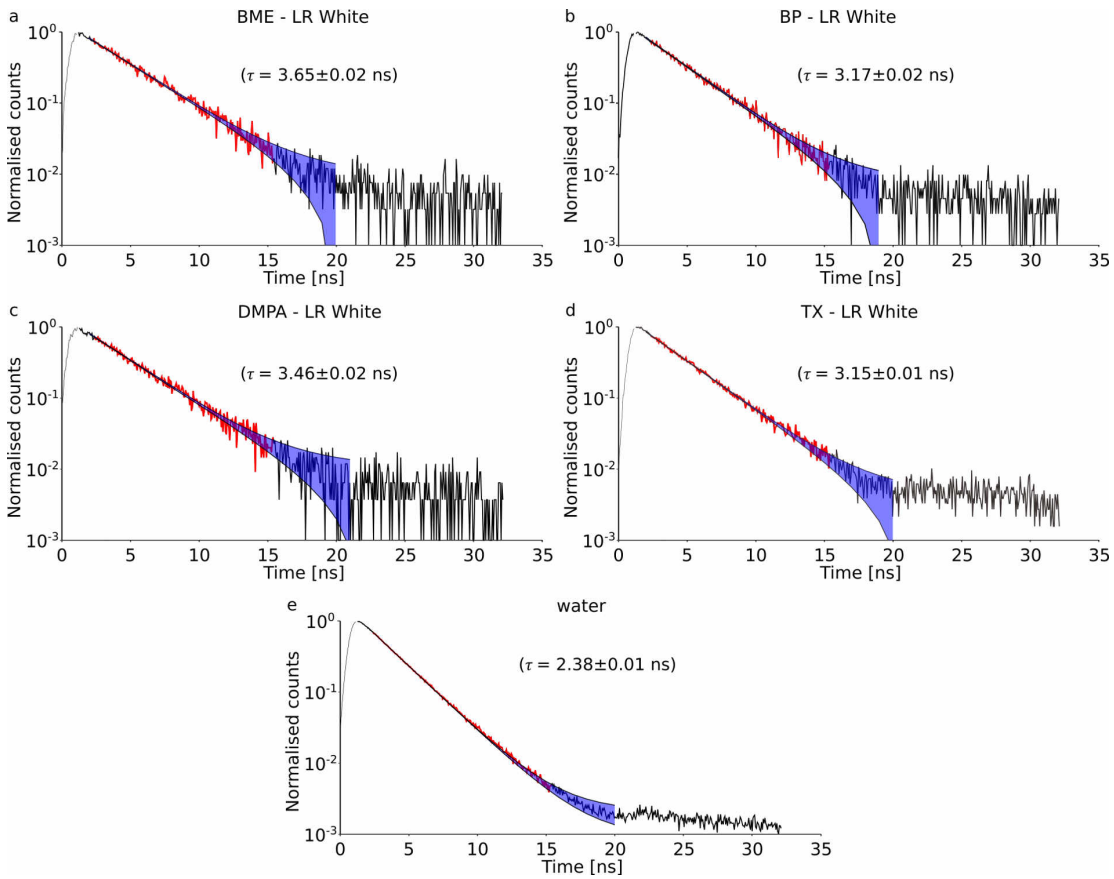

Fig. 5.8: Fluorescence lifetime of TMR. Representative fluorescent lifetime trace of TMR in novel resin compositions. a) BME, b) BP, c) DMPA, d) TX, and e) water. TMR exhibits an increased fluorescence lifetime in polymerised resin with the lifetime being most similar for resins consisting of the same Norrish type initiators (Norrish type I initiator: BME: 3.65±0.02 ns, DMPA: 3.46±0.02 ns; Norrish type II initiator: BP: 3.17±0.02 ns, TX: 3.15±0.01 ns; water: 2.38±0.01 ns). Red line represents analysed region. Blue ribbons represents 95% confidence interval (CI).

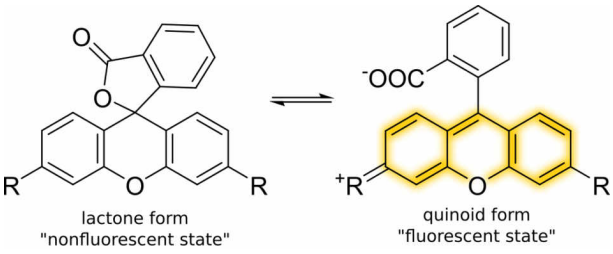

Fig. 5.9: Conformational states of xanthene-based fluorophores. Xanthene-based fluorophores can exist in a lactonised form (non-fluorescent state) being and a quinoid form (fluorescent state). Yellow highlights the chromophore in the excitable state.

5.2.2 Fluorescence microscopy

Overall, novel resin compositions have been developed and validated in ensemble measurements, outperforming the established protocols for LR White both for cold curing and thermal curing. Next, the performance in a cellular environment using array tomography was investigated.

5.2.2.1 Resin sections

To perform array tomography in both fluorescence and electron microscopy, the resin blocks need to be sectioned into ultrathin sections between 50-250 nm. To confirm the compatibility with sectioning, all resins underwent testing in an ultramicrotome (Fig. 5.3). Sections were collected and analysed using a profilometer. Initially, strong height instabilities were detected due to strong vibrations in the room, incompatible with the requirements for ultramicrotomy (Fig. SI 15 a, 3.22). This problem was overcome by moving to a location with reduced vibration profile. Here, for an intended section height of 100 nm, the experimental height of sections was found to be 104$\pm$9 nm (Mean$\pm$SD) with a SE_{mean} of 4 nm (Fig. 5.10). Additionally, the height within a section had a standard deviation of 1.3$\pm$0.2 nm. Frequency analysis confirmed that no individual frequency component was detected in the section height profile (Fig. SI 15).

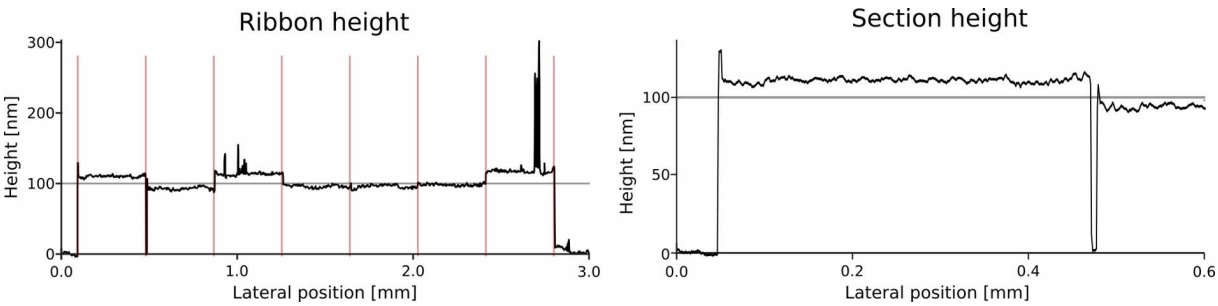

Fig. 5.10: Section height analysis. Representative height profile of a DMPA - LR White resin, sectioned at 100 nm. Sections were found to have a section height of 104±9 nm with an in-section variability of 1.3±0.2 nm. Mean±SD.

Sectioned samples were next validated in fluorescence microscopy. The photophysical properties of most fluorophores in resin blocks were found to be vastly different from their respective properties in aqueous media (Sec. 5.2.1.2). Furthermore, the resin ensemble measurments only measured the relative changes in fluorescence and absorption intensity pre- and post polymerisation. However, the fluorescence intensity in resin was found to be reduced compared to the intensity in aqueous media (Fig. SI 14). This observation was reverted after sectioning, where a high fluorescence intensity was confirmed in resin sections (Fig. 5.11 a). Similar to the strong increase in fluorescence intensity observed for TMR in DMPA resin after polymerisation, the fluorescence intensity was significantly increased compared to unembedded cells (Fig. 5.11 a). Additionally, due to the lack of out-of-focus fluorescence and no detectable autofluorescence of the resin itself, the signal-to-noise ratio (SNR) was significantly improved (Fig. 5.11 a).

The strong increase of fluorescence intensity after sectioning strongly indicated that the aqueous solvent is able to penetrate the resin. Yet, the significantly increased intensity of TMR in resin sections still indicates a measurable influence of solvatochromic effects of the resin itself. In dSTORM, a thiol containing small molecule (typically 2-mercaptoethylamine (MEA)) is needed to react with AF647 and convert it into a long lived-dark state. To test the accessibility of small molecules within the resin, initial trials

confirmed compatibility with dSTORM indicating the accessibility of small molecules to the fluorophores (data not shown). Using $NaBH_4$ a further validation was performed. $NaBH_4$ is a strong reducing agent, destroying the chromophore systems in organic fluorophores efficiently or causing a reversibly reduced non-fluorescent state (223). Within 3 s 50% of fluorescence is lost in sections (corrected for bleaching) compared to 8.5 s for whole cells (Fig. 5.11 b).

5.2.2.2 Molecular fluorophore preservation

Having confirmed the solvent accessibility for small molecules and shown good ensemble characteristics in resin, the molecular fluorophore preservation was investigated next. Here, various established methods have been investigated, namely protein-tag degree of labelling (ProDOL), Counting by photon statistics (CoPS), photobleaching step analysis (PBSA) and effective labelling efficiency (ELE) (See Sec. 4.2.2) (5, 82, 3, 86). The colocalisation-based analysis of the degree of labelling named ProDOL was found

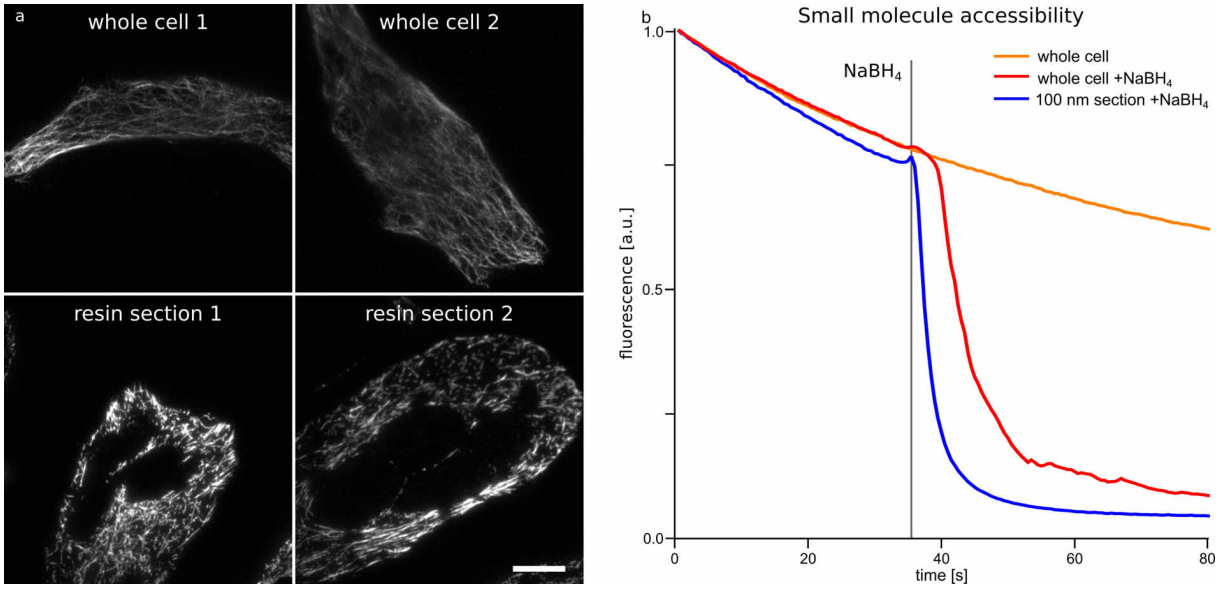

Fig. 5.11: Solvent accessibility of resin section. Sections of immunolabelled microtubules in HeLa cells were analysed for the solvent and small molecule accessibility. Addition of $NaBH_4$ at t=37 s resulted in a fast loss of fluorescence with a $t_{1/2}$=3 s in sections (corrected for bleaching) and 8.5 s for whole cells. Reanalysed from data acquired by Klaus Yserentant during his Master's thesis (224).

to be incompatible, as the fluorescent protein eGFP used in ProDOL is not well preserved in the novel resin compositions. The antibunching-based absolute counting technique CoPS and the photobleaching step detection-based quick-photobleaching step analysis (quickPBSA) on the other hand rely on well defined brightness states, with minimal blinking. Interestingly the fluorescence intensity for AF647 in resin blocks using SNAP-tag labelling was much less affected by the resin compared to immunolabelled samples. Still, analysis in resin blocks was not possible, as strong fluctuations were observed (Fig. 5.12 - red). While bleaching step traces showed detectable bleaching steps in sections (Fig. 5.12 - blue), the higher variability in brightness states combined with the high fluorophore count of up to 32 emitters per nuclear pore complex (NPC), made PBSA and CoPS not able to recover the stoichiometry (Fig. 5.12). Yet, acquired fluorescence microscopy images indicate a comparable labelling before and after embedding (e.g. Fig. 5.11). Still, some fluorophores might exhibit solvatochromic effects, changing the proportion of detectable fluorophore.

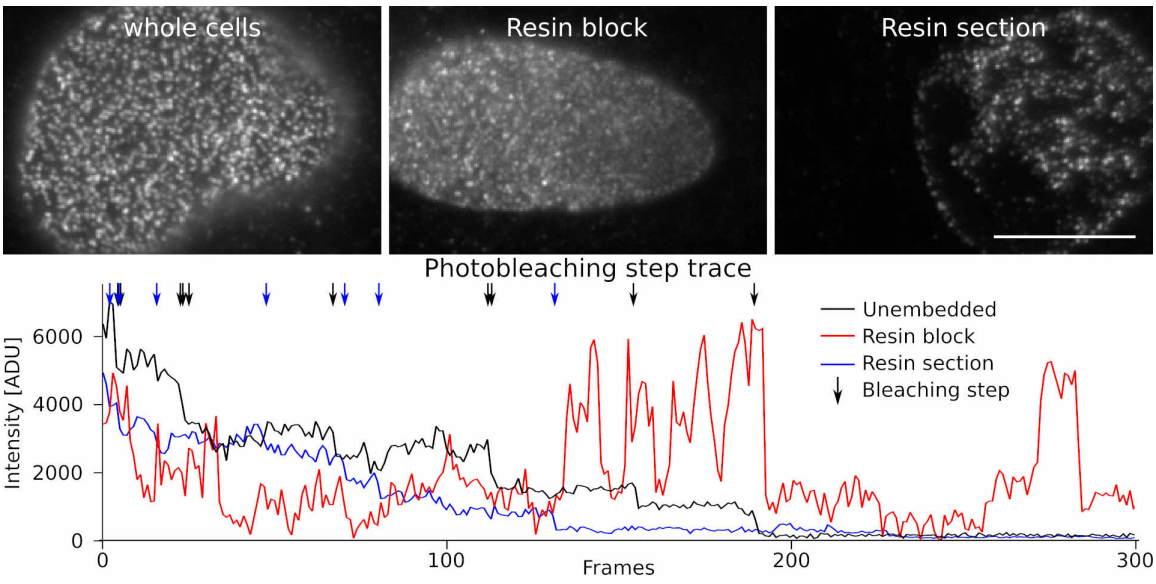

Fig. 5.12: Intensity traces of U2OS cells labelled for NUP107-SNAP-AF647. Extracted traces of an individual NPC in unembedded cells (black), resin blocks (red), and resin sections (blue). Unembedded cells and resin sections have detectable photobleaching steps in PBSA. Resin blocks show a high fluctuation in fluorescence intensity. PBSA analysis was not successful on resin sections as the fluorescent traces exhibited a higher variability compared to unembedded samples. Detected bleaching steps shown by arrow for unembedded sample (black) and in resin section (blue). Scale bar: 10 µm.

Lastly, ELE a super-resolution-based counting technique was tested to determine the molecular fluorophore preservation (Fig. 4.1 b, SI 13). Using ELE the molecular fluorophore preservation was limited to dyes compatible with dSTORM, namely AF647. Therefore the determination of quantitative preservation for all other dyes tested in Sec. 5.2.1.2 remains elusive. Importantly, in an ELE analysis of unembedded and embedded samples, no significant difference between conditions was found (Fig. 5.13). The higher variability in degree of labelling (DOL) can be attributed to the reduced number of NPC analysed per cell, as the nuclear membrane is not flat and therefore only a fraction of the nuclear membrane is within a resin section (see Fig. 5.12). Additionally, to confirm that all copies of Nup107 are present in the NPC within a section, only central regions around a nuclear membrane patch were analysed, further reducing the NPC count.

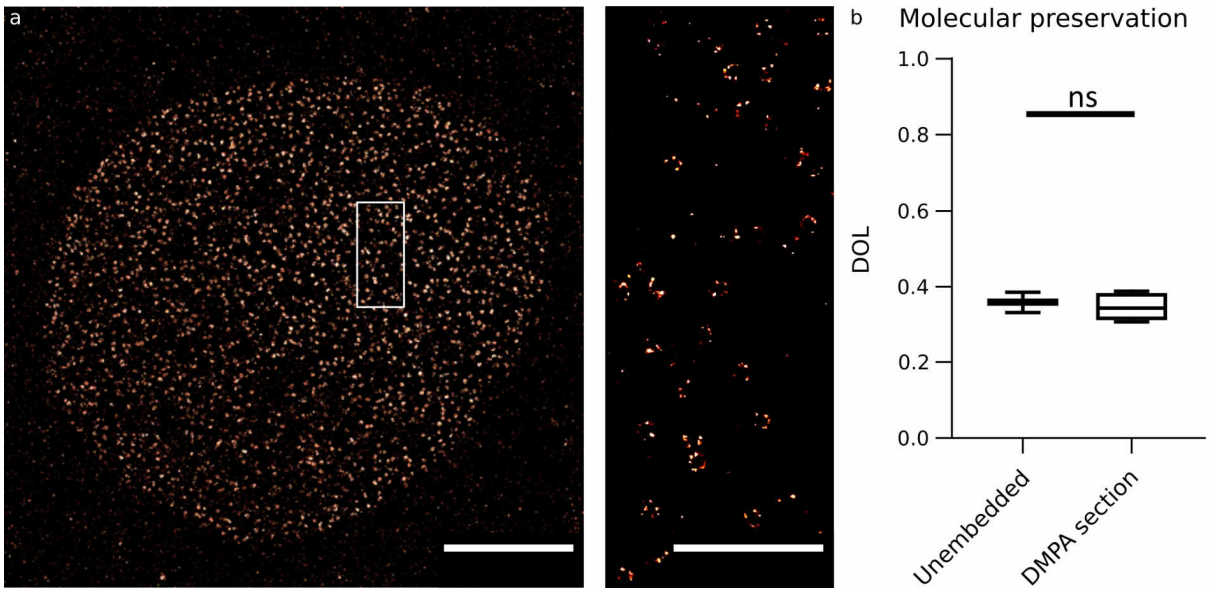

Fig. 5.13: Molecular preservation of AF647 using ELE analysis. Using ELE analysis in super-resolution microscopy analysis platform (SMAP), the degree of labelling was determined for unembedded cells and DMPA LR White embedded and sectioned cells. a) Representative image of unembedded Nup107-SNAP labelled U2OS cells. b) The degree of labelling is not significantly changed for embedded and sectioned samples, reflecting a quantitative preservation of fluorophores. Unembedded: n_{cells}=11, embedded: n_{cells}=5. Box-and-whisker plot. Scale bar: a) 5 µm, zoom in: 1 µm.

Nonetheless, as the DOL is a one dimensional readout parameter, multiple effects could compensate each other, resulting in a statistically non-significant result (see Sec. 5.3). To further investigate this hypothesis, the point pattern for each analysed nuclear pore was extracted and an averaged image is generated (see Fig. SI 13). Some effects such as restricted dipole orientation leading to reconstruction artefacts were thought to be detectable in the averaged image, but no visual difference indicating this effect was observed (data not shown). Next, the dSTORM fitting parameters were compared between embedded and unembedded samples. Generally, the localisation precision and overall performance were comparable. The variability in PSF width was reduced, as less out-of-focus emissions are expected. Additionally, the photons per blinking event were slightly increased. Further studies could be performed to investigate if this is caused by solvatochromic effects or reduced accessibility of the thiol compound, but was beyond the scope of this thesis.

5.2.3 SEM compatibility

To confirm the preservation of the cellular ultrastructure for the novel resins, sections were analysed in scanning electron microscopy (SEM) (Fig. 5.14). Here all developed resins compatible with polymerisation at -30 °C were compared to commercial heat cured LR white and EMbed 812 as well as UV polymerised HM20 resin. All novel resins developed within this thesis showed excellent preservation of the ultrastructure. For all tested resins, preservation of ultrastructural components such as cytoskeleton fibres, like actin (Fig. 5.15 - top left), the inner and outer membranes of mitochondria (Fig. 5.14, 5.15) and the nuclear envelope were comparable to the commercial resins

(Fig. 5.14, 5.15). The resins developed within this thesis on LR White basis and HM20 are methacrylate-based resins, EMbed 812 on the other hand is an epon-based resin. Therefore, the higher similarity in EM micrographs for these methacrylate-based resins is expected. Still, all resins show an excellent preservation of the ultrastructure (Fig. 5.15).

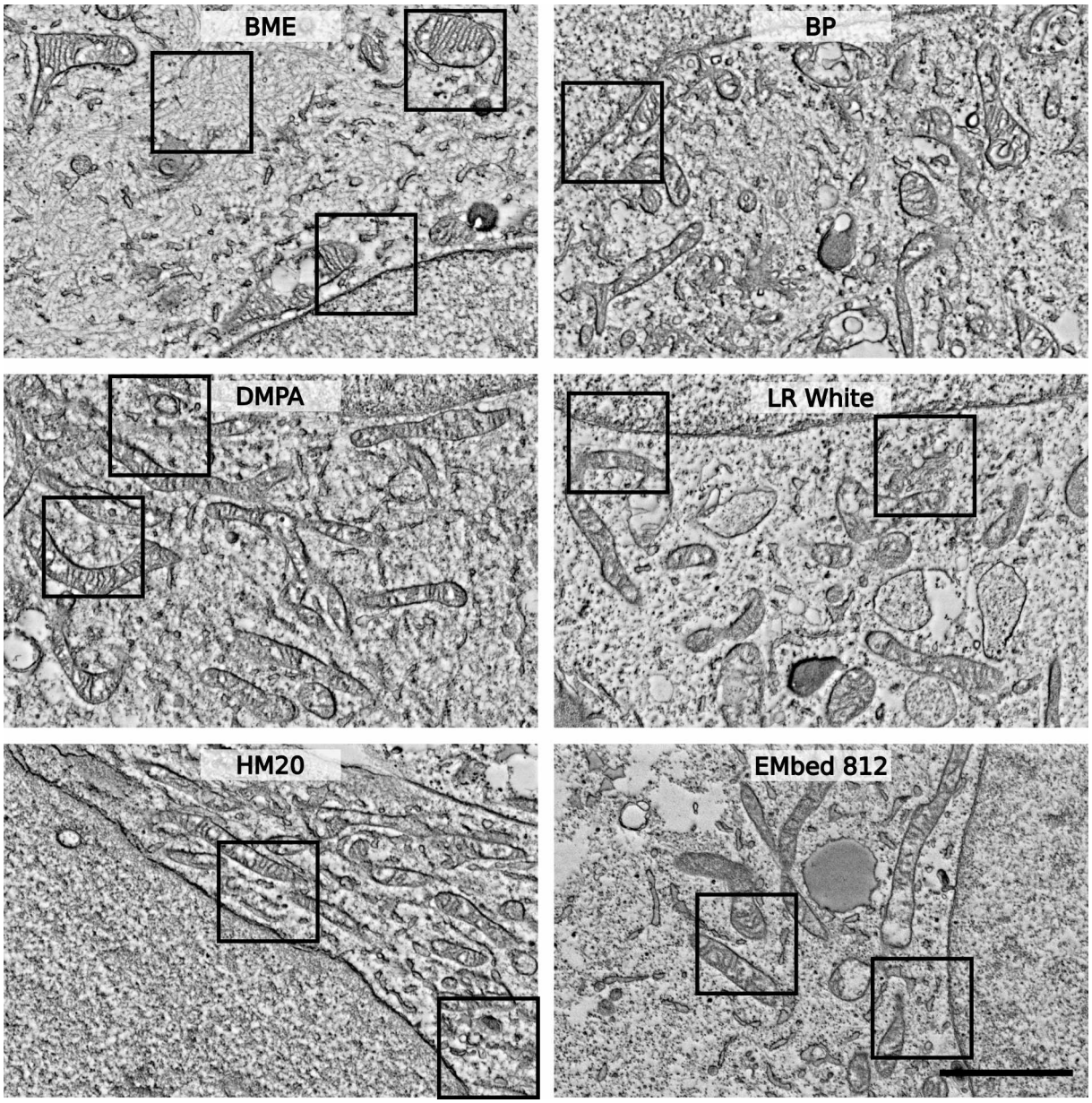

Fig. 5.14: Exemplary ultrastructural comparison of organelles and cellular structures in novel resins and commercially available resins. Zoom in from Fig. 5.14. All tested resin show excelled structural preservation of cytoskeletal fibres, mitochondria with outer and inner mitochondria membrane, the nuclear envelope among other ultrastructural components such as Golgi apparatus and vesicles. COS-7 cells were 4% paraformaldehyde (PFA) fixed and 2% glutaraldehyde (GA) post-fixed, contrasted with 2% OsO_4, 4% neodymium acetate. BME, BP, DMPA and HM20 resins were polymerised at -30 °C. LR White and EMbed812 were heat cured. On section staining with Reynolds' lead citrate and 2% uranyl acetate. Scale bar: 2 µm.

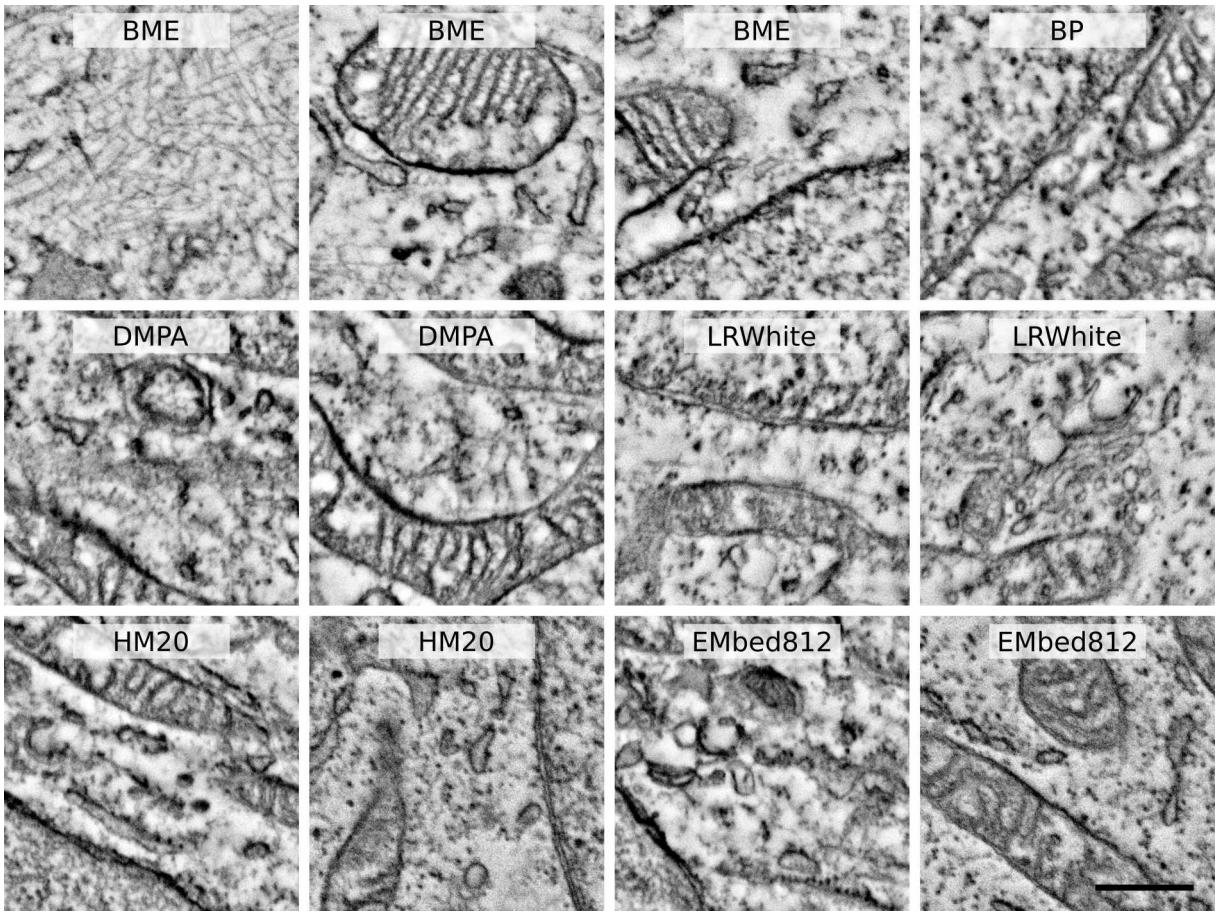

Fig. 5.15: Comparison of ultrastructural preservation in novel resins and commercially available resins. BME, BP, and DMPA show comparable structural preservation compared to commercial LR White, HM20 and EMbed812 resins. Black boxed represent the zoom ins shown in Fig. 5.15. U2OS cells were 4% PFA fixed and 2% GA post-fixed, contrasted with 2% OsO_4, 4% neodymium acetate. BME, BP, DMPA and HM20 resins were polymerised at -30 °C. LR White and EMbed812 were heat cured. On section staining with Reynolds' lead citrate and 2% uranyl acetate. Scale bar: 500 nm.

5.2.4 Alignment

Having confirmed the compatibility of these resins with both fluorescence and electron microscopy as well as demonstrating the quantitative preservation of fluorophores, the correlative three-dimensional reconstruction of serial sections was addressed next. Registration and subsequent alignment of serial sections is a computationally challenging process for which many manual, semi-automatic and automatic implementations exist (225, 226, 227, 228).

Generally, a pyramidal workflow was introduced to recover the global coarse position of sections. Using a light-microscopic image acquired after collection of the section on the substrate as reference, an automated overview of the global section position was recovered in both fluorescence and electron microscopy (Fig. 5.16). Next, in the fluorescence microscopic image, the consecutive position of the cellular sample of interest was recorded. The combination of global section alignment and local cellular position was then used to recover the same region for electron microscopy (Fig. 5.16).

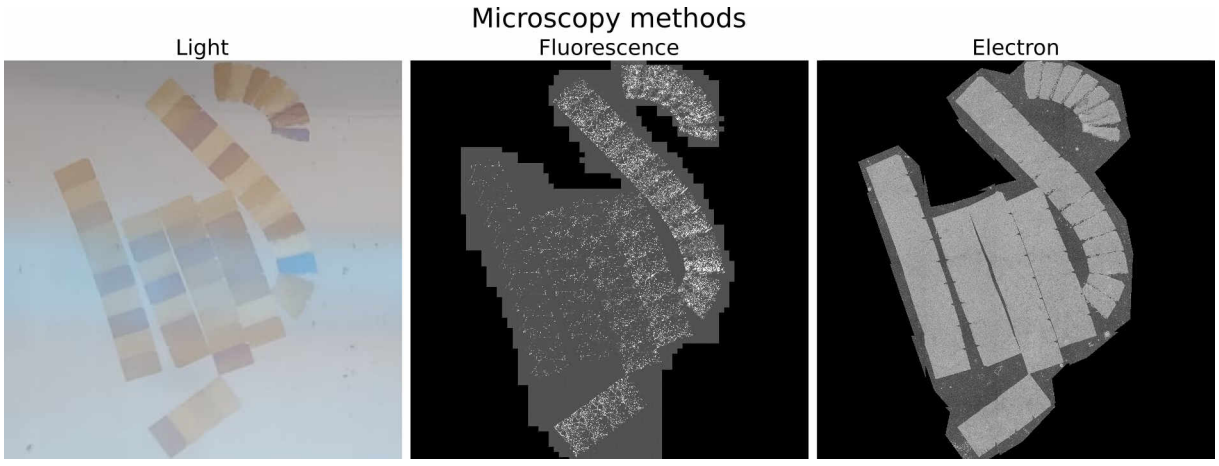

Fig. 5.16: Coarse correlative resin alignment in various imaging modalities. Light microscopic images of the grouped sections are used as reference to recover the serial section position in both fluorescence and electron microscopy. Resin sections have no detectable fluorescence, but the fluorescently labelled POI allows for correlation to the light microscopic reference. In SEM the resin has an altered contrast compared to the ITO coverslip.

5.2.4.1 Alignment strategies for electron microscopy

Recovering the volumetric reconstruction of micrographs recorded in SEM was performed using TrakEM2 or MultiStackReg using a manual coarse alignment followed by automatic registration (affine) with good results (Fig. 5.17) (227, 225). Here, the high information density of all visible ultrastructures makes alignment in electron microscopy more readily available. Manual post-processing was performed if local deformations were present in subsequent sections, introducing local artefacts not recoverable using global affine alignment strategies. Often the first section was showing local compression artefacts and local deformations, as the section height here was not consistent and often wedge shaped. This wedge shaped first section can be inferred from Section 1 in Fig. 5.17, where no resin is detected on the left side (black background) and the intensity of the micrograph signal increases as the section height increases.

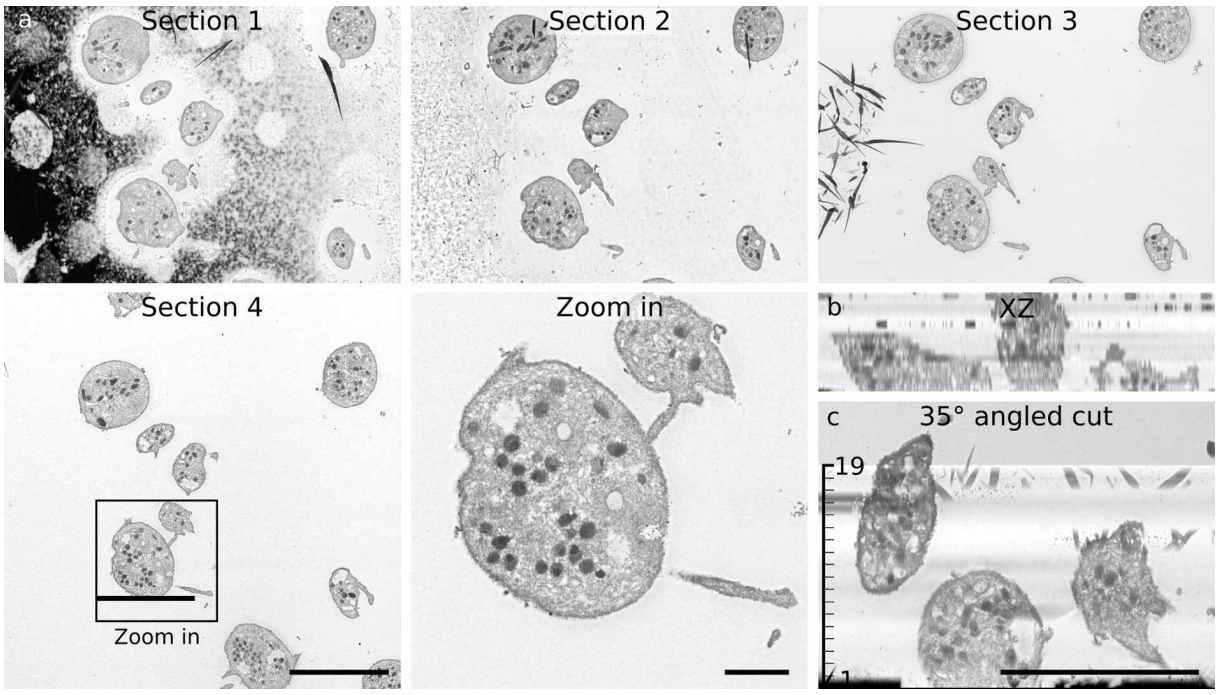

Fig. 5.17: Volumetric reconstruction of serial sections in SEM. Using TrakEM2 in combination with MultiStackReg, serial sections are coarse aligned manually followed by automatic alignment using an affine transformation based on preserved ultrastructural features of consecutive sections. Resting platelets were fixed in 4% PFA and post-fixed in 2% GA, contrasted with 0.1% OsO_4, and 4% neodymium acetate. DMPA LR White resin was polymerised at -30 °C. On section post-staining with Reynolds' lead citrate and 2% uranyl acetate. Scale bar: a-c) 5 µm, zoom in of a) 1 µm.

5.2.4.2 Alignment strategies in fluorescence microscopy

While the alignment of EM micrographs is a more established technique, fluorescence microscopic images are more sparse in nature, as only the structure of interest is detected. Therefore, the volumetric reconstruction can be more challenging.

As a proof of concept to recover the volumetric image from serial sections, microtubules were used. The continuous filamentous structure allows for the reconstruction of consecutive sections, as filaments have an overlapping region when transitioning between sections (Fig. 5.18). Generally, the alignment in fluorescence microscopy can potentially introduce artefacts. For example, both a parallelepiped (no right angles) and a rectangular cuboid can have the same section profile while having a different 3-dimensional (3D) shape. Here, the globally pseudo-random orientation of microtubules allows for the artefact-free reconstruction. Similarly, fluorescently labelled mitochondria were successfully used to reconstruct the volumetric information (106). Generally, between sections a global affine alignment led to an overlap with no detectable alignment error throughout the complete field of view (FOV) ($\ll$10 nm), confirming the suitability of microtubules (Fig. 5.18).

Using the established alignment procedure on all sections allows for the full reconstruction of the 3D volume (Fig. 5.19, SI 16). Here, the 3D reconstruction greatly benefits from the lack of out-of-focus fluorescence and premature bleaching along the axial direction typically occurring in volumetric dSTORM imaging. Additionally, regions with a high emitter density benefit from an improved reconstruction quality, as the sectioning introduces a ”quasi”-2D reduction, where the volumetric emitter density is effectively

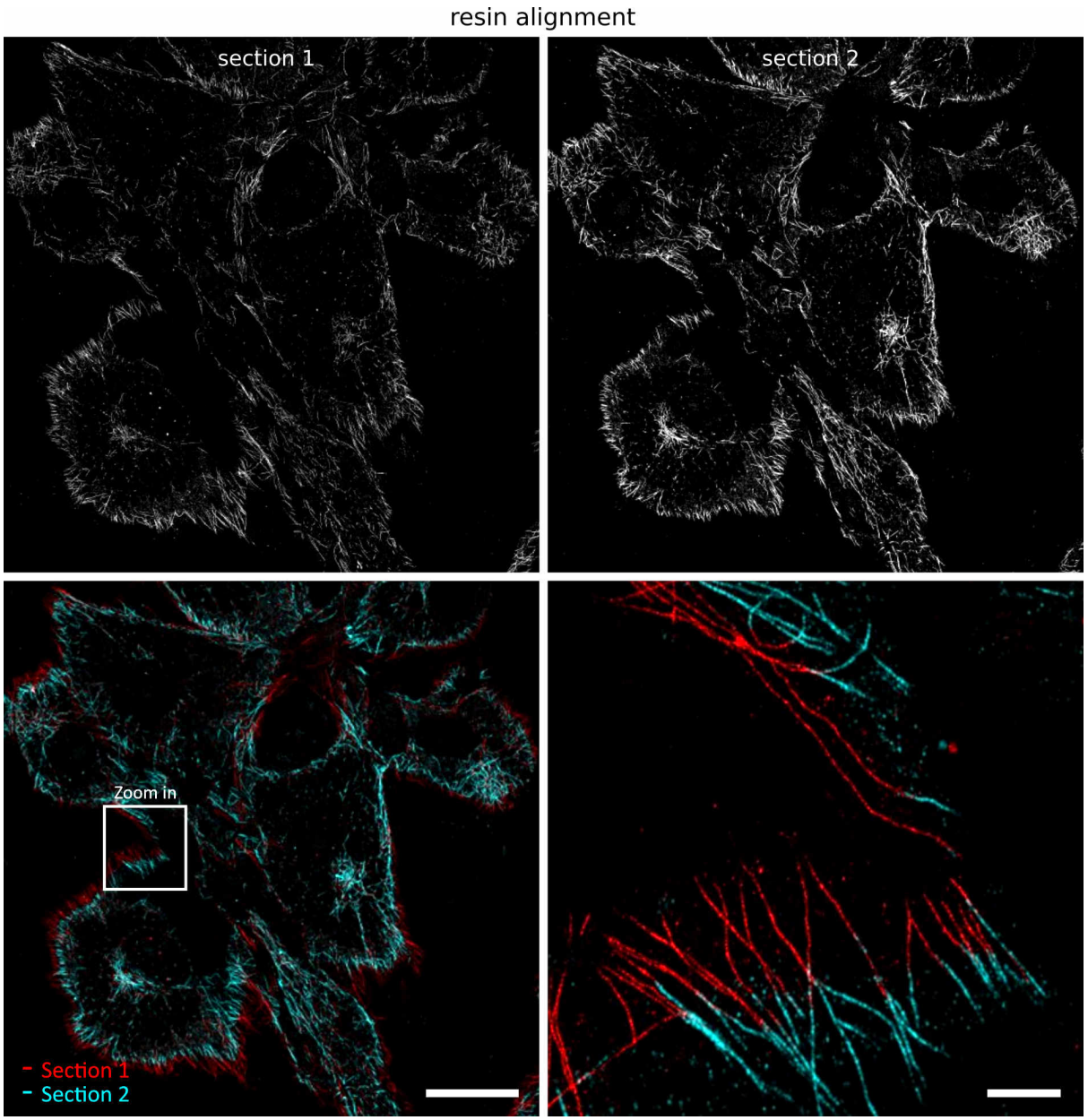

Fig. 5.18: Volumetric reconstruction of serial sections in direct stochastical optical reconstruction microscopy (dSTORM). Serial section dSTORM reconstruction were manually rotated and translocated as a first coarse alignment procedure. Next, automatic affine transformation in MultiStackReg with post-processing in TrakEM2 allowed for near artefact-free reconstruction of consecutive sections in dSTORM. Pseudo-random distribution and orientation of microtubules served as robust landmark. U2OS cells were fixed in 4% PFA, immunolabelled for microtubules and post-fixed in 1% GA (63). DMPA LR White resin was polymerised at 21 °C. dSTORM acquisition with 35 mM MEA in dSTORM-buffer at 15.000 frames per section and 50 ms exposure time. Scale bar: Full FOV) 20 µm, zoom in) 2 µm.

reduced. As the resin height of 50 nm now also corresponds to the axial resolution, the axial resolution is significantly improved without additional optics (see Fig. 3.20).

While volumetric dSTORM imaging in combination with astigmatic PSF is able to recover the 3D position of emitters for full cells, the ”photon budget”, at which most fluorophores

are bleached, limits the duration of acquisition (Fig. 5.21). This limitation is not present in dSTORM imaging using array tomography. Rather each section can be imaged until most fluorophores are bleached or a satisfactory emitter density is achieved. Additionally, depth dependent aberrations reduce the reconstruction quality with increasing penetration depth in whole cell dSTORM imaging (Fig. 5.21 c). Contrary, in serial section dSTORM imaging, all acquired sections have a comparable reconstruction quality as the sections all are attached to the coverslip allowing for TIRF imaging for the full reconstructed 3D volume. All the aformentioned factors contribute to a significantly improved reconstruction quality of volumetric dSTORM images, at the cost of additional processing steps and prolonged dSTORM acquisition times (Fig. 5.19, SI 16, 5.21).

Visual inspection of the reconstructed volumetric images shows continuity of the filamentous structure throughout the axial direction of a cell as well as throughout the full FOV (Fig. 5.20). In Fig. 5.20 e, a single microtubule is highlighted spanning from section 19 to section 80. This observation holds true for all of the inspected microtubules. Due to the separation of the axial profile into 50 nm bins, a similar length scale of the diameter of a single indirectly immunolabelled microtubules, regions with a high density of microtubules, still led to a good reconstruction and allowed for a robust tracing of a single microtubule (Fig. 5.20 e).

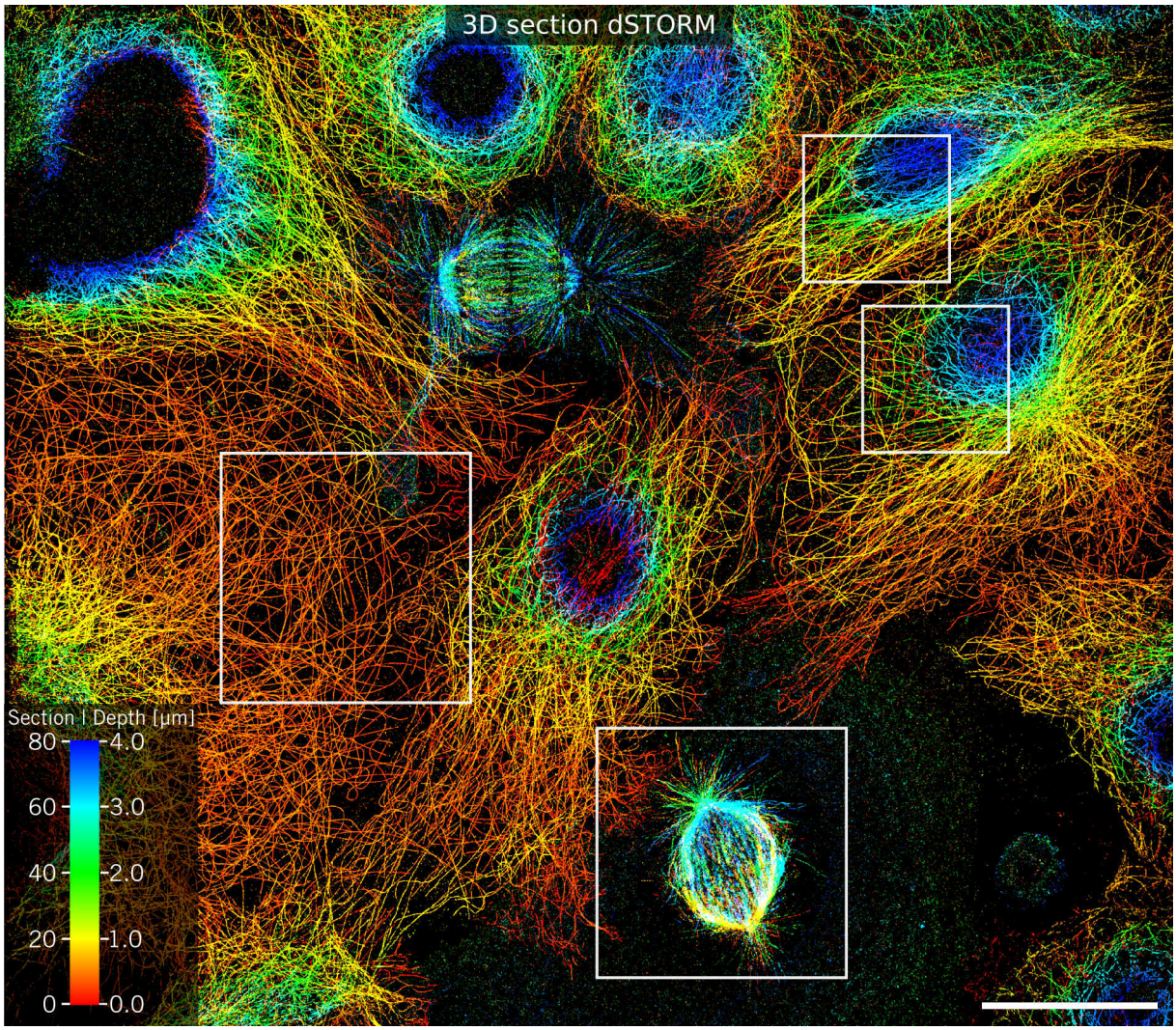

Fig. 5.19: Volumetric serial section dSTORM reconstruction of microtubeles in COS-7 cells. Automated affine reconstructions of 80 serial sections with 50 nm section height. COS-7 cells were fixed in 4% PFA, indirectly immunolabelled for microtubules and post-fixed in 1% GA (63). DMPA LR White resin was polymerised at 21 °C. dSTORM acquisition with 35 mM MEA in dSTORM-buffer at 15.000 frames per section and 50 ms exposure time. Rainbow look-up table (LUT) from red to green to blue. Scale bar: 20 µm.

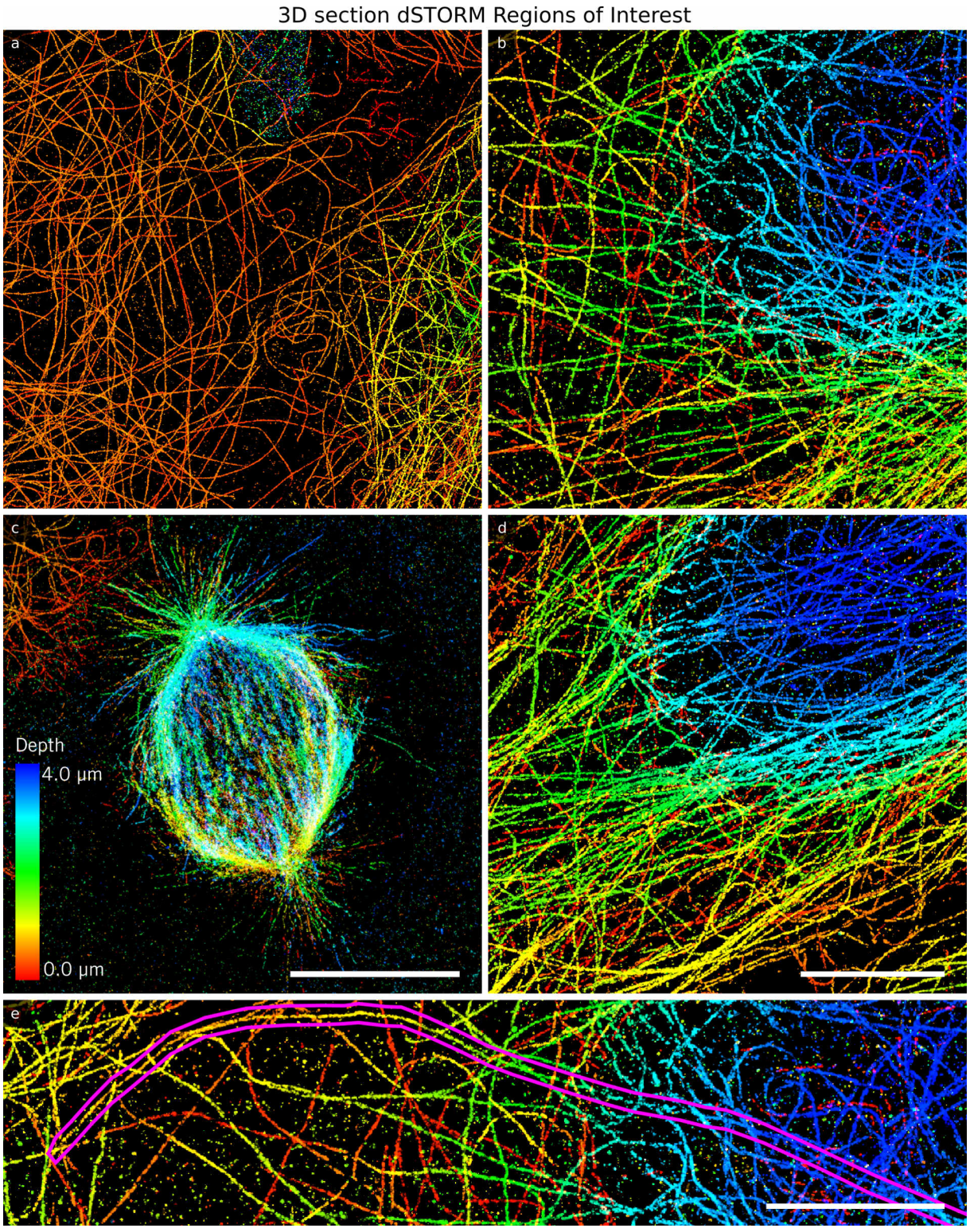

Fig. 5.20: Zoom in of volumetric serial section dSTORM reconstruction of microtubeles in COS-7 cells. a-e) Zoom in of volumetric serial section dSTORM reconstruction reveal high quality reconstructions at all cell depths with no premature bleaching and out of focus blinking due to physical separation of individual sections. e) No detectable alignment artefacts throughout the FOV with the ability to trace individual microtubules through all sections (purple region). Automated affine reconstructions of 80 serial sections with 50 nm section height. COS-7 cells were fixed in 4% PFA, indirectly immunolabelled for microtubules and post-fixed in 1% GA (63). DMPA LR White resin was polymerised at 21 °C. dSTORM acquisition with 35 mM MEA in dSTORM-buffer at 15.000 frames per section and 50 ms exposure time. Rainbow LUT from red to green to blue. Scale bar: a,c) 10 µm, b,d,e) 5 µm.

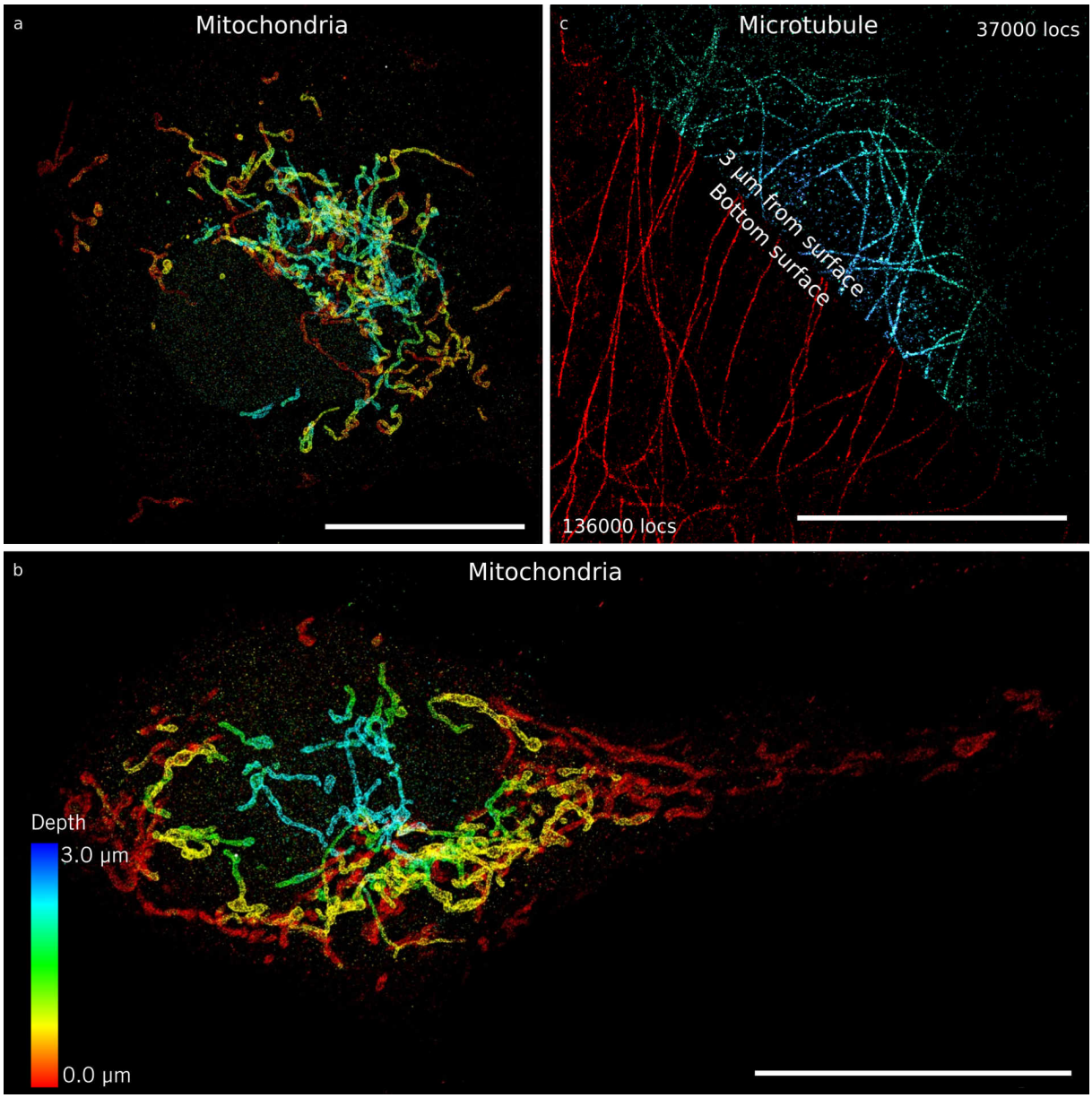

Fig. 5.21: Volumetric whole cell dSTORM reconstruction of mitochondria in COS-7 cells and microtubeles in LSEC. a,b) COS-7 cells expressing TOMM20-HaloTag were fixed in 4% PFA, tag-labelled with AF647-HaloTag. c) COS-7 were fixed in 4% PFA and indirectly immunolabelled for microtubules (63). c) Reconstruction quality in optical 3D dSTORM reduces with increased imaging depth, both from worse localisation precision (aberration) and reduced localisation count (premature bleaching). dSTORM acquisition with 30 mM MEA for mitochondria and 100 mM MEA for microtubules in dSTORM-buffer at 80.000 frames using 500 nm optical sectioning steps to reconstruct the full 3D volume. Rainbow LUT from red to green to blue. Scale bar: a,b) 20 µm, c) 10 µm.

Further, single section analysis revealed that the tube-like structure of axially oriented microtubule (cross-section) is readily resolved (Fig. 5.22 a-c). Here a peak to peak width of 52$\pm$4 nm is found, in line with previous whole cell analysis of indirectly labelled microtubules (Fig. 5.22 d, 4.4). Here, the peak separation is significantly improved

compared to whole cell 3D dSTORM, further demonstrating the potential of these novel resins with quantitative preservation of fluorophores for dSTORM.

Yet, not all cellular structures have a microtubule cytoskeleton suited for volumetric reconstruction. Resting platelets for example have a coiled microtubule structure, named marginal band, not suited as reference for 3D reconstruction of serial sections (230, 231). Similarly, to perform an affine alignment, at least 3 points shared between sections need to be identified. In the volumetric reconstruction of platelets using electron microscopy, mitochondria were traced between sections and in part due to the small volume of platelets the presence of three non-colinear mitochondria was not always given, making an affine alignment impossible (Fig. 5.17).

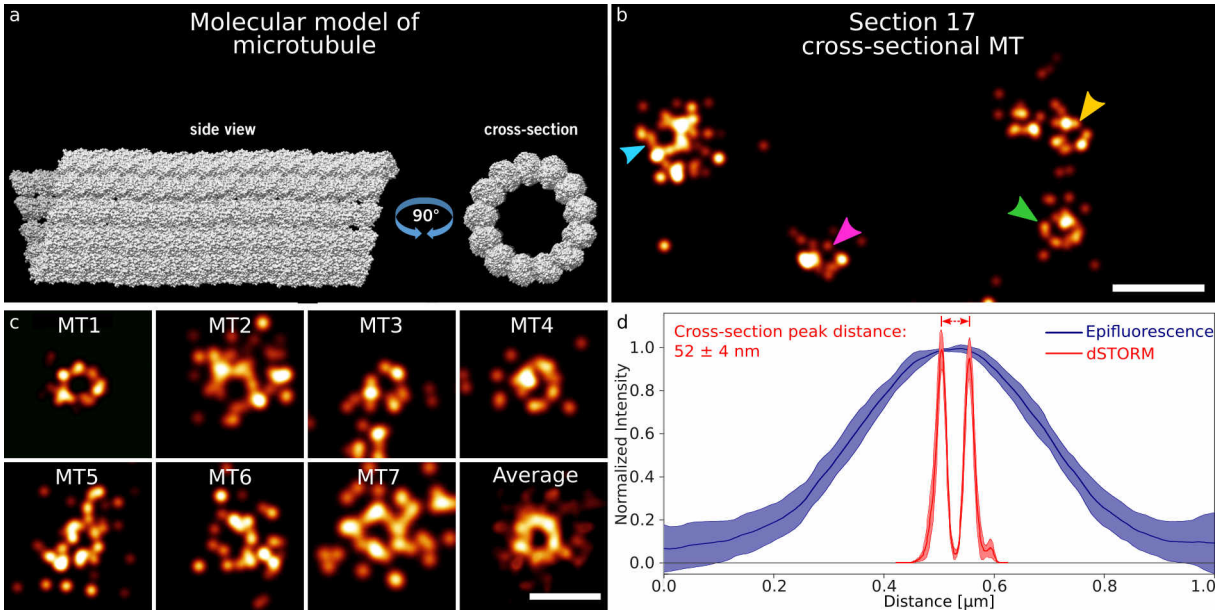

Fig. 5.22: Cross-sectional analysis of microtubule profiles in serial section dSTORM. a) Molecular model of microtubule in side profile and cross-sectional profile from PDB: 1jff (229). b) Representative region of interest (ROI) of microtubules oriented perpendicular with respect to sectioning. Arrows indicate detected microtubules. c) 7 cross-sectional microtubule profiles are shown to represent the quality of recovered tube-like structures. d) Peak-to-Peak analysis reveals a good separation of peaks with 52±4 nm for dSTORM reconstructions (red), in line with previous whole cell analysis. Blue line represents expected pseudo-diffraction limited profiles generated in SMAP (128). COS-7 cells were fixed in 4% PFA, indirectly immunolabelled for microtubules and post-fixed in 1% GA (63). DMPA LR White resin was polymerised at 21 °C. dSTORM acquisition with 35 mM MEA in dSTORM-buffer at 50.000 frames per section. d) Mean±SD. Reanalysed from data acquired by Jonas Euchner during his Master's thesis (49). Scale bar: b) 250 nm, c) 100 nm.

To address this shortcoming present in specific cell types, external spherical fiducial markers were investigated, as they could help with registration of fluorescent images in a spectrally separate channel and furthermore aid in the correlative alignment of the two modalities. Based on existing work, where fluorescent beads were used as correlative alignment marker on sections or embedded into the resin, FluoSpheres (Thermo Fisher Scientific) were tested for their compatibility with the resin (232, 233, 234). Unfortunately, the spheres disintegrated in the resin and released the bound fluorophore, resulting in a bright, non-specific staining of the resin (Fig. 5.23 a). Next, fluorophores covalently linked to a dextran were tested (fluorescein and rhodamine, Merck). The dextrans had a molecular weight of up to 2×10^6 Da, resulting in a Stokes radius of 27 nm. Here, the dextrans proved to be immiscible with the resin. Extensive testing using various pre-dilution solvents and ultrasonic preparation did not lead to satisfactory mixing (Fig. 5.23 b). Finally, bacteria and viral particles were tested (Fig. 5.23 c). Using fluorescently labelled *S. epidermis*, fiducial markers could be introduced to the resin, allowing for 3D reconstruction of light-microscopic images as well as aid in the correlative alignment as they are visible in both modalities (Fig. 5.23 d,e). Yet, as they have an average diameter of $\sim$650 nm, smaller viral particles which are closer to the diffraction limit of light were tested. Using the vaccinia virus as fiducial marker, in collaboration with Jason Mercer, was leading to promising first results. Still, this preliminary work can be used to expand upon if external fiducial markers are needed for studying e.g. individual platelets.

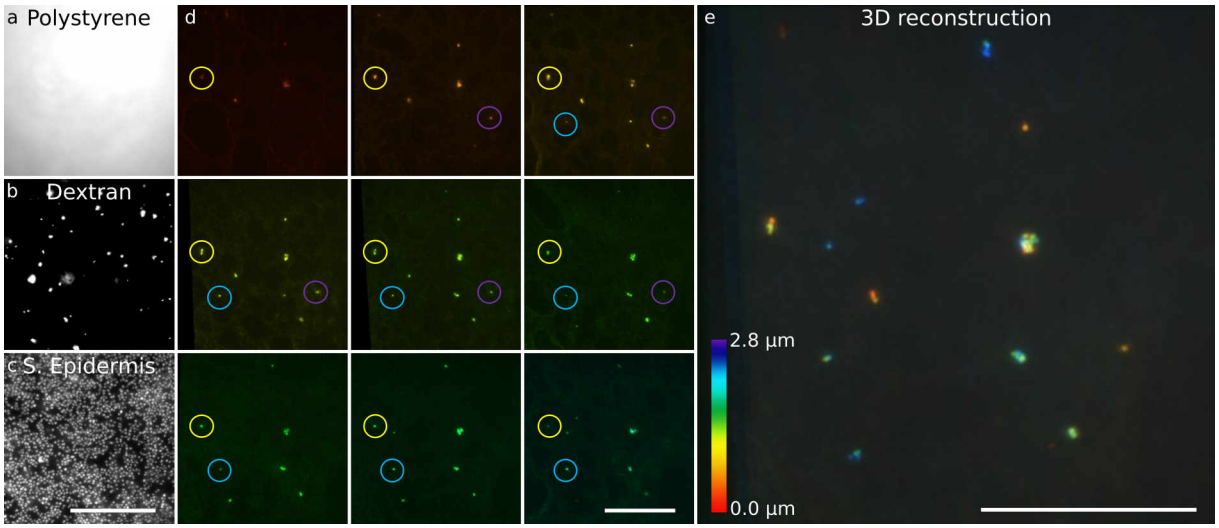

Fig. 5.23: Investigation of external fiducial markers for *in-resin* CLEM. Several organic structures were tested for their respective compatibility with resin polymerisation. a) Polystyrene FluoSpheres disintigrate in resin, releasing the fluorophore. b) Macromolecular dextrans do not dissolve in resin and form aggregates. c) Fluorescently labelled *S. epidermis* are compatible with the developed workflow. d,e) Serial section reconstruction of resin embedded *S. epidermis* at 200 nm section height. d) Colored circles represent cluster of *S. epidermis* used as landmarks for alignment of consecutive sections. Scale bar: 40 µm.

5.2.4.3 Correlative alignment

Finally, to perform a correlative analysis, the registration of the two modalities relative to each other needs to be performed. After coarse alignment based on the cell outline in both electron and fluorescence microscopy, nanoscale analysis allowed for visual identification of microtubules in both modalities (Fig. 5.24 - blue arrow). This analysis proved computationally challenging as the identification of ultrastructural features corresponding to the filamentous microtubules was not easily possible. On the one hand, using a combination of type II secondary electron (SE_{II}) and back-scattered electron (BSE) detectors in scanning electron microscopy combined with a low acceleration voltage of 1.5 kV resulted in a penetration depth of up to 20 nm only reconstructing the upper portion of a section and thus having the possibility of observing a fluorescent labelling with no matching landmark in electron microscopy (101, 235). On the other hand, filamentous structures can be detected in electron microscopy, not corresponding to microtubules (e.g. actin bundles), as the functional relation for an observed ultrastruc-

ture is not resolved in electron microscopy (Fig. 5.24 b - green arrow). Furthermore, the metallic ITO coverslip has a known electromagnetic coupling between the fluorophore and the metallic substrate, called metal-induced energy transfer (MIET), causing a reduction of the quantum yield and fluorescence lifetime in the near-field range of up to 10 nm for ITO (236, 237). Further testing using *in-resin* 3D dSTORM can be performed to investigate this effect on the dSTORM reconstruction for fluorophores in sub 10 nm proximity to the ITO coverslip.

Alternatively, a structure more readily detectable in both modalities could be chosen for correlative alignment. Here the mitochondria membrane is an established target leading to good results (Fig. SI 17). However, due to the use of a second fluorophore for alignment, the transformational mapping of both fluorescent channels must be considered. While novel deep learning based whole cell segmentation strategies have been shown to be feasible, implementation was beyond the scope of this thesis (238). Therefore classification and correlative alignment was performed manually using BigWarp with nanoscale alignment of both modalities (228).

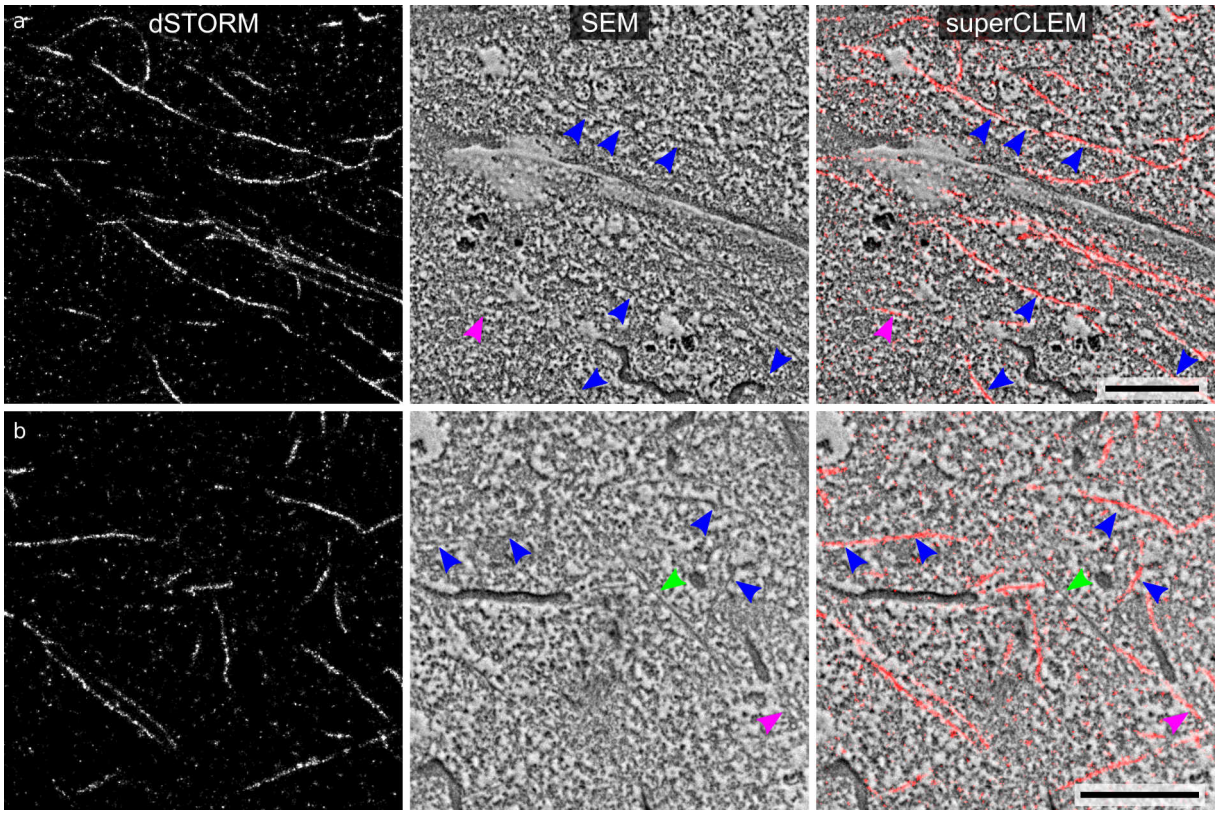

Fig. 5.24: Correlative alignment of dSTORM and SEM reconstruction. Representative ROIs demonstrating the manual nanoscale alignment in BigWarp based on the detection of microtubules in both dSTORM and SEM (228). Blue arrows represent fibrillar structures matching to microtubule specific fluorescent signals. Green arrows represent fibrillar structures with no matching microtubule specific fluorescence. Purple arrows represent microtubule specific fluorescence with no matching fibrillar structure observed in SEM. Specific fluorescent signal with no matching SEM correspondence is expected, as SE_{II} and BSE detectors in SEM cannot recover the full section height of 50 nm at 1.5 kV acceleration voltage. Scale bar: 2 µm

5.2.5 Application

Having confirmed the compatibility of the developed workflow with both light and electron microscopy, a target of biomedical relevance was chosen as a proof of concept. Here, LSECs were found to be ideally suited. They undergo morphological and functional changes when exposed to SASP, modulating the immune response and immune cell migration (209). Yet, this phenotype is also strongly associated with the progression of tumorigenesis (211, 118, 212, 213). Functional studies exist, linking SASP to an upregulation of the NFκB signalling pathway, increased expression of the adhesion modulator ICAM1 and remodelling of the microtubule cytoskeleton (118, 209). Recent studies have shown that targeting the senescence phenotype can be a viable anticancer

therapy (239, 240). Here, Colchicine, a microtubule inhibitor has been shown to effectively prevent senescence in endothelial cells (240). Furthermore, the microtubule cytoskeleton is known to interact and influence the expression of ICAM1 (241, 242). Therefore, investigating the microtubule cytoskeleton in a structure-function relationship in LSEC exposed to SASP and various microtubule-disrupting agents was an ideal validation target of biomedical relevance.

5.2.5.1 Effects of SASP on LSEC

First, a suitable culturing method of LSEC, compatible with the established workflow needed to be found. Here, generally rat tail collagen (RTC) type I is used to mediate adhesion of LSEC on coverslips. Most publications use polymer coverslips, incompatible with the established resin compositions (Fig. 5.25 a) (209, 118). When seeding on glass, a confluence of 60% was reported after 24 h, in line with our findings (Fig. 5.25 b) (118). Yet, the weak adhesion led to loss of the cells during labelling procedures and embedding. Additionally, over time the cells formed a morphologically aberrant patchy monolayer with increased cell polarity in unstimulated growing condition (Fig. 5.25 c).

Therefore, procedures were investigated to improve adhesion of LSEC on glass coverslips, compatible with resin embedding procedures. Here, several protocols for RTC hydrogel formation or thin coating of RTC have been tested with insufficient results (data not shown). Finally, in line with literature on stem cell work, covalent linking of RTC to glass using amino-silanisation and glutaraldehyde cross-linking was tested and found to result in consistent formation of LSEC monolayers comparable to on-plastic culturing and compatible with embedding (Fig. 5.25 d) (119, 243).

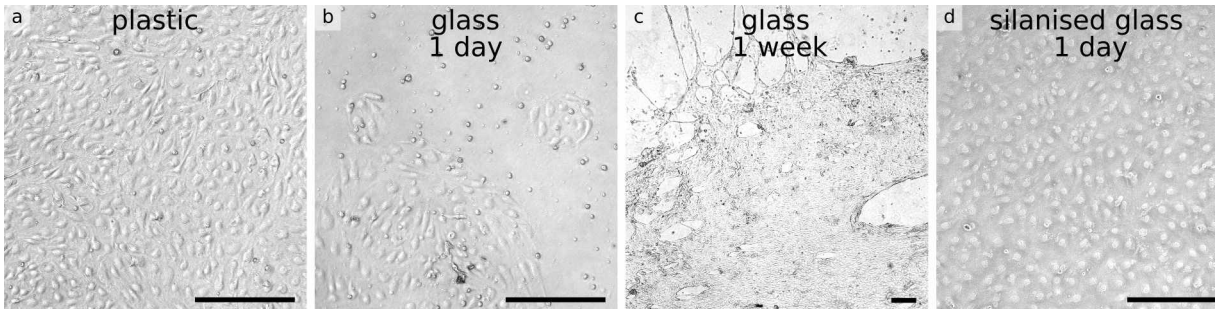

Fig. 5.25: Investigation of surface treatments for LSEC adhesion. The commonly used polymers for LSEC culturing are incompatible with resin embedding, therefore a surface treatment compatible with resin embedding was investigated. a) LSEC are grown on RTC type I pre-treated polymeric substrates with low Young's Modulus. b) Adaption of RTC type I pre-treatment on glass with reduced adhesion after 24 h and increased polar morphology. c) Culturing for 1 week on RTC type I pre-treated glass coverslips resulted in formation of morphologically aberrant patchy monolayer. d) Silanisation of glass and covalent linking of RTC type I to the aminosilan with glutaraldehyde resulted in LSEC monolayers of similar morphology to LSEC on plastic (a). Scale bar: 250 µm

Having established a protocol for seeding of LSEC, the morphological changes of the microtubule cytoskeleton were first investigated using whole cell dSTORM imaging (Fig. 5.26). Here, based on the software developed by Marcotti *et al.* named "Alignment by Fourier Transform", the spatially most prominent orientation of microtubules within a tiled subset of the FOV was determined and compared to neighbouring quadrants to determine both the alignment angle and the alignment order (See Methods 2.2.9.5) (131). An alignment order of 1 represents perfect alignment (blue), 0 random alignment (green) and -1 orthogonal alignment (red) (131).

Here, the microtubule cytoskeleton of SASP-primed LSEC was found to be significantly polarised compared to the control group, meaning the orientation of microtubule has increasingly become more parallel and aligned to neighbouring microtubules (SASP-primed LSEC: 0.84$\pm$0.23 vs. growth control LSEC: 0.56$\pm$0.33 for Mean$\pm$SD) (Fig. 5.26). Further analysis on the eccentricity of signal in Fourier-space was performed as a measure of alignment order within a region, but was not producing robust results. Additionally, for SASP-primed LSEC an increase in regions with high microtubules count and near perfect alignment order of close to S=1 is a commonly observed phenomenon

(see Fig. 5.26). To further analyse the microtubule architecture, other analyses were investigated, including recovering the spatial persistence length of all microtubules, but discontinued as no automated and robust implementation could be established (Fig. SI 18).

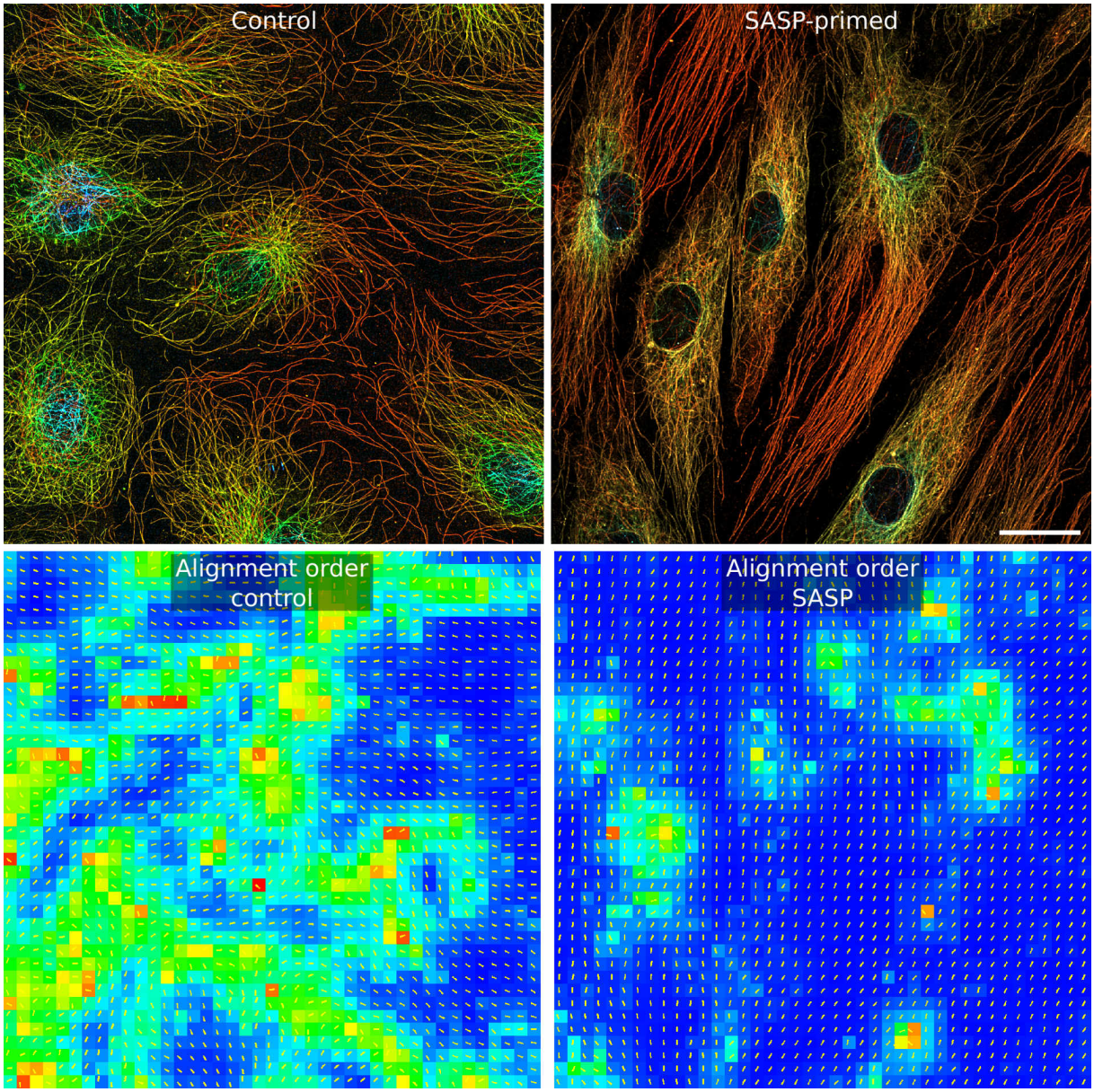

Fig. 5.26: Investigation of microtubule alignment order of LSEC in growth media and SASP media. Top panel) 3D dSTORM reconstruction of LSEC in normal growth condition and exposed to SASP. Bottom panel) Using "Alignment by Fourier Transform", the spatially most prominent orientation of microtubules within a 500 nm region is determined (yellow line) and compared to its 3×3 neighborhood to determine to alignment order of LSEC. 1 represent perfect alignment (blue), 0 random alignment (green) and -1 orthogonal alignment (red) (131). SASP-primed LSEC exhibit a significantly increased mean alignment order of 0.84±0.23 compared to 0.56±0.33 for growth control LSEC (Mean±SD, SE_{mean} each $<$0.01). Scale bar: 20 µm.

This metric was systematically used to investigate the effect microtubule polymerisation inhibitors have on the LSEC morphology in normal growth condition and SASP-primed LSEC (Fig. 5.27 a,b). Here, both Colchicine and Nocodazole led to an increase of unpolymerised tubulin, visible by the increase of non-filamentous signal within the cells. Notably, Nocodazole led to a near complete loss of detectable microtubule cytoskeleton (Fig. 5.27 c). In line with these observations, the order of microtubule orientation was reduced in SASP-primed LSEC when exposed to either drug, to a alignment order not significantly different to the control (Fig. 5.27 a). Here addition of colchicine to LSEC in normal growth condition did not change the alignment order of microtubules.

Contrary, when using the alignment analysis to be sensitive to the cellular polarity, Colchicine was found to not significantly alter the cellular alignment order, retaining an elevated alignment order of LSEC when exposed to SASP (Fig. 5.27 b). Nocodazole led to a further increase in mean alignment order indicating a further increase in aligned polarity of SASP-primed LSEC with unknown implications for the control of immune cell migration.

These results further demonstrate that a correlative light-electron microscopic investigation to resolve the ultrastructural context within this functional context can aid in revealing the underlying structure-function relationship of reverted microtubule alignment with maintained cellular polarity increase in SASP-primed LSEC under various treatment conditions.

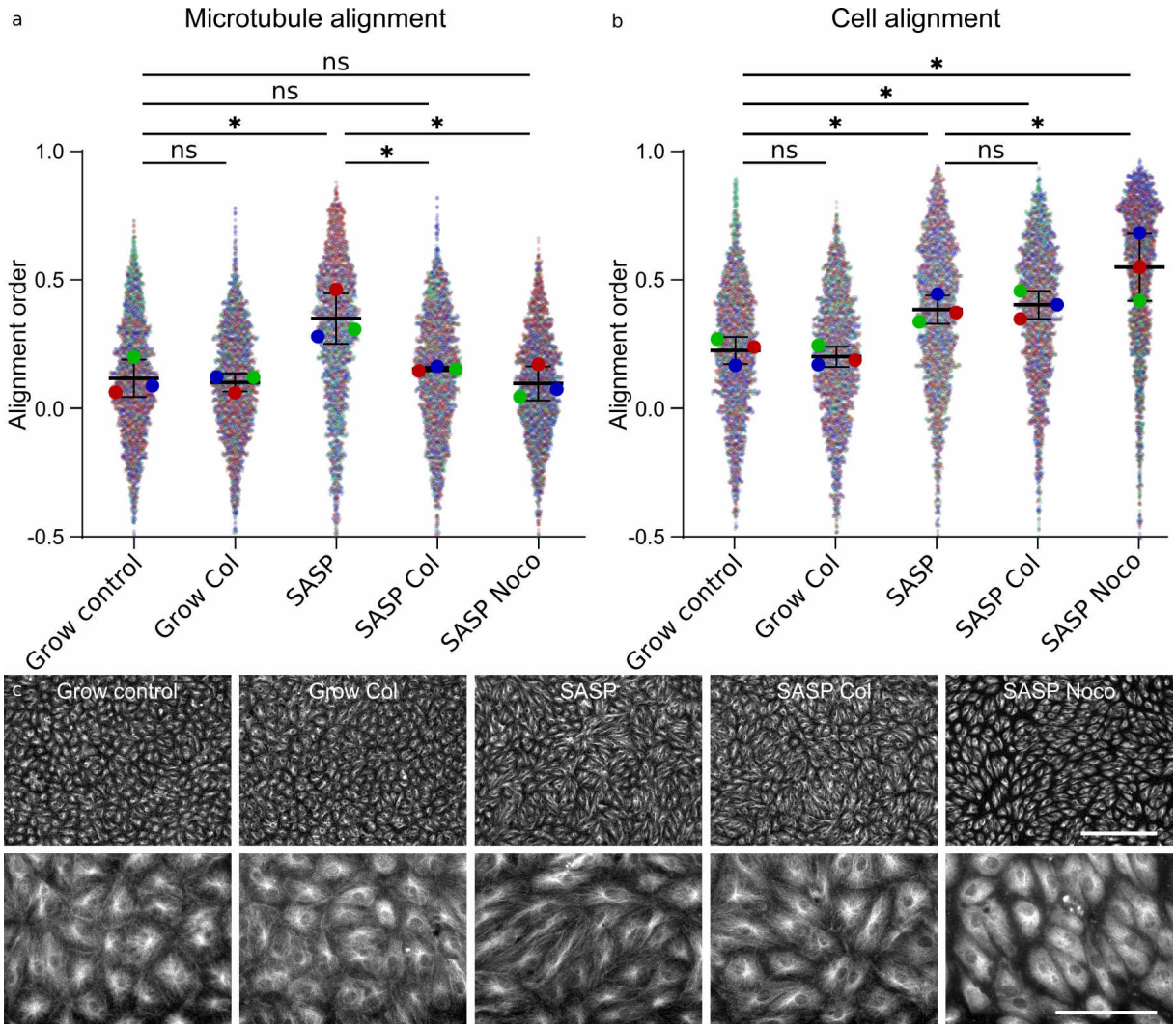

Fig. 5.27: Investigation of microtubule alignment and cellular alignment of LSEC treated with microtubule polymerisation inhibitors. Alignment order determined for microtubules and LSEC in normal growth condition (Grow control), exposed to SASP, and after treatment with Colchicine (Col) and Nocodazole (Noco). a) Using "Alignment by Fourier Transform", the spatially most prominent orientation of microtubules was determined (c) and compared to its 5×5 neighborhood extract the alignment order of microtubules (131). SASP-primed LSEC have a significantly increased alignment order that is reverted to non-significant alignment orders under both Colchicine and Nocodazole treatment. b) Using "Alignment by Fourier Transform", the cellular alignment order for all tested conditions was determined. LSEC show increased cellular polarity after SASP-priming, maintained after drug treatment. Colchicine does not significantly alter the cellular alignment order, while Nocodazole further leads to cellular morphology changes. c) Representative images used for treatment analysis. Scale bar: c, top panel) 300 µm, c, bottom panel) 100 µm.

5.2.5.2 Super-vCLEM in LSEC

Using the established techniques, LSECs were next investigated using super-resolution and volumetric CLEM (super-vCLEM). Here, both LSEC in regular growth condition (control) and SASP-primed LSEC were analysed (Fig. 5.28, 5.29, 5.30).

Initially, the SEM micrographs were reconstructed to a volumetric image showing a high content of pinocytic vesicles and lysosomes in line with reports in literature located close to the central regions of the cell (244). Due to the indirect fluorescent immunolabelling, membrane preservation was reduced. Additionally, the low OsO_4 concentration used to preserve fluorescence further led to a low contrasting of the preserved membranes. Yet, the established protocol for LSEC leads to significantly improved ultrastructural preservation as compared to protocols optimised for only dSTORM microscopy. In dSTORM procedures commonly used protocols include strong permeabilisation and $NaBH_4$-quenching. All are incompatible with good ultrastructural preservation (Fig SI 20).

Next, the serial section dSTORM reconstructions were aligned in 3D and cross-correlated to the SEM micrographs as shown in (Fig. 5.24). Here, an alignment error between sections of up to 100 nm was detected (Fig. SI 19). This problem was found to stem from the insufficient pre-treatment of the used ITO coverslips. Here, hydrophilicity pre-treatment was insufficient for the duration of sectioning, leading to droplet formation on the coverslip upon collection of the sections and subsequent deformations during drying. This problem has since been resolved using plasma cleaning of ITO coverslips.

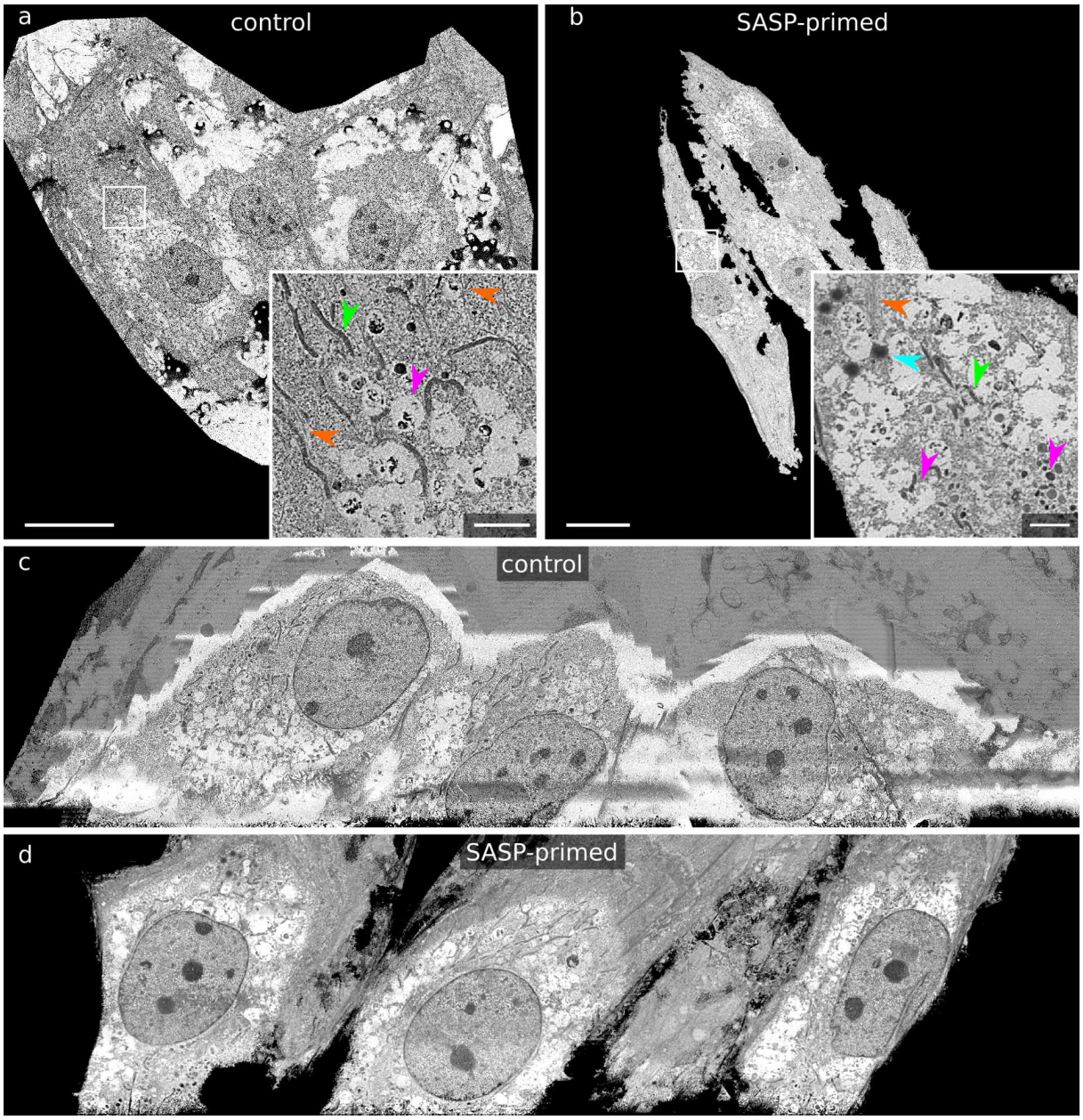

Fig. 5.28: Volumetric reconstruction of serial section of LSEC in SEM. Using TrakEM2 in combination with MultiStackReg, serial sections are coarse aligned manually followed by automatic alignment using an affine transformation based on preserved ultrastructural features of consecutive sections. a,b) Single section of LSEC in growth control (a) and SASP-primed LSEC (b). Zoom in with ultrastructural components highlighted by arrows. Cyan arrow: Weibel Palade body, green arrow: mitochondria, orange arrow: cytoskeleton, magenta arrow: vesicles. c,d) Cross section through volumetric reconstruction of growth control LSEC (c) and SASP-primed LSEC (d). LSEC were fixed in 4% PFA and post-fixed in 2% GA, contrasted with 0.1% OsO_4, and 4% neodymium acetate. DMPA LR White resin was polymerised at -30 °C. On section post-staining with Reynolds' lead citrate and 2% uranyl acetate. SE_{II} detector micrographs. Scale bar: a-c) 5 µm, zoom in of a) 1 µm.

Using super-vCLEM the volumetric images were successfully reconstructed in a correlative approach (Fig. 5.29), allowing for detailed ultrastructural analysis with respect to the functional context of the microtubule cytoskeleton (Fig. 5.30). Here, a multitude of ultrastructural components, such as NPC, Weibel Palade bodies, mitochondria or vesicles are visible throughout the cell (Fig. 5.30 b) and can be analysed both independently and in reference to the microtubule cytoskeleton.

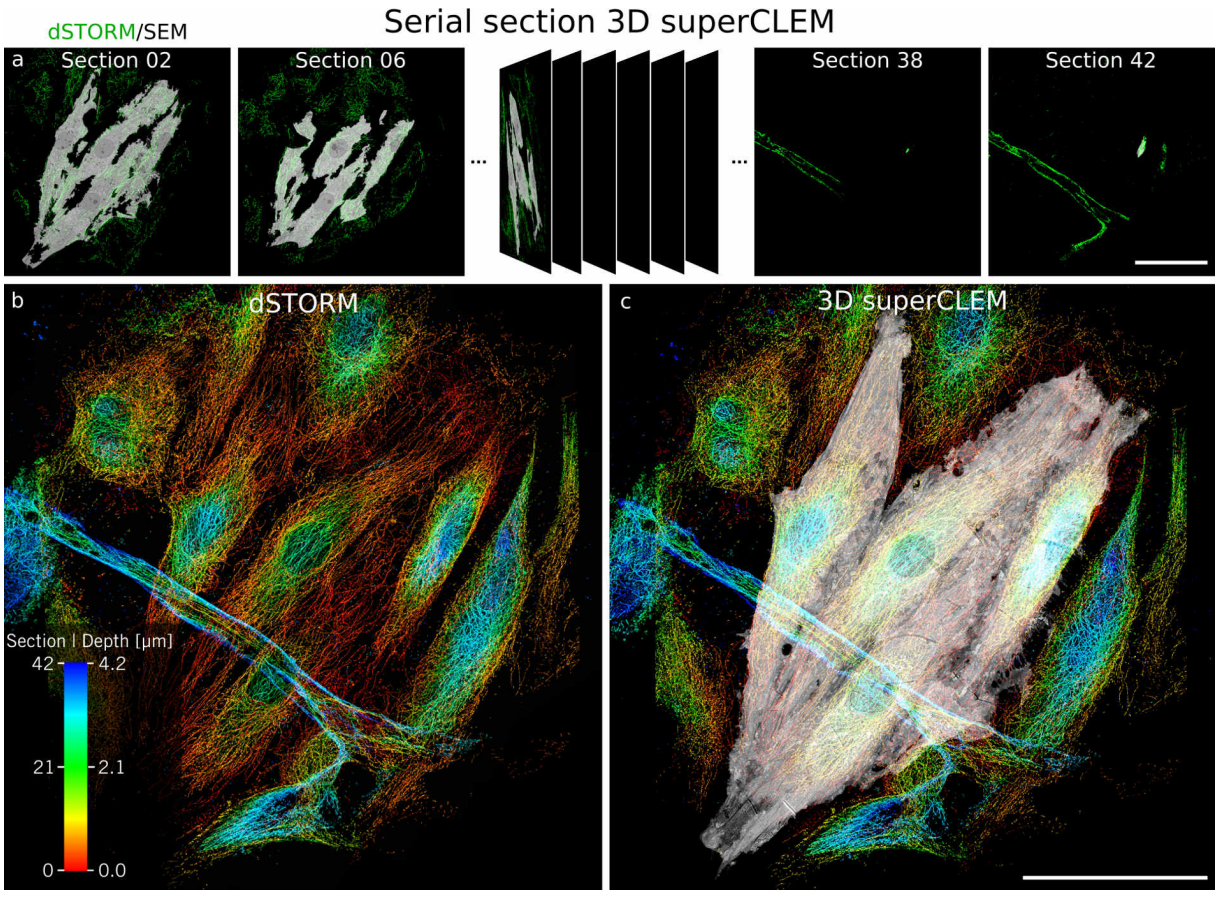

Fig. 5.29: Volumetric correlative reconstruction of serial sectioned SASP-primed LSEC in dSTORM and SEM. Using TrakEM2 in combination with MultiStackReg for individual volumetric alignment, followed by manual correlative registration using BigWarp, serial sections are volumetrically aligned. a) alignment of dSTORM reconstructions (green) and SEM micrographs (gray) for 42 sections at 100 nm section height. b) Volumetric serial section dSTORM reconstruction of microtubeles in SASP-primed LSECs. c) Super-vCLEM reconstruction of SASP-primed LSEC. LSEC were fixed in 4% PFA, indirectly immunolabelled for microtubules and post-fixed in 2% GA, contrasted with 0.1% OsO_4, and 4% neodymium acetate. DMPA LR White resin was polymerised at -30 °C. On section post-staining with Reynolds' lead citrate and 2% uranyl acetate. SEM acquisition using SE_{II} detector. Scale bar: a-c) 50 µm.

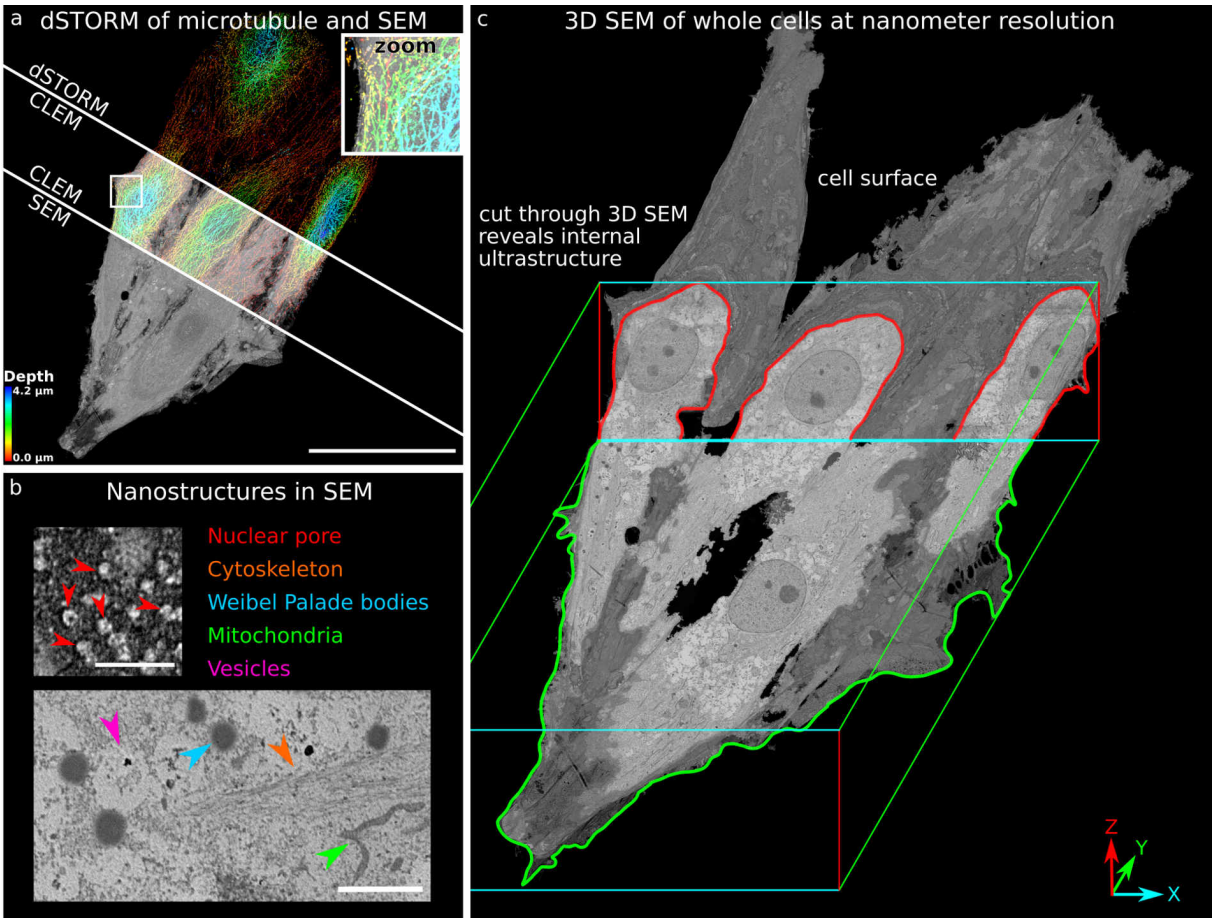

Fig. 5.30: Ultrastructural analysis of volumetric correlative reconstruction (3D superCLEM) of serial sectioned SASP-primed LSEC in dSTORM and SEM. a) Overlay of correlated modalities in dSTORM and SEM. b) Ultrastructures observed in SEM micrographs. c) Perspective cut through of SEM micrograph of SASP-primed LSEC reveals high resolution volumetric ultrastructural information at nanometre resolution. LSEC were fixed in 4% PFA, indirectly immunolabelled for microtubules and post-fixed in 2% GA, contrasted with 0.1% OsO_4, and 4% neodymium acetate. DMPA LR White resin was polymerised at -30 °C. On section post-staining with Reynolds' lead citrate and 2% uranyl acetate. SEM acquisition using SE_{II} detector. Scale bar: a) 50 µm, b - top) 1 µm, b - bottom) 2 µm.

5.3 Discussion

With the rise of vEM and vCLEM, the need for improved resin compositions better preserving the fluorescent signal has become a renewed focus (6). Within this chapter, the screening for novel resin compositions with quantitative preservation of fluorescence was successfully accomplished. Using these resin compositions, the cellular functional organisation can be studied in *in-resin* CLEM at a fidelity not obtainable before. Finally, the newly developed resin compositions were applied to investigate the structure-function relationship in LSEC exposed to SASP with a successful correlative 3D reconstruction of both dSTORM and SEM.

Limitations

As the development of novel resin compositions for quantitative fluorophore preservation in CLEM is a work in progress, many additional validations can be performed. For example, the absorption spectra were found to have a high variability in the absorption intensity, as the resins also developed a wide-band absorption spectrum during polymerisation. This made robust determination of the absorption spectrum of the fluorophore difficult. The current iteration to correct for the resin absorption uses a polynomial fit of degree 5 on a blank resin sample. This polynome is then scaled to best fit the observed baseline of the fluorophore-resin composite spectrum. Yet, fitting was often insufficient leading to exclusion of the sample from further analysis. Additionally, even though solvatochromic effects were commonly observed, altering both the absorption and emission spectrum, in the current analysis only the peak absorption and emission intensity were determined, potentially leading to systematic error when determining

the ensemble fluorescence preservation. A better implementation would be integration of the fluorophore specific signal. This was not implemented within this work, as this analysis is even more sensitive to a correct baseline determination for the absorption. Similarly, due to solvatochromic effects, the emission spectrum was often blue-shifted and therefore the emission profile close to the excitation was not recovered, making an analysis of the area under the curve prone to systematic errors.

Another limitation is that all photophysical properties were determined in polymerised resins and compared to pre polymerisation. By nature, the molecular preservation of fluorophores cannot exceed 100%, yet the fluorescence intensity on average increased in the polymerised resin due to changes in the chemical structure and altered solvatochromic effects, making the determination of the fluorescence preservation indirect. Determining the molecular preservation on the other hand proved challenging. While the ELE analysis of AF647 strongly indicates a quantitative preservation, the molecular preservation of all fluorophores incompatible with dSTORM imaging remains elusive. Analysis of bleaching step traces in sectioned samples in Fig. 5.12 showed successful detection of a limited amount of bleaching steps. Further optimisation of the imaging buffers could allow for PBSA or CoPS analysis of the nuclear pore complex to investigate the molecular preservation beyond AF647. Furthermore, the emission and excitation spectrum in sections was not determined within this work but is more relevant for the fluorophore characteristics in fluorescence microscopy. The high degree of solvent accessibility found for the established resin sections indicates that the photophysical properties likely are a superposition of aqueous and *in-resin* properties.

A second consideration currently not investigated is the ability of the fluorophores to rotate freely in resin. Steric hindrance of free rotation can result in localisation errors up to 10 nm (70). Here, using the quad-APD confocal setup, the polarisation and rotational diffusion coefficient could be determined to estimate the influence the resin has on the orientation of the fluorophore. Furthermore, using Nanorulers, the distance between two fluorophores can be analysed both pre and post polymerisation, further demonstrating the ability to resolve emitters with no measurable degradation in reconstruction quality.

A problem commonly observed in electron microscopy are deposits of needle-like appearance of unknown origin (see Fig. 5.17, Section 1 & 3). These were invisible in light and fluorescence microscopy but had a strong contrast in SEM, masking the underlying sections. Several attempts to remove them were unsuccessful. During testing it was confirmed, that these deposits were on top of the sections and not embedded into the resin, limiting the origin. Initially, the water source in Birmingham was suspected to release nanoscale ceramic shard, then the dSTORM buffer with its high salt, glucose and protein content was investigated. Replacing both the water source and imaging the sections in EM only without prior exposure to dSTORM buffer, still showed the presence of the needle-like deposits. Further testing needs to determine the origin of these deposits. Likely sources could be the glue used to connect the serial sections, the substance used to reversibly adhere the coverslips to the transport frame or the cleaning utensils and chemicals used for the ultramicrotome.

The fluorescence preservation in resins was only validated for LR White based resins. Several other methacrylate-based resins exist, including K4M or HM20. Notably, HM20 also uses BME as initiator and could therefore be suspected to have a similarly good

preservation of fluorescence. Yet, the validation shown within this work provided the first of a kind evidence for quantitative preservation of organic fluorophores during resin embedding. Future work will provide evidence to the extent of molecular fluorophore preservation as well as compatibility with dSTORM and other high resolution or quantitative imaging techniques.

Alternative workflows

Correlative light-electron microscopy has historically been a technique at which a multitude of workflows exist, each tailored to the specific needs and research foci, as they all have different drawbacks (107). For fixation, both chemical fixation and vitrification exist, similarly, samples could either be non-embedded or embedded in resin or sucrose. Furthermore, many orthogonal imaging acquisition techniques exist, including serial sectioning, FIB milling, but also the imaging technique itself where either SEM or transmission electron microscopy could be used. Lastly, the utilisation of light microscopy can have various purposes, from only being used to target the region of interest to a correlative analysis methology using super-resolution microscopy (107).

The newly developed resins address the challenges of *in-resin* CLEM. *In-resin* CLEM benefits from the easier correlation as no or very low deformations between the two modalities exist, as both modalities are acquired after embedding where local deformations can occur from shear stresses. But both contrasting and resin polymerisation have historically led to a loss of fluorophores limiting the use (6). Specialised applications have been developed using fluorescent proteins that can partially withstand embedding and osmium contrasting, named mEosEM (38). Alternatively, nanocrystals (245) or high abundant targets where fluorophore loss is less critical have been used (113, 246).

In 2020 Hoffman *et al.* published a work using high pressure freezing and a cryoCLEM workflow with 4 nm isotropic EM resolution and two-colour cryo-SMLM with 40 nm accuracy (106). Here cryo-SMLM was performed at 8 K, where organic fluorophores exhibit a natural blinking behaviour (106). Next samples were freeze substituted and imaged using FIB-SEM. Freeze substitution and embedding after cryo-SMLM was found to introduce spatially non-linear deformations with a median of 89 nm (106). Yet, using organelle landmarks, these could be compensated for using computational post-processing, leading to the highest fidelity CLEM reconstructions to date (6). The implementation by Hoffman *et al.* exceeds the quality of the established approach within this thesis but utilises highly specialised and custom equipment. Using our approach, commercial equipment can be utilised making the application of these novel resin compositions more easily adaptable by other laboratories. Additionally, the implementation established within this work is non-destructive, compared to FIB-SEM, allowing the re-analysis of relevant regions with additional techniques. Yet compression and knife artefacts are a potential risk when utilising the serial sectioning technique.

Outlook

While this workflow allows for super-vCLEM imaging of biological targets, many future improvements can be implemented into this workflow. Currently, 50% of fluorescence is lost due to OsO_4 contrasting. Here, improvements in the detectors used in electron microscopy or optimisation in image acquisition could help in minimising the contrasting agents, especially OsO_4 (247, 248, 108). Additionally, an investigation could be performed to test whether OsO_4 could be only performed in on-section post staining after fluorescent acquisition, similar to lead citrate and uranyl acetate post staining currently

performed. Alternatively, OsO_4 could be used for contrasting prior to immunolabelling (and tag-labelling) if the epitopes and tags remain functional after embedding. Destruction of fluorescent proteins and their chromophore system in presence of OsO_4 is not necessarily an indicator of destruction of the catalytic activity of SNAP and HaloTag. Additionally, on section immunolabelling is an established technique in CLEM, demonstrating that epitopes are at least partially preserved (249).

Besides changes to the contrasting agents, resin heights measured with a profilometer could be routinely taken into account to reconstruct the volumetric images using the actual resin height, compensating the 9 nm section to section variability. Further improvements could consist of using astigmatic 3D dSTORM imaging, to resolve the in-section 3D localisation with higher axial resolution. This would allow to increase the section height, without reducing the axial resolution in dSTORM increasing acquisition speeds.

As a next technical project, the classification, segmentation and correlative analysis of acquired super-vCLEM volumes is investigated to extract meaningful parameters and explore the structure-function relationship observed for LSEC. Here, dual-colour ICAM1 and microtubule CLEM imaging could prove beneficial. ICAM1 is an adhesion molecule upregulated in LSEC when exposed to SASP and co-responsible for the immune migration (118). Additionally, the microtubule cytoskeleton is known to interact and influence the expression of ICAM1 (241, 242). In first tests, three ICAM1 antibodies were evaluated but resulted in either low specific labelling or high unspecific labelling. Further optimisation is needed to then allow for utilisation in dual-colour dSTORM imaging. Additionally, performing super-vCLEM on drug treated SASP-primed LSEC

could unravel why Nocodazole and Colchicine allow for recovery of the microtubule alignment order, while the polarity of cells remains elevated (Fig. 5.27).

Besides the use of LSEC, T cells and platelets are currently investigated as targets for super-vCLEM. Platelets benefit from being relatively small, allowing for acquisition of tens of platelets within a single FOV and faster acquisition in EM, generating a robust statistical analysis currently beyond reach for LSEC with their large cellular volume ($50 \times 50 \times 4$ µm^3). Here, external fiducials such as the established *S. epidermis* biological markers are crucial to generate robust volumetric reconstruction with sufficient landmarks in fluorescence microscopy (Fig. 5.23).

Overall, the developed resins allow for the routine use in CLEM with near quantitative preservation of fluorophores. Additionally, volumetric serial section dSTORM was found to be a suitable technique by itself for specialised application, further expanding the applicability of these resins. Here, complete fluorophore preservation results in volumetric reconstruction of cells of unprecedented quality for large image depths (Fig. 5.19, SI 16).

Chapter 6

General Discussion

6.1 Conclusion

Advancements in microscopy have long been pivotal for improving our understanding of the intricate cellular architecture. This thesis highlights several advancements in the field of cellular nanoscale imaging through the development of novel super-resolution and volumetric imaging techniques. These breakthroughs allow for an unprecedented visualisation of the functional context within the cellular ultrastructure. The integration of cross-disciplinary approaches, melding science, technology, engineering, and mathematics, has been instrumental in pushing the boundaries of biomedical research. This fusion of diverse fields not only proved successful but will likely become increasingly important for future explorations of biomedical samples. The outcomes of this work are expected to have far-reaching implications in understanding complex biological systems.

The system developed in Chap. 3 functions as the basis for all subsequent method developments of Chap. 4, 5. While novel developments of microscopy systems exist, approaching molecular resolution with Ångström localisation precision, their application is often limited by the imperfect labelling efficiency of state-of-the-art labelling techniques, typically between 20-70%, and the linkage-error between fluorescent label and the structure of interest (250, 251, 252, 74). Additionally, photophysical effects between fluorophores become prominent for sub-10 nm of distance, further limiting the general applicability (68). Therefore, the comparatively simplified acquisition with routine super-resolution imaging techniques such as dSTORM and PAINT, limited to a resolution of 11 nm under ideal conditions, provides sufficiently high spatial resolution for most techniques. Contrary, the non-complete labelling of a POI hightlights the importance of improved labelling calibration techniques, such as ProDOL to determine and optimise

the labelling efficiency and absolute counting techniques such as quickPBSA and CoPS. In Chap. 4, the application and development of a novel DOL technique has been established and cross-validated, allowing for accurate, robust and fast calibration of the labelling efficiency, compared to the use of counting standards such as NPC with an absolute counting technique, as this needs homozygous knock-in cell lines, specialised equipment for CoPS or fluorophores compatible with dSTORM for ELE.

In Chap. 4 various other applications of the established single-molecule localisation microscopy (SMLM) system are shown which highlight the potential of super-resolution microscopy in the study of nanoscale cellular processes of biomedical relevance. Alarmin S100A8/A9 is correlated with COVID-19 disease severity and prognostic outcome (191). By studying the distribution of the most relevant binding partners for S100A8/A9 in platelets such as GPIbα, TLR4, or CD36 and their heterogeneous cellular-response can assist in unraveling the mechanism of COVID-19 related thrombosis, potentially linked to a subpopulation of procoagulant platelets (121, 253). Similarly, the method developed to detect the presence of persistent nanoscale homologies of membrane order using ratiometric PAINT can be beneficial for studying tumourigenesis and tumour progression. The dysregulation of membrane composition is a key player in affecting the signal transduction, linking the extracellular with the intracellular, and therefore the correct homeostasis of a cell (176, 254).

Finally, the established resin compositions with quantitative preservation of fluorophores during resin embedding allow for significantly improved *in-resin* super-vCLEM. This year, the journal Nature chose volume EM as one of the seven technologies to look out for (255). Similarly in 2023, Rita Strack and Lucy Collinson both highlighted the ”quiet

revolution" volume EM and the often accompanying correlative fluorescence microscopy (vCLEM) have undergone, as vEM does not reveal the functional organisation of a POI within the ultrastructural context by itself (1, 2). This *in situ* structural cell biology has become a key player and the Chan Zuckerberg Initiative has a continued interest in the establishment of simplified CLEM workflows and improved CLEM labelling strategies to advance our understanding of cellular biology[1]. Therefore, novel resin compositions can be of high relevance for the advancement of vEM and vCLEM, improving the correlative super-resolution microscopy fidelity and thereby bridging the gap between functional fluorescence microscopy and ultrastructural electron microscopy.

6.2 Outlook

The system developed in Chap. 3 is a highly versatile system, well suited for various experiments and applications. Several projects have been initiated, applying the 3D and multi-colour dSTORM capabilites to samples of biomedical relevance for investigation of T cell microclusters and platelet receptor organisation. This system will not only benefit SMLM techniques but can also find use in other microscopy methods, including expansion microscopy and SRRF. Here, the relatively large FOV with high illumination uniformity and significantly improved edge steepness compared to a Gaussian illumination profile allows for routine acquisition of high fidelity images. Additionally, the high degree of calibration and repeatability has proven beneficial for the establishment of imaging correction routines as highlighted in its use for the generation of calibration data for vector-based PSF correction, and Bayesian illumination correction.

[1] `https://chanzuckerberg.com/science/programs-resources/imaging/frontiers/`, 01/01/2024

Similarly, the need for strategies to determine the cellular labelling efficiency and absolute protein copy number has become of increasing importance, as the achievable resolution in SMLM approaches the molecular resolution. Thus, a high labelling efficiency is required to achieve a sufficient sampling density which is necessary for the reconstruction of oligomeric stoichiometries (256, 257, 68). Here, the developed and validated ProDOL approach in Chap. 4, based on previous work by Yserentant and Hänselmann, can be expanded upon (5, 188, 187). The ProDOL construct is currently limited to HaloTag and SNAP-tag, but could be expanded to other protein-tags, such as the reversible trimethoprim (TMP)-tag and other cellular compartments, such as the mitochondria membrane (201, 258). Additionally, the construct can find its application in determining the labelling efficiency of immunolabelling, though here the performance must be further validated, as the apparent DOL distribution will be convoluted with an additional dye-to-antibody distribution and the primary-to-secondary antibody ratio.

Improvement of the routine determination of DOL is synergistic with improvements in absolute counting techniques. The rise of artificial intelligence can prove beneficial in recovering the stoichiometry and clustering of large complexes where an analytical solution can no longer be achieved in a timely manner (259, 260). Novel robust U-net neural networks could lead to an increased counting range in various absolute counting techniques such as PBSA and CoPS (Fig. 6.1) (259).

Last but not least, the developed resins with quantitative preservation of fluorophores during embedding will be applied in future collaborations as well as continued to be applied to study the structure-function relationship in SASP-primed LSEC. In future collaboration, the resin compositions can be tested and applied to CLEM workflows

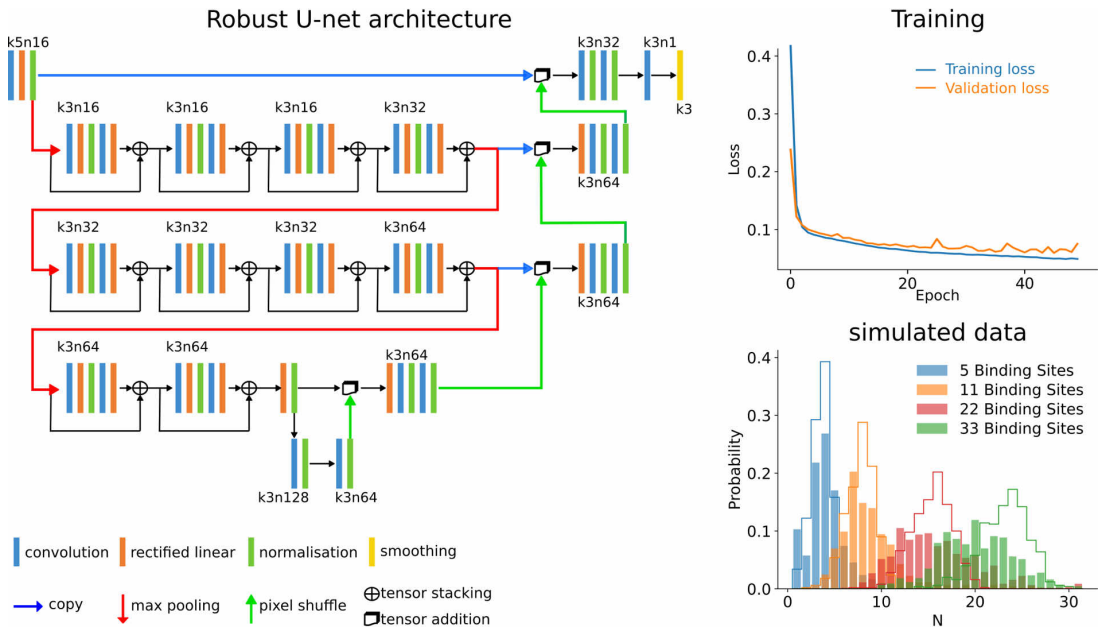

Fig. 6.1: Exemplary neural network for determination of absolute emitter numbers. A modified robust U-net architecture is used for emitter density recovery from CoPS data (261). The network improves the spatial resolution while simultaneously allows for emitter number determination from the determined emitter density map. The neural network performs well on simulated data up to 22 binding sites but shows an undercounting for 33 binding sites. Adapted from unpublished work developed in cooperation with Johan Hummert.

utilising high-pressure freezing followed by freeze substitution. The superior structural preservation of cryo-CLEM can further improve the fidelity of samples and will demonstrate the broad application these resins have for CLEM. In a next step, the compatibility of established polymerisation initiators is validated with other commercial acrylic embedding resins such as HM20 or K4M. Furthermore, methods to recover the *in-resin* 3D localisation are currently investigated to further improve the axial resolution. Here, MIET, total internal reflection fluorescence (TIRF)-based axial localisation determination and astigmatic 3D dSTORM are investigated, each posing different benefits and challenges (262, 128, 135, 236, 237, 243).

In summary, this thesis marks a significant leap in cellular nanoscale imaging, blending interdisciplinary approaches to develop novel super-resolution and volumetric imaging techniques, thereby significantly advancing the understanding of the functional cellular organisation in an ultrastructural context.

Chapter 7

List of References

1. Collinson LM, Bosch C, Bullen A, Burden JJ, Carzaniga R, Cheng C, et al. Volume EM: a quiet revolution takes shape. Nature Methods. 2023;20(6):777-82.

2. Strack R. Fluorescence in structural biology. Nature Methods. 2023;20(1):35.

3. Hummert J, Yserentant K, Fink T, Euchner J, Ho YX, Tashev SA, et al. Photobleaching step analysis for robust determination of protein complex stoichiometries. Molecular Biology of the Cell. 2021 9;32(21):ar35.

4. Lelek M, Gyparaki MT, Beliu G, Schueder F, Griffié J, Manley S, et al. Single-molecule localization microscopy. Nature Reviews Methods Primers. 2021;1(1):39.

5. Tashev SA, Euchner J, Yserentant K, Hänselmann S, Hild F, Chmielewicz W, et al. A General Method to Accurately Count Molecular Complexes and Determine the Degree of Labelling in Cells Using Protein Tags. bioRxiv. 2023 1:2023.09.08.556847.

6. van den Dries K, Fransen J, Cambi A. Fluorescence CLEM in biology: historic developments and current super-resolution applications. FEBS Letters. 2022 10;596(19):2486-96.

7. Hooke R. Micrographia: or, Some physiological descriptions of minute bodies made by magnifying glasses. With observations and inquiries thereupon. London: Rosenwald Collection; 1665.

8. van Leewenhoeck A. Observations, Communicated to the Publisher by Mr. Antony van Leewenhoeck, in a Dutch Letter of the 9th of Octob. 1676. Here English'd: concerning Little Animals by Him Observed in Rain-Well-Sea. and Snow Water; as Also in Water Wherein Pepper Had Lain Infused. Philosophical Transactions (1665-1678). 1677;12:821-31.

9. Lane N. The unseen World: Reflections on Leeuwenhoek (1677) 'Concerning little animals'. Philosophical Transactions of The Royal Society B Biological Sciences. 2015 4;370.

10. von Fraunhofer J. Bestimmung des Brechungs- und des Farben-Zerstreuungsvermögens verschiedener Glasarten, in Bezug auf die Vervollkommnung achromatischer Fernröhre. München: Königliche Akademie der Wissenschaften; 1814.

11. Abbe E. Beiträge zur Theorie des Mikroskops und der mikroskopischen Wahrnehmung. Archiv für Mikroskopische Anatomie. 1873;9(1):413-68.

12. Zanacchi FC, Bianchini P, Vicidomini G. Fluorescence microscopy in the spotlight. Microscopy Research and Technique. 2014 7;77(7):479-82.

13. Coons AH, Creech HJ, Jones RN. Immunological Properties of an Antibody Containing a Fluorescent Group. Proceedings of the Society for Experimental Biology and Medicine. 1941 6;47(2):200-2.

14. Shimomura O, Johnson FH, Saiga Y. Purification and properties of Cypridina luciferase. Journal of Cellular and Comparative Physiology. 1961 10;58(2):113-23.

15. Chalfie M, Tu Y, Euskirchen G, Ward WW, Prasher DC. Green Fluorescent Protein as a Marker for Gene Expression. Science. 1994 2;263(5148):802-5.

16. Heim R, Cubitt AB, Tsien RY. Improved green fluorescence. Nature. 1995;373(6516):663-4.

17. Jablonski A. Efficiency of Anti-Stokes Fluorescence in Dyes. Nature. 1933;131(3319):839-40.

18. Dzebo D. Photon Upconversion through Triplet-Triplet Annihilation: Towards Higher Efficiency and Solid State Applications; 2016.

19. Đačanin Far L, Dramićanin MD. Luminescence Thermometry with Nanoparticles: A Review. Nanomaterials. 2023;13(21).

20. Pauli W. Über den Zusammenhang des Abschlusses der Elektronengruppen im Atom mit der Komplexstruktur der Spektren. Zeitschrift für Physik. 1925;31(1):765-83.

21. Albani JR. Chapter 2 - Fluorescence: Principles and Observables. In: Albani JR, editor. Structure and Dynamics of Macromolecules: Absorption and Fluorescence Studies. Amsterdam: Elsevier Science; 2004. p. 55-98.

22. Ashoka AH, Aparin IO, Reisch A, Klymchenko AS. Brightness of fluorescent organic nanomaterials. Chemical Society Reviews. 2023;52(14):4525-48.

23. Berezin MY, Achilefu S. Fluorescence Lifetime Measurements and Biological Imaging. Chemical Reviews. 2010 5;110(5):2641-84.

24. Hell S, Belov V, Mitronova G, Bossi M, Moneron G, Wurm C, et al. Fluorinated rhodamines as photostable fluorescent dyes for labelling and imaging techniques. USPTO. 2009;US8735444B2.

25. Grimm JB, Brown TA, Tkachuk AN, Lavis LD. General Synthetic Method for Si-Fluoresceins and Si-Rhodamines. ACS Central Science. 2017 9;3(9):975-85.

26. Ye Z, Xiao Y, Guo H, Wang C. Specific and photostable rhodamine-based tracker for 3D video imaging of single acidic organelles. RSC Advances. 2014;4(71):37547-55.

27. Perfilov MM, Gurskaya NG, Serebrovskaya EO, Melnikov PA, Kharitonov SL, Lewis TR, et al. Highly photostable fluorescent labeling of proteins in live cells using exchangeable coiled coils heterodimerization. Cellular and Molecular Life Sciences. 2020;77(21):4429-40.

28. Icha J, Weber M, Waters JC, Norden C. Phototoxicity in live fluorescence microscopy, and how to avoid it. BioEssays. 2017 8;39(8):1700003.

29. Grimm JB, Muthusamy AK, Liang Y, Brown TA, Lemon WC, Patel R, et al. A general method to fine-tune fluorophores for live-cell and in vivo imaging. Nature Methods. 2017;14(10):987-94.

30. Chozinski TJ, Gagnon LA, Vaughan JC. Twinkle, twinkle little star: Photoswitchable fluorophores for super-resolution imaging. FEBS Letters. 2014;588(19):3603-12.

31. Samanta S, Lai K, Wu F, Liu Y, Cai S, Yang X, et al. Xanthene, cyanine, oxazine and BODIPY: the four pillars of the fluorophore empire for super-resolution bioimaging. Chemical Society Reviews. 2023;52(20):7197-261.

32. Grimm JB, Lavis LD. Caveat fluorophore: an insiders' guide to small-molecule fluorescent labels. Nature Methods. 2022;19(2):149-58.

33. Latt SA, Stetten G, Juergens LA, Willard HF, Scher CD. Recent developments in the detection of deoxyribonucleic acid synthesis by 33258 Hoechst fluorescence. Journal of Histochemistry & Cytochemistry. 1975 7;23(7):493-505.

34. Tsien R. Constructing and Exploiting the Fluorescent Protein Paintbox (Nobel Lecture). Angewandte Chemie International Edition. 2009 7;48(31):5612-26.

35. Shinoda H, Shannon M, Nagai T. Fluorescent Proteins for Investigating Biological Events in Acidic Environments. International Journal of Molecular Sciences. 2018;19(6).

36. Lukyanov KA, Chudakov DM, Lukyanov S, Verkhusha VV. Photoactivatable fluorescent proteins. Nature Reviews Molecular Cell Biology. 2005;6(11):885-90.

37. Shcherbakova DM, Sengupta P, Lippincott-Schwartz J, Verkhusha VV. Photocontrollable Fluorescent Proteins for Superresolution Imaging. Annual Review of Biophysics. 2014.

38. Fu Z, Peng D, Zhang M, Xue F, Zhang R, He W, et al. mEosEM withstands osmium staining and Epon embedding for super-resolution CLEM. Nature Methods. 2020;17(1):55-8.

39. Hirano M, Ando R, Shimozono S, Sugiyama M, Takeda N, Kurokawa H, et al. A highly photostable and bright green fluorescent protein. Nature Biotechnology. 2022;40(7):1132-42.

40. Hermanson GT. Chapter 3 - The Reactions of Bioconjugation. In: Hermanson GT, editor. Bioconjugate Techniques (Third Edition). Boston: Academic Press; 2013. p. 229-58.

41. Bragg PD, Hou C. Subunit composition, function, and spatial arrangement in the Ca2+- and Mg2+-activated adenosine triphosphatases of Escherichia coli and Salmonella typhimurium. Archives of Biochemistry and Biophysics. 1975;167(1):311-21.

42. Vázquez-Gutiérrez JL, Langton M. Current potential and limitations of immunolabeling in cereal grain research. Trends in Food Science & Technology. 2015;41(2):105-17.

43. Wani MC, Taylor HL, Wall ME, Coggon P, McPhail AT. Plant antitumor agents. VI. Isolation and structure of taxol, a novel antileukemic and antitumor agent from Taxus brevifolia. Journal of the American Chemical Society. 1971 5;93(9):2325-7.

44. Sung DB, Lee JS. Natural-product-based fluorescent probes: recent advances and applications. RSC Medicinal Chemistry. 2023;14(3):412-32.

45. Wieczorek A, Werther P, Euchner J, Wombacher R. Green- to far-red-emitting fluorogenic tetrazine probes – synthetic access and no-wash protein imaging inside living cells. Chemical Science. 2017;8(2):1506-10.

46. Leonetti MD, Sekine S, Kamiyama D, Weissman JS, Huang B. A scalable strategy for high-throughput GFP tagging of endogenous human proteins. Proceedings of the National Academy of Sciences. 2016 6;113(25):E3501-8.

47. Los GV, Encell LP, McDougall MG, Hartzell DD, Karassina N, Zimprich C, et al. HaloTag: A Novel Protein Labeling Technology for Cell Imaging and Protein Analysis. ACS Chemical Biology. 2008 6;3(6):373-82.

48. Keppler A, Pick H, Arrivoli C, Vogel H, Johnsson K. Labeling of fusion proteins with synthetic fluorophores in live cells. Proceedings of the National Academy of Sciences. 2004 7;101(27):9955-9.

49. Euchner J. Achieving 3D Super-Resolution Correlative Light- Electron Microscopy. Master's thesis. Heidelberg: University of Heidelberg; 2020.

50. Klar TA, Hell SW. Subdiffraction resolution in far-field fluorescence microscopy. Optics Letters. 1999;24(14):954-6.

51. Betzig E, Patterson GH, Sougrat R, Lindwasser OW, Olenych S, Bonifacino JS, et al. Imaging Intracellular Fluorescent Proteins at Nanometer Resolution. Science. 2006 9;313(5793):1642-5.

52. Rust MJ, Bates M, Zhuang X. Sub-diffraction-limit imaging by stochastic optical reconstruction microscopy (STORM). Nature Methods. 2006;3(10):793-6.

53. Dyba M, Hell SW. Photostability of a fluorescent marker under pulsed excited-state depletion through stimulated emission. Applied Optics. 2003;42(25):5123-9.

54. Willig KI, Kellner RR, Medda R, Hein B, Jakobs S, Hell SW. Nanoscale resolution in GFP-based microscopy. Nature Methods. 2006;3(9):721-3.

55. Moerner WE. Single-molecule mountains yield nanoscale cell images. Nature Methods. 2006;3(10):781-2.

56. Heilemann M, van de Linde S, Schüttpelz M, Kasper R, Seefeldt B, Mukherjee A, et al. Subdiffraction-Resolution Fluorescence Imaging with Conventional Fluorescent Probes. Angewandte Chemie International Edition. 2008 8;47(33):6172-6.

57. Shroff H, Galbraith CG, Galbraith JA, White H, Gillette J, Olenych S, et al. Dual-color superresolution imaging of genetically expressed probes within individual

adhesion complexes. Proceedings of the National Academy of Sciences. 2007 12;104(51):20308-13.

58. Huang B, Wang W, Bates M, Zhuang X. Three-Dimensional Super-Resolution Imaging by Stochastic Optical Reconstruction Microscopy. Science. 2008 2;319(5864):810-3.

59. Dempsey GT, Bates M, Kowtoniuk WE, Liu DR, Tsien RY, Zhuang X. Photoswitching Mechanism of Cyanine Dyes. Journal of the American Chemical Society. 2009 12;131(51):18192-3.

60. Sharonov A, Hochstrasser RM. Wide-field subdiffraction imaging by accumulated binding of diffusing probes. Proceedings of the National Academy of Sciences. 2006 12;103(50):18911-6.

61. Thompson RE, Larson DR, Webb WW. Precise Nanometer Localization Analysis for Individual Fluorescent Probes. Biophysical Journal. 2002;82(5):2775-83.

62. Mortensen KI, Churchman LS, Spudich JA, Flyvbjerg H. Optimized localization analysis for single-molecule tracking and super-resolution microscopy. Nature Methods. 2010;7(5):377-81.

63. Jimenez A, Friedl K, Leterrier C. About samples, giving examples: Optimized Single Molecule Localization Microscopy. Methods. 2020;174:100-14.

64. Nyquist H. Certain Topics in Telegraph Transmission Theory. Transactions of the American Institute of Electrical Engineers. 1928;47(2):617-44.

65. Shannon CE. Communication in the Presence of Noise. Proceedings of the IRE. 1949;37(1):10-21.

66. Kulaitis G, Munk A, Werner F. What is resolution? A statistical minimax testing perspective on super-resolution microscopy. ArXiv. 2020.

67. Koho S, Tortarolo G, Castello M, Deguchi T, Diaspro A, Vicidomini G. Fourier ring correlation simplifies image restoration in fluorescence microscopy. Nature Communications. 2019;10(1):3103.

68. Helmerich DA, Beliu G, Taban D, Meub M, Streit M, Kuhlemann A, et al. Photoswitching fingerprint analysis bypasses the 10-nm resolution barrier. Nature Methods. 2022;19(8):986-94.

69. Deschout H, Zanacchi FC, Mlodzianoski M, Diaspro A, Bewersdorf J, Hess ST, et al. Precisely and accurately localizing single emitters in fluorescence microscopy. Nature Methods. 2014;11(3):253-66.

70. Enderlein J, Toprak E, Selvin PR. Polarization effect on position accuracy of fluorophore localization. Optics Express. 2006;14(18):8111-20.

71. Gross D, Webb WW. Molecular counting of low-density lipoprotein particles as individuals and small clusters on cell surfaces. Biophysical Journal. 1986;49(4):901-11.

72. Alberts B, Bray D, Lewis J, Raff M, Roberts K, Watson JD. Molecular Biology of the Cell. 4th ed. Garland; 2002.

73. Grußmayer KS, Yserentant K, Herten DP. Photons in - numbers out: perspectives in quantitative fluorescence microscopy for in situ protein counting. Methods and Applications in Fluorescence. 2019 1;7(1):12003.

74. Hummert J, Tashev SA, Herten DP. An update on molecular counting in fluorescence microscopy. The International Journal of Biochemistry & Cell Biology. 2021;135:105978.

75. Tsai YC, Tsai TH, Chang CP, Chen SF, Lee YM, Shyue SK. Linear correlation between average fluorescence intensity of green fluorescent protein and the multiplicity of infection of recombinant adenovirus. Journal of Biomedical Science. 2015;22(1):31.

76. Finan K, Raulf A, Heilemann M. A Set of Homo-Oligomeric Standards Allows Accurate Protein Counting. Angewandte Chemie International Edition. 2015 10;54(41):12049-52.

77. Schmidt T, Schütz GJ, Baumgartner W, Gruber HJ, Schindler H. Imaging of single molecule diffusion. Proceedings of the National Academy of Sciences. 1996 4;93(7):2926-9.

78. Tsekouras K, Custer TC, Jashnsaz H, Walter NG, Pressé S. A novel method to accurately locate and count large numbers of steps by photobleaching. Molecular Biology of the Cell. 2016 9;27(22):3601-15.

79. Geissbuehler S, Bocchio NL, Dellagiacoma C, Berclaz C, Leutenegger M, Lasser T. Mapping molecular statistics with balanced super-resolution optical fluctuation imaging (bSOFI). Optical Nanoscopy. 2012;1(1):4.

80. Hedde PN, Stakic M, Gratton E. Rapid Measurement of Molecular Transport and Interaction inside Living Cells Using Single Plane Illumination. Scientific Reports. 2014;4(1):7048.

81. Cutrale F, Rodriguez D, Hortigüela V, Chiu CL, Otterstrom J, Mieruszynski S, et al. Using enhanced number and brightness to measure protein oligomerization dynamics in live cells. Nature Protocols. 2019;14(2):616-38.

82. Grußmayer KS, Kurz A, Herten DP. Single-Molecule Studies on the Label Number Distribution of Fluorescent Markers. ChemPhysChem. 2014 3;15(4):734-42.

83. Basché T, Moerner WE, Orrit M, Talon H. Photon antibunching in the fluorescence of a single dye molecule trapped in a solid. Physical Review Letters. 1992 9;69(10):1516-9.

84. Jungmann R, Avendaño MS, Dai M, Woehrstein JB, Agasti SS, Feiger Z, et al. Quantitative super-resolution imaging with qPAINT. Nature Methods. 2016;13(5):439-42.

85. Zwettler FU, Reinhard S, Gambarotto D, Bell TDM, Hamel V, Guichard P, et al. Molecular resolution imaging by post-labeling expansion single-molecule localization microscopy (Ex-SMLM). Nature Communications. 2020;11(1):3388.

86. Thevathasan JV, Kahnwald M, Cieśliński K, Hoess P, Peneti SK, Reitberger M, et al. Nuclear pores as versatile reference standards for quantitative superresolution microscopy. Nature Methods. 2019 10;16(10):1045-53.

87. Dunsing V, Luckner M, Zühlke B, Petazzi RA, Herrmann A, Chiantia S. Optimal fluorescent protein tags for quantifying protein oligomerization in living cells. Scientific Reports. 2018;8(1):10634.

88. Mund M, Ries J. How good are my data? Reference standards in superresolution microscopy. Molecular Biology of the Cell. 2020 8;31(19):2093-6.

89. Virant D, Vojnovic I, Winkelmeier J, Endesfelder M, Turkowyd B, Lando D, et al. Unraveling the kinetochore nanostructure in Schizosaccharomyces pombe using multi-color SMLM imaging. Journal of Cell Biology. 2023 1;222(4).

90. Jablonski A, Salvat F, Powell C, Lee A. NIST Electron Elastic-Scattering Cross-Section Database, Version 4.0. Natl Std. Ref. Data Series (NIST NSRDS), National Institute of Standards and Technology, Gaithersburg, MD; 2016.

91. Baatsen P, Gabarre S, Vints K, Wouters R, Vandael D, Goodchild R, et al. Preservation of Fluorescence Signal and Imaging Optimization for Integrated Light and Electron Microscopy. Frontiers in Cell and Developmental Biology. 2021;9.

92. Seligman AM, Wasserkrug HL, Hanker JS. A new staining method (OTO) for enhancing contrast of lipid-containing membranes and droplets in osmium tetroxide-fixed tissue with osmiophilic thiocarbohydrazide (TCH). Journal of Cell Biology. 1966 8;30(2):424-32.

93. Watson ML. Staining of Tissue Sections for Electron Microscopy with Heavy Metals. The Journal of Biophysical and Biochemical Cytology. 1958 7;4(4):475-8.

94. Huxley HE, Zubay G. Preferential Staining of Nucleic Acid-Containing Structures for Electron Microscopy. The Journal of Biophysical and Biochemical Cytology. 1961;11(2):273-96.

95. Reynolds ES. The use of lead citrate at high pH as an electron-opaque stain in electron microscopy. Journal of Cell Biology. 1963 4;17(1):208-12.

96. Kuipers J, Giepmans BNG. Neodymium as an alternative contrast for uranium in electron microscopy. Histochemistry and Cell Biology. 2020;153(4):271-7.

97. Koster A, Klumperman J. Electron microscopy in cell biology: Integrating structure and function. Nature reviews Molecular cell biology. 2003 10.

98. Cheville NF, Stasko J. Techniques in Electron Microscopy of Animal Tissue. Veterinary Pathology. 2013 10;51(1):28-41.

99. Drummy LF, Yang J, Martin DC. Low-voltage electron microscopy of polymer and organic molecular thin films. Ultramicroscopy. 2004;99(4):247-56.

100. Postek MT, Vladár AE, Villarrubia JS, Muto A. Comparison of Electron Imaging Modes for Dimensional Measurements in the Scanning Electron Microscope†. Microscopy and Microanalysis. 2016 8;22(4):768-77.

101. Bouwer JC, Deerinck TJ, Bushong E, Astakhov V, Ramachandra R, Peltier ST, et al. Deceleration of probe beam by stage bias potential improves resolution of serial block-face scanning electron microscopic images. Advanced Structural and Chemical Imaging. 2016;2(1):11.

102. Garitagoitia Cid A, Rosenkranz R, Zschech E. Optimization of the SEM Working Conditions: EsB Detector at Low Voltage. Advanced Engineering Materials. 2016 2;18(2):185-93.

103. Griffin BJ. A comparison of conventional Everhart-Thornley style and in-lens secondary electron detectors—a further variable in scanning electron microscopy. Scanning. 2011 5;33(3):162-73.

104. Guthrey H, Moseley J. A Review and Perspective on Cathodoluminescence Analysis of Halide Perovskites. Advanced Energy Materials. 2020 7;10(26):1903840.

105. Rieder CL, Bowser SS. Correlative immunofluorescence and electron microscopy on the same section of epon-embedded material. Journal of Histochemistry & Cytochemistry. 1985 2;33(2):165-71.

106. Hoffman DP, Shtengel G, Xu CS, Campbell KR, Freeman M, Wang L, et al. Correlative three-dimensional super-resolution and block-face electron microscopy of whole vitreously frozen cells. Science. 2020 1;367(6475).

107. Bykov YS, Cortese M, Briggs JAG, Bartenschlager R. Correlative light and electron microscopy methods for the study of virus–cell interactions. FEBS Letters. 2016 7;590(13):1877-95.

108. Heiligenstein X, Lucas MS. One for All, All for One: A Close Look at In-Resin Fluorescence Protocols for CLEM. Frontiers in Cell and Developmental Biology. 2022;10.

109. Mironov AA, Beznoussenko GV. Correlative microscopy: a potent tool for the study of rare or unique cellular and tissue events. Journal of Microscopy. 2009 9;235(3):308-21.

110. Möbius W, Posthuma G. Sugar and ice: Immunoelectron microscopy using cryosections according to the Tokuyasu method. Tissue and Cell. 2019;57:90-102.

111. Micheva KD, Smith SJ. Array Tomography: A New Tool for Imaging the Molecular Architecture and Ultrastructure of Neural Circuits. Neuron. 2007 7;55(1):25-36.

112. Wacker I, Schröder RR. Array tomography. Journal of Microscopy. 2013 11;252(2):93-9.

113. Watanabe S, Punge A, Hollopeter G, Willig KI, Hobson RJ, Davis MW, et al. Protein localization in electron micrographs using fluorescence nanoscopy. Nature Methods. 2011;8(1):80-4.

114. Hoare M, Ito Y, Kang TW, Weekes MP, Matheson NJ, Patten DA, et al. NOTCH1 mediates a switch between two distinct secretomes during senescence. Nature Cell Biology. 2016;18(9):979-92.

115. Jooss NJ, Smith CW, Slater A, Montague SJ, Di Y, O'Shea C, et al. Anti-GPVI nanobody blocks collagen- and atherosclerotic plaque-induced GPVI clustering, signaling, and thrombus formation. Journal of Thrombosis and Haemostasis. 2022 11;20(11):2617-31.

116. Hauke S, von Appen A, Quidwai T, Ries J, Wombacher R. Specific protein labeling with caged fluorophores for dual-color imaging and super-resolution microscopy in living cells. Chemical Science. 2017;8(1):559-66.

117. Edelstein A, Amodaj N, Hoover K, Vale R, Stuurman N. Computer Control of Microscopes Using μManager. Current Protocols in Molecular Biology. 2010 10;92(1):1-14.

118. Yin K, Patten D, Gough S, de Barros Gonçalves S, Chan A, Olan I, et al. Senescence-induced endothelial phenotypes underpin immune-mediated senescence surveillance. Genes & Development. 2022 5;36(9-10):533-49.

119. Kuddannaya S, Chuah YJ, Lee MHA, Menon NV, Kang Y, Zhang Y. Surface Chemical Modification of Poly(dimethylsiloxane) for the Enhanced Adhesion and Proliferation of Mesenchymal Stem Cells. ACS Applied Materials & Interfaces. 2013 10;5(19):9777-84.

120. Morales-Penningston NF, Wu J, Farkas ER, Goh SL, Konyakhina TM, Zheng JY, et al. GUV preparation and imaging: Minimizing artifacts. Biochimica et Biophysica Acta (BBA) - Biomembranes. 2010;1798(7):1324-32.

121. Colicchia M, Schrottmaier WC, Perrella G, Reyat JS, Begum J, Slater A, et al. S100A8/A9 drives the formation of procoagulant platelets through GPIbα. Blood. 2022 12;140(24):2626-43.

122. Lord SJ, Velle KB, Mullins RD, Fritz-Laylin LK. SuperPlots: Communicating reproducibility and variability in cell biology. Journal of Cell Biology. 2020 4;219(6).

123. Noël VP, Masoumi S, Parham E, Genest G, Bégin L, Vigneault MA, et al. Tools and tutorial on practical ray tracing for microscopy. Neurophotonics. 2021 1;8(1):010801.

124. Ibrahim KA, Mahecic D, Manley S. Characterization of flat-fielding systems for quantitative microscopy. Optics Express. 2020;28(15):22036-48.

125. Caceci M, Cacheris W. Fitting curves to data: The simplex algorithm is the answer. Byte. 1984 1;9.

126. Mandracchia B, Hua X, Guo C, Son J, Urner T, Jia S. Fast and accurate sCMOS noise correction for fluorescence microscopy. Nature Communications. 2020;11(1):94.

127. Foi A, Trimeche M, Katkovnik V, Egiazarian K. Practical Poissonian-Gaussian Noise Modeling and Fitting for Single-Image Raw-Data. IEEE Transactions on Image Processing. 2008;17(10):1737-54.

128. Ries J. SMAP: a modular super-resolution microscopy analysis platform for SMLM data. Nature Methods. 2020;17(9):870-2.

129. Schmid B, Tripal P, Fraaß T, Kersten C, Ruder B, Grüneboom A, et al. 3Dscript: animating 3D/4D microscopy data using a natural-language-based syntax. Nature Methods. 2019;16(4):278-80.

130. Cetera M, Ramirez-San Juan GR, Oakes PW, Lewellyn L, Fairchild MJ, Tanentzapf G, et al. Epithelial rotation promotes the global alignment of contractile actin bundles during Drosophila egg chamber elongation. Nature Communications. 2014;5(1):5511.

131. Marcotti S, Belo de Freitas D, Troughton LD, Kenny FN, Shaw TJ, Stramer BM, et al. A Workflow for Rapid Unbiased Quantification of Fibrillar Feature Alignment in Biological Images. Frontiers in Computer Science. 2021;3.

132. Power RM, Tschanz A, Zimmermann T, Ries J. Automated 3D multi-color single-molecule localization microscopy. bioRxiv. 2023 1:2023.10.23.563122.

133. Badieirostami M, Lew MD, Thompson MA, Moerner WE. Three-dimensional localization precision of the double-helix point spread function versus astigmatism and biplane. Applied Physics Letters. 2010 10;97(16):161103.

134. Juette MF, Gould TJ, Lessard MD, Mlodzianoski MJ, Nagpure BS, Bennett BT, et al. Three-dimensional sub–100 nm resolution fluorescence microscopy of thick samples. Nature Methods. 2008;5(6):527-9.

135. Szalai AM, Siarry B, Lukin J, Williamson DJ, Unsain N, Cáceres A, et al. Three-dimensional total-internal reflection fluorescence nanoscopy with nanometric axial resolution by photometric localization of single molecules. Nature Communications. 2021;12(1):517.

136. Chen SY, Bestvater F, Schaufler W, Heintzmann R, Cremer C. Patterned illumination single molecule localization microscopy (piSMLM): user defined blinking regions of interest. Optics Express. 2018;26(23):30009-20.

137. Stehr F, Stein J, Schueder F, Schwille P, Jungmann R. Flat-top TIRF illumination boosts DNA-PAINT imaging and quantification. Nature Communications. 2019;10(1):1268.

138. Deschamps J, Rowald A, Ries J. Efficient homogeneous illumination and optical sectioning for quantitative single-molecule localization microscopy. Optics Express. 2016;24(24):28080-90.

139. Douglass KM, Sieben C, Archetti A, Lambert A, Manley S. Super-resolution imaging of multiple cells by optimized flat-field epi-illumination. Nature Photonics. 2016;10(11):705-8.

140. Mau A, Friedl K, Leterrier C, Bourg N, Lévêque-Fort S. Fast widefield scan provides tunable and uniform illumination optimizing super-resolution microscopy on large fields. Nature Communications. 2021;12(1):3077.

141. Chun RF. A High Voltage Charge-Coupled Device (CCD) Controller ASIC for the Large Synoptic Survey Telescope (LSST). In: TRACE. University of Tennessee. Tennessee: University of Tennessee; 2010. p. 1.

142. Theuwissen AJP. CMOS image sensors: State-of-the-art. Solid-State Electronics. 2008;52(9):1401-6.

143. Diekmann R, Till K, Müller M, Simonis M, Schüttpelz M, Huser T. Characterization of an industry-grade CMOS camera well suited for single molecule localization microscopy – high performance super-resolution at low cost. Scientific Reports. 2017;7(1):14425.

144. Slenders E, Perego E, Buttafava M, Tortarolo G, Conca E, Zappone S, et al. Cooled SPAD array detector for low light-dose fluorescence laser scanning microscopy. Biophysical Reports. 2021;1(2):100025.

145. Buttafava M, Villa F, Castello M, Tortarolo G, Conca E, Sanzaro M, et al. SPAD-based asynchronous-readout array detectors for image-scanning microscopy. Optica. 2020;7(7):755-65.

146. Qi L, Sluyterman S, Kooijman K, Mok KRC, Nanver LK. PureB single-photon avalanche diodes for low-energy electron detection down to 200eV. Optics Letters. 2015;40(3):300-3.

147. Ulku AC, Bruschini C, Antolović IM, Kuo Y, Ankri R, Weiss S, et al. A 512 × 512 SPAD Image Sensor With Integrated Gating for Widefield FLIM. IEEE Journal of Selected Topics in Quantum Electronics. 2019;25(1):1-12.

148. Pediredla AK, Sankaranarayanan AC, Buttafava M, Tosi A, Veeraraghavan A. Signal Processing Based Pile-up Compensation for Gated Single-Photon Avalanche Diodes. arXiv. 2018 11.

149. Diekmann R, Deschamps J, Li Y, Deguchi T, Tschanz A, Kahnwald M, et al. Photon-free (s)CMOS camera characterization for artifact reduction in high- and super-resolution microscopy. Nature Communications. 2022;13(1):3362.

150. Lundberg KH. Noise Sources in Bulk CMOS. Boston: MIT; 2002.

151. Wei K, Fu Y, Yang J, Huang H. A Physics-based Noise Formation Model for Extreme Low-light Raw Denoising. arXiv. 2020.

152. Fowler B, McGrath D, Bartkovjak P. Read Noise Distribution Modeling for CMOS Image Sensors. In: Proceedings of the 2013 International Image Sensor Workshop. Snowbird Utah; 2013. p. 1-3.

153. Porter WC, Kopp B, Dunlap JC, Widenhorn R, Bodegom E. Dark current measurements in a CMOS imager. In: Proc.SPIE. vol. 6816; 2008. p. 68160.

154. Chung J, Jeong U, Jeong D, Go S, Kim D. Development of a New Approach for Low-Laser-Power Super-Resolution Fluorescence Imaging. Analytical Chemistry. 2022 1;94(2):618-27.

155. Diekmann R, Kahnwald M, Schoenit A, Deschamps J, Matti U, Ries J. Optimizing imaging speed and excitation intensity for single-molecule localization microscopy. Nature Methods. 2020;17(9):909-12.

156. Laskin A, Laskin V, Ostrun A. Refractive beam shapers for focused laser beams. In: Proc.SPIE. vol. 9950; 2016. p. 995002.

157. Lightley J, Kumar S, Lim MQ, Garcia E, Görlitz F, Alexandrov Y, et al. openFrame: A modular, sustainable, open microscopy platform with single-shot, dual-axis optical autofocus module providing high precision and long range of operation. Journal of Microscopy. 2023 11;292(2):64-77.

158. Mandai M, Yamaguchi K. Immersion microscope objective lens . USPTO. 2005;US7046451B2.

159. Kurvits JA, Jiang M, Zia R. Comparative analysis of imaging configurations and objectives for Fourier microscopy. Journal of the Optical Society of America A. 2015;32(11):2082-92.

160. Chang W, Dai F, Na Q. The challenge of sCMOS image sensor technology to EMCCD. In: Proc.SPIE. vol. 10697; 2018. p. 1069711.

161. Gul B, Ashraf S, Khan S, Nisar H, Ahmad I. Cell refractive index: Models, insights, applications and future perspectives. Photodiagnosis and Photodynamic Therapy. 2021 3;33:102096.

162. Beuthan J, Minet O, Helfmann J, Herrig M, Müller G. The spatial variation of the refractive index in biological cells. Physics in Medicine and Biology. 1996 3;41(3):369-82.

163. Jones C, Suhling K. Refractive index sensing using Fluorescence Lifetime Imaging (FLIM). Journal of Physics: Conference Series. 2006 7;45:223-30.

164. Pinkard H, Stuurman N, Ivanov IE, Anthony NM, Ouyang W, Li B, et al. Pycro-Manager: open-source software for customized and reproducible microscope control. Nature Methods. 2021;18(3):226-8.

165. Etheridge TJ, Carr AM, Herbert AD. GDSC SMLM: Single-molecule localisation microscopy software for ImageJ. Wellcome Open Research. 2022;7(241).

166. Li L, Li M, Zhang Z, Huang ZL. Assessing low-light cameras with photon transfer curve method. Journal of Innovative Optical Health Sciences. 2016 4;09(03):1630008.

167. Institute of Environmental Sciences I. Considerations in Clean Room Design IES-RP-CC012.2, Appendix C. IEST, Rolling Meadows, IL. 2005.

168. Huang F, Hartwich TMP, Rivera-Molina FE, Lin Y, Duim WC, Long JJ, et al. Video-rate nanoscopy using sCMOS camera–specific single-molecule localization algorithms. Nature Methods. 2013;10(7):653-8.

169. McGorty R, Kamiyama D, Huang B. Active microscope stabilization in three dimensions using image correlation. Optical Nanoscopy. 2013;2(1):3.

170. Stallinga S, Rieger B. Accuracy of the Gaussian Point Spread Function model in 2D localization microscopy. Optics Express. 2010;18(24):24461-76.

171. Zhao N, Papa JC, Fuerschbach K, Qiao Y, Thompson KP, Rolland JP. Experimental investigation in nodal aberration theory (NAT) with a customized Ritchey-Chrétien system: third-order coma. Optics Express. 2018;26(7):8729-43.

172. Zhu W, Li Q, Gong S, Feng G. Cell membrane targetable NIR fluorescent polarity probe for selective visualization of cancer cells and early tumor. Analytica Chimica Acta. 2023;1278:341748.

173. Reichardt C. Solvatochromic Dyes as Solvent Polarity Indicators. Chemical Reviews. 1994 12;94(8):2319-58.

174. Klymchenko A. Solvatochromic fluorescent dyes as universal tools for biological research. Actualite Chimique. 2012 1;359.

175. Klymchenko AS. Solvatochromic and Fluorogenic Dyes as Environment-Sensitive Probes: Design and Biological Applications. Accounts of Chemical Research. 2017 2;50(2):366-75.

176. Li B, Qin Y, Yu X, Xu X, Yu W. Lipid raft involvement in signal transduction in cancer cell survival, cell death and metastasis. Cell Proliferation. 2022 1;55(1).

177. Grußmayer KS, Herten DP. Time-resolved molecule counting by photon statistics across the visible spectrum. Physical Chemistry Chemical Physics. 2017;19(13):8962-9.

178. Latty S, Felce J, Weimann L, Lee S, Davis S, Klenerman D. Referenced Single-Molecule Measurements Differentiate between GPCR Oligomerization States. Biophysical Journal. 2015;109(9):1798-806.

179. Wilmes S, Beutel O, Li Z, Francois-Newton V, Richter CP, Janning D, et al. Receptor dimerization dynamics as a regulatory valve for plasticity of type I interferon signaling. Journal of Cell Biology. 2015 5;209(4):579-93.

180. Andronov L, Genthial R, Hentsch D, Klaholz BP. splitSMLM, a spectral demixing method for high-precision multi-color localization microscopy applied to nuclear pore complexes. Communications Biology. 2022;5(1):1100.

181. Klevanski M, Herrmannsdoerfer F, Sass S, Venkataramani V, Heilemann M, Kuner T. Automated highly multiplexed super-resolution imaging of protein nano-architecture in cells and tissues. Nature Communications. 2020;11(1):1552.

182. Levental I, Levental KR, Heberle FA. Lipid Rafts: Controversies Resolved, Mysteries Remain. Trends in Cell Biology. 2020 5;30(5):341-53.

183. Sezgin E, Levental I, Mayor S, Eggeling C. The mystery of membrane organization: composition, regulation and roles of lipid rafts. Nature Reviews Molecular Cell Biology. 2017;18(6):361-74.

184. Danylchuk DI, Moon S, Xu K, Klymchenko AS. Switchable Solvatochromic Probes for Live-Cell Super-resolution Imaging of Plasma Membrane Organization. Angewandte Chemie International Edition. 2019 10;58(42):14920-4.

185. Nieves DJ, Owen DM. Quantitative mapping of membrane nanoenvironments through single-molecule imaging of solvatochromic probes. bioRxiv. 2020 1:2020.07.19.209908.

186. Barbotin A, Urbančič I, Galiani S, Eggeling C, Booth M, Sezgin E. z-STED Imaging and Spectroscopy to Investigate Nanoscale Membrane Structure and Dynamics. Biophysical Journal. 2020 5;118(10):2448-57.

187. Hänselmann S. Quantitative Microscopy: Measuring membrane receptor interactions in live cells. Ph.D. thesis. Heidelberg: Heidelberg University; 2017.

188. Yserentant K. Tools for quantitative Fluorescence Microscopy on the Nanoscale. Ph.D. thesis. Heidelberg: Heidelberg University; 2022.

189. Owen DM, Rentero C, Magenau A, Abu-Siniyeh A, Gaus K. Quantitative imaging of membrane lipid order in cells and organisms. Nature Protocols. 2012;7(1):24-35.

190. Wang Y, Schnitzbauer J, Hu Z, Li X, Cheng Y, Huang ZL, et al. Localization events-based sample drift correction for localization microscopy with redundant cross-correlation algorithm. Optics Express. 2014;22(13):15982-91.

191. Fortmann SD, Patton MJ, Frey BF, Tipper JL, Reddy SB, Vieira CP, et al. Circulating SARS-CoV-2+ megakaryocytes are associated with severe viral infection in COVID-19. Blood Advances. 2023 8;7(15):4200-14.

192. Heller H, Schaefer M, Schulten K. Molecular dynamics simulation of a bilayer of 200 lipids in the gel and in the liquid crystal phase. The Journal of Physical Chemistry. 1993 8;97(31):8343-60.

193. Sezgin E, Waithe D, Bernardino de la Serna J, Eggeling C. Spectral Imaging to Measure Heterogeneity in Membrane Lipid Packing. ChemPhysChem. 2015 5;16(7):1387-94.

194. Amaro M, Reina F, Hof M, Eggeling C, Sezgin E. Laurdan and Di-4-ANEPPDHQ probe different properties of the membrane. Journal of Physics D: Applied Physics. 2017;50(13):134004.

195. Cebecauer M, Amaro M, Jurkiewicz P, Sarmento MJ, Šachl R, Cwiklik L, et al. Membrane Lipid Nanodomains. Chemical Reviews. 2018 12;118(23):11259-97.

196. Descloux A, Grußmayer KS, Radenovic A. Parameter-free image resolution estimation based on decorrelation analysis. Nature Methods. 2019;16(9):918-24.

197. Chazotte B. Labeling Mitochondria with Rhodamine 123. Cold Spring Harbor Protocols. 2011 7;2011(7).

198. Bryan IV JS, Sgouralis I, Pressé S. Diffraction-limited molecular cluster quantification with Bayesian nonparametrics. Nature Computational Science. 2022;2(2):102-11.

199. Bryan IV S, Pressé S, Herten DP, Tashev S, Hummert J, Yserentant K. Quantifying binding kinetics with fluorescence microscopy. Biophysical Journal. 2023;122(3):140a.

200. Gautier A, Juillerat A, Heinis C, Corrêa IR, Kindermann M, Beaufils F, et al. An Engineered Protein Tag for Multiprotein Labeling in Living Cells. Chemistry & Biology. 2008;15(2):128-36.

201. Wombacher R, Heidbreder M, van de Linde S, Sheetz MP, Heilemann M, Cornish VW, et al. Live-cell super-resolution imaging with trimethoprim conjugates. Nature Methods. 2010;7(9):717-9.

202. Field J, Nikawa JI, Broek D, MacDonald B, Rodgers L, Wilson IA, et al. Purification of a RAS-Responsive Adenylyl Cyclase Complex from Saccharomyces cerevisiae by Use of an Epitope Addition Method. Molecular and Cellular Biology. 1988 5;8(5):2159-65.

203. Oleksiievets N, Sargsyan Y, Thiele JC, Mougios N, Sograte-Idrissi S, Nevskyi O, et al. Fluorescence lifetime DNA-PAINT for multiplexed super-resolution imaging of cells. Communications Biology. 2022;5(1):38.

204. Zhanghao K, Liu W, Li M, Wu Z, Wang X, Chen X, et al. High-dimensional super-resolution imaging reveals heterogeneity and dynamics of subcellular lipid membranes. Nature Communications. 2020;11(1):5890.

205. Tuijtel MW, Koster AJ, Jakobs S, Faas FGA, Sharp TH. Correlative cryo super-resolution light and electron microscopy on mammalian cells using fluorescent proteins. Scientific Reports. 2019;9(1):1369.

206. Trefts E, Gannon M, Wasserman DH. The liver. Current Biology. 2017 11;27(21):1147-51.

207. Robinson MW, Harmon C, O'Farrelly C. Liver immunology and its role in inflammation and homeostasis. Cellular & Molecular Immunology. 2016;13(3):267-76.

208. Brandl K, Kumar V, Eckmann L. Gut-liver axis at the frontier of host-microbial interactions. American Journal of Physiology-Gastrointestinal and Liver Physiology. 2017 2;312(5):G413-9.

209. Wilkinson AL, Qurashi M, Shetty S. The Role of Sinusoidal Endothelial Cells in the Axis of Inflammation and Cancer Within the Liver. Frontiers in Physiology. 2020;11.

210. Sampaio Gonçalves D, Keyes WM. Endothelial cells give a boost to senescence surveillance. Genes & Development. 2022 5;36(9-10):511-3.

211. Huang Y, Yang X, Meng Y, Shao C, Liao J, Li F, et al. The hepatic senescence-associated secretory phenotype promotes hepatocarcinogenesis through Bcl3-dependent activation of macrophages. Cell & Bioscience. 2021;11(1):173.

212. Coppé JP, Desprez PY, Krtolica A, Campisi J. The Senescence-Associated Secretory Phenotype: The Dark Side of Tumor Suppression. Annual Review of Pathology: Mechanisms of Disease. 2010 1;5(1):99-118.

213. Irvine KM, Skoien R, Bokil NJ, Melino M, Thomas GP, Loo D, et al. Senescent human hepatocytes express a unique secretory phenotype and promote macrophage migration. World journal of gastroenterology: WJG. 2014;20(47):17851.

214. Llovet JM, Kelley RK, Villanueva A, Singal AG, Pikarsky E, Roayaie S, et al. Hepatocellular carcinoma. Nature Reviews Disease Primers. 2021;7(1):6.

215. Pappas SP, Asmus RA. Photoinitiated polymerization of methyl methacrylate with benzoin methyl ether. III. Independent photogeneration of the ether radical. Journal of Polymer Science: Polymer Chemistry Edition. 1982 9;20(9):2643-53.

216. He X, Zang L, Xin Y, Zou Y. An overview of photopolymerization and its diverse applications. Applied Research. 2023 12;2(6).

217. Charlot V, Ibrahim A, Allonas X, Croutxé-Barghorn C, Delaite C. Photopolymerization of methyl methacrylate: effects of photochemical and photonic parameters on the chain length. Polymer Chemistry. 2014;5(21):6236-43.

218. Tanida I, Yamaguchi J, Kakuta S, Uchiyama Y. Osmium-Resistant Fluorescent Proteins and In-Resin Correlative Light-Electron Microscopy of Epon-Embedded Mammalian Cultured Cells. In: Sharma M, editor. Fluorescent Proteins: Methods and Protocols. New York, NY: Springer US; 2023. p. 287-97.

219. Sanada T, Yamaguchi J, Furuta Y, Kakuta S, Tanida I, Uchiyama Y. In-resin CLEM of Epon-embedded cells using proximity labeling. Scientific Reports. 2022;12(1):11130.

220. Korn L. Einzelmolekülmikroskopie. 1. Staatsexamen - Lehramt. Heidelberg: Heidelberg University; 2016.

221. Liu M, Jia M, Pan H, Li L, Chang M, Ren H, et al. Instrument Response Standard in Time-Resolved Fluorescence Spectroscopy at Visible Wavelength: Quenched Fluorescein Sodium. Applied Spectroscopy. 2014 5;68(5):577-83.

222. Birtalan E, Rudat B, Kölmel DK, Fritz D, Vollrath SBL, Schepers U, et al. Investigating rhodamine B-labeled peptoids: Scopes and limitations of its applications. Peptide Science. 2011 1;96(5):694-701.

223. Vaughan JC, Jia S, Zhuang X. Ultrabright photoactivatable fluorophores created by reductive caging. Nature Methods. 2012;9(12):1181-4.

224. Yserentant K. Towards quantitative correlative light and electron microscopy in three dimensions. Master's thesis. Heidelberg: Heidelberg University; 2015.

225. Thevenaz P, Ruttimann UE, Unser M. A pyramid approach to subpixel registration based on intensity. IEEE Transactions on Image Processing. 1998;7(1):27-41.

226. Kybic J, Unser M. Multidimensional elastic registration of images using splines. In: Proceedings 2000 International Conference on Image Processing (Cat. No.00CH37101). vol. 2; 2000. p. 455-8.

227. Cardona A, Saalfeld S, Schindelin J, Arganda-Carreras I, Preibisch S, Longair M, et al. TrakEM2 Software for Neural Circuit Reconstruction. PLOS ONE. 2012 6;7(6):38011.

228. Bogovic JA, Hanslovsky P, Wong A, Saalfeld S. Robust registration of calcium images by learned contrast synthesis. In: 2016 IEEE 13th International Symposium on Biomedical Imaging (ISBI); 2016. p. 1123-6.

229. Löwe J, Li H, Downing KH, Nogales E. Refined structure of $\alpha\beta$-tubulin at 3.5 Å resolution. Journal of Molecular Biology. 2001;313(5):1045-57.

230. Patel-Hett S, Richardson JL, Schulze H, Drabek K, Isaac NA, Hoffmeister K, et al. Visualization of microtubule growth in living platelets reveals a dynamic marginal band with multiple microtubules. Blood. 2008 5;111(9):4605-16.

231. Mathur A, Correia SR, Dmitrieff S, Gibeaux R, Kalinina I, Quidwai T, et al. Cytoskeleton mechanics determine resting size and activation dynamics of platelets. bioRxiv. 2018 1:413377.

232. Templier T. MagC, magnetic collection of ultrathin sections for volumetric correlative light and electron microscopy. eLife. 2019;8:45696.

233. Masich S, Östberg T, Norlén L, Shupliakov O, Daneholt B. A procedure to deposit fiducial markers on vitreous cryo-sections for cellular tomography. Journal of Structural Biology. 2006;156(3):461-8.

234. Scher N, Rechav K, Paul-Gilloteaux P, Avinoam O. In situ fiducial markers for 3D correlative cryo-fluorescence and FIB-SEM imaging. iScience. 2021;24(7):102714.

235. Suga M, Asahina S, Sakuda Y, Kazumori H, Nishiyama H, Nokuo T, et al. Recent progress in scanning electron microscopy for the characterization of fine structural details of nano materials. Progress in Solid State Chemistry. 2014;42(1):1-21.

236. Moerland RJ, Hoogenboom JP. Subnanometer-accuracy optical distance ruler based on fluorescence quenching by transparent conductors. Optica. 2016;3(2):112-7.

237. Gregor I, Chizhik A, Karedla N, Enderlein J. Metal-induced energy transfer. Nanophotonics. 2019;8(10):1689-99.

238. Heinrich L, Bennett D, Ackerman D, Park W, Bogovic J, Eckstein N, et al. Whole-cell organelle segmentation in volume electron microscopy. Nature. 2021;599(7883):141-6.

239. Bousset L, Gil J. Targeting senescence as an anticancer therapy. Molecular Oncology. 2022 11;16(21):3855-80.

240. Zhou H, Khan D, Gerdes N, Hagenbeck C, Rana M, Cornelius JF, et al. Colchicine Protects against Ethanol-Induced Senescence and Senescence-Associated Secretory Phenotype in Endothelial Cells. Antioxidants. 2023;12(4).

241. Kevil CG, Orr AW, Langston W, Mickett K, Murphy-Ullrich J, Patel RP, et al. Intercellular Adhesion Molecule-1 (ICAM-1) Regulates Endothelial Cell Motility through a Nitric Oxide-dependent Pathway*. Journal of Biological Chemistry. 2004;279(18):19230-8.

242. Kaatz M, Berod L, Lagadari M, Fluhr JW, Elsner P, Norgauer J. Microtubules Regulate Expression of ICAM-1 in Epidermoid Cells (KB Cells). Skin Pharmacology and Physiology. 2006 11;19(6):322-8.

243. Hauke L, Isbaner S, Ghosh A, Guido I, Turco L, Chizhik AI, et al. Metal-Induced Energy Transfer (MIET) for Live-Cell Imaging with Fluorescent Proteins. ACS Nano. 2023 5;17(9):8242-51.

244. Blouin A, Bolender RP, Weibel ER. Distribution of organelles and membranes between hepatocytes and nonhepatocytes in the rat liver parenchyma. A stereological study. Journal of Cell Biology. 1977 2;72(2):441-55.

245. Keevend K, Krummenacher R, Kungas E, Gerken LRH, Gogos A, Stiefel M, et al. Correlative Cathodoluminescence Electron Microscopy: Immunolabeling Using Rare-Earth Element Doped Nanoparticles. Small. 2020 11;16(44):2004615.

246. Balagopalan L, Yi J, Nguyen T, McIntire KM, Harned AS, Narayan K, et al. Plasma membrane LAT activation precedes vesicular recruitment defining two phases of early T-cell activation. Nature Communications. 2018;9(1):2013.

247. Levin BDA. Direct detectors and their applications in electron microscopy for materials science. Journal of Physics: Materials. 2021;4(4):042005.

248. Lane R, Vos Y, Wolters AHG, Kessel Lv, Chen SE, Liv N, et al. Optimization of negative stage bias potential for faster imaging in large-scale electron microscopy. Journal of Structural Biology: X. 2021;5:100046.

249. Han X, Lu X, Li PH, Wang S, Schalek R, Meirovitch Y, et al. Multiplexed volumetric CLEM enabled by antibody derivatives provides new insights into the cytology of the mouse cerebellar cortex. bioRxiv. 2023 1:2023.05.20.540091.

250. Reinhardt SCM, Masullo LA, Baudrexel I, Steen PR, Kowalewski R, Eklund AS, et al. Ångström-resolution fluorescence microscopy. Nature. 2023;617(7962):711-6.

251. Wolff JO, Scheiderer L, Engelhardt T, Engelhardt J, Matthias J, Hell SW. MINFLUX dissects the unimpeded walking of kinesin-1. Science. 2023 3;379(6636):1004-10.

252. Deguchi T, Iwanski MK, Schentarra EM, Heidebrecht C, Schmidt L, Heck J, et al. Direct observation of motor protein stepping in living cells using MINFLUX. Science. 2023 3;379(6636):1010-5.

253. Cheng NM, Chan YC, Cheng SW. COVID-19 related thrombosis: A mini-review. Phlebology. 2022 4;37(5):326-37.

254. Erazo-Oliveras A, Muñoz-Vega M, Salinas ML, Wang X, Chapkin RS. Dysregulation of cellular membrane homeostasis as a crucial modulator of cancer risk. The FEBS Journal. 2022 10.

255. Eisenstein M. Seven technologies to watch in 2023. Nature. 2023 1;613:794-7.

256. Jung SR, Fujimoto BS, Chiu DT. Quantitative microscopy based on single-molecule fluorescence. Current Opinion in Chemical Biology. 2017;39:64-73.

257. Dankovich TM, Rizzoli SO. Challenges facing quantitative large-scale optical super-resolution, and some simple solutions. iScience. 2021;24(3):102134.

258. Chen Z, Jing C, Gallagher SS, Sheetz MP, Cornish VW. Second-Generation Covalent TMP-Tag for Live Cell Imaging. Journal of the American Chemical Society. 2012 8;134(33):13692-9.

259. Xu J, Qin G, Luo F, Wang L, Zhao R, Li N, et al. Automated Stoichiometry Analysis of Single-Molecule Fluorescence Imaging Traces via Deep Learning. Journal of the American Chemical Society. 2019 5;141(17):6976-85.

260. Williamson DJ, Burn GL, Simoncelli S, Griffié J, Peters R, Davis DM, et al. Machine learning for cluster analysis of localization microscopy data. Nature Communications. 2020;11(1):1493.

261. Hu X, Naiel MA, Wong A, Lamm M, Fieguth P. RUNet: A Robust UNet Architecture for Image Super-Resolution. In: 2019 IEEE/CVF Conference on Computer Vision and Pattern Recognition Workshops (CVPRW); 2019. p. 505-7.

262. Wang W, Wu B, Zhang B, Li X, Tan J. Correction of refractive index mismatch-induced aberrations under radially polarized illumination by deep learning. Optics Express. 2020;28(18):26028-40.

263. Spomer W, Wacker IU, Bartels C, Hofmann A, Scharnowell R, Schröder RR, et al. Towards reliable preparation of serial sections for correlative array tomography and 3D reconstruction. In: 18th International Microscopy Congress, Praha, CZ, September 7-12, 2014. Ed.: P. Hozak. Czechoslovak Microscopy Society; 2014. p. 10.

Chapter 8

Appendices

Appendices

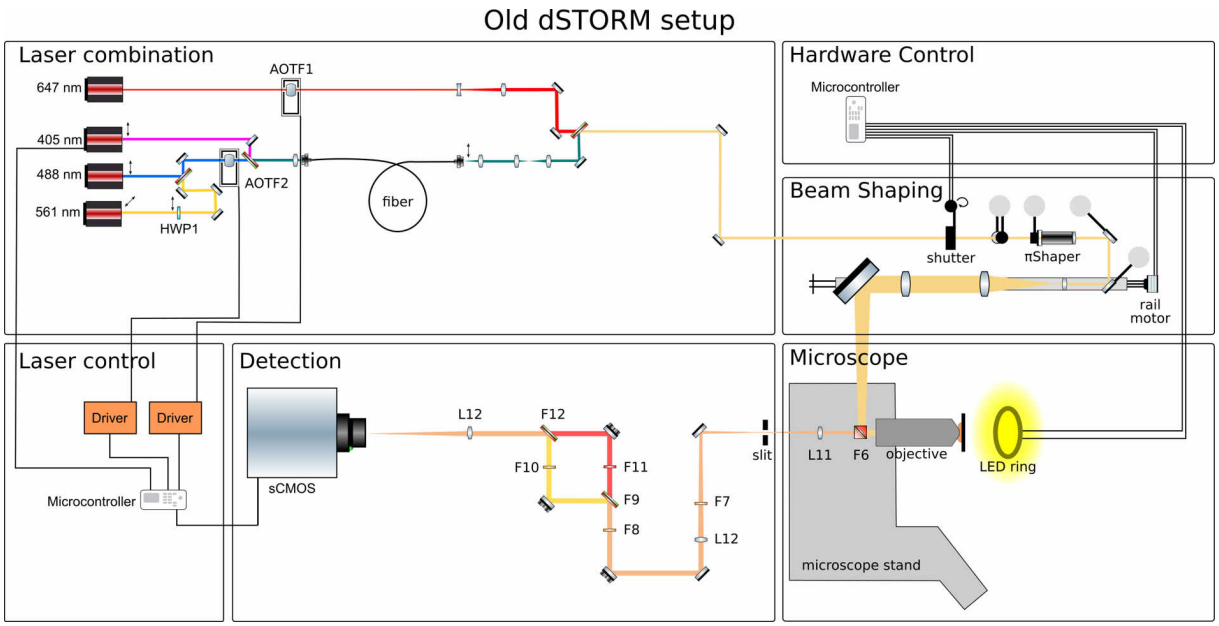

Fig. SI 1: Microscope setup. Schematic of a large field of view dSTORM setup with homogeneous illumination. To obtain a high TEM_{00} beam uniformity, laser lines are coupled into a single-mode fibre. Taken from the master's thesis of Jonas Euchner (49).

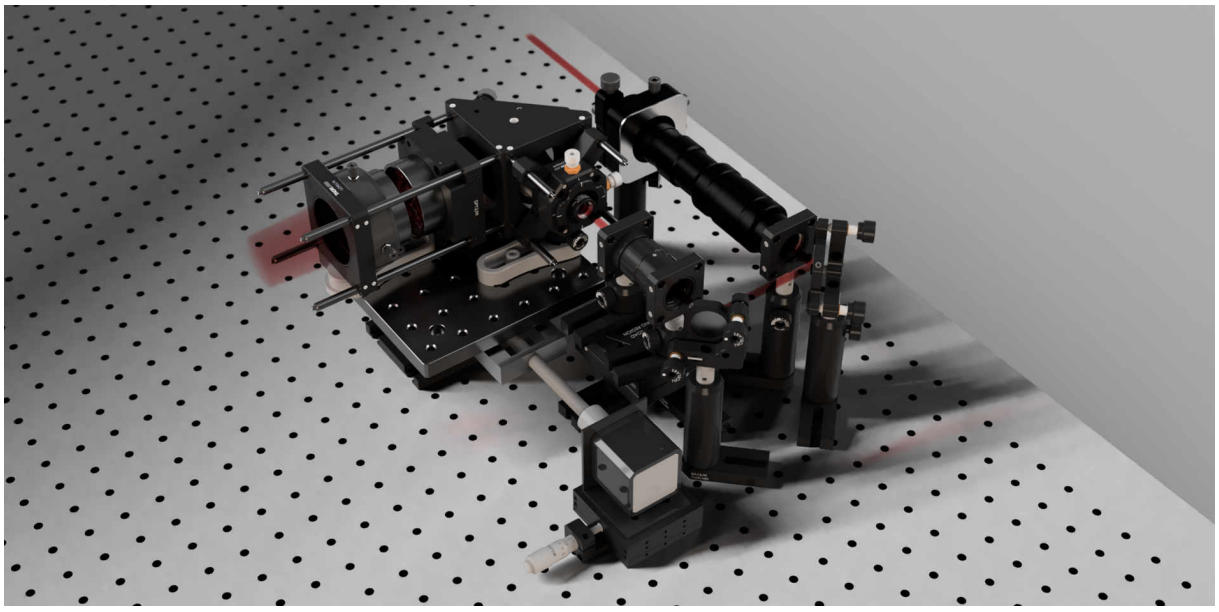

Fig. SI 2: 3D render of previous iteration of the beam shaping module.

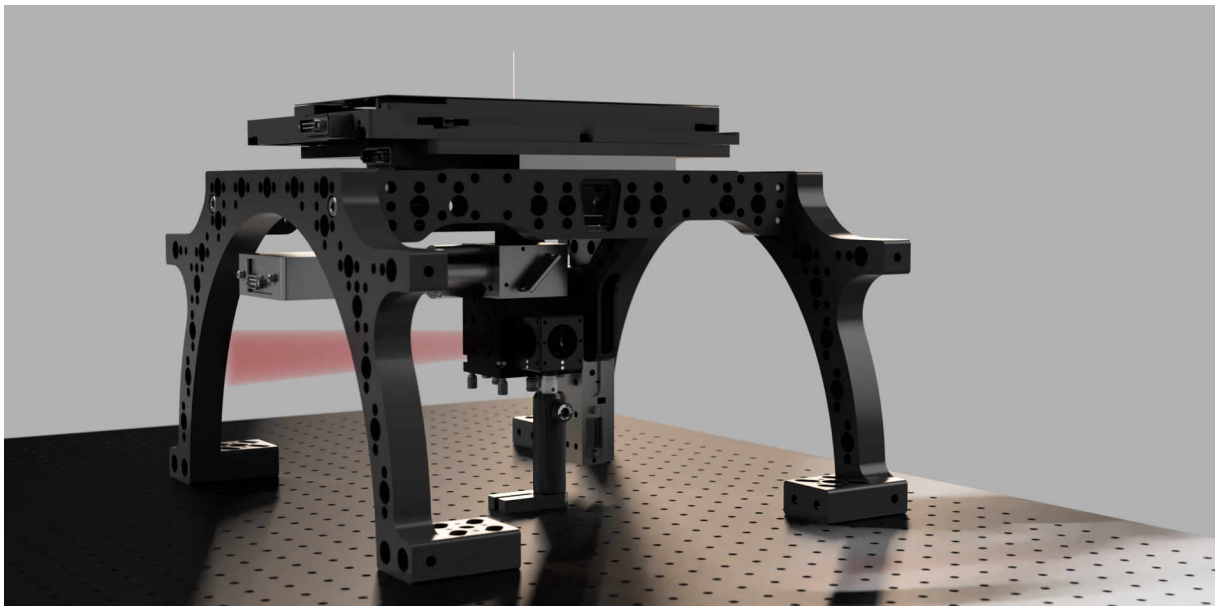

Fig. SI 3: 3D render of previous iteration of the RAMM module..

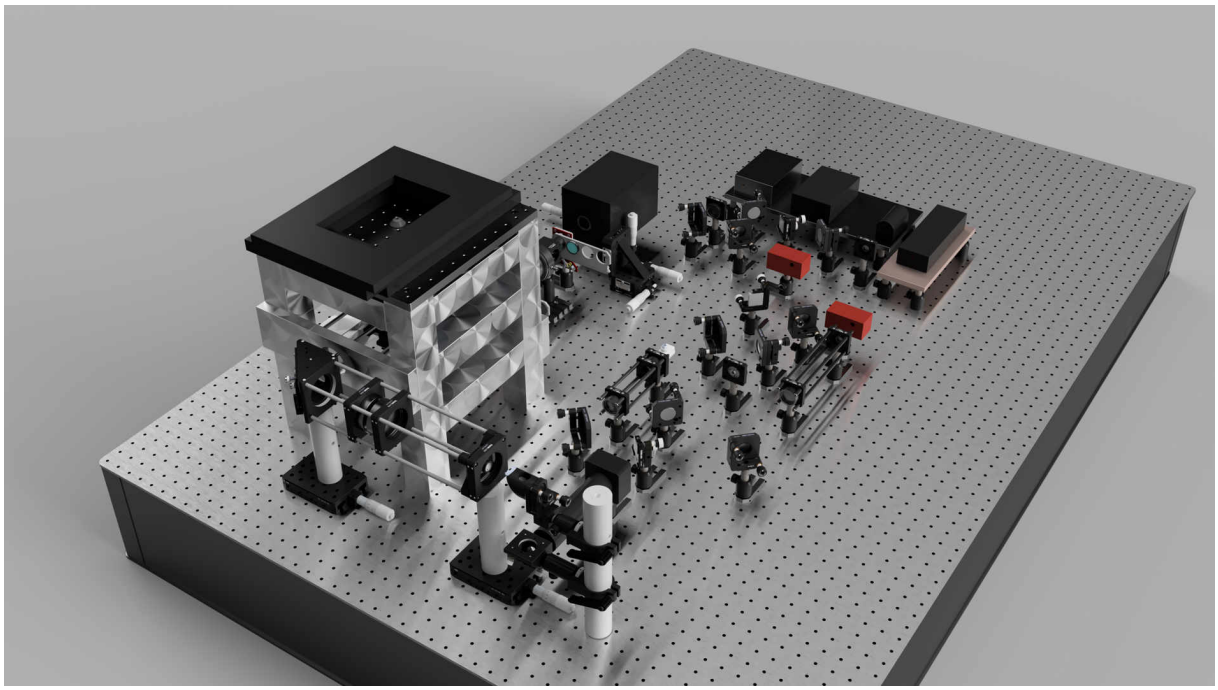

Fig. SI 4: 3D render of previous iteration utilising a custom built microscopy body. Microscope body based on the design of a RM21 (MadCityLabs). Validated using modal frequency analysis and static stress simulation.

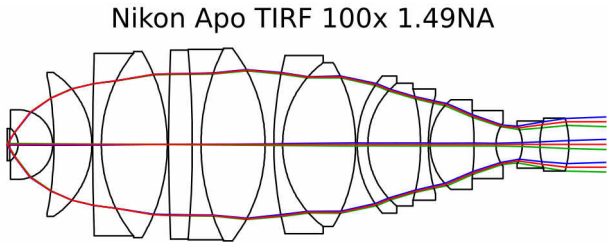

Fig. SI 5: Nikon Apo TIRF 100x 1.49NA immersion oil objective. Optical elements in a Nikon Apo TIRF 100x 1.49NA immersion oil objective with rays modelled for 3 emitters (point source on principal axis: red; point source 100 µm above principal axis: green; point source 100 µm below principal axis: blue), based on (158, 159).

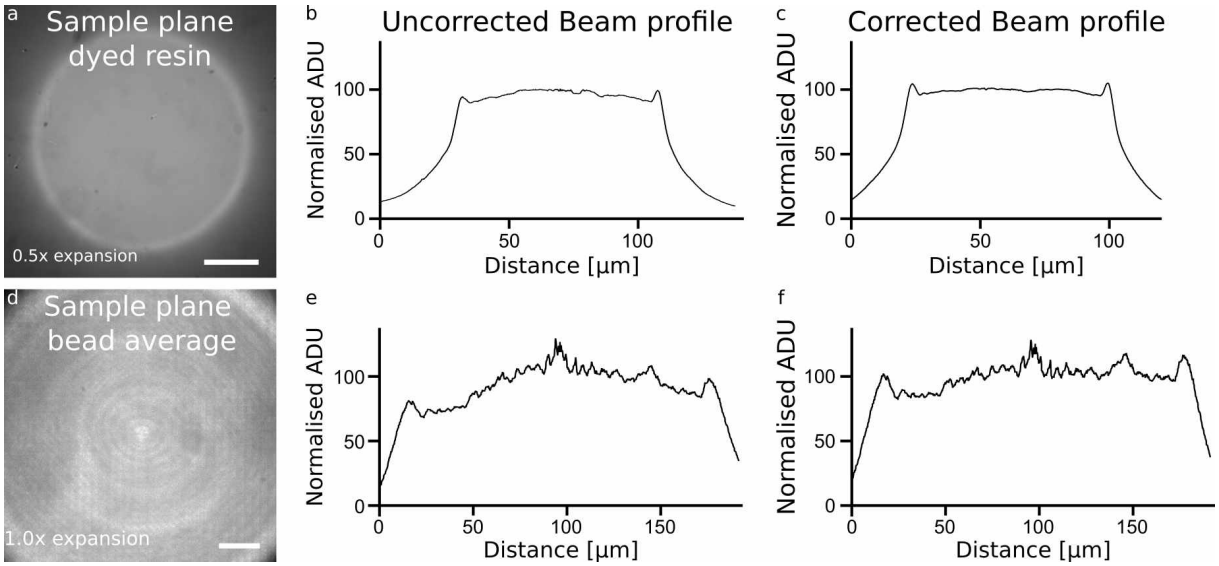

Fig. SI 6: Comparison of uncorrected and corrected *in-sample* beam profiles. a-c) Beam profile of a fluorescent resin sample. d-f) Beam profile based on averaging of a coverslip with the surface coated in TetraSpeck MicroSpheres. a,d) Image acquired in camera. b,d) Raw intensity profile for a diagonal line. c,f) Results of intensity correct illumination profile using the theoretical position-dependent transmission efficiency for compensation (Fig. 3.12). Scale bar: a,d) 20 µm

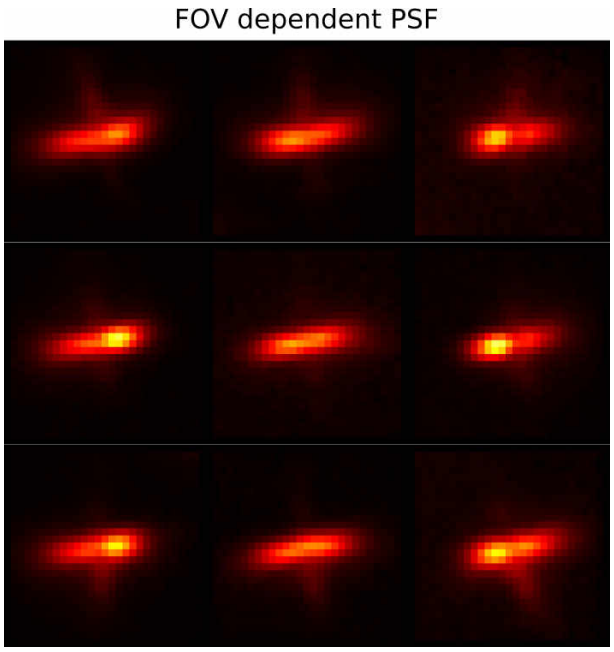

Fig. SI 7: Position dependent astigmatic PSF. Spline interpolation of the astigmatic PSF at 500 nm out of focus. The position dependent PSF calibration was performed on a 3x3 subset of the full FOV.

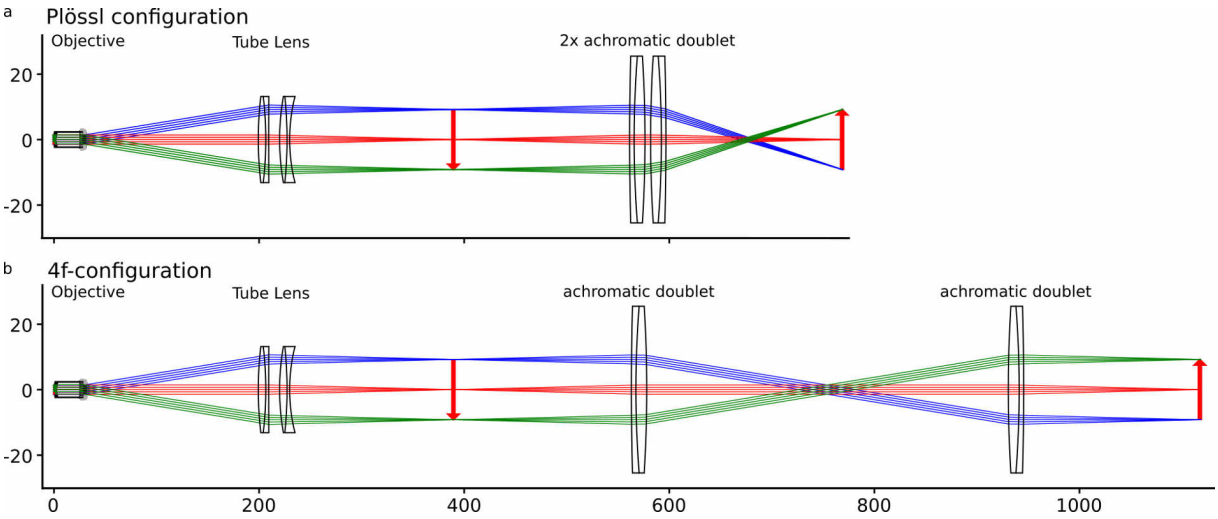

Fig. SI 8: Optical Raytracing analysis. Approximation of the optical detection pathway, simulated in Raytracing for a) Plössl configuration and b) 4f configuration (123).

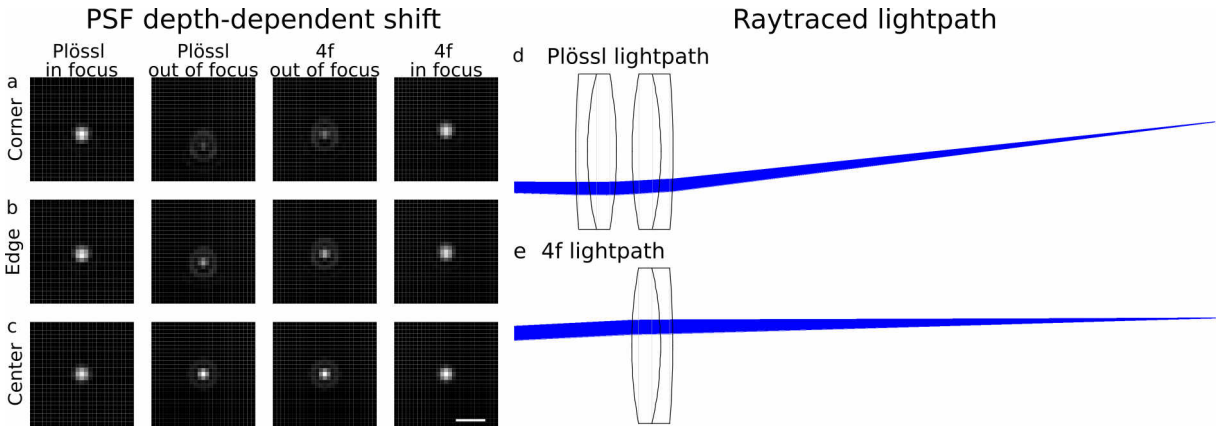

Fig. SI 9: Simulation of depth-dependent shift of PSF. a-c) Performance of the detection pathway for a simulated spherically emitting point source at a) the corner of the FOV, b) at the edge of the FOV, and c) the centre of the FOV for in focus and out of focus position, modelled for the Plössl configuration and 4f configuration. d,e) Exemplary raytraced lightpath of the full detection pathway for an emitter at the distal location of the FOV.

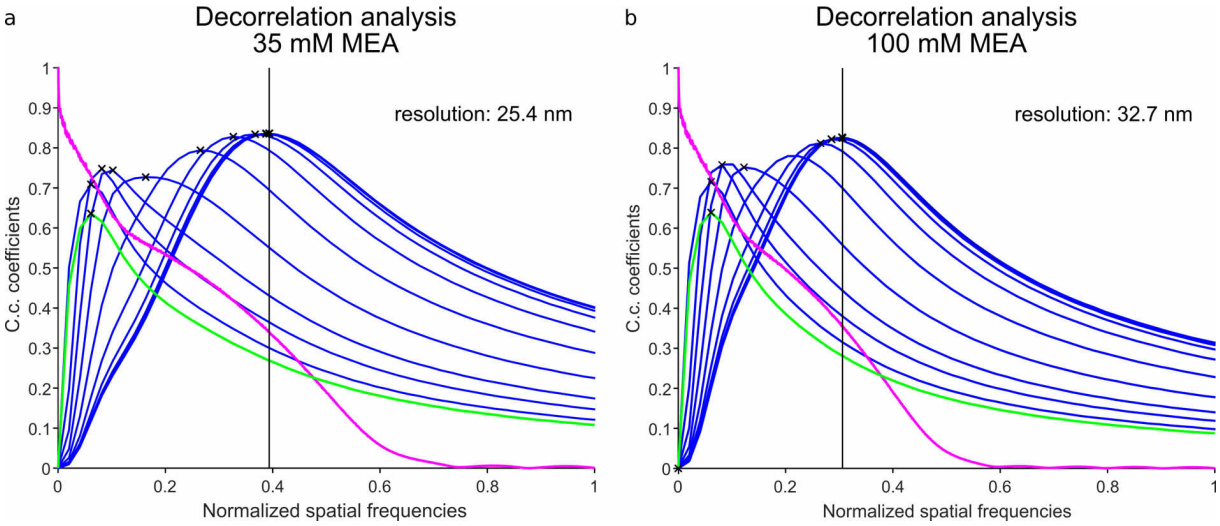

Fig. SI 10: Resolution estimation based on decorrelation analysis. a,b) Resolution estimation of microtubule in dSTORM from Fig. 4.4. Estimation for a) 35 mM and b) 100 mM MEA in dSTORM buffer.

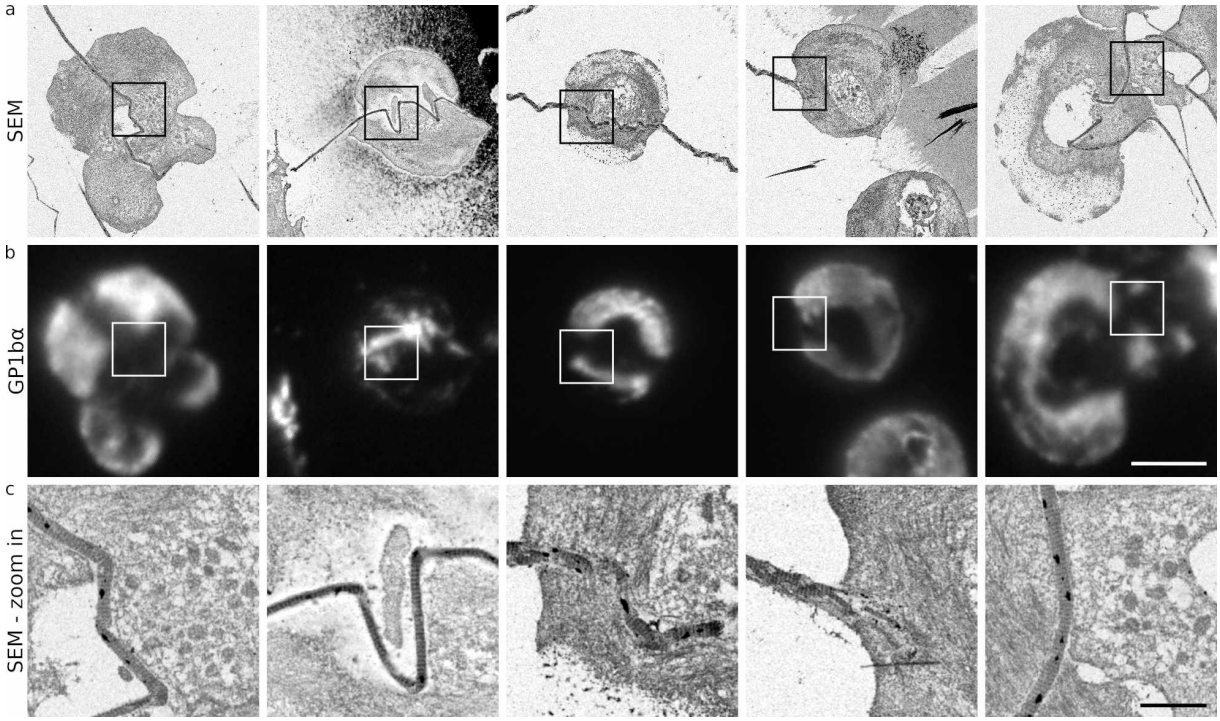

Fig. SI 11: CLEM of GP1bα in platelets on collagen-coated surface. a) SEM micrographs of platelets from a healthy donor on a collagen-coated surface, sectioned at 100 nm section height. b) Indirect immunolabelling of GP1bα, indicating a differential distribution of GP1bα in proximity to collagen. c) Zoom in on relevant interaction of platelets with collagen. Platelets were fixed in 4% paraformaldehyde (PFA), indirectly immunolabelled for GP1bα and post-fixed in 2% glutaraldehyde (GA), contrasted with 0.1% OsO_4, and 4% neodymium acetate. DMPA LR White resin was polymerised at 21 °C. On section post-staining with Reynolds' lead citrate and 2% uranyl acetate. SEM acquisition using InLens and energy selective back-scattered electron detector (ESB) detector. Scale bar: a,b) 5 µm, c) 1 µm

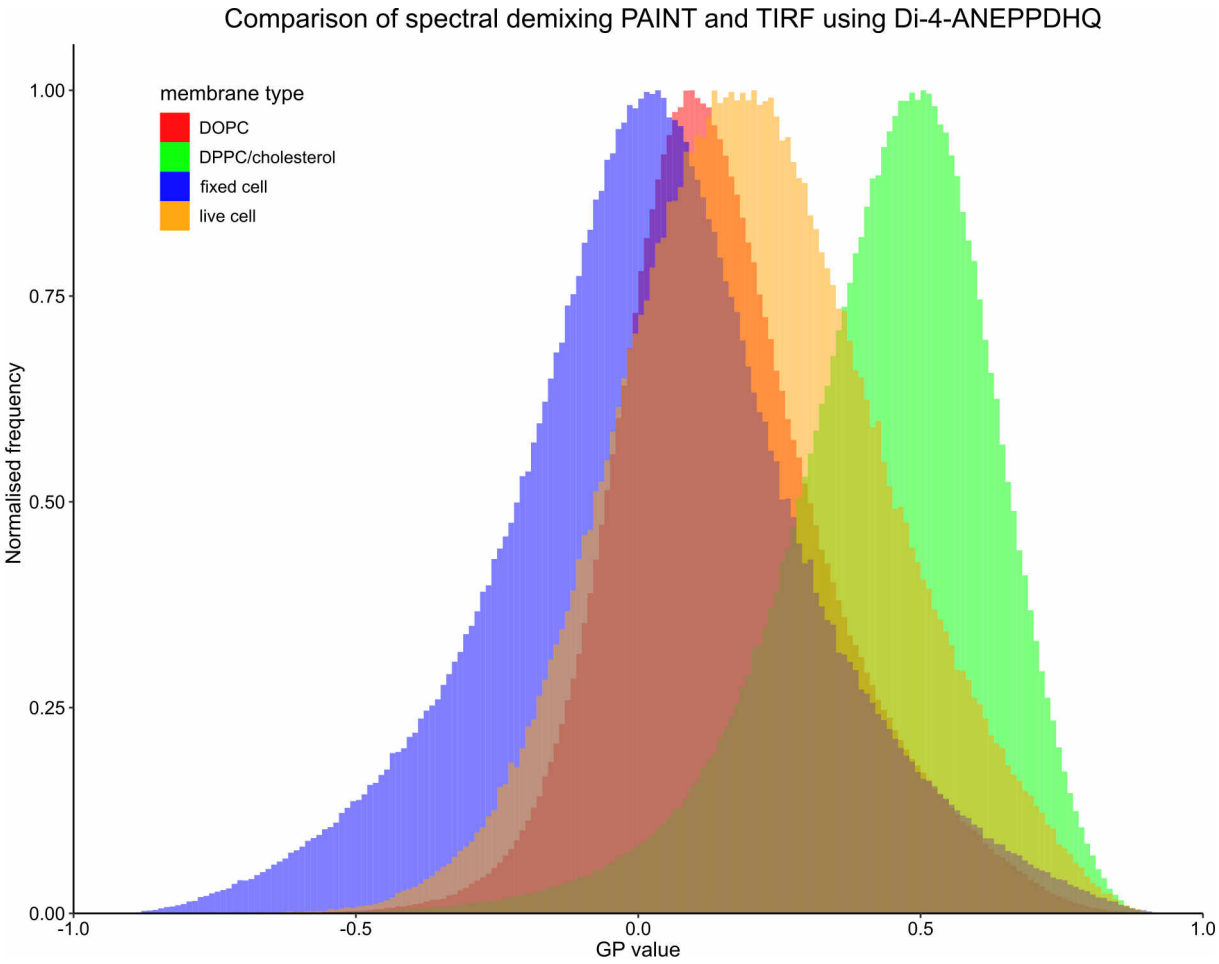

Fig. SI 12: Distribution of raw GP values in membranes. Histogram of the calculated raw GP values for all localisations in membranes, from Fig. 4.11.

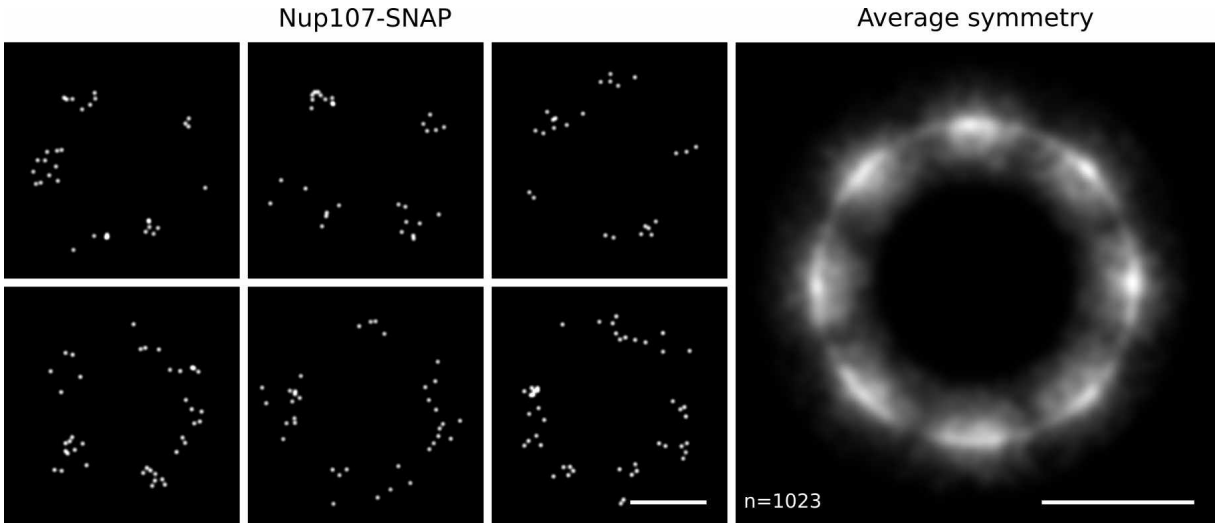

Fig. SI 13: Reconstruction of 8-fold symmetry of NPC. Left panel) Representative selection of 6 nuclear pore complexes showing the pointillist emitter position for AF647 labelled Nup107-SNAP. Right panel) Average symmmetry recovered from 1023 optimally oriented nuclear pore complexes labelled for Nup107-SNAP. Scale bar: 50 nm.

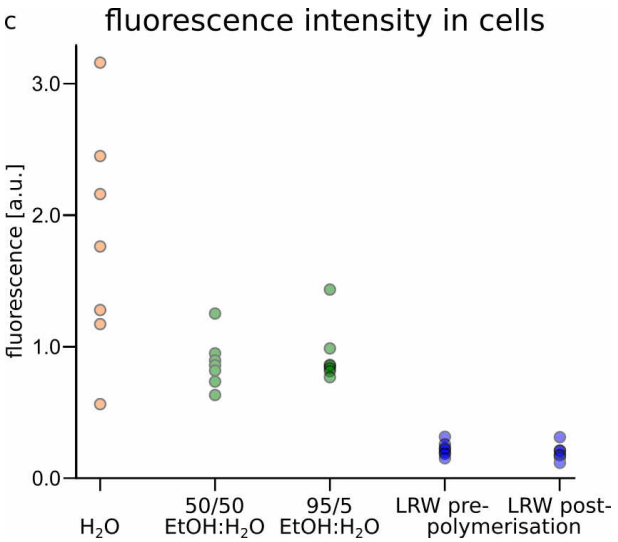

Fig. SI 14: Observed cellular fluorophore intensity of AF647 at various stages during dehydration and embedding. Indirectly immunolabelled microtubule in HeLa with AF647 were recorded in water (orange), ethanol in water (50% and 95% - green), pre-polymerisation and post polymerisation (blue). Fluorescence intensity in ethanol was reduced compared to water and was further reduced in resin. Polymerisation did not results in a significant change of fluorescence intensity. Reanalysed from data acquired by Klaus Yserentant during his Master's thesis (224).

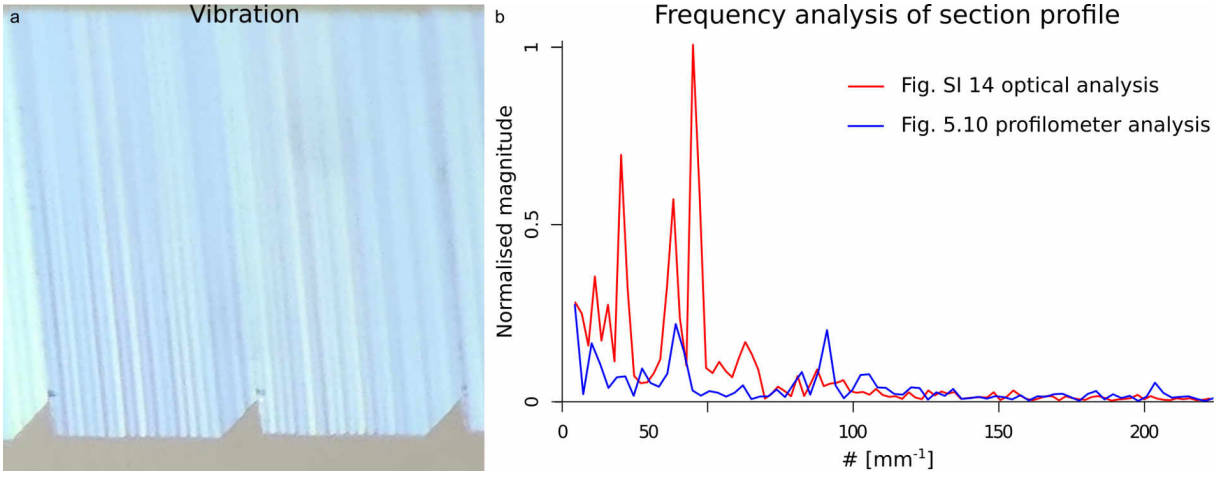

Fig. SI 15: Vibration induced resin defects. a) LR White DMPA resin sections prepared in an RMC Powertome XL. Vibration isolation of the damped table was activated, but did not sufficiently reduce the vibrations present in the laboratory. b) Analysis of frequency components in resin section from a laboratory with improper (red) and sufficient vibrational isolation (blue). Frequency magnitude analysed from line profile using FFT analysis. Blue) FFT analysis based on profilometer analysis of Fig. 5.10. Red) FFT analysis based on interference-based height estimation from section colour (263).

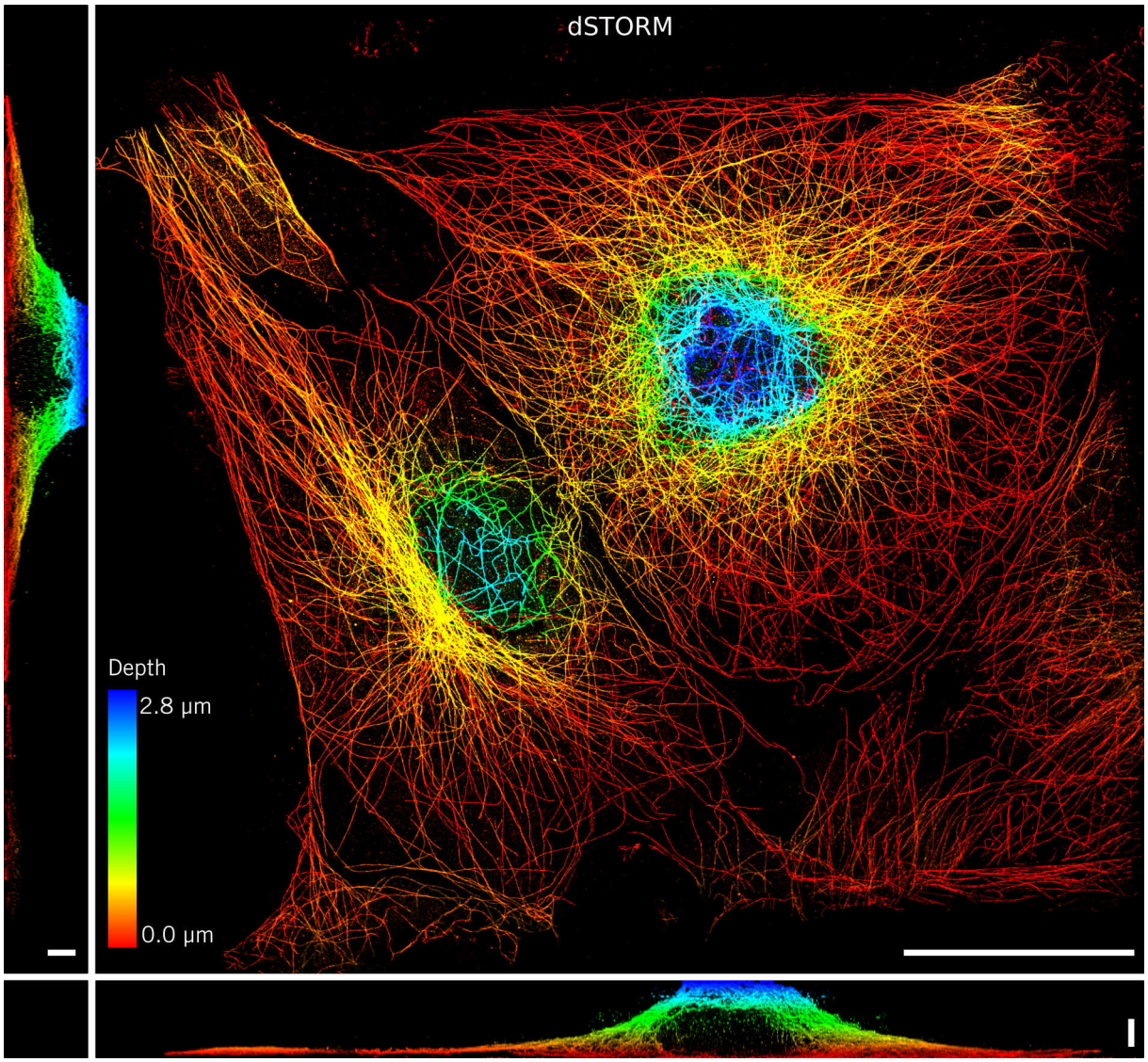

Fig. SI 16: Volumetric serial section dSTORM reconstruction of microtubeles in COS7 cells. Automated affine reconstructions of 56 serial sections at 50 nm section height. COS7 cells were fixed in 4% PFA, indirectly immunolabelled for microtubules and post-fixed in 1% GA. DMPA LR White resin was polymerised at 21 °C. dSTORM acquisition with 35 mM MEA in dSTORM buffer. Reanalysed from data acquired by Jonas Euchner during his Master's thesis (49). Rainbow look-up table from red to green to blue. Scale bar: XY) 20 µm, Z=1 µm.

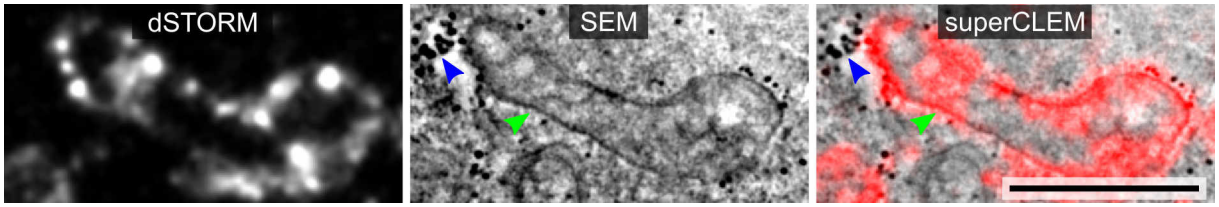

Fig. SI 17: CLEM alignment based on the mitochondria membrane. Correlative alignment of SEM micrograph and dSTORM reconstruction of AF647 labelled TOMM20-HaloTag in COS7 cells. Reanalysed from data acquired by Jonas Euchner during his Master's thesis (49). Scale bar: 1 µm.

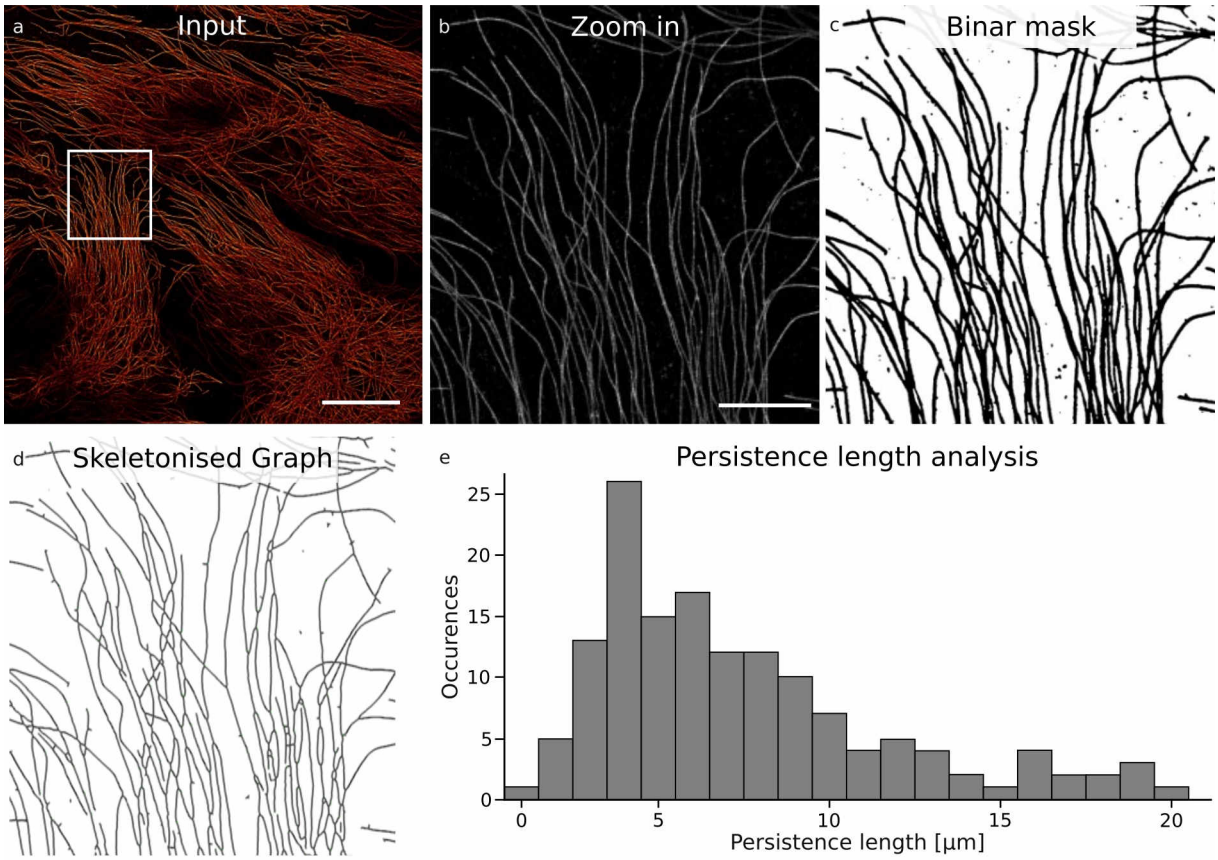

Fig. SI 18: Analysis of microtubule cytoskeleton based on persistence length. LSEC indirectly immunolabelled for microtubule were analysed in dSTORM. dSTORM data was used to determine the persistence length of microtubule in SASP-primed LSEC. a,b) dSTORM reconstruction. c) Generation of binary mask specific to the microtubule cytoskeleton. d) Skeletonisation of binary mask, followed by generation of network graph. e) Analysis of persistence length based on the skeletonised graph of microtubules. Scale bar: Scale bar: a) 20 µm, b-d) 5 µm.

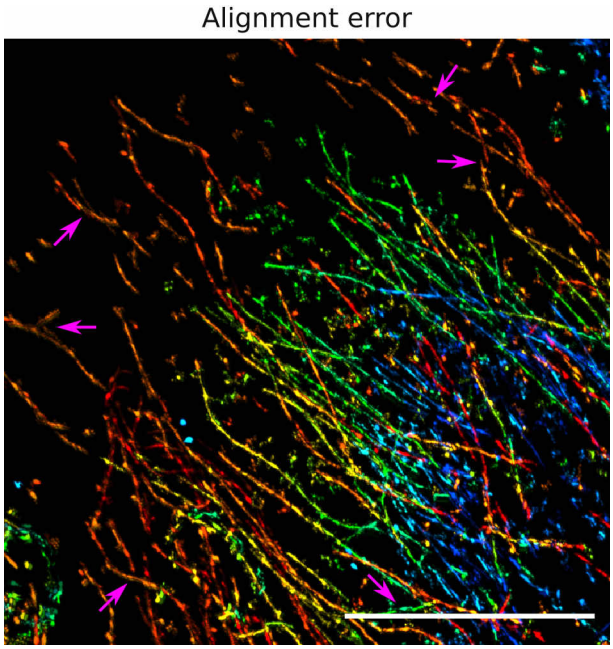

Fig. SI 19: Alignment error of serial sections on ITO coverslips. Purple arrows show imperfect alignment of serial sections. Local deformations were observed for sections deposited on ITO coverslips, caused by deactivation of the ITO surface during serial section generation. Surface passivation resulted in incomplete surface wetting and buckling of sections during the drying process. Scale bar: 10 µm.

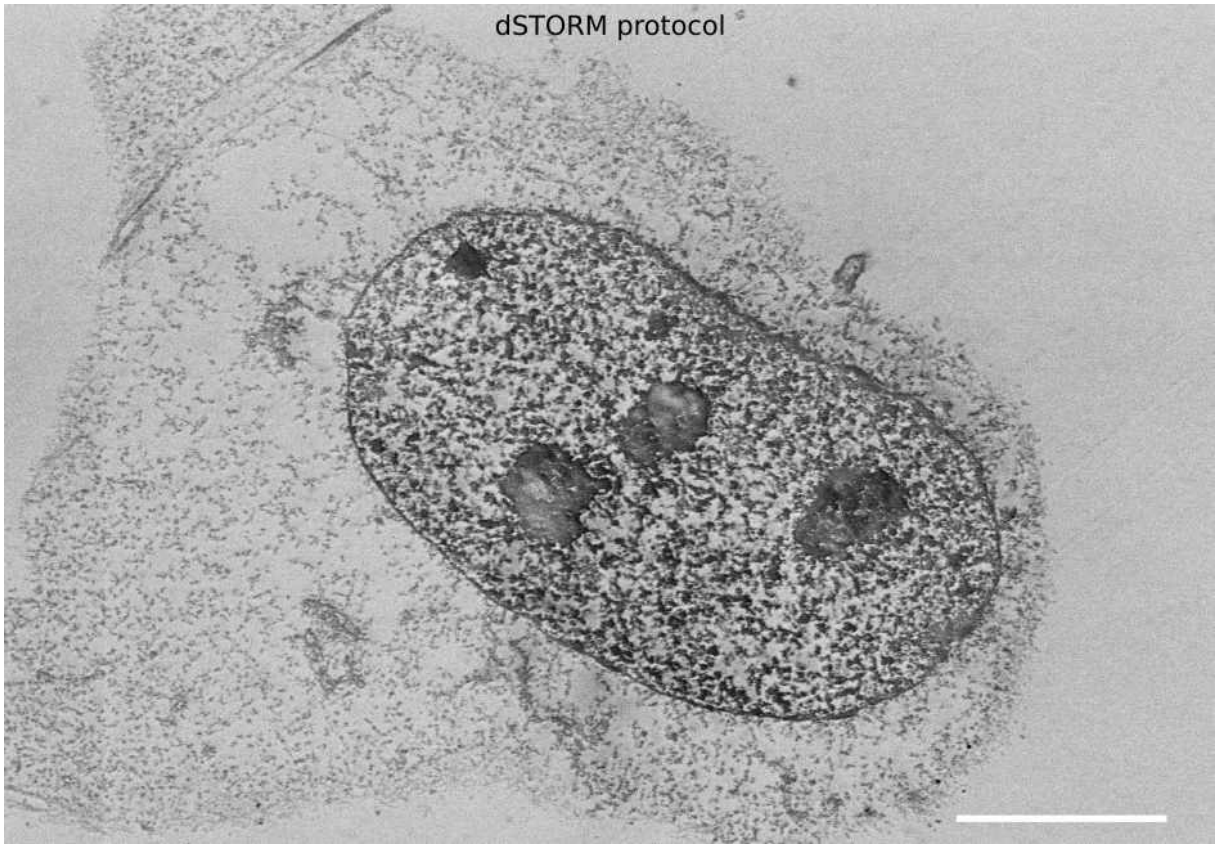

Fig. SI 20: Analysis of ultrastructural preservation in dSTORM protocol. SEM micrograph of cells prepared following a dSTORM protocol using high concentration Triton X-100 for permeabilisation and blocking (0.25%) with pre-fixation extraction step and $NaBH_4$ quenching (63). Scale bar: 5 µm.